Lapham, Paul (2023) *Atomistic simulations of nanoscale molecular and metal oxide junctions.* PhD thesis.

http://theses.gla.ac.uk/83647/

Copyright and moral rights for this work are retained by the author

A copy can be downloaded for personal non-commercial research or study, without prior permission or charge

This work cannot be reproduced or quoted extensively from without first obtaining permission in writing from the author

The content must not be changed in any way or sold commercially in any format or medium without the formal permission of the author

When referring to this work, full bibliographic details including the author, title, awarding institution and date of the thesis must be given

Enlighten: Theses
https://theses.gla.ac.uk/
research-enlighten@glasgow.ac.uk

Atomistic Simulations of Nanoscale Molecular and Metal Oxide Junctions

Paul Lapham

Submitted in fulfilment of the requirements for the Degree of Doctor of Philosophy

School of Engineering
College of Science and Engineering
University of Glasgow

University of Glasgow

May 2023

Abstract

The push to continually improve computing power through the further miniaturisation of electronic devices has led to an explosion of "post-Moore" technologies such as molecular electronics and quantum computing. The downscaling of electronic devices has enhanced the importance of quantum effects. As a result to aid in the understanding and development of new devices, accurate and efficient atomistic material modelling methods are crucial for guiding experiments. In this thesis first principle material modelling (e.g Density Functional Theory) is combined with the atomistic Non Equilibrium Green's Function quantum transport method to study how the electronic structure of two interesting junction systems relate to the electron transport through the junction. These two types of junctions, molecular and metal oxide, have crucial roles to play in the development of molecular based memories and superconducting quantum computing respectively.

The first half of this thesis shows how the electronic structure of Polyoxometalate molecules dominate their electron transport properties whilst their redox ability makes them promising for memory applications. The results of the simulations reveal how the charge-balancing counterions of Polyoxometalates increase the conductance of the molecular junctions by stabilisation of unoccupied states, this is a key discovery as the effect of counterions are typically ignored. Polyoxometalates can be altered easily by changing the identity of the central caged atom, enhancing device engineering possibilities. The IV characteristics and capacitance are computed for Polyoxometalates with different caged atoms, the results show how the charge transport and storage can be engineered by choice of caged species and redox state.

In the second half of this work, the archetypal Josephson junction, $Al/AlO_x/Al$ is explored. The goal was to understand from an atomistic point of view how the nature of the amorphous barrier influences the electron transport. The calculations provide evidence that the oxide concentration of the amorphous barrier significantly influences the resistance of the junction, it is found that oxygen deficient barriers lead to higher than expected critical currents. Unexpectedly the simulations here fail to show an exponential relationship between barrier length and resistance of the device. It is argued that there is an effective barrier length smaller than the physical barrier length due to thinner regions of the barrier. This highlights how important an understanding of the atomic structure of these junctions are for designing high quality junctions for superconducting qubits.

Statement of Originality

I certify that the thesis presented here for examination for a PhD degree of the University of Glasgow is solely my own work other than where I have clearly indicated that it is the work of others (in which case the extent of any work carried out jointly by me and any other person is clearly identified in it) and that the thesis has not been edited by a third party beyond what is permitted by the University's PGR Code of Practice. The copyright of this thesis rests with the author. No quotation from it is permitted without full acknowledgement. I declare that the thesis does not include work forming part of a thesis presented successfully for another degree. I declare that this thesis has been produced in accordance with the University of Glasgow's Code of Good Practice in Research. I acknowledge that if any issues are raised regarding good research practice based on review of the thesis, the examination may be postponed pending the outcome of any investigation of the issues

Acknowledgements

I would like to give my sincere thanks to my supervisor Professor Vihar Georgiev. I could not have wished for a better mentor, I am truly grateful for your continuous support over the last three years, you always made time for me and helped guide my academic and professional development. I will miss our extensive chats about science and of course football. Thank you for everything.

I would like to extend my gratitude to the Device Modelling Group, it was great to be part of a team with such great people and your support has been invaluable. I wish you all the greatest success for the future. I also want to thank Dr Oves Badami for helping me achieve my first journal article and for very stimulating chats on science and world affairs. A special mention must also go to Dr Ali Rezaei for your help with Josephson Junctions, NEGF and my brief voyage into the structure generator. But more importantly for your support and friendship.

Last but not least, I want to thank my fiancée Lucy. It is not an exaggeration to say I would not have reached this stage without your understanding, support and encouragement. You never let the little milestones go without celebration and have always believed in me. Thank you.

Contents

Abstract i

Statement of Originality ii

Acknowledgements iii

List of Publications xiv

List of Abbreviations xv

Introduction xvi

1 Theoretical Foundations **1**

1.1 The Electronic Structure Problem 1

1.1.1 Born-Oppenheimer Approximation 2

1.1.2 The Variational Principle 2

1.1.3 LCAO Basis Set approach for constructing wave functions 4

1.1.4 Many-electron wave functions 5

1.1.5 The Hartee Fock Method 6

1.2 Density Functional Theory 8

1.2.1 Initial Approximations 8

1.2.2 The Hohenberg-Kohn Existence Theorem 9

1.2.3 The Hohenberg-Kohn Variational Theorem 10

1.2.4 Kohn-Sham Self-consistent Field Methodology 11

1.2.5 The E_{xc} Functional 12

1.3 Tight Binding Density Functional Theory (DFTB) 15

1.3.1 Tight Binding Theory from Density Functional Theory 15

1.3.2 Zeroth Order Standard DFTB 16

1.3.3 SCC-DFTB Self Consistent Charge Extension 17

1.4 Nanoelectronic Transport 19

1.4.1 Background Concepts 19

1.4.2 Quantized Conductance 21

1.4.3 NEGF Method . . . 23
1.4.4 Poisson Equation . . . 25
1.5 Conclusion . . . 26

2 Molecular Memory 27
2.1 Introduction to Molecular Electronics . . . 27
2.2 Non-Volatile Flash Memory . . . 28
2.3 Molecular Memory . . . 30
2.3.1 Redox-Based Molecular Memory . . . 31
2.3.2 Polyoxometalates for Flash Memory . . . 33

3 Studying the electron transport of $[W_{18}O_{54}(SO_3)_2]^{4-}$ 36
3.1 Introduction . . . 36
3.2 Computational Methodology . . . 37
3.3 Results and Discussion . . . 37
3.3.1 Initial Molecule Exploration . . . 37
3.3.2 Single POM Molecular Junction Studies . . . 39
3.3.3 Exploring the Effects of Counterions . . . 47
3.4 Conclusion . . . 56

4 Further POM Studies 57
4.1 Exploring the Moiety Space of a POM . . . 57
4.1.1 Introduction . . . 57
4.2 Simulation Methodology . . . 58
4.2.1 General Computational Settings . . . 58
4.2.2 Estimating the Atomic-Scale Capacitance . . . 58
4.3 Results and Discussion . . . 59
4.3.1 Electronic structure of the POM Single Molecules . . . 59
4.3.2 Electronic structure of the POM Molecular Junctions . . . 64
4.3.3 Transport in the Molecular Junctions . . . 68
4.3.4 Estimating the Capacitance . . . 78
4.4 POM on SiO_2 for flash memory, challenges and next steps . . . 81
4.5 Conclusions . . . 83

5 Introduction to Josephson Junctions 85
5.1 A brief introduction to Quantum Computing . . . 85
5.1.1 What is a Qubit? . . . 86
5.1.2 Josephson junction Physics . . . 88
5.2 Variability and Noise in Josephson Junctions . . . 90
5.2.1 Examples of Simulating $Al/AlO_x/Al$ . . . 91

5.2.2 Conclusions 95

6 Studying the Oxide Stoichiometry of Al/AlO$_x$/Al 97
6.1 Introduction 97
6.2 Simulation Methodology 98
6.2.1 Computational Details 98
6.2.2 Creating the Junctions models using Molecular Dynamics 99
6.2.3 Transport Simulations 100
6.3 Results and Discussion 101
6.3.1 Creating the Junction Models 101
6.3.2 Studying the Influence of Oxide Stoichiometry on Current-Voltage Characteristics of Al/AlO$_x$/Al 103
6.3.3 Junction to Junction Variability of Al/AlO$_x$/Al models 110
6.3.4 Analysis of Transmission Pathways 113
6.3.5 Transmission Pathway Experiments 117
6.4 Conclusions 126

7 Exploring the barrier length of Al/AlO$_x$/Al 128
7.1 Introduction 128
7.2 Creating the Junctions Models 128
7.3 Initial Exploration of the barrier length 130
7.4 Further Study of the barrier length in Al/AlO$_{1.1}$/Al Josephson Junctions 137
7.4.1 Analysis of the Electron Density and Transmission Pathways Through the Barrier 140
7.4.2 The Simmons model for The Electron Tunnel effect. 147
7.4.3 Fitting to the Simmons model 150
7.5 Critical Discussion of the Findings of this Study 165
7.6 Conclusions 168

Conclusion 170

List of Tables

1 List of Abbreviations commonly used throughout this thesis. xv

3.1 Comparison of Selected Bond Lengths (Å) and Bond Angles (deg), HOMO-LUMO gaps for different DFT settings. 38

4.1 List of POM molecules and the caged species explored in this chapter. 58
4.2 Calculated Capacitance for the different POM Junctions in this study. 79
4.3 Respective Energy Gaps for different DFT functionals for SiO_2 and POM. In all cases SG15 Pseudopotential was used with a High Basis Set. 82

6.1 Calculated Resistance-Area Values (RA) and Critical Current density for the different aluminium oxide stoichiometries. 110
6.2 Calculated Resistance-Area Values (RA) and Critical Current density for the different Junction Samples. 112

7.1 Size and density parameters for the $AlO_{1.5}$ model barriers 130
7.2 Size and density parameters for the $AlO_{1.1}$ model barriers. 134
7.3 Fitted barrier heights (eV) for the model junctions in this study given by their physical barrier lengths. 152
7.4 Fitted barrier heights (eV) for the model junctions in this study given by their physical barrier lengths. 155
7.5 The extracted area and length parameters from the Simmons fitting. 163

List of Figures

1.1 Flowchart depicting the iterative process for solving the Electronic structure problem with Density Functional Theory 14
1.2 Visual representation of a simple device system. 20
1.3 Simple Picture of Electron Transport in a nanoscale device. 21
1.4 Device Structure for NEGF formalism, illustrating Source-Channel-Drain, self-energies for the contacts and central region (∑), H is the Hamiltonian of the central region. 23
1.5 Poisson iterative process. 25

2.1 Diagram of a typical Flash Memory Structure. 28
2.2 Current vs Gate Voltage Characteristics which illustrate typical program and erase functionality in a flash cell. 29
2.3 Fc-BzOH molecule studied by Li et al. [1] 31
2.4 Por-BzOH molecule studied by Li et al. [1] 31
2.5 Ferrocenylethanol used in the work by Zhu et al [2]. 32
2.6 Ruthenium Complex studied in the work by Zhu et al [2]. 32
2.7 A few examples of Polyoxometalate Structures showing the diversity of these class of molecules. Red= Oxygen, blue = Tungsten, turquoise = Molybdenum, orange = Phosphorus, yellow = Sulfur. 33

3.1 POM molecule in this study, with atom labels for bond data. W = blue, O = red, and S = yellow. O_1, O_2, and O_3 are all oxygen atoms which are labeled according to the oxo band in the molecule. O_1 = capping, O_2 = central, and O_3 = upper oxo bands. 38
3.2 a) Highest Occupied Molecular Orbital (HOMO) b) Lowest Unoccupied Molecular Orbital (LUMO). 39
3.3 The three Au-POM-Au configurations studied. 40
3.4 Comparison of HOMO-LUMO relative energy positioning and their respective frontier Kohn-Sham molecular orbitals. The blue dotted line marks the positioning Fermi energy of the electrodes. 41

3.5 Projected Local Density of States (LDOS) calculated at zero bias for (a) configuration 1, (b) configuration 2, and (c) configuration 3. The region spanning from 10 to 22 Å is the central region of the molecule. The pink regions are where there is high electron density. The green dotted line is the Fermi energy, which is set at 0 eV. 42
3.6 (a) Transmission spectra for all three configurations. (b) Transmission spectra with the dominant transmission eigenstates visualized for selected peaks. All energies are relative to E_F, which is set at zero. 44
3.7 Transmission Spectra showing $E - E_f$ vs log(T(E)) showing resonance broadening of transmission peaks. 45
3.8 Computed Current-Voltage (I-V) characteristics for all configurations. The current is electronic current rather than conventional: i.e. positive current describes electron movement from the source (left electrode) to the drain (right electrode). 46
3.9 Theoretical transmission spectra under applied bias (-1.0 to 1.0 V) for (a) configuration 1, (b) configuration 2, and (c) configuration 3. The yellow line corresponds to the energy range of the applied bias window. 48
3.10 Illustration of $[W_{18}O_{54}(SO_3)_2]^{4-}$ POM molecules surrounded by tetrapropylammonium (TPA) counterions. 49
3.11 Junction configuration for systems including the counterions TMA (left) and Cs^+ (right). 50
3.12 Comparison of HOMO-LUMO energies and the respective frontier Kohn-Sham molecular orbitals. The blue dotted line marks the Fermi Energy dominated by the electrodes. 51
3.13 PLDOS for the counterion-containing systems: (a) TMA containing system; (b) Cs containing system. 52
3.14 (a) Zero bias transmission spectra for configuration 1, with Cs^+ and TMA counterions. (b) Visualized transmission eigenstates for the first four peaks above the Fermi energy. Comparison of the energy states for the TMA-containing system (left) with the Cs^+-containing system (right). 53
3.15 Computed I-V curves for the counterion-containing systems. 55

4.1 Visualisation of the respective HOMO, LUMO and other unoccupied molecular orbital energies for all the POM molecules in this study. 60
4.2 Visualisation of the HOMO levels for the POMs in this study. 61
4.3 Visualisation of the LUMO levels for the POMs in this study. 62
4.4 Visualisation of the HOMO-LUMO levels for $W_{18}O_{54}$ ("Empty" POM). 62
4.5 Visualisation of the respective HOMO, LUMO and other unoccupied molecular orbital energies for all the POM molecular junctions in this study. 66
4.6 Visualisation of HOMO levels for the POM Junctions in this study. 67

4.7 Visualisation of LUMO levels for the POM Junctions in this study. 67
4.8 HOMO-LUMO levels for $W_{18}O_{54}$. 68
4.9 Transmission Spectrum for the POM Junctions with selected caged species (empty ($W_{18}O_{54}$), $(SO_3)_2^{-4}$, $(SO_4)_2^{-4}$, $(SeO_3)_2^{-2}$, $(SeO_3)_2^{-4}$) 69
4.10 Transmission Spectrum in log scale for the POM junctions with selected caged species (Empty ($W_{18}O_{54}$), $(SO_3)_2{}^{-4}$, $(SO_4)_2{}^{-4}$, $(SeO_3)_2{}^{-2}$, $(SeO_3)_2{}^{-4}$) 69
4.11 The Computed I-V curve for the Au-$[W_{18}O_{54}(SO_3)_2]^{4-}$-Au junction. The shape of the IV curve is typical for all of the POM junctions in this chapter. 71
4.12 Comparison of the Current-voltage characteristics for the POM Junctions with selected caged species (empty ($W_{18}O_{54}$), $(SO_3)_2^{-4}$, $(SO_4)_2^{-4}$, $(SeO_3)_2^{-2}$, $(SeO_3)_2^{-4}$) 72
4.13 Transmission Spectra for $[W_{18}O_{56}(WO_6)]^{6-}$ and $[W_{18}O_{56}(IO_6)]^{6-}$ molecular Junctions 73
4.14 The log scale Transmision spectrum for the $[W_{18}O_{56}(WO_6)]^{6-}$ molecular junction. spin-dependence is shown. 75
4.15 The log scale Transmission spectrum for the $[W_{18}O_{56}(IO_6)]^{6-}$ molecular junction with spin-dependence is shown. 76
4.16 Computed IV curves for both spin states in the $[W_{18}O_{56}(WO_6)]^{6-}$ molecular junction. 77
4.17 Computed IV curves for both spin states in the $[W_{18}O_{56}(IO_6)]^{6-}$ molecular junction. 78
4.18 Plot of electrostatic energy vs applied bias for the $[W_{18}O_{54}(SO_3)_2]^{4-}$ molecular junction. The capacitance is then extracted from this curve, given by $C = \frac{E}{V^2}$. . 79
4.19 Depiction of a hypothesized flash memory device using POMs as the storage element. 81
4.20 Example of SiO_2 slab and molecule configuration 82

5.1 Bloch Sphere representation of quantum states of a Qubit 86
5.2 Circuit diagram of a transmon 87
5.3 The energy diagram for a Quantum Harmonic Oscillator and Transmon illustrates the importance of anharmonicity in the Transmon circuit. 88
5.4 Diagram of a typical Josephson junction. In this case the archetypal Al/AlO_x/Al is considered. Where the two superconductors are Aluminium and the insulating barrier is Aluminium Oxide. It is shown the tunneling of a Cooper pair given by the Josephson Energy. 89

6.1 Illustration of the Al/AlO_x/Al Junction Model. 101
6.2 Radial Distribution comparing corundum (Crystalline Al_2O_3) and amorphous Al_2O_3 before and after optimization. 102

6.3 Comparison of Coordination Number and atomic structure for the different steps in junction creation. 103
6.4 PLDOS for the different oxide stoichioimetries; top left=0.8, top right= 1.1, centre left =1.2, centre right = 1.3, bottom left = 1.4, bottom right = 1.5. 104
6.5 Coordination Number Analysis to quantify difference in atomic structure across different aluminium oxide stoichiometries. 105
6.6 Current-Voltage (I-V) Curves for different oxide stoichiometries (0.8-1.5). . . . 106
6.7 Current-Voltage (I-V) Curves for different oxide stoichiometries (excluding 0.8). 107
6.8 PLDOS of $AlO_{1.5}$ at zero bias (top) and a bias of 1V (below). 108
6.9 RA vs Stoichiometry. 109
6.10 Comparison of the IV Curves 5 different $AlO_{1.1}$ Junction samples. 111
6.11 RA comparison across the five different samples. 111
6.12 Coordination Number Analysis across 5 samples of $Al/AlO_{1.1}/Al$. 112
6.13 PLDOS comparison for Sample B(top), D(middle), E(bottom). 114
6.14 Transmission Spectrum for the five different $AlO_{1.1}$ samples. 115
6.15 Sample B transmission spectra. Dotted box highlights the peaks associated with the IV curves. 116
6.16 Transmission Pathway for the peak at 0.03 eV in the transmission spectra for Sample B. 116
6.17 Transmission Pathway for Junction A at -0.04eV. 117
6.18 Transmission Pathway for Junction B at -0.03eV. 118
6.19 Transmission Pathway for Junction C at -0.17eV. 118
6.20 Transmission Pathway for Junction D at -0.15eV. 119
6.21 Transmission Pathway for Junction E at 0.013eV. 119
6.22 Highlighted atoms (in purple) for which the Transmission is concentrated at 0.03eV for Junction B. 120
6.23 a) Transmission Pathway at 0.03eV b) Complete Removal test structure. 121
6.24 Complete removal test transmission spectra. The respective resistances are also shown in the table. 121
6.25 a) Transmission Pathways at 0.21 eV for Junction B b) Transmission Pathways at 0.24eV for Junction B after removal of "hotspot" 122
6.26 Transmission Pathway at 0.4eV for Junction with removed hotspots 122
6.27 a)Junction B Pathway at 0.03eV with Al atoms circled that are to be removed b) The Pathway removal structure studied with the remaining dominant atoms highlighted in purple 123
6.28 transmission spectra for the Pathway Removal structure compared to Junction B with resistance values in the table insert 123

6.29 a) Transmission Pathway at 0.21eV for Junction B b) 0.25eV for the modified Junction 124
6.30 The transmission pathway from the disruption test. The highlighted atoms are oxygen atoms that have been converted from Al. 124
6.31 transmission spectra for Junction B and the disrupted pathway model. 125
6.32 a)Transmission Pathway for Junction B at 0.21eV, the circled atoms are the Al atoms that have been converted to oxygen b) Pathway after the change. 126

7.1 Illustration of how barrier length was measured in this work. Overlay of the Electrostatic difference potential with the junction configuration's YZ coordinates.130
7.2 Log of Resistance vs barrier length Data for $AlO_{1.5}$ Junctions. 131
7.3 Comparison of the Electrostatic Difference Potential for the $AlO_{1.5}$ barriers. The length is given as a multiple of the lenght in the "Z" coordinate. 132
7.4 Al-O Coordination Number comparison for the $AlO_{1.5}$ Junctions with different barrier lengths. 133
7.5 Resistance vs barrier length for the $AlO_{1.1}$ Junction models in this initial study. 134
7.6 Electrostatic difference potential for the 5 created barriers 0.5-0.9L with $AlO_{1.1}$. 135
7.7 Al-O Coordination Number for the amorphous barrier in the different $AlO_{1.1}$ junction models giving an insight to the local atomic structure in the barrier. . . 135
7.8 Comparison between log(Resistance) of $AlO_{1.1}$ and $AlO_{1.5}$ vs barrier length. . 136
7.9 Resistance vs barrier length for simulated Al/$AlO_{1.1}$/Al model junctions.The red line is a fit to the exponential function $y = ae^{bx}$. 137
7.10 Example of a hypothetical Crystalline Al/Al_2O_3/Al tunnel barrier studied in this work. 139
7.11 Plot of log(R) vs barrier length for the Al/Crystalline Al_2O_3/Al model junctions. The data shows a straight line fit (red dotted line) showing exponential relationship between R (resistance) and barrier length. 139
7.12 A Al/AlO_x/Al model studied here with a physical barrier length of 13.5 Å, with the direction of visualization of the XY cut planes clearly indicated (above). XY plane view is shown below. 141
7.13 Electron density cuts illustrating thinner regions in the barrier. Going across the barrier it is split evenly in 10 segments in the XY plane. Top left is the beginning of the barrier, bottom right is the end of the barrier. 141
7.14 Transmission Spectrum for the Al/AlO_x/Al model with 13.5Å barrier length. . 142
7.15 Transmission Pathway at Fermi Level for Junction Model with 13.5 Å barrier length. 143
7.16 Transmission Pathway at 0.2eV above Fermi for Junction Model with 13.5 Å barrier length. 143

7.17 Transmission Pathway at 0.31eV above Fermi for Junction Model with 13.5 Å barrier length. 144
7.18 Electon Density XY cuts evenly distributed across the 7.6 Å barrier model. . . 144
7.19 Transmission Spectrum for the Al/AlO_x/Al model with 13.5 Å barrier length. . 145
7.20 Transmission Pathway at Fermi Level for Junction Model with 7.6 Å barrier length. 146
7.21 Transmission Pathway at 0.04eV above Fermi for Junction Model with 7.6 Å barrier length. 146
7.22 Transmission Pathway at 0.37eV below Fermi for Junction Model with 7.6 Å barrier length. 147
7.23 Pictorial representation of a general case of a thin insulating barrier between two electrodes as described by Simmons [3]. 148
7.24 Diagrams for the rectangular barrier model under different bias conditions. . . . 149
7.25 Typical computed IV curve for one of the model junctions studied in this work. This example is for a Junction with a 10.7 Å barrier length. 150
7.26 Simmons Fit IV Curve for a barrier with 8.41 Åphysical barrier length fitted to the Rectangular Simmons model. 151
7.27 Plot of log(RA) vs Length for Resistance and Area values extracted from Simmons model fitting. 153
7.28 Plot of RA vs Length for model Junctions with barrier height 2.8-2.93 eV. . . . 153
7.29 Fitting of IV Curve from small voltage range to Simmons model. 154
7.30 Computed RA vs barrier length, using the extracted values for area and length from the small voltage Simmons fit. 156
7.31 Computed RA_{eff} vs barrier length for the Junctions with barrier height $\approx$ 2.9 eV. 157
7.32 logRA vs barrier length for Junctions with barrier heights ranging between 0.5-0.9eV. 158
7.33 IV Curves for voltages 0-100mV for all the junctions in this study. The dashed lines correspond to the junctions with barrier heights of 0.5-0.9eV. 159
7.34 Projected Density of States for all Junction models with barrier heights ranging from 0.56-0.90 eV. The Physical length (and length from Simmons fit) is also indicated in the title of the subplots. 160
7.35 Projected Density of States for Junction models with barrier heights $\approx$ 2.9 eV. The Physical length (and length from Simmons fit) is also indicated in the title of the subplots. 161
7.36 Projected Density of States for Junction models with barrier heights $\approx$ 2.9 eV. The Physical length (and length from Simmons fit) is also indicated in the title of the subplots. 162

List of Publications

1. Paul Lapham and Vihar Georgiev. Theoretically probing the relationship between barrier length and resistance in al/alox/al tunnel junctions. Solid-State Electronics, 197:108442, 2022

2. Paul Lapham and Vihar P Georgiev. Computational study of oxide stoichiometry and variability in the al/alox/al tunnel junction. Nanotechnology, 33(26):265201, 2022

3. Paul Lapham, Laia Vilà-Nadal, Leroy Cronin, and Vihar P. Georgiev. Influence of the contact geometry and counterions on the current flow and charge transfer in polyoxometalate molecular junctions: A density functional theory study. J. Phys. Chem. C, 125(6):3599–3610, 2021.

4. P. Lapham, O. Badami, C. Medina-Bailon, F. Adamu-Lema, T. Dutta, D. Nagy, V. Georgiev, and A. Asenov. A combined first principles and kinetic monte carlo study of polyoxometalate based molecular memory devices.2020 International Conference on Simulation of Semiconductor Processes and Devices (SISPAD), Kobe, Japan, 2020, pages 273–276, 2020.

5. Oves Badami, Toufik Sadi, Fikru Adamu-Lema, Paul Lapham, Dejiang Mu, Daniel Nagy, Vihar Georgiev, Jie Ding, and Asen Asenov. A Kinetic Monte Carlo study of retention time in a POM molecule-based flash memory. IEEE Trans. Nanotechnol., 14(8):1–1, 2020.

List of Abbreviations

Abbreviation	Meaning
C-AFM	Conductive Atomic Force Microscopy
CMOS	Complimentary Metal Oxide Semiconductor
DFT	Density Functional Theory
DFTB	Tight Binding Density Functional Theory
DOS	Density of States
EDP	Electron Difference Potential
FCC	Face Centred Cubic
GGA	Generalized Gradient Approach
HF	Hartree Fock
HOMO	Highest Occupied Molecular Orbital
JJ	Josephson Junctions
LCAO	Linear Combination of Atomic Orbitals
LDA	Local Density Approximation
LDOS	Local Density of Statea
LUMO	Lowest Unoccupied Molecular Orbital
MD	Molecular Dynamics
NEGF	Non Equlibrium Green's Function
PLDOS	Projected Local Density of States
POM	Polyoxometalate
SCF	Self-Consistent Field
SONOS	Silicon–Oxide-Nitride–Oxide–Silicon
SQUIDS	Superconducting Quantum Interference Device
TLS	Two Level System
VDW	Van der Waal Interactions

Table 1: List of Abbreviations commonly used throughout this thesis.

Introduction

The twentieth and twenty first century have seen rapid improvements in the quality of life, manufacturing, medicine, and scientific discovery thanks to the exponential growth in technology. Computational modelling is a vital tool for advancing knowledge of scientific phenomena, material discovery and engineering. It gives access to scales and experiments that are not accessible through practical methods, it also reduces costs and development time for taking products to market.

One of the greatest challenges faced in science and engineering is overcoming the limit in the miniaturisation of electronic devices in order to circumvent the slowing of Moore's law. Moore's law predicts that computing power of integrated circuits (number of transistors) will double approximately every two years [4]. The scaling limit is currently being reached. With devices down to the nanoscale, quantum phenomena play a vital role in electronic device performance [5]. Because of this, efficient nanoscale modelling techniques are required for understanding, designing and improving the next generation of electronic devices and nanotechnology.

Since the technology is reaching the quantum realms, first principle modelling techniques (ab-initio) take centre stage. The need for parameter free, quantum mechanics based modelling frameworks has never been greater. This when combined with quantum transport methods can give researchers a detailed, accurate and efficient toolkit for advancing nanotechnology. This thesis focuses on applying such a modelling framework to study two different interesting nanoscale devices from an atomistic approach (bottom up). The goal is to aid in the understanding of these devices and the challenges faced for their applications. The two different devices are both part of proposed post-Moore's law technologies. In this thesis, two main junction systems are explored computationally: Polyoxometalate (POM) molecular junctions, which show promise for molecular memory applications. The other system is so-called Josephson junctions (JJ), which are critical component of superconducting qubits, a leading quantum computing architecture.

Chapter 1 of this thesis describes in detail the modelling approach. Specifically, the first principles electronic structure method; Density Functional Theory (DFT), which is the most popular for exploring and describing material systems is explained in detail including its historical context of solving the many body problem. Additionally a semi-empirical approximation to Density Functional Theory is discussed as a more efficient tool for studying nanoscale devices.

Finally, the theory for nanoscale electronic transport is discussed and the state-of-the-art device modelling method Non Equilibrium Green's Function (NEGF) is explained.

In Chapter 2 a brief overview of molecular electronics and flash memory technology is given and the literature concerning molecular memories is critically reviewed. The previous work on the POM molecule is discussed to give the context for the work in this thesis. Chapter 3 thoroughly explores the properties and electron transport in $[W_{18}O_{54}(SO_3)_2]^{4-}$, a POM molecule, including the effects of charge balancing counterions. Chapter 4 builds on Chapter 3 by exploring other POM molecules as junctions and exploring the atomic scale capacitance.

In Chapter 5, the focus of the thesis shifts to Josephson junctions for superconducting qubit applications. A brief introduction to quantum computing is given and the challenges with Josephson junctions is discussed. Previous works in simulating Josephson junctions in the literature is critically reviewed to place this work into context. In Chapter 6 the oxide stoichiometry is of model Josephson junction is studied computationally and the junction to junction variability is studied. Finally, in Chapter 7 the barrier length, considered a key parameter in Josephson junctions, is studied with respect to its effect on the electron transport of this device.

Chapter 1

Theoretical Foundations

1.1 The Electronic Structure Problem

To understand the behaviour of materials and molecular systems it is essential to understand the underlying electronic structure of the components that build that system. Hence a correct description of the electronic structure is vital for studying material systems and their properties..

Understanding the electronic structure of molecules and condensed matter requires solving the time-independent *Schrödinger* equation [6].

$$\hat{H}\Psi = E\Psi \tag{1.1}$$

where H is the Hamiltonian operator, Ψ is the wavefuction and E is the total energy of the system. From equation 1.1 it can be deduced that the wave function is an eigenfunction of the Hamiltonian. Therefore by correctly describing the wave function of a given system, the properties of that system can be calculated and understood.

The Hamiltonian operator, H, consists of all the different energy interactions of a system that make up the total energy. For a molecular or condensed matter state, the total energy is made up by the sum of coloumbic interactions between the nuclei(n,m) and the electrons(e) [7].

$$\hat{H} = \hat{T}_n + \hat{T}_e + \hat{V}_{ee} + \hat{V}_{ne} + \hat{V}_{nm} \tag{1.2}$$

$$= -\sum_i \frac{\hbar}{2m_e}\nabla_i^2 - \sum_k \frac{\hbar}{2m_k}\nabla_k^2 + \sum_{i<j}\frac{e^2}{r_i j} - \sum_i\sum_k \frac{e^2 Z_k}{r_{ik}} + \sum_{k<l}\frac{e^2 Z_k Z_l}{r_{kl}} \tag{1.3}$$

where T and V are the kinetic and potential energy operators, i and j denote electrons, k and l are nuclei, r denotes particle distance, m is mass and $\hbar$ is Planck's constant divided by 2π (Dirac's constant), e is the fundamental electron charge, Z is the atomic number and finally ∇^2 is the Laplacian operator.

1.1.1 Born-Oppenheimer Approximation

Given the multiple interactions involved in many-electron systems, the *Schrödinger* equation can only be solved exactly for hydrogen. As a result, approximations are required to find meaningful solutions to this problem.

The first approximation which significantly simplifies the problem is the Born-Oppenheimer approximation. Since nuclear motion is on the timescale of 10^{15}s, much slower than the 10^{18}s of electronic motion (due to their difference in mass), then the nuclei can be treated as if they are fixed bodies with electrons moving around them reducing the terms of the Hamiltonian and the computational effort drastically. The Hamiltonian therefore becomes:

$$\hat{H}_{el} = -\sum_{i} \frac{\hbar}{2m_e} \nabla_i^2 + \sum_{i<j} \frac{e^2}{r_i j} - \sum_{i} \sum_{k} \frac{e^2 Z_k}{r_{ik}} \tag{1.4}$$

In general, the *Schrödinger* equation has many acceptable wave functions for a given molecule or system, each of which are characterized by different eigenvalues E. For this to remain true, the many wave functions are assumed to be orthonormal. Mathematically, in Cartesian space, this can be described as follows:

$$\int \psi_i \psi_j dr = \int \int \int \psi_i \psi_j dx dy dz = \delta_{ij} \tag{1.5}$$

where δ_{ij} is the Kronecker delta. The assumption of orthogonality implies that the integral described above is zero when i$\neq$ j and 1 when i=j.

1.1.2 The Variational Principle

The fundamental postulate of quantum mechanics is that a wave function exists for any system and through operators acting on this wave function the observable properties of the system can be obtained. Unfortunately, none of the equations so far offer any insight into how a set of orthonormal wave functions of a system are found. As a starting point, assume it is possible to select arbitrarily a function, Φ, which is a function of electronic and nuclear coordinates through which a Hamiltonian can operate on. If, as declared before, a set of orthonormal wave functions, ψ_i are complete and potentially infinite, then said function Φ has to be a linear combination of ψ_i, mathematically:

$$\Phi = \sum_{i} c_i \psi_i \tag{1.6}$$

where c_i refers to coefficients relative to the combination. Indeed, the individual ψ_i is still unknown as are the coefficients. However, given the constraint of normality of Φ :

$$\begin{aligned}\int \Phi^2 dr = 1 &= \int \sum_i c_i \psi_i \sum_j c_j \psi_j \\ &= \sum_{ij} c_i^* c_j \int \psi_i \psi_j dr \\ &= \sum_{ij} c_i^* c_j \delta_{ij} \\ &= \sum_i c_i^2\end{aligned} \tag{1.7}$$

To evaluate the energy of this eigenfunction, we rearrange the *Schrödinger* equation to solve for E by taking the intergration over cartesian space, dr:

$$\begin{aligned}\int \Phi H \Phi dr &= \int (\sum_i c_i \psi_i) H (\sum_j c_j \psi_j) dr \\ &= \sum_{ij} c_i^* c_j \int \psi_i H \psi_j dr \\ &= \sum_{ij} c_i^* c_j E_{ij} \delta_{ij} \\ &= \sum_i c_i^2 E_i\end{aligned} \tag{1.8}$$

This shows that the coefficients, c_i, can determine the energy associated with the generic wave function ϕ. Though, their values are still unknown. What is known from quantum mechanics, is there must be a lowest energy value for E, the ground state, E_0. Therefore:

$$\int \Phi H \Phi dr - E_0 \int \Phi^2 dr = \sum_i c_i^2 (E_i - E_0) \tag{1.9}$$

By definition of the ground state, the term $(E_i - E_0)$ is greater than or equal to zero, assuming the coefficients are real numbers, also greater than or equal to zero results in:

$$\begin{aligned}\int \phi H \phi dr - E_0 \int \phi^2 dr \geq 0 \\ \frac{\int \phi H \phi dr}{\int \phi^2 dr} \geq E_0\end{aligned} \tag{1.10}$$

This equation, known as the variational principle, is extremely important for solving the electronic structure problem. It gives a platform for finding the best wave function to describe the ground state of a system. In essence, the lower the energy the better the guess. Note, the choice of wave function is not restricted to a linear combination of wave functions but can be constructed using all mathematical tools that have been developed.

1.1.3 LCAO Basis Set approach for constructing wave functions

The Linear Combination of Atomic Orbitals (LCAO) Basis set approach is a method for choosing a guess wave function to obtain the ground state of a system. The approach is to construct a wave function as a linear combination of atomic orbitals, φ.

$$\phi = \sum_{i=1}^{N} a_i \varphi_i \tag{1.11}$$

where a_i is a coefficient, and the set of N functions is the 'basis set' to describe the molecular orbitals in a system. The atomic orbitals (atomic wave functions) correspond to the 1s, 2s, 3p, 3s, 3p etc.. orbitals which arise from the eigenfunctions of Hydrogen. The square of the wave function represents a probability density, intuitively giving a probability of where the electrons are likely to be in space. Hence, for molecular systems, combining atomic orbitals is a sensible and efficient approach to describing the molecular orbitals as the basis set for the wave function of a multi-electronic system.

Using the guess wave function, the basis set, the energy of the system can be evaluated using the equation of the variational principle.

$$\begin{aligned} E &= \frac{(\sum_i a_i \varphi_i) H (\sum_j a_j \varphi_j) dr}{\int (\sum_i a_i \varphi_i)(\sum_j a_j \varphi_j) dr} \\ &= \frac{\sum_{ij} a_i^* a_j \int \varphi_i H \varphi_j dr}{\sum_{ij} a_i^* a_j \int \varphi_i \varphi_j dr} \\ &= \frac{\sum_{ij} a_i^* a_j H_{ij}}{\sum_{ij} a_i^* a_j S_{ij}} \end{aligned} \tag{1.12}$$

Here the "matrix elements" have been introduced, H_{ij} the "resonance integral" and S_{ij} the "overlap integral". The overlap integral describes the extent to which any two basis functions overlap in space. The goal is a minimization problem, find the value of the coefficients, a, for which the energy is at its minimum. Mathematically this is:

$$\frac{\delta E}{\delta a_k} = 0 \qquad - \forall k \tag{1.13}$$

Solving this partial derivative leads to the N equations which must be satisfied:

$$\sum_{i=1}^{N} a_i (H_{ki} - E S_{ki}) = 0 \qquad - \forall k \tag{1.14}$$

The set of N equations involves N number of "a_i" unknowns. These types of equations have a non-trivial solution if and only if the determinant is equal zero. This determinant is the secular

equation.

$$\begin{vmatrix} H_{11}-ES_{11} & H_{12}-ES_{12} & \cdots & H_{1N}-ES_{1N} \\ H_{21}-ES_{21} & H_{22}-ES_{22} & \cdots & H_{2N}-ES_{2N} \\ \vdots & \vdots & \ddots & \vdots \\ H_{N1}-ES_{N1} & H_{N2}-ES_{N2} & \cdots & H_{NN}-ES_{NN} \end{vmatrix} = 0 \tag{1.15}$$

For this secular equation, there will be N energies E_j which result in a different set of coefficients, a_{ij}. These coefficients will result in the optimum wave function for that given basis set.

1.1.4 Many-electron wave functions

The previous section described how to construct one electron wave functions. As a consequence, inter-electronic repulsion is not taken into account, though it is key for computing the electronic structure of materials. If we consider the one electron Hamiltonian:

$$h_i = -\frac{1}{2}\nabla_i^2 - \sum_{k=1}^{M} \frac{Z_k}{r_{ik}} \tag{1.16}$$

where M is the total number of Nuclei. The eigenfunctions of this Hamiltonian must satisfy the corresponding one electron *Schrödinger* equation:

$$h_i \psi_i = \varepsilon_i \psi_i \tag{1.17}$$

Since, the Hamiltonian operator is separable and can be seen as the sum of single electron Hamiltonians, similarly, a many-electron wave function can be constructed as products of one-electron eigenfunctions. Given by the "Hartree Product" wave function:

$$\Psi_{HP} = \psi_1 \psi_2 ... \psi_N \tag{1.18}$$

To take into account the inter-electronic repulsion, the operator for which its eigenfunction is a single electron wave function, ψ_i, becomes:

$$h_i = -\frac{1}{2}\nabla_i^2 - \sum_{k=1}^{M} \frac{Z_k}{r_{ik}} + V_i(j) \tag{1.19}$$

The $V_i(j)$ term is an interaction potential with all other electrons in occupied orbitals (j), this repulsion is given by

$$V_i(j) = \sum_j \int \frac{\rho_j}{r_{ij}} dr \tag{1.20}$$

where ρ_j is the probability density for electron j.This repulsive term is analogous to the attractive nuclear-electron term, except the nuclei are treated as point charges, however, electrons are

described by as wave functions, therefore the charge is spread out. It is worth noting that the probability density of an electron is given by the square modulus of its wave function.

An initial guess for the ground-state many electron wave function is constructed through the use of Slater Determinants. When constructing Slater-Determinants, it is vital to remember that all electrons have the property spin, given by a spin quantum number. In addition, the Pauli exclusion principle must always be obeyed; that is two electrons cannot be characterized by the same set of quantum numbers. In general, a Slater Determinant is expressed as:

$$\Psi_{SD} = \frac{1}{\sqrt{N!}} \begin{vmatrix} \chi_1(1) & \chi_2(1) & \cdots & \chi_N(1) \\ \chi_1(2) & \chi_2(2) & \cdots & \chi_N(2) \\ \vdots & \vdots & \ddots & \vdots \\ \chi_1(N) & \chi_2(N) & \cdots & \chi_N(N) \end{vmatrix} \tag{1.21}$$

Where N is the total number of electrons and χ is the product of the spatial orbital and the electron spin, i.e spin-oribtal. Manifested in the Slater Determinant construction is the indistinguishability of quantum particles, the quantum mechanical spin exchange, and the orthogonality of two different spins.

1.1.5 The Hartee Fock Method

With the ground work of the electronic structure problem in place, in this section one of the first "successful" methods for solving the *Schrödinger* equation of many-electron systems will be discussed: The Hartree Fock self-consistent field method [8]. The equations that will be presented will assume the use of wave functions represented by a single Slater Determinant:

In the same vein as the Hamiltonian operator, the one electron Fock operator is given as

$$f_i = -\frac{1}{2}\nabla_i^2 - \sum_{k}^{Nuclei} \frac{Z_k}{r_{ik}} + V_i^{HF}(j) \tag{1.22}$$

The final term of the equation is the HF potential, which describes the average potential experienced by the electron i, due to the other electons, mathematically it is given by:

$$V_i^{HF}(j) = \sum_j (\hat{J}_i(j) - \hat{K}_i(j)) \tag{1.23}$$

$\hat{J}_i$ is the Coulomb operator defined as:

$$\hat{J}_i \left| \psi_j(2) \right\rangle = \langle \psi_i(1) | \frac{1}{r_{12}} \left| \psi_i(1) \psi_j(2) \right\rangle \tag{1.24}$$

and $\hat{K}_i$ is the exchange operator, akin to a correction term of the classical Coulomb electron repulsion. This term takes into account the effects of spin correlation and is given by:

$$\hat{K}_i \left|\psi_j(2)\right\rangle = \langle\psi_i(1)| \frac{1}{r_{12}} \left|\psi_i(1)\psi_j(2)\right\rangle \tag{1.25}$$

With the Fock operator described, the many-body problem can be reduced to a set of one-particle eigenvalue problems, for which the best wave functions that describe the lowest energy based on the variational principle need to be found. As a result the so-called Hartree Fock equations can be derived as:

$$\hat{f}_i \psi_i = \varepsilon_i \psi_i \tag{1.26}$$

The equation clearly mirrors the *Schrödinger* equation. Here, the orbital ψ_i is an eigenfunction of the Fock operator with a corresponding eigenvalue, ε_i, which describes the energy of the system. The HF method, consists of obtaining the ψ_i by solving this eigenvalue problem with the Fock operator. However, careful examination of the Fock operator shows that it depends on the orbitals of all the other electrons, so the problem has to be solved self consistently. Essentially, an initial guess of the wave function is made and its average potential is calculated. This calculated field potential is used to find a new set of orbitals from the HF equation. This is repeated until self-consistency is achieved. Practically, this is done by using a finite set of basis functions, known as basis set (ϕ_α, which is made up from atomic orbitals following the LCAO method as described above). So an initial wave function guess has the form:

$$\psi_i = \sum_{\alpha=1}^{M} c_{\alpha i}\phi_\alpha \tag{1.27}$$

The Hartree-Fock equations can be rewritten as:

$$\hat{f}_i \sum_{\alpha=1}^{M} c_{\alpha i}\phi_\alpha = \varepsilon_i \sum_{\alpha=1}^{M} c_{\alpha i}\phi_\alpha \tag{1.28}$$

The M equations can be described a a set of matrix equations for the expansion coefficients given by the Roothan-Hall equation [9]:

$$FC = SC\varepsilon \tag{1.29}$$

where ε is a diagonal matrix of all the orbital energies, S is the overlap matrix, F contains all the Fock matrix elements and C is an M×M matrix for the expansion coefficients $c_{\alpha i}$.

$$S_{\alpha\beta} = \left\langle\phi_\alpha\middle|\phi_\beta\right\rangle \tag{1.30}$$

$$F_{\alpha\beta} = \left\langle\phi_\alpha\middle|\hat{f}\middle|\phi_\beta\right\rangle \tag{1.31}$$

The Hartree-Fock method becomes a matrix eigenvalue problem, where by solving the

Roothan-Hall equations with an M basis function for a system of N electrons results in 2M spin orbitals, N are occupied, 2M-N unoccupied orbitals of the system. Therefore, the larger the basis set, usually described as a Slater determinant, the greater the flexibility in solving the expectation value for the energy of the system,thus improving the accuracy.

Whilst the Hartree Fock method was a significant step forward in the field of theoretical and computational chemistry, it suffered from a few flaws which meant although qualitatively it could describe a plethora of systems very well, it is not quantitatively accurate enough. Its major drawback is it uses a mean-field approximation and as a result electron correlation (Coloumbic correlation in particular) is not accounted for and leads to large deviations from experiments.

1.2 Density Functional Theory

The motivation for Density Functional Theory (DFT) stems from the non-intuitive nature of the wave function. Though the wave function can be described mathematically and operators can be applied to it to extract physical meaning, the wave function itself has no physical interpretation. Only that the square modulus returns a probability density. A wave function cannot be determined experimentally, the goal is to have a theoretical framework based on a physical observable that can solve the Schr*ödinger* equation. As described previously, the Hamiltonian operator which acts on the wave function, only depends on the physical positions of atoms, their atomic number and the number of electrons. Thus, a far more intuitive observable would be to use the electron density, ρ, which can be measured experimentally and also is related to the total number of electrons in the system. Integrating the electron density with respect to space gives the number of electrons in that given space:

$$N = \int \rho(r)dr \tag{1.32}$$

In addition, the local maxima of the electron density result from the positions of the nuclei which act effectively as point charges, hence information of the nuclei can be deduced from the electron density of a given system. Another considerable advantage of using electron density is that electron correlation (how much the movement of one electron is influenced by the presence of all other electrons) is already taken into account.

1.2.1 Initial Approximations

Early approximations consisted of describing the energy of a system with respect to density [7]. In the simplest approach, the system is considered to be classical, thus the potential energy the nucleus-electron potential is given by:

$$V_{ne}[\rho(r)] = \sum_{k}^{nuclei} \int \frac{Z_k}{|r - r_k|} \rho(r) dr \tag{1.33}$$

and for the self-repulsion of electrons:

$$V_{ee}[\rho(r)] = \frac{1}{2} \int \int \frac{\rho(r_1)\rho(r_2)}{|r_1 - r_2|} dr_1 dr_2 \tag{1.34}$$

The kinetic energy for a continuous charge distribution was calculated by Thomas and Fermi in 1927 and is given by [10]:

$$T_{ueg}[\rho(r)] = \frac{3}{10}(3\pi^2)^{2/3} \int \rho^{5/3}(r) dr \tag{1.35}$$

As the V and T terms introduced above are functions of density, and density is a function of three-dimensional space coordinates, these terms are "density functionals" hence the term DFT. However, the initial foundations of DFT were not accurate or rigorous enough for molecular systems, and found application only within solid-state physics. Although discarding the wave function and focusing on a physical observable, the electron density, gave a more intuitive approach, there was still no rigorous formulation to effectively solve the many-body problem. The problem lay in how to effectively describe the Hamiltonian based on the electron density. The first steps to turn DFT into the successful quantum chemical methodology it is today, relied on two critical theorems by Hohenberg and Kohn in 1964 [11].

1.2.2 The Hohenberg-Kohn Existence Theorem

The “Existence Theorem” states that the external potential applied on a system is defined as a unique functional of the electronic density; the external potential V_{ext} which is dependent on the presence of the nuclei [11].

$$\rho_0 => N, Z, R => V_{ext} => \hat{H} => \psi_0 => E_0 \tag{1.36}$$

In DFT, electrons interact with each other and with an "external potential" based on the attraction to the nuclei. This must be unique to the ground state electron density and thus relates to a unique Hamiltonian operator and wave function. This creates a link between the wave function and electron density. The proof relies on showing that an assumption to the contrary gives an impossible result. Assume that two different external potentials (v_a and v_b) can correspond to the same nondegenerate ground state density, ρ_0. Applying the variational theorem of molecular orbital theory described above:

$$E_{0,a} < \left\langle \psi_{0,b} \middle| H_a \middle| \psi_{0,b} \right\rangle \tag{1.37}$$

This is that the expectation value of Hamiltonian a (containing v_a) over the wave function b,

must be higher than ground state energy of a. Manipulating the expression above:

$$\begin{aligned} E_{0,a} &< \langle \psi_{0,b} | H_a - H_b + H_b | \psi_{0,b} \rangle \\ &< \langle \psi_{0,b} | H_a - H_b | \psi_{0,b} \rangle + \langle \psi_{0,b} | H_b | \psi_{0,b} \rangle \\ &< \langle \psi_{0,b} | v_a - v_b | \psi_{0,b} \rangle + E_{0,b} \end{aligned} \tag{1.38}$$

Given that the potentials, v, are one electron operators, the integral can be re-written in terms of density:

$$E_{0,a} < \int [v_a(r) - v_b(r)] \rho_0(r) dr + E_{0,b} \tag{1.39}$$

As a and b just correspond to different potentials for the same system, these indices can be interchanged in the above inequality to give:

$$E_{0,b} < \int [v_b(r) - v_a(r)] \rho_0(r) dr + E_{0,a} \tag{1.40}$$

By adding these two inequalities and noting that the ground state densities associated with wave functions a and b are the same, then the integrals must sum to zero.

$$\begin{aligned} E_{0,a} + E_{0,b} &< \int [v_a(r) - v_b(r)] \rho_0(r) dr + \int [v_b(r) - v_a(r)] \rho_0(r) dr + E_{0,b} + E_{0,a} \\ &< \int [v_a(r) - v_b(r) + v_b(r) - v_a(r)] \rho_0(r) dr + E_{0,b} + E_{0,a} \\ &< E_{0,b} + E_{0,a} \end{aligned} \tag{1.41}$$

The result, is that the sum of two energies is less than itself, which is of course impossible. Hence, the non-degenerate ground state density must determine a unique external potential and Hamiltonian, and thus the wave function, finally providing a crucial link between wave function and density.

1.2.3 The Hohenberg-Kohn Variational Theorem

The first theorem was crucially important in showing that a unique functional of density exists, but offers no indication of how the density of a system can be predicted. Like in Molecular Orbital theory it can be shown that the density of a system obeys a variational principle, providing a means to find the ground-state density. So for a given system there exists a candidate density, for which the integral provides the number of electrons, N. Taking into account that for that density there exists a candidate wave function and Hamiltonian. The the energy expectation value can be evaluated given:

$$\langle \psi_{cand} | H_{cand} | \psi_{cand} \rangle = E_{cand} \geq E_0 \tag{1.42}$$

Thus, the density cam be varied, and the lowest evaluated energy is closest to the true ground-state density. Though pivotal in determining a framework for solving the many-body problem as a function of density, there is still no rational procedure to choosing improved density. In addition, at this stage, the process still relies on solving the *Schrödinger* equation, which defeats the purpose of the motivation behind using electron density. Although it has been shown that the electron density can be related directly to the wave function and follows a variational principle, this procedure is still not simpler than wave function based calculations.

1.2.4 Kohn-Sham Self-consistent Field Methodology

As described above, though the electron density can be linked to the Hamiltonian and the wave function,until now a simpler method is yet to be described. The main difficulty is in the electron-electron interaction term for the Hamiltonian. In 1965, Kohn and Sham suggested that the problem would be much simpler for a non-interacting system of electrons [12]. So the approach is to start from a fictitious system of non-interacting electrons with a ground-state density that is the same as the ground state density of a system that do interact [13, 14]. For this case, the energy can be given by:

$$E[\rho(r)] = T_{ni}[\rho(r)] + V_{ne}[\rho(r)] + V_{ee}[\rho(r) + \Delta T[\rho(r)] + \Delta V_{ee}[\rho(r)] \tag{1.43}$$

where the energy is the sum of the kinetic energy of the non-interacting electrons, the nuclear-electron interaction, the classical electron-electron repulsion, the correction to the kinetic energy based on the interacting nature of electrons and all non-classical corrections to the electron electron repulsion. For the case where, density is expressed as Slater-Determinantal wave functions, χ_i, for N number of electrons:

$$E[\rho(r)] = \sum_i^N (\langle\chi_i| - \frac{1}{2}\nabla_i^2 |\chi_i\rangle) - \langle\chi_i| \sum_k^{nuclei} \frac{Z_k}{|r_i - r_k|} |\chi_i\rangle) + \sum_i^N (\langle\chi_i| \frac{1}{2} \int \frac{\rho(r')}{|r_i - r'|} dr' |\chi_i\rangle + E_{xc}[\rho(r)]$$

In this expression, a new term $E_{xc}[\rho(r)]$, which is the exchange-correlation (XC) energy has been introduced. This term includes the ΔT and ΔV_{ee} terms from before that are "difficult" to solve. Although known as exchange-correlation energy, in addition, the correction for classical self-interaction and also the difference in kinetic energy of the fictitious system and the real one is also included.

The strategy to solve this problem, as before, is to find the orbitals,χ_i, that minimize E, creating a pseudo-eigenvalue problem:

$$h_i^{KS} \chi_i = \varepsilon_i \chi_i \tag{1.44}$$

where h_i^{KS} is the Kohn-Sham(KS) one electron operator, which is defined by:

$$h_i^{KS} = -\frac{1}{2}\nabla_i^2 - \sum_k^{nuclei} \frac{Z_k}{|r_i - r_k|} + \frac{1}{2}\int \frac{\rho(r')}{|r_i - r'|}dr' + V_{xc} \quad (1.45)$$

V_{xc} is the functional derivative which can be thought of as the one electron operator for which the expectation value of the KS slater determinant is E_{xc} and is given by:

$$V_{xc} = \frac{\delta E_{xc}}{\delta \rho} \quad (1.46)$$

The energy that is being minimized is exact, so the orbitals χ must provide the exact density. To determine the KS orbitals, the approach is similar to before, expressing a basis set of functions, ϕ and determining the orbital coefficients by solving the secular equation as an iterative SCF procedure (analogous to that for HF theory), where the elements $F_{\alpha\beta}$ are replaced by $K_{\alpha\beta}$ such that:

$$K_{\alpha\beta} = \langle\phi_\alpha| -\frac{1}{2}\nabla_i^2 - \sum_k^{nuclei} \frac{Z_k}{|r_i - r_k|} + \frac{1}{2}\int \frac{\rho(r')}{|r_i - r'|}dr' + V_{xc}\,|\phi_\beta\rangle \quad (1.47)$$

An important point about DFT, as derived to this point, is that it is an exact theory (there are no approximations). Compared to HF which is an approximate theory. However, the E_{xc} operator is unknown and so the equations are solved approximately.

1.2.5 The E_{xc} Functional

Previously, DFT was derived and shown to be an exact theory. The caveat is that the form of the exchange-correlation functional is unknown, thus the DFT equations and Kohn-Sham SCF methodology cannot be solved exactly. Instead, approximations have to be made for the E_{xc} in order to solve DFT. This is the key problem in DFT, choosing the right functional for the exchange-correlation term to accurately describe the system of interest. In general, the E_{xc} is expressed as:

$$E_{xc}[\rho(r)] = \int \rho(r)\varepsilon_{xc}[\rho(r)]dr \quad (1.48)$$

where the functional depends on the electron density and its interaction with an electron density dependent ε_{xc} which is the 'energy density'. This term is considered a sum of the exchange and correlation contribution. Spin can also be introduced into DFT, given by the normalized spin polarization $\zeta(r)$.

$$\zeta(r) = \frac{\rho^\alpha(r) - \rho^\beta(r)}{\rho(r)} \quad (1.49)$$

where $\rho^{\alpha/\beta}$ are the up and down spin densities at any position.

There are many approaches to approximating the exchange correlation functionals in DFT

[15, 16]. One of the simplest is the "Local Density Approximation" (LDA). The majority of succesful LDA functionals were derived from the homogeneous electron gas model. In "LDA" the exchange correlation energy depends solely on the value of electron density at each point in space. The typical form is given by:

$$E^{LDA}[n] = \int n(r)\varepsilon^{LDA}(n(r))dr \tag{1.50}$$

where $\varepsilon^{LDA}(n(r))$ is the exchange correlation energy density derived from a homogeneous gas of density $n(r)$. The different LDA functionals consist of different parameterizations designed to be applicable to different systems. The most commonly used general LDA functional is the PZ functional, parameterized by Perdew and Zunger [17]. In LDA functionals the density is assumed to be the same everywhere, this leads to an underestimation of exchange energy and an overestimation of correlation. Thus have limited applications (often a successful approximation for metals). To correct for the spatially uniform electron density, local variations in the density are taken into account. In other words, the gradient of the density. This led to the next set of highly succesful functionals, known as the 'Generalized Gradient Approximation' (GGA). In the GGA the functional is expanded in terms of the gradient of the density and is commonly given by:

$$E^{GGA}[n] = \int n(r)\varepsilon^{GGA}(n(r),(r)dr \tag{1.51}$$

These functionals produce excellent results for molecular geometries and ground-state energies and have a wide range of applications. Examples of commonly used and successful functionals are BLYP, BP86, PBE, PW91 [17–20]. Further still are the meta-GGA which extend the GGA approximation by including a dependency on either the laplacian of the density or the kinetic energy density of both. The meta-GGA can often improve (at computational cost) the energetics of systems and the description of band gaps. Another popular family of functionals are hybrid functionals, which incorporate the exact exchange from Hartree-Fock theory with exchange-correlation from DFT, these have found great success in improving atomization energies, bond lengths and other molecular properties. Commonly used functionals are the B3LYP, PBE0 and HSE [21–24].

In the Quantum ATK implementation of DFT methods, to further improve speed and efficiency, pseudo-potentials are used [25]. In essence, the nuclear potential and core electrons are not dealt with explicitly and are replaced by an effective potential (which acts on the valence electrons). This allows for the valence electrons and the system to be described by a smaller number of basis functions, vastly improving the computational efficiency. The most successful ones are the norm conserving SG15 and Pseudodojo pseudopotentials, which are the two mainly applied in the work in this thesis [26–29].

A brief introduction to different exchange correlation functional families has been given. It

should be clear to this point, that the nuance for successfully using DFT is to pick the right functional (and basis sets) to describe the system of interest. In this section, some examples of successful functionals have been introduced. In general, these functionals have been developed from fitting procedures with properties from experiments, the nomenclature stems from the authors that developed them. The background, the fitting, the use-cases and successes of the different functionals are beyond the scope of this thesis. The take home message is that there is a sizeable "Zoo" of functionals which makes DFT a very versatile and adaptable first principle method for solving the electronic structure problem for a wide range of systems. The general work flow of a DFT calculation is shown in the flowchart in Fig 1.1.

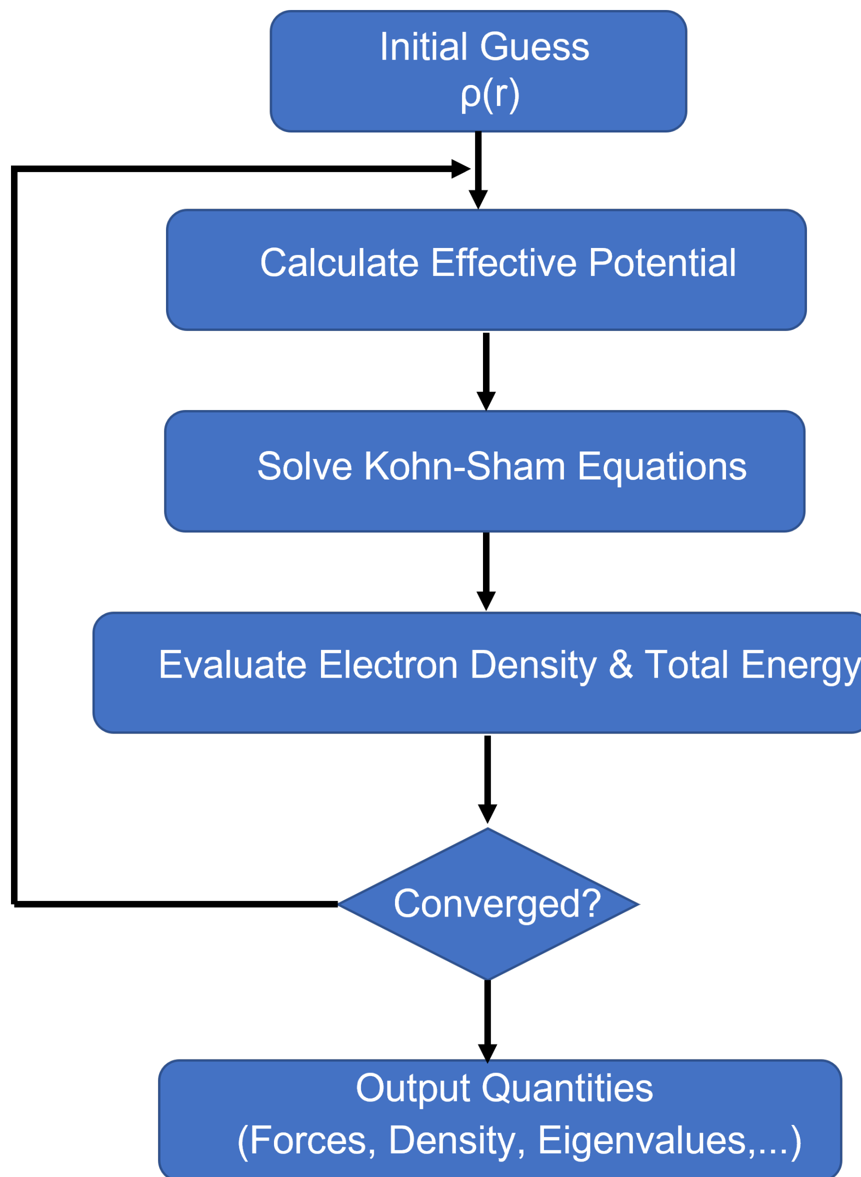

Figure 1.1: Flowchart depicting the iterative process for solving the Electronic structure problem with Density Functional Theory

1.3 Tight Binding Density Functional Theory (DFTB)

Although versatile and accurate, as a first principle method it is computationally expensive. The computational cost of most DFT codes scales N^3 with number of atoms. As the size of the system increases, it becomes impractical to study using DFT methods. An alternative method, based from DFT, is the density-functional tight-binding method (DFTB). This is a semi-empirical method, parameterized from DFT which is an efficient, robust, rapid and transferable computational tool for accurate electronic structure method for molecules and bulk solids. In this section, the theoretical framework will be described as is implemented in Quantum ATK software packages [25].

1.3.1 Tight Binding Theory from Density Functional Theory

The starting point for DFTB, is to describe the total energy of a system of M electrons in a field of N nuclei [30–33]. In simplest terms it can be considered:

$$E_{tot} = E_{bs} + E_{rep} \tag{1.52}$$

Where E_{bs} is the energy from the sum over the occupied orbital energies from the diagonalization of the electronic Hamiltonian. E_{rep} is the short-range repulsive energy from two-particle interactions. From DFT this can be rewritten as a system of M electrons in a field of N nuclei at positions R, in terms of the charge density n(r):

$$E = \sum_i^{occ} \langle \psi_i | -\frac{\Delta}{2} + V_{ext} + \frac{1}{2}\int \frac{n(r')}{|r-r'|} |\psi_i\rangle + E_{xc}[n(r)] + \frac{1}{2}\sum_{\alpha,\beta}^{N} \frac{Z_\alpha Z_\beta}{|R_\alpha - R_\beta} \tag{1.53}$$

In this form, the first sum is the occupied Kohn-Sham eigenstates, the second term is the exchange-correlation energy and finally, the last term is the core repulsion. However, it is more useful to rewrite this form with respect to an input density, substituting for charge density.

$$E = \sum_i^{occ} \langle \psi_i | -\frac{\Delta}{2} + V_{ext} + \frac{1}{2}\int' \frac{n'_0}{|r-r'|} + V_{xc}[n_0] |\psi_i\rangle - \frac{1}{2}\int\int' \frac{n'_0(n_0+\delta n)}{|r-r'} - \int V_{XC}[n_0](n_0+)$$
$$+ \frac{1}{2}\int\int' \frac{'(n_0+)}{|r-r'|} + E_{XC}[n_0+] + E_{ii} \tag{1.54}$$

Here, the charge density has been replaced by $n'_0 = n_0(r')$ which is a superposition of reference density, $'$ is a small fluctuation whilst $\int'$ refers to $\int dr'$. The second term is a correction for double counting in energy. The last term E_{ii} is the ion-ion core repulsion energy. Lastly, E_{XC} can be expanded at the reference density to give the total energy correct to second order density fluctuations.

$$E = \sum_i^{occ} \langle \psi_i | \hat{(H)}_0 | \psi_i \rangle - \frac{1}{2} \int \int' \frac{n'_0(n_0 + \delta n)}{|r - r'} + E_{XC}[n_0] - \int V_{XC}[n_0] n_0 + E_{ii} + \frac{1}{2} \int \int' (\frac{1}{|r - r'|} + \frac{\delta^2 E_{XC}}{\delta n \delta n'}) \delta n \delta n' \tag{1.55}$$

1.3.2 Zeroth Order Standard DFTB

In the non-SCC(self consistent charge) approach, the last term of the equation above is neglected. A frozen-core approximation is applied and only valence orbitals are considered [34, 35]. The Kohn-Sham equations are solved non-self-consistently whilst neglecting the second order correction. The total energy becomes:

$$E_0^{TB} = \sum_i^{occ} \langle \Psi_i | \hat{H} | \Psi_i \rangle + E_{rep} \tag{1.56}$$

the single-particle wave functions are expanded into a set of localized Slater-type atomic orbitals, ψ_V:

$$\Psi_i(r) = \sum_v c_{vi} \psi_v (r - R) \tag{1.57}$$

where c are the coefficients, r is the electron coordinates and R is the nuclei coordinates. These localised atomic orbiatals are solved for free "pseudoatoms" using SCF-LDA calculations. The non-SCF Kohn-Sham equations can be obtained through applying the variational principle to the E_0^{TB}.

$$\sum_v^M c_{vi} (H - \varepsilon_i S) = 0 \tag{1.58}$$

where Hamiltonian and overlap matrices are given by:

$$H^0 = \langle \psi_\mu | \hat{H}_0 | \psi_v \rangle \tag{1.59}$$

$$S = \langle \psi_\mu | \psi_v \rangle \tag{1.60}$$

Only two-center Hamiltonian matrix elements are treated explicitly along with two centre overlap matrices. The eigenvalues of the free atoms are the diagonal elements of the Hamiltonian. When the general eigenvalue problem is solved, E_{rep} is given as the difference between the SCF-LDA energy of the system and the tight binding band structure energy for a reference system.

$$E_{rep}(R) = [E_{LDA}^{SCF}(R) - \sum_i^{occ} n_i \varepsilon_i (R)]|_{reference} \tag{1.61}$$

This non-SCC DFTB approach has been succesfully applied to various different materials,

systems and problems in material science. However, in cases where the structure of the system is better described by a charge balance between different constituents such as heteronuclear and polar systems. Then this approach is too crude.

1.3.3 SCC-DFTB Self Consistent Charge Extension

To deal with heteroatomic molecules and polar systems, the approach described before is extended to improve the description of energies, total forces and transferability by including long-range Coloumbic interactions. In this case, the second-order term in the density fluctuations is considered explicitly. Hence, this is often known as the second order extension DFTB.

The second order term includes the decomposition of (r) into atomic centered contributions that decay quickly as the distance increases from the centre. The second-order term is expressed as:

$$E_{2nd} = \frac{1}{2} \sum_{\alpha,\beta}^{N} \int \int' \Gamma[r, r', n_0] \delta n_\alpha(r) \delta n_\beta(r') \tag{1.62}$$

in this form, Γ is a functional that includes the Hartree and XC coefficients, and $\delta n_{\alpha/\beta}$ is the atomic centred expansion, which can be expanded into radial and angular functions:

$$\delta n_\alpha(r) = \sum_{l,m} K_{ml} F_{ml}^{\alpha}(|r - R_\alpha|) Y_{lm}(\frac{r - R_\alpha}{|r - R_\alpha}) \approx \Delta q_\alpha F_{00}^{\alpha}(|r - R_\alpha|) Y_{00} \tag{1.63}$$

F_{ml}^{α} is the normalized radial dependence of the density fluctuation on atom α.Thus expression also ensures the total charge of the system is preserved (i.e the sum of the charge will give the intergral of the charge density). Combining the two equations above, gives the short-hand form:

$$E_{2nd} = \frac{1}{2} \sum_{\alpha,\beta}^{N} \Delta q_\alpha \Delta q_\beta \gamma_{\alpha,\beta} \tag{1.64}$$

where

$$\gamma_{\alpha,\beta} = \int \int' \Gamma[r, r', n_0] \frac{F_{00}^{\alpha}(|r - R_\alpha|) F_{00}^{\beta}(|r - R_\beta|}{4\pi} \tag{1.65}$$

In the situation where there are large inter-atomic distances, in the LDA the XC contribution vanishes. In which case, the E_{2nd} becomes a pure Coulomb interaction between the point charges of α, β. In the case where there is no interatomic distance, i.e the charges are located on the same atom, $\gamma_{\alpha\alpha}$, it would need to be calculated through the expansion of the charge density into an appropriate basis set of localized orbitals. However, to avoid the numerical effort associated with this case, $\gamma_{\alpha\alpha}$ is approximated as the difference between the ionization potential and electron affinity of the associated atom. In semi-empirical quantum chemistry this is related to the idea of chemical hardness η_α or the Hubbard parameter, U_α [36]. More generally:

$$\gamma_{\alpha\alpha} \approx I_\alpha - A_\alpha \approx 2\eta\alpha \approx U_\alpha \tag{1.66}$$

These parameters can be calculated for any atom within LDA-DFT, simply the second derivative of the total energy of the atom with respect to the occupation number of the highest occupied atomic orbital. Taking an assumption of exponential decay of a normalized spherical charge densities (like for the case of using a basis set of Slater-type orbitals to solve the Kohn-Sham equations), a well-defined expression for extended and periodic systems can be derived for $\gamma_{\alpha\beta}$:

$$\gamma_{\alpha\beta} = \frac{1}{R} - S(\tau_\alpha, \tau_\beta, R). \tag{1.67}$$

where τ is a parameter that arises from the spherical charge density for the atom, $R = |R_\alpha - R\beta|$ and S is an exponentially decaying short range function given by:

$$S(\tau_\alpha, \tau_\beta, R) = \frac{5}{16}\tau_\alpha + \frac{1}{R} \tag{1.68}$$

Assuming that at $R = 0$, the second order contribution can be approximated via the Hubbard parameter, then $\tau_\alpha = \frac{16}{5}U_\alpha$. From this approximation, chemical hardness is calculated with a fully self-consistent ab initio method which includes the influence of E_{XC}. In the limit of large interatomic distance it becomes a Coloumb interaction between the point charges ($\Delta\ q_\alpha$ and Δq_β). For periodic systems, the standard Ewald technique is used to evaluate the long range part. For the short range, S is summed over a small number of unit cells.

Including this second-order expansion, the TB energy can now be written in the form:

$$E_2^{TB} = \sum_i^{occ} \langle \Psi_i | \hat{H} | \Psi_i \rangle + \frac{1}{2} \sum_{\alpha,\beta}^{N} \Delta q_\alpha \Delta q_\beta \gamma_{\alpha,\beta} + E_{rep} \tag{1.69}$$

The atomic charges are dependent on one particle wave functions, thus a self-consistent procedure is required to find the minimum E^{TB}. As before, to solve the Kohn-Sham equations, ψ_i are expanded into localized atomic orbital φ_v using confined Slater-type orbitals. SCF-LDA calculations for free atoms are used to determine the localized orbitals and expansion coefficients. Applying the variational principal to E^{TB} within the pseudoatomic basis, the Kohn-Sham equations are obtained. The charge fluctuations (δq) are estimated through Mulliken charge analysis. The final set of algebraic equations are:

$$\sum_V^M c_{vi}(H_{\mu v} - \varepsilon_i S) = 0 \qquad -\forall \mu, i \tag{1.70}$$

$$\begin{aligned} H_{\mu\nu} &= \langle \varphi_\mu | \hat{H}_0 | \varphi_\nu \rangle + \frac{1}{2} S_{\mu\nu} \sum_{\xi}^{N} (\gamma_{\alpha\xi} + \gamma_{\beta\xi}) \Delta q_\xi \\ &= H^0_{\mu\nu} + H^1_{\mu\nu}, \quad -\forall \mu \in \alpha, \nu \in \beta \end{aligned} \tag{1.71}$$

$$S_{\mu\nu} = \langle \varphi_\mu | \varphi_\nu \rangle, \quad -\forall \mu \in \alpha, \nu \in \beta \tag{1.72}$$

Multiparticle interactions are accounted for through the overlap matrix, as it generally extends over few nearest-neighbour distances. A nondiagonal Mulliken charge contribution is added to the matrix elements to account for the charge fluctuations. As before, a two center approximation is used but now spherical pseudoatomic charge densities are superposed instead of pseudoatom potentials. The effective potential for the resulting charge density is then evaluated. Consistent with before, the E_{rep} is determined as the difference between SCF-LDA energy and SCC-DFTB electronic energy for suitable reference structure. Now that the charge transfer effects have been included explicitly, the transferability of this term and DFTB in general is significantly improved.

In this section, the DFTB method has been described starting from DFT. It is a very flexible method, that provides a highly efficient and accurate electronic structure method, that allows the computation of systems too costly for DFT. As will be seen, it can be combined with transport simulation tools such as NEGF to provide a flexible method for atomistic simulations of nanoelectronic devices.

1.4 Nanoelectronic Transport

Understanding the current flow of nanoscale junction devices requires an appreciation for how electrons move through a solid. From the classical picture of a particle going on a random walk through a device to the quantum picture of electron transmission through quantum tunneling. There are several concepts and models critical to being able to explore the functionality of novel and new devices. In this section, these concepts will be introduced to give an understanding of how the current flows through devices in the nanoscale. Followed by a description the Non-Equilibrium Green's function (NEGF) method for describing quantum transport. These concepts can in general be applied to wide range of devices, however the focus here will be with respect to molecular and metal oxide junction devices.

1.4.1 Background Concepts

The classical picture of electron transport through a conductor is one of 'diffusive' transport, where an electron goes on a random walk and scatters through any obstacles. The nature of this random walk would largely depend on the scale of the device and the types of materials. As you

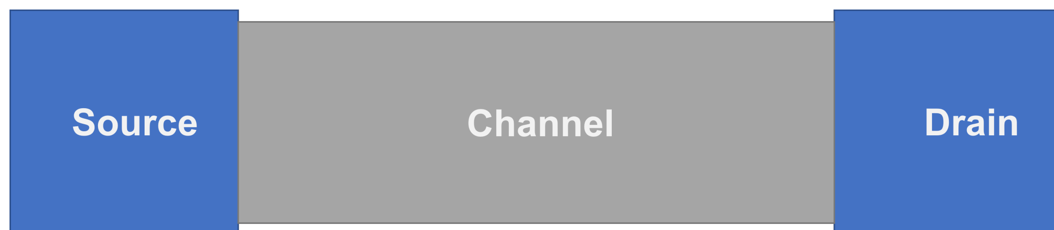

Figure 1.2: Visual representation of a simple device system.

go to smaller channel lengths (see Fig 1.2), transport becomes ballistic and electron transport can be compared to that of a bullet. As you approach the nanoscale it is vitally important that quantum effects are included when treating the transport of an electron through a device and the macroscopic view commonly held becomes somewhat obsolete [37, 38].

To understand how an electron flows through a device, it becomes important to comprehend why electrons flow? To answer this question, the concept of Density of States (DOS) is required. Density of States is a probability density function that describes the number of states in a system that can be occupied by an electron with a specific energy. For molecules this would be discrete energy levels, whereas for condensed matter a more continuous Density of States can be expected. In terms of transport, the Density of States of the channel is key as it describes how many states per unit energy are available for electron occupation.

Although in molecules you would expect discrete states, in molecular junctions, coupling between the molecule and electrodes and phonon effects lead the broadening of energy levels. In this case the Density of States can be represented by a Lorentz function [39]:

$$D(E) = \frac{1}{2\pi} \frac{\Gamma}{(E - E_0)^2 + (\Gamma/2)^2} \tag{1.73}$$

where Γ is an energy parameter that describes the coupling strength between the molecule (or central region) to the device.

Another key concept in understanding why electrons flow is location of the electrochemical potential, μ_0. At equilibrium the electrochemical potential of the device is the same everywhere. At absolute zero, this is the energy for which below it (E<μ_0) all states will be filled and above it the states are empty. The transition from full energy states to empty is described by the Fermi function. The Fermi function is derived from Fermi-Dirac statistical mechanics.

$$f(e) = \frac{1}{exp(\frac{E-\mu}{kT}) + 1} \tag{1.74}$$

where μ is the chemical potential, k is the boltzman constant. From this function it should be obvious that states with high energy are empty and states with low energy and filled, as electrons will always fill lowest energies first, and due to the Pauli exclusion principle electrons cannot occupy the same state. The transition from $f = 1$ to $f = 0$ occurs $\pm$ 2kT around μ_0.

Of course, in a device, such as a molecular or metal oxide junction the interesting physics

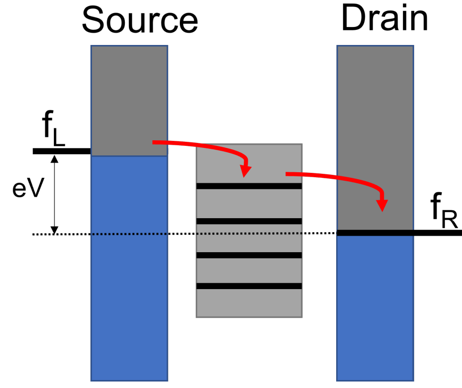

Figure 1.3: Simple Picture of Electron Transport in a nanoscale device.

happens when not in equilibrium, i.e electrons flowing. In equilibrium the Fermi function describes how the electrons are distributed across the system, but when out of equilibrium, the contacts of the device (see source and drain in Fig 1.3) remain in a local equilibrium with its own electrochemical potential. As a result, the device can be seen as having two different Fermi functions for each contact.

$$f_L(e) = \frac{1}{exp(\frac{E-\mu_L}{kT})+1} \tag{1.75}$$

$$f_R(e) = \frac{1}{exp(\frac{E-\mu_R}{kT})+1} \tag{1.76}$$

The channel in between the two contacts, reacts to the two Fermi functions. The source will fill the states in the channel, whilst the drain empties them. As a result, current flow happens due to the difference in the Fermi functions of the two contacts. The resulting current, number of electrons per unit time, that flows is proportional to the difference in Fermi functions

$$I(E) \approx f_L(E) - f_R(E) \approx \frac{\delta f_0}{\delta E} qV \tag{1.77}$$

The quality of transport through the channel depends on the availability of states in the energy window (difference in Fermi levels), i.e. the materials Density of States [40,41].

1.4.2 Quantized Conductance

In classical macroscopic physics, conductance is described by Ohm's law:

$$G = \frac{I}{V} = \rho \frac{A}{L} \tag{1.78}$$

where I is the current through the device, V is the applied voltage, ρ is the conductivity which is material and temperature dependant, A is the cross-sectional area and L is the length of the device. This law predicts that the Resistance approaches 0 as the length of the device reduces to

zero, i.e conductance becomes infinitely large. Experiments show there is a minimum interface resistance, regardless of contact quality. Further experiments since the 1980's demonstrated that in small conductors, the conductance does not scale linearly with the area. In fact, in the ballistic conductance regime the conductance reduces by multiples of conductance quantum.

$$G_B = \frac{e^2}{h} M(E) \tag{1.79}$$

where G_B is the ballistic conductance, e is the electron charge, h is Planck's constant and $M(E)$ is an integer, which refers to the number of transmission channels for a given energy(not to be confused with physical channel of the device, can be thought as transmission modes). This equation, illustrates that there is a limit of conductance known as the conductance quantum given by G_0 where

$$G_0 = \frac{2e^2}{h} \tag{1.80}$$

The factor of 2 stems from both spin up and spin down states for an electron, the value is 7.74 μS. This limit can be thought of as the maximum conductance of a transmission channel in a device.

Metal-Molecule-Metal and Metal-Oxide-Metal Junctions are considered to be a phase coherent conductor connected to two electron reservoirs. Hence, the transport can be modelled using the Landauer-Buttiker Formalism [42,43]. In this regime the conductance can be expressed as:

$$G = \frac{2e^2}{h} \sum_n T(E) = G_0 \sum_n T(E) \tag{1.81}$$

where T(E) is the transmission probability of an electron tunneling through the central scattering region with that specific energy. This sets out a quantum picture of transport on the nanoscale. It shows that the conductance is directly related to the probability of the wave function passing through the central region, with an upper limit of conductance quantum G_0 [44,45].

Landauer-Buttiker showed that for this system the current can be expressed as

$$I = \frac{2e}{h} \int T(E)[f_L(E) - f_R(E)]dE \tag{1.82}$$

where $f_{L/R}$ are the Fermi functions of the left and right electrodes with a given electrochemical potential, μ.

This formula for current underpins all of molecular electronics and other phase coherent conducting systems such as metal oxide tunneling barriers. This section has highlighted the key physical picture for electron transport in the nanoscale. In the next section, this will be expanded on with the Non-Equilibrium Green's Function (NEGF) method which provides the mathematical tool for solving this transport picture.

1.4.3 NEGF Method

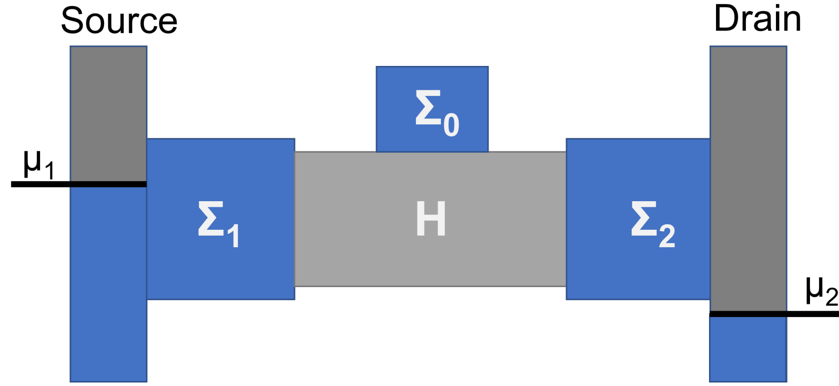

Figure 1.4: Device Structure for NEGF formalism, illustrating Source-Channel-Drain, self-energies for the contacts and central region ($\sum$), H is the Hamiltonian of the central region.

NEGF is the state of the art, three-dimensional atomistic electron transport method for atomistic device modelling. Whilst there are alternative methods and transport models such as the Boltzmann Transport Equation (BTE) based on classical statistical mechanics or Monte Carlo Transport methods, NEGF provides a fully quantum mechanical treatment of electron transport, whilst taking into account several electron-electron and electron-phonon interactions. It is solved self-consistently and is well suited for both nanoscale and mesoscopic systems. As the systems studied in this work rely on quantum phenomena, the NEGF method is a reliable way to model them and explore their properties [46, 47].

For the NEGF method, the device is split into three main regions: the two contacts (source and drain) and the channel which is the central scattering region where the interesting physics happens, this is shown in Fig 1.4. It starts from a bottom-up approach the starting point is the time-independent *Schrödinger* equation to describe the scattering region of the device, but two extra terms are included to cover the inflow and outflow of electrons: [48]

$$E[\psi] = [H][\psi] + [\Sigma_1 + \Sigma_2][\psi] + [s] \tag{1.83}$$

Where Σ are the self-energy matrices which describe the connection of the channel to the contacts, $[\Sigma_1 + \Sigma_2]\psi$ is the outflow and s is the inflow from the contacts. These terms are a result from imposing open boundary conditions on the *Schrödinger* equation describing the central region. From this modified equation, the wave function can be expressed as:

$$\Psi = [s][EI - H - \Sigma_1 - \Sigma_2]^{-1} \tag{1.84}$$

where I is the identity matrix. Given that the inflow of electrons into the system will be from multiple sources and thus incoherent. These terms cannot be superposed, therefore more conve-

nient to express the equations in terms of the conjugate transpose.

$$[G^n] = [\psi][\psi^\dagger] \tag{1.85}$$

$$[\Sigma^{in}] = [s][s^\dagger] \tag{1.86}$$

These quantities can be superposed and thus easier to work with. Further definitions are the retarded and advanced Green's functions, G^R and G^A given by:

$$G^R = [EI - H - \Sigma_1 - \Sigma_2]^{-1} \tag{1.87}$$

$$G^A = [G^R]^\dagger \tag{1.88}$$

given that the wave function, ψ = [G^R][s], then:

$$G^n = G^R \Sigma^{in} G^A \tag{1.89}$$

Another key quantity with respect to the Green's functions is the spectral function, A, which is the matrix representation of the Density of States.

$$A = G^{RA} = i[G^R - G^A] \tag{1.90}$$

$$\Gamma_{1/2} = i[\Sigma_{1/2} - \Sigma^\dagger_{1/2}] \tag{1.91}$$

where Γ is the anti-Hermitian parts of the $\Sigma' s$, which is essentially a description of the coupling between the electrons in the channel and the contacts.

Finally, the Green function equations can be used to describe the conductance and current for Coherent Transport discussed earlier (Landauer-Buttiker formalism). The current is expressed by

$$I = \frac{2e}{h} Tr[\Gamma_1 G^R \Gamma_2 G^A](f_1(E) - f_2(E)) \tag{1.92}$$

Comparing to the same equation expressed previously, it should be obvious that the transmission function can be calculated from the Green's function as:

$$T(E) = Tr[\Gamma_1 G^R \Gamma_2 G^A] \tag{1.93}$$

and thus the quantum expression for conductance, G(E) can be expressed as:

$$G(E) = \frac{2e^2}{h} Tr[\Gamma_1 G^R \Gamma_2 G^A] \tag{1.94}$$

The equations presented thus far are general and their application to different problems of transport relies on how the important physics is described by the Hamiltonian and self-energy matrices. NEGF provides a rigorous methodology for including all types of interactions within the channel both elastic and inelastic. The key quantity to be calculated is the retarded Green's Function, G^R, from which the main properties of interest of the system can be calculated.

A common approach, and the one used in the work of this thesis, is to combine NEGF with ab initio methods for an accurate atomistic treatment of transport at the nanoscale [49–51]. For this, the Hamiltonian, self-energies are described using ab initio methods described in the section above, from which the retarded Green's function and transport properties can be calculated.

1.4.4 Poisson Equation

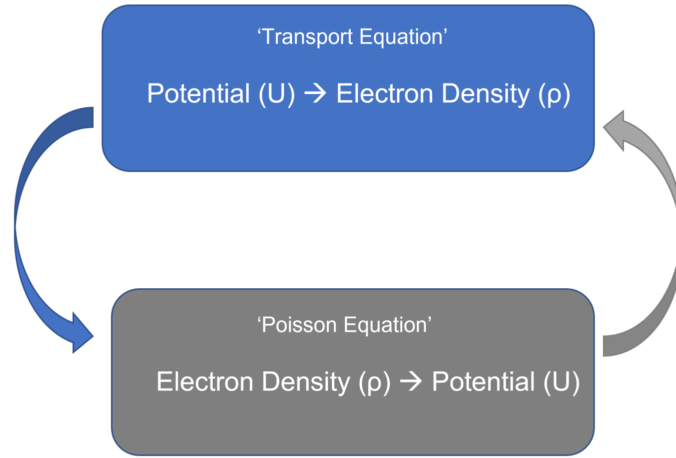

Figure 1.5: Poisson iterative process.

For accurate and realistic device simulations it is essential that the potential (which describes charge distribution and transfer) is calculated self-consistently. The first step, the Hamiltonian for the device (whether it be from DFT, DFTB or other methods) gives a description of the device and its electron density. This electron density can then be used to solve the potential (Hartree potential) using the Poisson equation [52, 53].

$$\nabla^2 V^H[n](r) = -\frac{e^2}{4\pi\varepsilon_0} n(r) \tag{1.95}$$

where V^H is the Hartree potential, $n(r)$ is the electron density as described, ε_0 is the vacuum permittivity. The Poisson equation is a second-order differential equation which is typically solved by applying appropriate boundary condition for the problem in question.

The iterative process consists of using an effective potential (Hartree potential) from the Hamiltonian of the device, in the transport equation, to calculate the number of electrons that flows into the device, this will change the electron density. This new electron density, is used

within the Poisson equation to calculate the potential that another electron feels due to the presence of all electrons. The two equations are solved self-consistently for values of n and V^H. This is vital for describing the charge distribution of devices.

1.5 Conclusion

In this chapter the theoretical framework for simulating nano-scale electronic devices from a "bottom-up" approach has been given. In the simplest view, any device is simply a task for solving the many-body electronic structure problem using the *Schrödinger* equation. The foundations for tackling this problem was discussed and the LCAO and wave function approach and the limitations of this approach was introduced. This gave context for the development of Density Functional Theory (DFT) which is the most popular and successful ab initio modelling method. The mathematical formulation of DFT has been given in this chapter and its uses have been reviewed. Additionally, the tight-binding approximation to DFT was also described as it is a very versatile, accurate and more efficient method for simulating larger systems. Finally, the theory for nanoelectronic transport was described to give a clear picture to the reader before describing the state of the art NEGF method for accurately simulating nanoscale devices from the "bottom-up approach". When this is combined with ab initio methods, it is an effective first principle device modelling tool which is the main approach used to study the devices in this thesis. This chapter has provided the theoretical foundation for the modelling methods and tools used in this work.

Chapter 2

Molecular Memory

2.1 Introduction to Molecular Electronics

Molecular electronics is an exciting, relatively new, growing field of interdisciplinary study that is attempting to combat the inherent limit of miniaturization of electronic devices based on conventional silicon circuits [54].

Extending Moore's law and miniaturizing electronic devices is becoming more challenging primarily due to the limitations of current techniques for producing bulk semiconductor devices from the top-down approach. Molecular electronics offers an alternative "bottom-up" approach by creating devices using single molecules, as they are the smallest stable structures that can be created [55].

Molecular electronics is simply the concept of creating functional electrical circuits from individual molecules or from molecular ensembles. Some of the advantages compared to traditional silicon technology include increased capability and faster performance due to the extremely reduced size. There is potential for incredible versatility due to the abundant diversity in molecular structures that can be designed and chemically altered for desirable functions. Another potential advantage is low-cost manufacturing, due to the ease of bulk synthesis and the potential availability of a plethora of functional molecules [56]. However, despite the clear advantages, substantial research efforts and progress in the field, it is still in its infancy and the production of commercial molecular devices are still a long way off. There are two main challenges: Techniques for designing, controlling and measuring electronic components at the atomic scale and a fundamental understanding of transport mechanisms at the molecular scale [57].

The simplest device that has been developed and extensively studied both experimentally and theoretically is the molecular junction. Broadly speaking, this is a single molecule which is connected to bulk electrodes (gold predominantly but there are several studies looking into silicon and carbon based electrodes) [58, 59]. The bulk electrodes act as a "reservoir of electrons" whilst the transport properties are dominated by the molecule and its connection to the electrodes. These junctions are probed experimentally using break junction techniques and the-

oretically by combination of DFT and NEGF [60, 61].

The first half of this thesis is concerned with a class of molecules known as Polyoxometalates (POM) and their promise for use in memory applications. To give an overview to the reader this chapter will be presented as follows: A brief introduction to Flash memory technology and the challenges faced will be given. A review of the literature concerning 'molecular memory' will be presented before discussing previous research on POMs and POM based memory.

2.2 Non-Volatile Flash Memory

Flash memory is a type of solid state non-volatile computer memory storage device which can be reprogrammed and erased. Non-volatile refers to the ability for the device to hold information even when power has been removed. In the modern, increasingly digital world, it is a key technology. Flash memory devices have an array of floating gate transistors that make up memory cells that store information. The floating gate of the transistor can be conductive (polysilicon) or non-conductive as is the case with SONOS. (silicon–oxide–nitride–oxide–silicon) flash memory [62]. There are two main types of flash memory which are named based on their respective logic gates: NAND and NOR. They differ predominantly on their connections to the memory cells. In NOR cells, they are connected in parallel to the bit cells. As a result, the cells can be read and programmed individually. In NAND cells, they are connected in series just like in a CMOS NAND gate. The series connection is more space efficient, thus NAND cells are cheaper to produce. Another considerable differentiator is that NOR allows random-access for reading whilst NAND only allows page access [63].

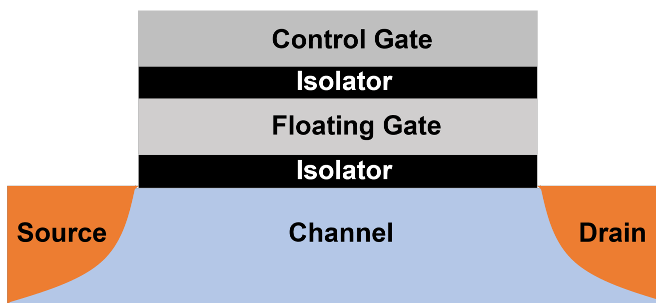

Figure 2.1: Diagram of a typical Flash Memory Structure.

The memory cells in Flash memory act as a switch in which current flows between the source and drain. The current is controlled by a floating gate (FG) and by a control gate (CG). The FG is insulated by an oxide layer and sits between the CG and the channel of the MOSFET, this is illustrated in Fig. 2.1. It is in the floating gate where the electrons are trapped as it is isolated by the oxide layer. The floating gate remains in the state induced by the trapped electrons even after the power is removed, hence it is a non-volatile memory technology [64]. When the FG is charged with electrons, the charge shields the electric field from the control gate, this results in

an increase in the "threshold voltage" (the voltage required to pass current through the device, i.e. to switch it on), V_{T0}. In order to switch on the device, a higher voltage, V_{T1}, needs to be applied. This is how the transistor stores memory.

In order to "read" the information stored in the transistor, an intermediate voltage between the two threshold voltages is applied to the control gate. If current fails to flow in the channel, it suggests that the FG is charged, since the required voltage for conduction is V_{T1}. In this instance, a logical "0" is stored in the gate. In the case that current flows, the FG is uncharged and a logic of "1" is stored. Determining whether the current flows at an intermediate voltage is how the logical memory is retrieved. This process is described graphically in Fig. 2.2. In a multi-bit storage cell, the amount of current that flows is measured and the precise charge in the FG is determined.

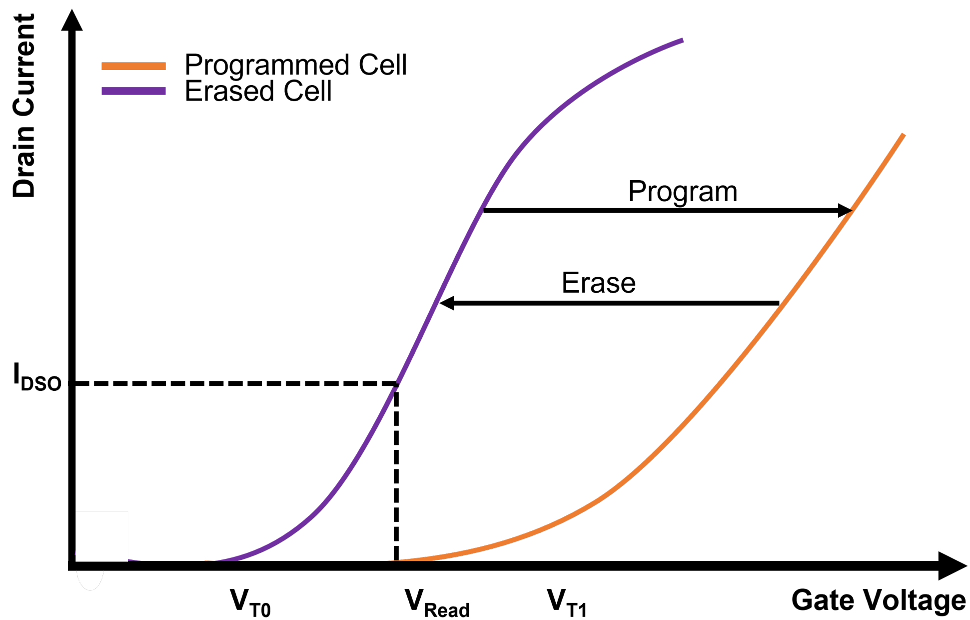

Figure 2.2: Current vs Gate Voltage Characteristics which illustrate typical program and erase functionality in a flash cell.

Due to their excellent properties and non-volatile memory retention, flash memory devices have become ubiquitous and find applications in computers, portable audio players, digital cameras, GPS systems, mobile phones, game consoles, medical electronics, USB flash drives, memory cards amongst others [65]. In addition to its operating properties, flash memory is advantageous as its fabrication process is compatible with current CMOS technology and can be used in embedded memory applications.

One of the major drawbacks of flash memory technology is the reliability issues which are linked to the thin tunnel oxide, which is typically amorphous. This leads to a reduction in operation voltage and deterioration after a finite number of program and erase cycles [66]. Additionally, as the scale-down of devices gathers pace, floating gate flash memories require the

tunnel oxide layer to be at least 8nm in order to guarantee a 10 year retention time and prevent charge loss.

To deal with the scalability drawbacks of floating gate flash memory, SONOS memory technology was proposed. SONOS technology consists of a MOSFET where the floating gate has been replaced by an oxide-nitride-oxide dielectric. It shows better charge retention with tunneling oxides less than 10nm. Furthermore, SONOS memory devices are easy to fabricate, have high program/erase speed, low operating voltage and power consumption and can potentially be scaled down more effectively [67].

Unfortunately, SONOS flash memory only slightly relieves the scalability issue. The gate dielectric still has a thickness of approximately 7nm and further scaling down has been shown to be problematic. The main challenge is maintaining acceptable charge capability and consistency in the fabrication of the nitride [68]. Thus to overcome these issues and continue the scale down of memory technology, alternative device architectures need to be innovated.

The current innovative architecture change in NAND flash to deal with the above mentioned issues is the shift from planar 2D to 3D NAND flash memory devices, which is currently used in solid-state drives (SSD's) and other memory devices [69]. 3D NAND flash consists of vertically stacked memory cells on a single ship. The stacking results in a higher memory density improving storage space [70]. In addition, the vertical stacking reduces the cell to cell interference, which vastly improves read and write speeds [71].

Despite the improvements to planar flash technology, the increased complexity of stacking the memory cell has lead to more intricate fabrication techniques which increases production costs. They have lower write endurance overall which affects the lifespan of the memory cells. The multi layer structure results in a more complex error correcting mechanism. Finally, as with the planar flash memory, there's a limitation to the scalibility. As the number of vertical layers increases it becomes more challenging to maintain the performance and reliability [64]. Because of these potential issues, alternative memory technologies are still relevant as a route to overcome these issues. One promising alternative is the idea of molecular-based memory devices. This will be discussed in the next section.

2.3 Molecular Memory

In the previous section Flash Memory technology was introduced and its limitations and challenges were discussed. In order to continue the downscaling over memory devices, new technology innovations have to be made. As already discussed, the growing field of molecular electronics is being explored to aid the downscaling of electronic devices through a "bottom-up" approach. As part of this research, molecular memories have been proposed as a promising technology for efficient, multi-bit and high storage density non-volatile memory technology.

Molecular memories refer to any technology concerned with storage of information, where

the data storage component consists of single molecules or molecular networks. Commercial molecular memories are yet to be realised and several challenges still need to be addressed. But extensive research is being dedicated to this growing field. In this section a short review of non-volatile molecular memories being studied in the literature and some of their limitations will be given.

2.3.1 Redox-Based Molecular Memory

The main candidates for molecular memory devices are redox-active molecules. Redox-active molecules can be simultaneously oxidised (lose an electron) and reduced (gain an electron) commonly stimulated by external factors such as temperature, electric field or environment. The intrinsic charge storage capabilities of these molecules show promise for high speed operation, low operation voltage and high reliability [72].

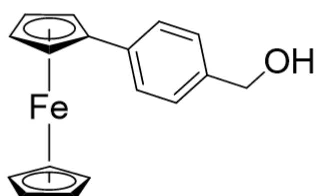

Figure 2.3: Fc-BzOH molecule studied by Li et al. [1]

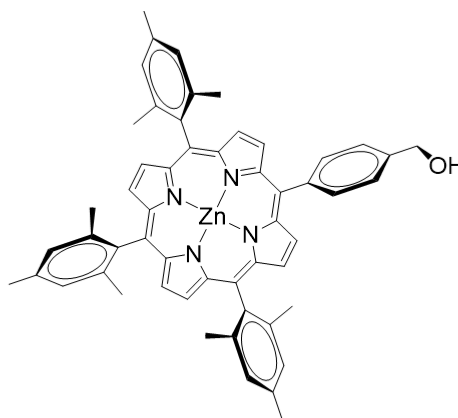

Figure 2.4: Por-BzOH molecule studied by Li et al. [1]

Two excellent examples of redox-active molecules for memory applications were proposed by Li et.al [1], they are Fc-BzOH a ferrocene containing molecule and Por-BzOH a porphyrin containing molecule, both renowned for their redox properties. They are shown in Fig. 2.3 and 2.4. The general idea is that the redox active centre, Iron or Zn will act as the charge storage component. These centres can be in neutral and positively charged states through the loss/gain of electrons. The ferrocene/porphyrin structures can assist in maintaining the redox

centre stable whilst minimising charge loss. The electrolyte/molecule interface between the molecule and top gate electrode will also act as a barrier to prevent the reduction of the molecule. Using chemical solution deposition, the molecules can be self-assembled onto Si, SiO_2 or other surfaces, typically through the OH groups or the aromatic rings. Cyclic Voltammetry studies by the researchers showed that Fc-BzOH show two reversible charge storage states neutral and one positively charged state, whilst Por-BzOH shows two positively charged states and one neutral (potential for multi-bit storage). They also studied the capacitance, conductance-voltage characteristics which showed peaks corresponding two charge trapping and de-trapping at the redox centres. They proposed a mixing of both molecules within the one device to help create a more reliable multi-bit storage device [1]. This device is easily fabricated by self-assembly and shows well defined redox states. However, a significant challenge to incorporating these molecules as a memory device is they appear to show low density of conductance which could inhibit storage and device operation [73].

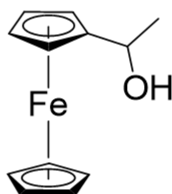

Figure 2.5: Ferrocenylethanol used in the work by Zhu et al [2].

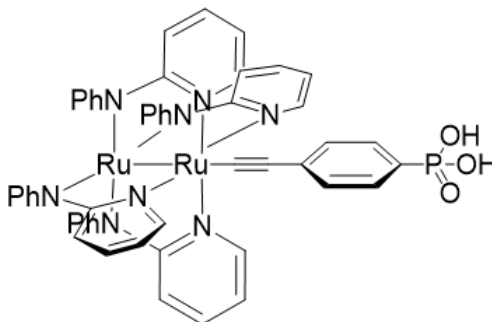

Figure 2.6: Ruthenium Complex studied in the work by Zhu et al [2].

Zhu et al. [2] also investigated a set of redox active molecules for high-density non-volatile memory applications. They report a CMOS-compatible molecular non-volatile flash memory based on self-aligned top-gate Si nanowire FET. They used low-cost techniques to self-assemble ferrocenylethanol (Fig 2.5) and $Ru_2(ap)_4(C_2C_6H_4P(O)(OH)_2)$ (Fig 2.6) and encapsulate them between layers of an oxide dielectric. They studied the memory behaviour and showed fast program/erase times, multi-bit storage (the Ruthenium complex shows two redox states), large

memory window and sufficient charge-trap density [2].

It is also reported that the devices are capable of good charge retention. Their experiments project that over a 10-year window, the devices would only lose around 20% charge. This is attributed to the stable redox behaviour of the molecules and the high-quality encapsulation within the device architecture. The endurance properties, which are key to flash memory devices, have not yet been studied. Nevertheless, the species investigated here again show the potential of redox-active molecules for flash memory applications. From these examples it should be clear that redox-active molecules are the most promising for molecular memory devices thanks to their ease of synthesis, the potential diversity due to their chemical functionality and their ability to gain and lose electrons whilst maintaining stability. All important for reliable memory technology.

2.3.2 Polyoxometalates for Flash Memory

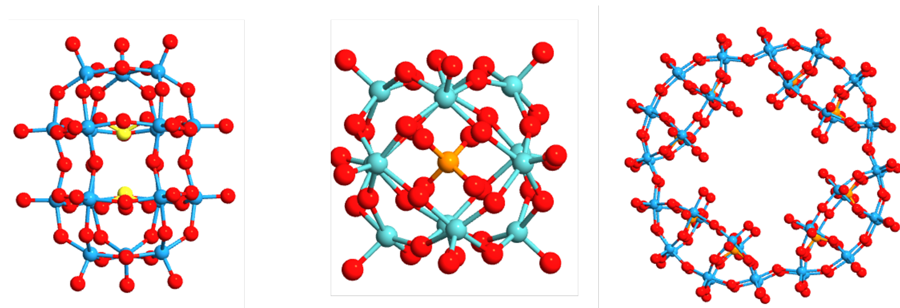

Figure 2.7: A few examples of Polyoxometalate Structures showing the diversity of these class of molecules. Red= Oxygen, blue = Tungsten, turquoise = Molybdenum, orange = Phosphorus, yellow = Sulfur.

In the last section it was argued that redox-active molecules are the preferred candidates for memory applications with some promising examples from the literature being reviewed. The examples presented in the last section, like the majority of those being explored are organic molecules (carbon based). However, the integration of organic molecules in devices suffers from high resistance and power, low performance and more problematic fabrication and reproducibility. All of which lead to poor performance and variability. An alternative would be molecules which have a natural complimentarity to CMOS technology: highly oxidic inorganic molecules. A class of inorganic molecules which show excellent redox properties, potentially improved complimentarity with CMOS and promise for non-volatile flash memory applications are Polyoxometalates also known as POMs.

Polyoxometalates (POM) are a class of polyatomic anions that form 3D networks made up from early transition metals linked together by oxo ligands (oxygen atoms). The most common metal ions are Mo(VI) and W(VI). The structural variety of POMs (few of which are shown in Fig 2.7) coupled with their multiple redox chemistry capabilities, photochemical characteristics,

high ionic charge (improved conductivity) and their molecular weights has led to great interest in the field for a wide variety of applications. POMs find use as industrial catalysts, for example in oxidation of organic products. In addition to catalysis, thanks to their remarkable versatility they are being explored for application in photochemistry [74], medicinal chemistry [75], magnetic materials, sensors and nanotechnology [76]. Importantly for this work, they are being investigated for molecular electronic applications, specifically molecular memory.

In their concept paper in 2013, Vila-Nadal et al. [77] proposed, thanks to their nanoscale size, oxidic nature and the fact they are highly redox active, a type of non-conventional Wells-Dawson POMs would make excellent candidates for non-volatile molecular memory. In the paper, it is suggested replacing the nitride oxide charge trapping layers of the floating gate of SONOS flash memories with a layer of POM molecules. The logical state of the memory cell is determined by the net charge of charge polarisation in a layer of the molecules in a specific redox state. POM's generally have multiple stable redox states making them highly attractive for multi-bit storage applications.

The advantages of using these redox-active POM molecules is that the cross-cell capacitive coupling (a critical issue with flash memory) will be minimised as the charge storage of the POMs will be highly localised. Also, the chemical synthesis and molecular self-assembly yields a regular distribution of the charge storage centres [78]. POM molecules have more stable redox states than organic molecules as well as higher redox potentials which should lead to better retention time. Lastly, the chemistry of POMs makes them a better option for integration in current CMOS technology, since their oxidic in nature, they have better complementarity with SiO_2.

Vila-Nadal et al. study a set of POM molecules through a multi-level computational framework to model their potential in flash memory devices. The framework uses DFT to ascertain the electronic structure of the molecules whilst they employ mesoscopic device modelling to study the use of the molecules in a flash cell. Their DFT simulations show that there is little structural change upon oxidation and reduction for non-conventional Well Dawson anions. They studied $[W_{18}O_{54}(SO_3)_2]^{4-}$ and $[Mo_{18}O_{54}(SO_3)_2]^{4-}$. One of the most important results are the shapes of the HOMO (Highest Occupied Molecular Orbital) and LUMO (Lowest Unoccupied Molecular Orbital). The HOMO is delocalised over the ${SO_3}^{2-}$ moiety whereas the LUMO is predominantly localised on the equatorial metal atoms. This explains the structural stability upon multiple reductions and how the net charge on the internal heteroatoms doesn't change. This aids in the excellent charge localisation for memory applications.

The mesoscopic device simulation showed that the reduction of the POM molecules in the molecular layer of a flash memory cell leads to a lowering in the threshold voltage. These theoretical results demonstrate the exciting prospect of molecular flash memories using POMs and is the foundation for the topic of the first half of this PhD.

Following on from the previous study, Georgiev et al. [79] further investigated the use of

POM molecules for molecular metal oxide memory storage. They applied a multiscale simulation framework to further evaluate the variability in the programming window of the flash cell which includes the molecules. DFT calculations on $[W_{18}O_{54}(SO_3)_2]^{4-}$ showed that the HOMO and LUMO are aligned below the conduction band of Si and could be insulated by the high potential barrier of SiO_2. This is highly advantageous for effective charge storage and implementation of the molecules within the floating gate structure. As the LUMO levels are well below the SiO_2. conduction band (-4.05 eV), good retention is expected. The details of the charge distribution of the POMs ascertained from DFT simulations was used for setting up a theoretical flash cell where the poly-Si FG was replaced with an array of POMs.

The variability in the programming window of the flash cell was investigated. They define the programming window ΔV_T, as the difference between the V_T when all POMs are once reduced vs the V_T of the erased cell, i.e. When no charge is being held by the POMS. It is also worth noting that the POM molecules were modelled with point charge counter-cations to account for the Pr4N that are present from chemical synthesis. An 18nm gate length was modelled and the statistical variability was studied. There are two main sources of Statistical Variability, one of which is Random Dopant Fluctuation (RDF), which is known to have a significant impact on device and circuit performance. The other is the random distribution of the POMs, labelled POM fluctuations (POMF). It is found that the variability is most effected by the number of POMs in the device, causing variability of almost a factor of 10 more than from RDF.

This device study is interesting in particular, as it suggests that the nature of the POM (through its charge distribution) as well as the density of POMS in the cell most strongly influences the device operation and leads to higher variability within the device. More importantly, the POMs have been modelled in the device based on charge distribution of the single molecule in vacuum. However, in order to assess the molecules capabilities in a flash memory cell, it is important to understand the charge distribution of the molecule when it is incorporated in a gate stack. Moreover, understanding the electron transport through this or other POM molecules could improve understanding of their potential applications both in memory and molecular electronics in general and the challenges faced with POM based molecular electronic devices. Understanding the electronic structure and charge transport of POM molecules, not as an isolated system, but in a possible device setup was the starting goal of this PhD thesis.

In this section the foundational work for the first part of this PhD has been presented. POMs have been introduced and their properties discussed. Focus on the previous published research on the $[W_{18}O_{54}(SO_3)_2]^{4-}$ molecule, its electronic structure and potential application in flash memory has been presented and reviewed. This PhD is dedicated to building on the previous work and gaining a fundamental understanding of the transport properties of this molecule and other POMS and assessing their potential use in memory devices.

Chapter 3

Studying the electron transport of $[W_{18}O_{54}(SO_3)_2]^{4-}$

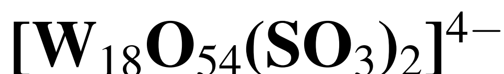

3.1 Introduction

Polyoxometalates (POMs) are promising candidates for molecular electronic applications. As discussed in the previous chapter POMs are inorganic anionic clusters typically composed of high valent group V and VI transition metals (such as Mn and W) linked via oxo ligands to make 3D networks [80]. Their promise for use in the next generation of molecular electronic applications is thanks to the fact that; 1) They have better CMOS compatibility due to their inorganic nature (compared to organic molecules); 2) Their synthesis is predominantly carried out through one-pot reactions from metal oxides through self-assembly); 3) POMs have a wide range of possible shapes and configurations and thus can be tailored for specific device performance; 4) they are redox active with multiple states which have a very low voltage switching between polarised states. The potential of incorporating POM clusters in flash memory devices is an exciting idea, specifically this possibility was explored with a Tungsten based POM molecule, $[W_{18}O_{54}(SO_3)_2]^{4-}$ [81]. This molecule shows excellent promise due to its ideal sized HOMO-LUMO gap, the orbital shape of the HOMO and the relatively close post-LUMO levels which could in theory result in multibit storage. However, a fundamental understanding of electron transport through POM molecules is lacking but pivotal if commercial molecular memories are to become a reality. The simplest way to explore the electron transport through molecules, both experimentally and with modeling, is as a molecular junction (molecule sandwiched between two metal electrodes). Thus the starting goal of this PhD project was to explore theoretically the electron transport of through this molecule and assess the characteristics that make it suitable for memory applications. The aims of the work in this chapter was to establish a link between the underlying electronic structure of $[W_{18}O_{54}(SO_3)_2]^{4-}$ and its transport properties, to explore how the different electrode-molecule contact geometries influence the transport, predict how the molecule will behave under an applied bias and finally how the charge balancing counter ions

influence the transport. The results reported in this chapter were published in the Journal of Physical Chemistry C and thus is referenced here for the entire chapter [82].

3.2 Computational Methodology

Throughout this chapter the calculations of the POM molecule and POM junctions were performed by using the QuantumATK-2018.06 software and QuantumATK 2019.12 (for the counterion containing systems), both versions were compared to ensure continuity [25]. The electronic properties of the molecule were calculated by using the generalized gradient approximation (GGA) and the BP86 functional with spin polarization. This was chosen as it has successfully described POMs in previous publications compared to other functional/basis set combinations that were tested [77, 83]. The SG15 pseudopotential [84] and a medium basis set (comparable to double-zeta polarized) satisfactorily reproduced the geometry and electronic properties of $[W_{18}O_{54}(SO_3)_2]^{4-}$. For the gold electrodes, single zeta polarized basis set was used to reduce the computational cost. The geometry of the molecule was optimized in the gas phase, and its energy levels were calculated.

For the transport calculations the NEGF method was then used to calculate the transmission spectra and the current flow through the molecule under applied drain bias. For the transport simulations a large transverse k-point sampling is required for accuracy. Thus, a Monkhorst Pack grid of $3 \times 3 \times 300$ k-point sampling was implemented. The Current-Voltage calculations were carried out following the Landauer-Buttiker formalism introduced in Chapter 1.

3.3 Results and Discussion

3.3.1 Initial Molecule Exploration

For any first-principles modelling study using DFT, the accuracy relies on careful choice of the functional, basis set and any pseudopotential and their potential to accurately describe the system of interest. The main focus for this study is to reproduce the HOMO-LUMO gap and the molecular geometry. DFT calculations of the isolated molecule in vacuum was carried out and several functionals and basis sets were tested and the results benchmarked against the results reported by Vila-Nadal et al. [77].

Fig 3.1 shows the structure of the $[W_{18}O_{54}(SO_3)_2]^{4-}$ POM cluster. As is evident from Table 3.1, the BP86 functional, with SG15 pseudopotential and medium basis set, satisfactorily reproduces the bond lengths and bond angles of the theoretical and experimental benchmarks. There are only slight variations, most notably with the bond angle. Furthermore, DFT at this level reproduces the HOMO-LUMO gap with a difference of only 0.02 eV. The table highlights how important it is to select the right functional/basis set. Although all tested computational

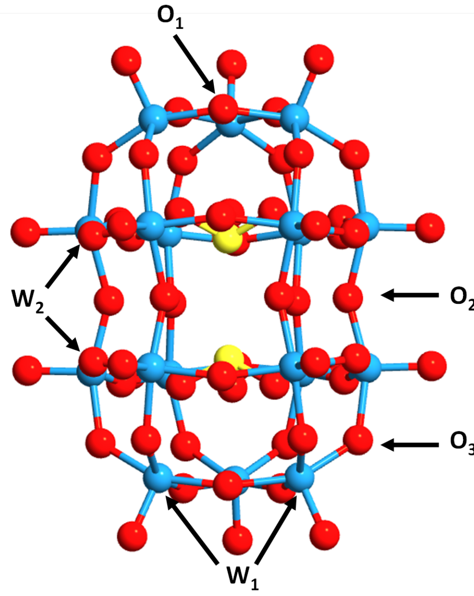

Figure 3.1: POM molecule in this study, with atom labels for bond data. W = blue, O = red, and S = yellow. O_1, O_2, and O_3 are all oxygen atoms which are labeled according to the oxo band in the molecule. O_1 = capping, O_2 = central, and O_3 = upper oxo bands.

	W_1-O_1	W_1-O_3	W_2-O_2	$W_2-O_2-W_2$	$\Delta E_{HL}(eV)$
Experimental [85]	1.89	1.93	1.92	145.58	N/A
Theoretical [77]	1.92	1.93	1.92	147.55	1.87
BP86, SG15 medium basis set	1.92	1.93	1.92	148.75	1.89
BP86, PseudoDojo Medium Basis set	1.93	1.94	1.93	148	1.77
BP86, FHI DZP	1.95	1.95	1.95	141	1.51
PBE, FHI DZP	1.97	1.99	1.99	135	2.04

Table 3.1: Comparison of Selected Bond Lengths (Å) and Bond Angles (deg), HOMO-LUMO gaps for different DFT settings.

settings show reasonable bond angle and bond lengths, the PseudoDojo pseudopotential results in an underestimation of the HOMO-LUMO gap, as does the PBE functional even more so. Thus prediction of the transport properties would be strongly affected. Hence, through these benchmark tests and following the literature, the BP86, SG15 and medium basis set satisfactorily reproduces the electronic structure of $[W_{18}O_{54}(SO_3)_2]^{4-}$.

Fig 3.2 shows the nature of the HOMO and LUMO of the molecule. The nature of the HOMO and LUMO also offers insight into how the transport might behave and potential memory capabilities. The HOMO level is delocalized across the $(SO_3)_2$ moieties, suggesting the important role this moiety has within the POM cluster, changing this moiety could influence the transport and thus provide further flexibility in POM based nanoelectronics. The LUMO level is mostly delocalized across the metal d-bands and are metallic in character. From the Fig it can be seen that there is antibonding character between the metal-oxygen and also between adjacent

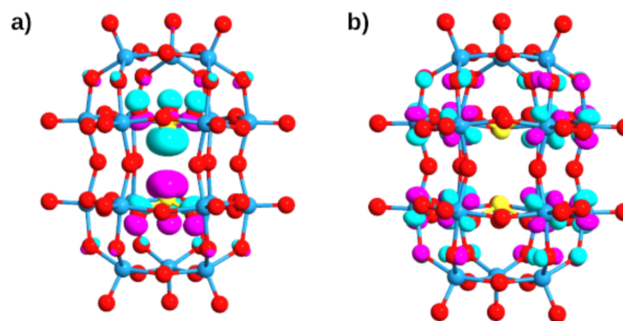

Figure 3.2: a) Highest Occupied Molecular Orbital (HOMO) b) Lowest Unoccupied Molecular Orbital (LUMO).

tungstens. Reduction therefore would raise the energy of the LUMO level and further levels which could potentially influence the multi-bit storage capabilities of the molecule. Multi-bit storage relies on the filling of subsequent energy levels of the molecule.

3.3.2 Single POM Molecular Junction Studies

In order to understand the electron transport through the $[W_{18}O_{54}(SO_3)_2]^{4-}$ POM molecule, a model molecular junction was created using gold electrodes, gold is chosen due to its conductive properties and the experimental techniques for probing molecule electronics devices predominantly consist of a molecule adsorbed on gold and/or gold tips in STM (Scanning Tunneling Microscopy) [86]. A major challenge in studying single molecule junctions is a lack of structural detail in how the molecules are actually attached to the electrodes. In reality, there a many orientations with similar probabilities of occurring. Due to thermal vibrations of the molecule and the stochastic nature of the binding process of the molecule to the contacts, it is practically impossible to accurately determine the exact position of the molecule in relation to the contacts. It is computationally too expensive and time-consuming to study all possible configurations.

One of the first goals of this project was to assess how different molecule orientations and contact geometries of the electrode-molecule-electrode system influence the resulting transport of the device. In addition, these differences should be linked to the underlying electronic structure of the molecule. Therefore, the strategy was to model several configurations that will cover the different "extremes" of effects of the junctions. It is typical for molecules to be linked to the electrodes through linkers, such as sulfur containing organic ligands, which can aid the strength of connection to the electrodes, whilst having very little effect of the electronic structure of the junction. This was considered, but as at the time the investigations were carried out, there were no reported or known studies of this particular molecule with any linker and to avoid the extra computational burden of more atoms in the junction, it was decided to build the model junctions through connections of the oxygen in the POM and gold adsorption at the FCC site. The focus was on three different junction congifurations as shown in Fig 3.3.

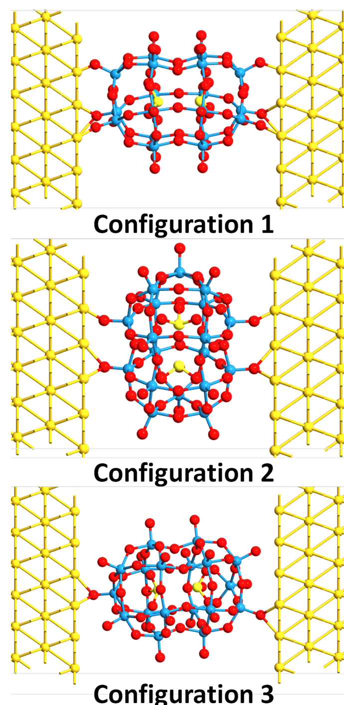

Figure 3.3: The three Au-POM-Au configurations studied.

It is established that the nature of the molecule to electrode contact has a significant impact on the current flow in molecular electronic systems [87, 88]. To explore this in POM junctions, junction setups with 1, 2, and 3 direct contacts of oxygen to gold (Au) on either side have been modeled as shown in Fig 3.3. In addition to molecule-electrode contact strength(through number of contacts), molecule orientation is also important, the different orientations are horizontal/flat (Configuration 1 and 3) or vertical/upright (configuration 2). Studying this set of configurations can provide insight into how different factors influence the transport of POM molecular junctions.

To understand the electronic structure of the molecular junctions and how the gold electrodes influence the underlying electronic structure of the molecule, the energy levels were calculated and the HOMO-LUMO levels were visualised. The model junctions were simulated under zero bias using DFT for the electronic structure in combination with NEGF to evaluate the charge flow through the junction. As with the isolated molecule, the calculations were carried out in the gas phase. It is important to stress that the following analysis is qualitative, it is the comparison between the systems calculated using the same consistent method. However, GGA functionals have been shown to be reasonably accurate in calculating HOMO-LUMO and other energy level gaps and distances [89].

Fig 3.4 shows the relative alignment of the HOMO, HOMO-1, HOMO-2, and the LUMO for all three configurations with respect to the Fermi energy of the junctions (dominated by the electrodes). The diagram clearly illustrates that the molecule to electrode configuration influences the energy levels of the molecule. The HOMO-LUMO gap in all cases differs from the

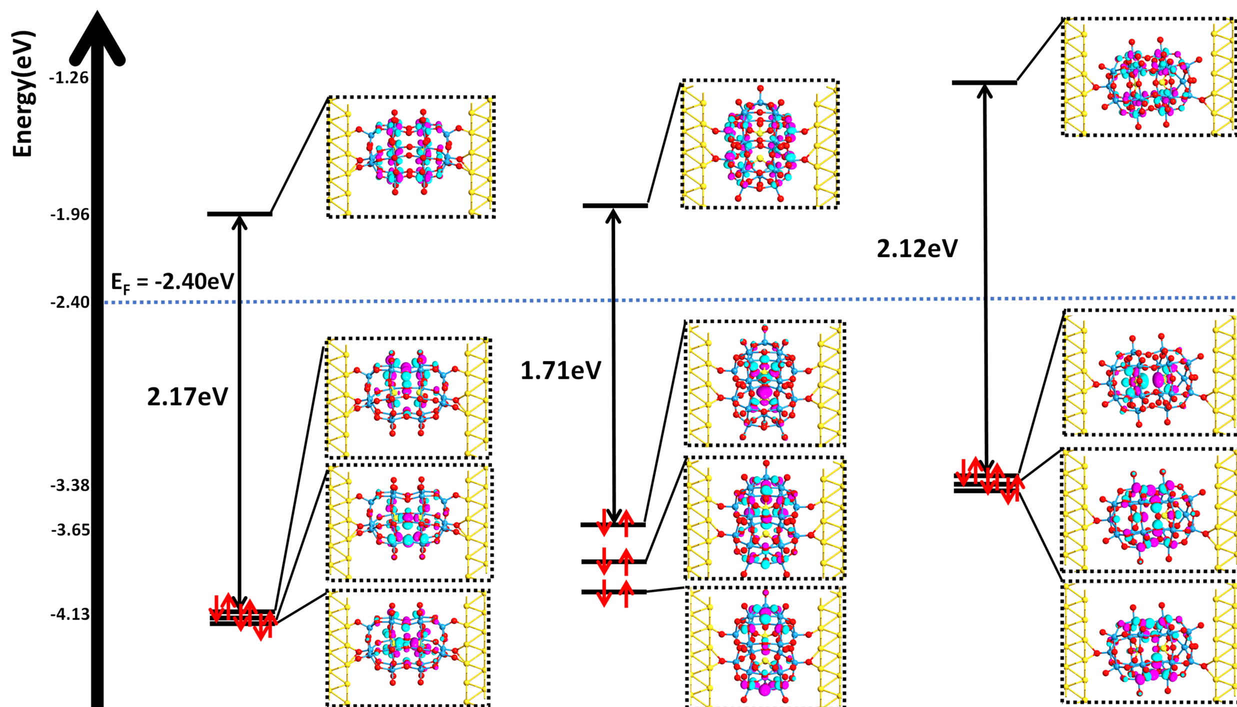

Figure 3.4: Comparison of HOMO-LUMO relative energy positioning and their respective frontier Kohn-Sham molecular orbitals. The blue dotted line marks the positioning Fermi energy of the electrodes.

value of the isolated molecule, 1.89 eV (see Table 3.1). The alignment of the energy levels with respect to the Fermi energy (E_f) for each configuration also differs. For configurations 1 and 2, the Fermi energy lies closer to the HOMO than the LUMO, whereas for configuration 3 it lies approximately halfway between the HOMO and LUMO. An explanation for these observations is that the HOMO level is stabilized by the increased contact strength to the electrodes and the LUMO is pulled closer to the Fermi energy. This observation is directly linked to the number of bonds between the POM cluster and the electrode. As configuration 1 has three contacts (bonds) between the POM-Au electrode, and this would result in a stronger contact compared to configuration 3 (which only has 1).

Another important observation is that the symmetry of the molecular orbitals of the HOMO and LUMO levels for configuration 2 and 3 is identical with the energy levels in the isolated molecule as shown in Fig 3.2 [77]. The HOMO is delocalized around the $[SO_3]^{2-}$ moieties. The LUMO level is delocalized around the tungsten cage and show d-like symmetry and character. For configuration 1 the HOMO-2 resembles the HOMO of the isolated molecule, while the LUMO level is identical. However, the HOMO-2, HOMO-1, and HOMO all lie within 0.02 eV of each other and thus are almost degenerate states. Similar degeneracy is seen for configuration 3, suggesting that the “horizontal” orientation brings these energy levels closer. This can be explained by the fact that for these configurations the energy states show that the electron density lies on part of the central oxo bands. Whereas for configuration 2 the densities for these levels

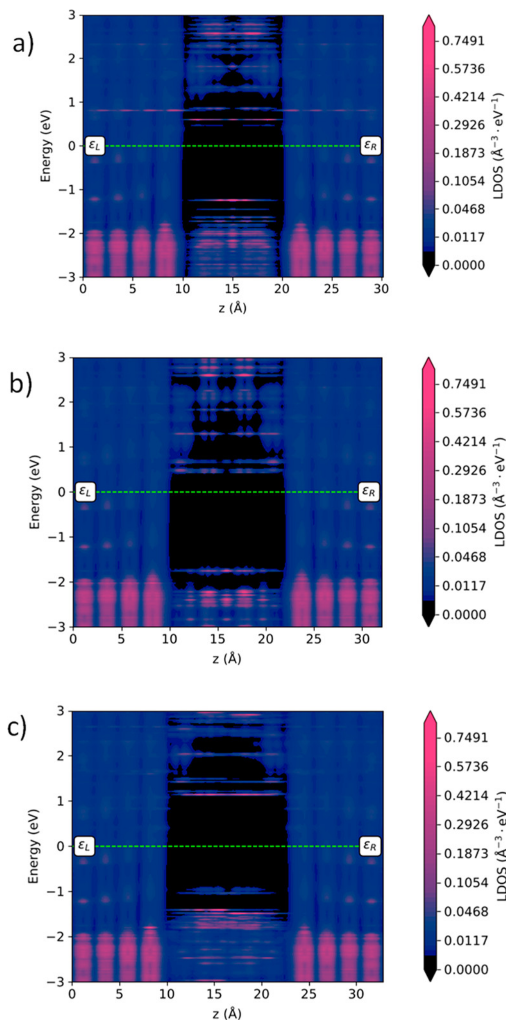

Figure 3.5: Projected Local Density of States (LDOS) calculated at zero bias for (a) configuration 1, (b) configuration 2, and (c) configuration 3. The region spanning from 10 to 22 Å is the central region of the molecule. The pink regions are where there is high electron density. The green dotted line is the Fermi energy, which is set at 0 eV.

lie on the upper and lower oxo bands (see Fig 3.1), and thus the levels are more discrete and as a result differ in energy.

Fig 3.3 highlights the influence of the configuration of the device on the HOMO-LUMO gap. From a electronic device perspective, the HOMO level can be associated with the valence band edge (E_V) and the LUMO level with the conduction band edge (E_C). For configuration 2, "the vertical" orientation results in a smaller HOMO-LUMO gap of 1.71 eV compared to the 1.89 eV of the isolated molecule. However, for the "horizontal" orientation, the HOMO-LUMO gap increases (2.17 eV and 2.12 eV). The orientation of the molecule seems to affect mostly the HOMO and near-HOMO levels, resulting in them being pulled closer together and stabilized; hence, the gap to the LUMO widens. This may be due to the alignment of the HOMO with the junction structure in configuration 1 and 2. Clearly, the orientation of the molecule influences the energy levels of the resulting junction.

To further analyze the electronic structure of the junction devices, the Local Density of States (LDOS) was computed. It shows where in the molecular device there are available energy states and their relative occupations. The LDOS for all configurations projected onto the device coordinates is shown in Fig 3.5. The Fermi levels for the source (ε_L) and the drain (ε_R) are the same as the calculation is done at zero bias. The Fermi-level is set to 0 eV with everything else positioned relative to this energy. In general, the pink regions are regions of high electron density and the black regions are without any states. In Fig 3.5 the Z-axis is the transport direction, and the continuous regions at 0-10 and 22-32 Å are the LDOS for the electrodes, while the region in-between 10-22 Å is the molecule.

The PLDOS echoes the results for the energy level alignment in Fig 3.4 and shows significant differences across all three configurations. This highlights the effect of molecule-electrode contact and orientation on the electronic structure of the device. Increased contact to the electrodes shifts the energy levels and subsequently the available density of states downward in energy. This is evident as for configurations 1 and 2 the LDOS lie closer to the Fermi energy. The gaps between the states on either side of the Fermi energy are consistent with the calculated HOMO-LUMO gaps.

What is also clear by analyzing the PLDOS is the available DOS are highly localized around the molecule. Thus, the positioning of the localization is highly dependent on the configuration. Specifically, in the states around the Fermi level, which are critical to transport, there are clear differences between the configurations, with split resonances across the molecule. It shows that the contact to the electrodes and molecular orientation dictates both the energy and atomic localization of the DOS of the molecule.

The computed zero bias transmission spectra (T(E) vs Energy) is shown in Fig 3.6. This is a very useful quantity which can be obtained from the NEGF method as it shows the different energies at which electrons can scatter through the device and the relative probability. The different peaks and their corresponding energies can be linked to the energy levels of the molecule and the respective transmission eigenstates. Hence, a powerful tool for exploring the transport through the molecule.

In Fig 3.6, all energies are calculated relative to the Fermi energy (which is set as zero) at zero drain bias. Despite differences in T(E) and energy positions of the peaks, the spectra are similar for all three configurations. This demonstrates a clear link between the electronic structure of the POM and its transport. However, differences arise in the spectra due to the different electrode-molecule configurations, consistent with the differences in energy levels discussed previously. Plotting the transmission spectra as $E - E_f(eV)$ vs log(T(E)) provides a clear visualization of resonance broadening near the Fermi energy, this is shown in Fig 3.7.

There is an evident trend in Fig 3.6a regarding the effect of molecule-electrode contact strength. Focusing on the first peaks above the Fermi energy (E_F = 0.0 V) for each configuration, the closest peak is for configuration 1, followed by configuration 2 and then configuration

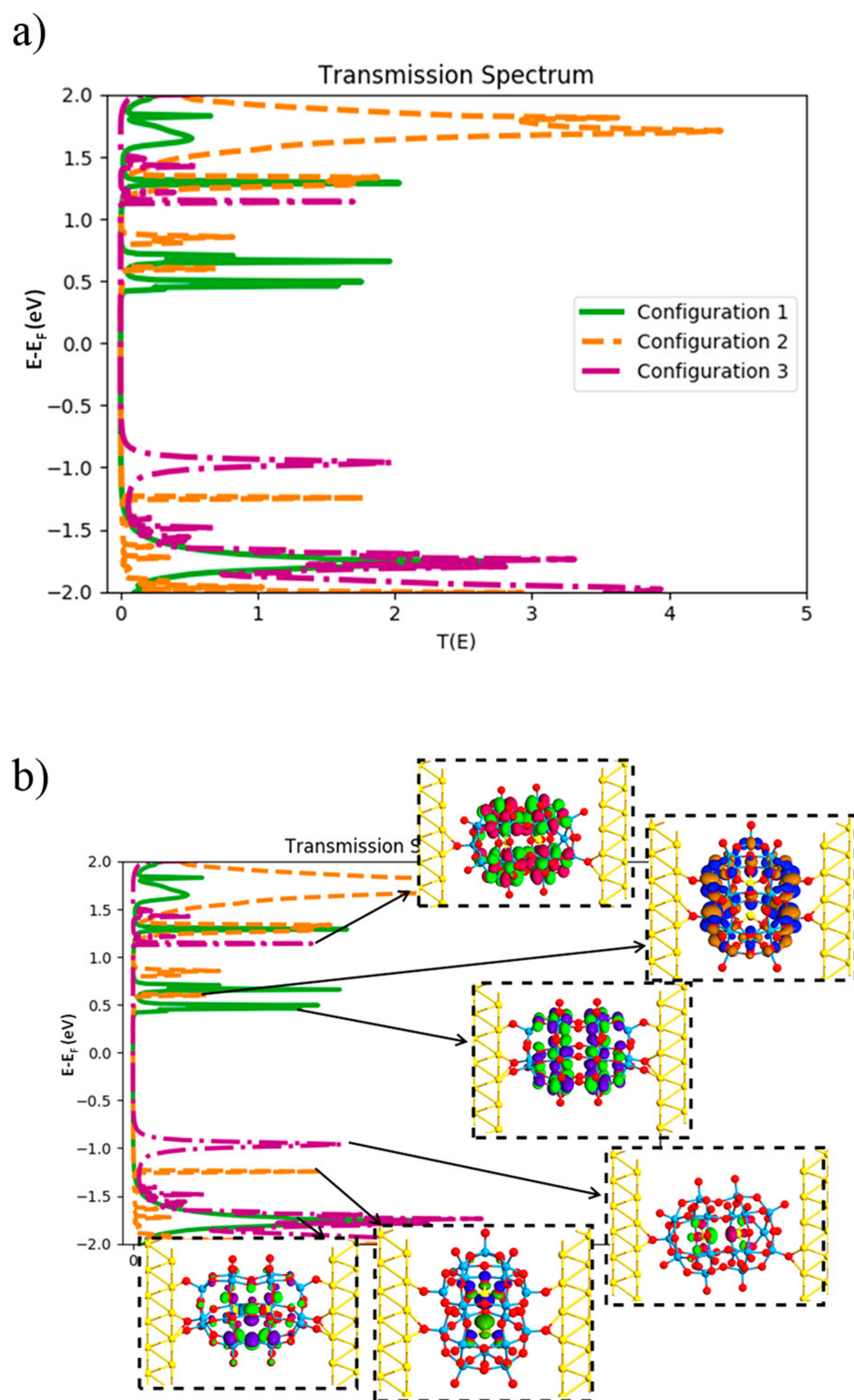

Figure 3.6: (a) Transmission spectra for all three configurations. (b) Transmission spectra with the dominant transmission eigenstates visualized for selected peaks. All energies are relative to E_F, which is set at zero.

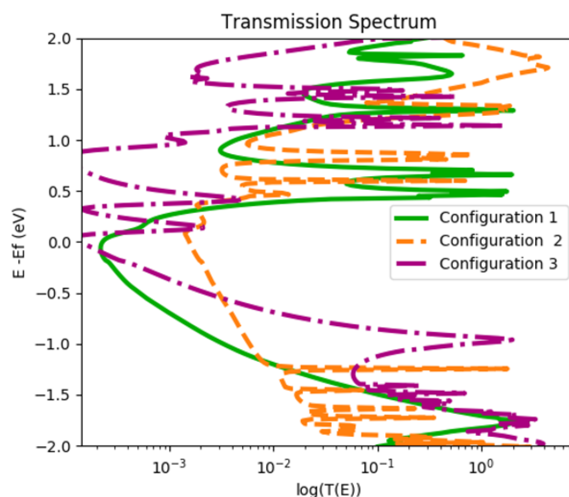

Figure 3.7: Transmission Spectra showing $E - E_f$ vs log(T(E)) showing resonance broadening of transmission peaks.

3. A similar trend is seen for the other peaks, and below E_F, the peak for configuration 1 is lowest in energy. This reflects the HOMO-LUMO positioning in Fig 3.3. Configuration 1 has three oxygen atoms bonded to the gold electrode on either side, while only two for configuration 2 and just one contact either side for configuration 3 (see Fig 3.3). Introducing more points of contact to the electrodes lowers the energy of the transmission modes intrinsic to the molecule. This can also be viewed as creating more than one conducting channel which allow the electrons to move from the source to the molecule. As a result, the transmission spectra and transport are strongly dependent on the molecule-electrode geometry.

A series of studies on organic and organometallic molecules also found similar dependence of the molecule-electrode geometry on the properties of tunnel junctions including junctions with a series of different electrodes. These results show that the same is true for POM-based junctions [90–92].

Another key disagreement between the transmission spectra of the configurations is the differences in T(E), i.e. the intensity of the peaks. Focusing on the region of 0-1.5 eV in Fig 3.6a, the peaks for configuration 1 are much larger than those of 2, but similar to the size of the peaks for configuration 3. This indicates that at these energies the "horizontal" orientation provides more favorable alignment of the transport modes than the "vertical" configuration. The peaks closest to E_F will be the transmission modes which will contribute to the transport under applied bias; as transmission is directly related to conductance, it can be expected that the horizontal orientation results in a higher conductance. Below the Fermi energy, the peaks correspond to the filled energy levels of the molecule and gold. The differences in T(E) are not so prominent. This can be explained by the fact that these states are already filled, and so the probabilities of the electrons scattering at these energies are all similar. Given that they are low-lying, a high applied bias would be required for these peaks to contribute to the current flow.

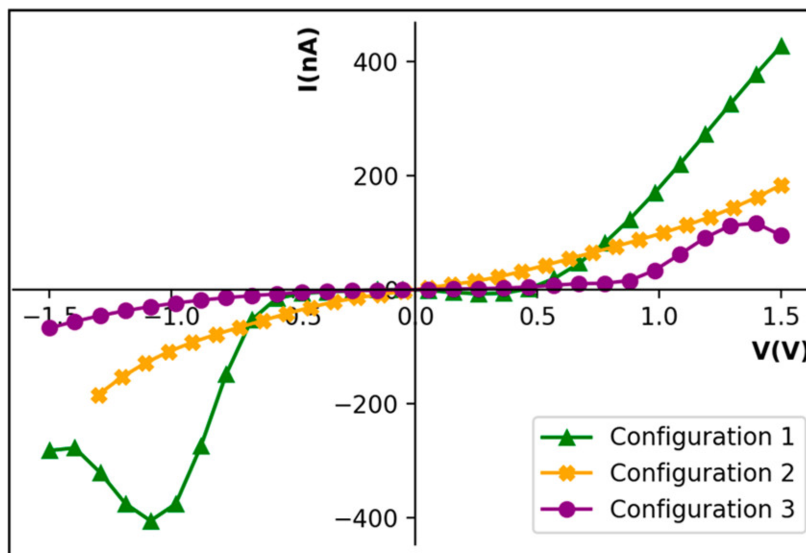

Figure 3.8: Computed Current-Voltage (I-V) characteristics for all configurations. The current is electronic current rather than conventional: i.e. positive current describes electron movement from the source (left electrode) to the drain (right electrode).

In Fig 3.6b, the dominant transmission eigenstates responsible for the transmission of the first peaks above and below the Fermi energy have been visualized for all configurations. The transmission eigenstates provide insight into where in the molecule the transmission is occurring and the molecular orbitals responsible. This helps to understand the link between electronic structure with the transport at the molecular level. The first peaks below the E_F for all configurations (in the range 1 to 2 eV) unsurprisingly resemble the HOMO energy level of the molecule for all configurations.

The peaks above E_F for all three configurations provide the most interesting results with regards to transport. All peaks resemble the LUMO of the molecule, indicating that the main transport pathways in the POM-based molecular junctions will be LUMO dominated at low drain bias. This is consistent with other studies of other POM-based molecular electronic transport [93, 94]. In addition, the eigenstates are identical for all configurations, providing further evidence that the transport of a molecular system is dominated by the molecular electronic structure of the POMs. However, other features that influence the alignment of the molecular energy levels will influence the transport characteristics, specifically, differences in molecule to electrode strength and in molecule-electrode contact orientation.

One of the main aims of this project was to explore how the molecule behaved under an applied bias. To model this, the Current-Voltage (I-V) characteristics of the three configurations were calculated. Fig 3.8 shows the theoretical I-V curves for the three junction configurations and reaffirms the predictions from the zero bias transmission spectra. The computed curves predict low current flow between the bias of -1.5 to 1.5 V, with magnitudes ranging from 19.5 to 425 nA. The low current flow is consistent with the transmission spectra of the devices. This can be explained first by the size of the HOMO-LUMO gap, where there are no transmission modes.

In addition, the transmission peaks are all sharp and narrow, as only a few energy levels/states contribute to the transmission in the junction.

Unsurprisingly, with a current of 427 nA at 1.5V and 387 nA at -1V, configuration 1 shows the highest predicted current flow between the bias of -1.5 to 1.5 V. Configuration 3 shows the lowest maximum current flow, reaching 95 nA at 1.5 V and 67.5 nA at 1.5 V bias. Configuration 2 shows a higher current flow than 3, but significantly less than 1, with the predicted current reaching 184 nA. These results are highly suggestive that the contact strength between electrode and molecule most strongly influences the current flow of the molecular device,with more contacts resulting in a higher current.

The computed current is directly related to the number and magnitude of transmission modes within an energy range due to the applied bias (in previous chapter). Hence, by analyzing how the transmission spectrum changes under bias the I-V characteristics can be rationalized. Fig 3.9 shows how the transmission changes under applied bias with peaks highlighted at ± 0.5 and ± 1 V. In general, with increased magnitude of the applied bias the intensity of the peaks (value of T(E)) decreases. This results in a lower than expected current. By comparison across the three configurations, in configuration 1 the energy window from the applied bias (yellow line) reaches transmission peaks under an applied bias of 1 and -1 V. Under negative applied bias the transmission peaks are not shifted as much as under positive bias; as a result, there are two small peaks included in the window. This explains why the current for configuration 1 at -1 V (387 nA) is predicted to be more than double the current at +1 V (179 nA). The transport under an applied bias is subsequently dominated by the spacing of the LUMO energy levels responsible for the main transmission peaks, which in turn are affected by both the orientation of the molecule and the molecule-electrode strength.

In summary, the transport properties of $[W_{18}O_{54}(SO_3)_4]^{4-}$ molecular junction in three different junction configurations have been studied with first-principle methods. The DFT-NEGF calculations demonstrate that the number of contacts between the molecule and the gold electrode determines the bond strength. A higher molecule to electrode contact strength lowers the energy levels of the molecule, bringing the transmission peaks closer to the Fermi Energy (E_F) and, as a result, increasing current flow in the junction under bias. Moreover, the molecular orientation to electrode has a strong influence on the transport. Specifically, it affects the magnitude of T(E) at energies close to the E_f, with the calculations suggesting the “horizontal” configuration is the most favorable for transport.

3.3.3 Exploring the Effects of Counterions

Due to the anionic nature of POMs, countercations are required for charge balance and to isolate the molecule in the pure phase. Typically the role of countercations in POM chemistry and the chemistry of other metal-oxo clusters is overlooked, as reported in the review by Nyman et. al [95]. However, several studies show that countercations are not only important for charge

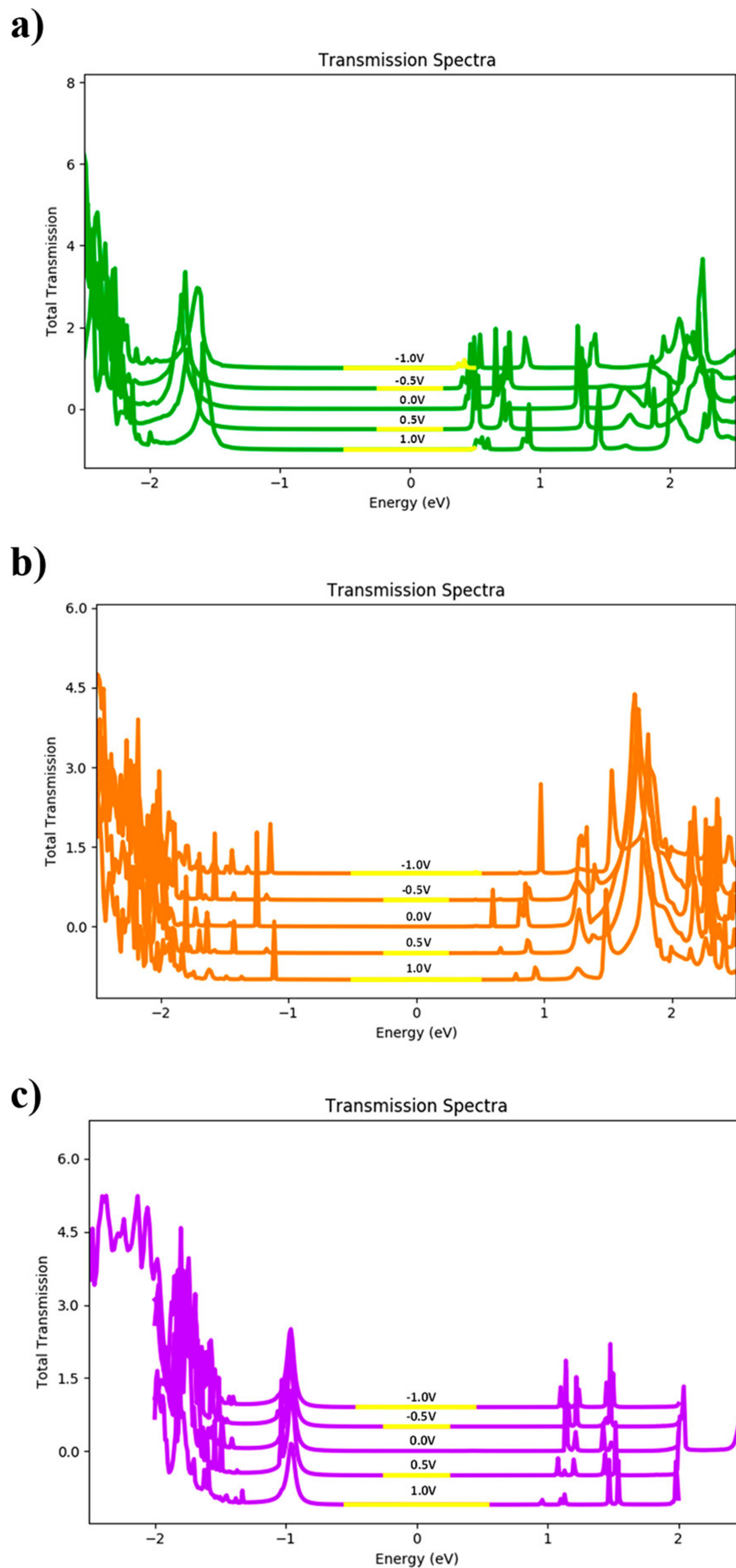

Figure 3.9: Theoretical transmission spectra under applied bias (-1.0 to 1.0 V) for (a) configuration 1, (b) configuration 2, and (c) configuration 3. The yellow line corresponds to the energy range of the applied bias window.

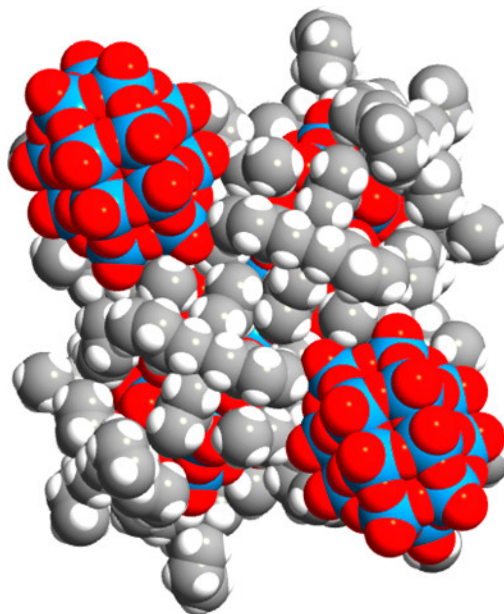

Figure 3.10: Illustration of $[W_{18}O_{54}(SO_3)_2]^{4-}$ POM molecules surrounded by tetrapropylammonium (TPA) counterions.

balance but play a larger role. In some applications, such as heterogeneous catalysis, their role is critical [96]. In most computational studies of POM systems, the counterions are ignored and treated as spectator ions. The reality is that in a real device system the POMs will be surrounded by relatively large organic cations (see Fig 3.10). Han et al. and Goswami et al. report the stabilizing effect of counterions, which in turn have a crucial influence on the charge transport of organometallic based tunnel junctions [97, 98]. Given this, it is expected that from an electronic device perspective the influence of these counterions is not negligible.

If commercial POM molecular electronic devices are to become a reality, it is important to understand how counterions will affect the transport properties of $[W_{18}O_{54}(SO_3)_2]^4$ and by extension other POM molecules. This was explored using the same computational methods as described above. $[W_{18}O_{54}(SO_3)_2]^{4-}$ is commonly isolated as a salt with four tetrapropylammonium cations (TPA) [99]. In a proposed device structure these cations or similar ones would be present. To reduce the computational cost, the size of the alkyl chains were reduced to methyl groups as is common in DFT simulations of other long chain systems. Subsequently the influence of tetramethylammonium (TMA) on the POM junction is explored. Previous device calculations modeled the presence of counterions as point charges [81]. Hence to be consistent with the previous work, the influence of Cs^+ counterions was investigated. Cs^+ was chosen for two main reasons: Its ionic radius is similar to that of ammonium (which has similar properties to TMA) [100]. Also, there are several examples of Cs^+ POM salts in the literature [95, 96, 101, 102].

The main challenge with modeling counterions is realistic positioning of the counterions with respect to the molecule, especially given the vast array of possibilities. One strategy, is

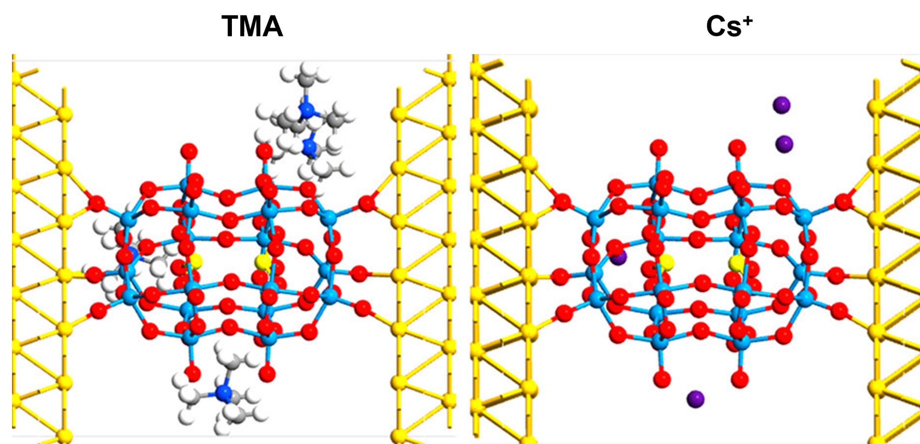

Figure 3.11: Junction configuration for systems including the counterions TMA (left) and Cs^+ (right).

to use Molecular Dynamics (classical or ab-initio) to create a range of different counterion positionings and then relax the geometry with DFT. This was explored briefly, but there were several difficult computational challenges (such as convergence of the relaxation simulations). This method also has the downside that it is still a crude approximation of potential counterion-molecule geometry. In this study, the counterion positioning was taken directly from X-ray crystallography coordinates of four TPA cations around $[W_{18}O_{54}(SO_3)_2]^{4-}$. Although this is only one arrangement of many possibilities and also the different sizes of TPA, TMA and Cs^+ means there will be differences in counterion-molecule geometry. However, it is a reasonable approximation in order to gauge the influence of the counterions on the POM junction transport properties.

A junction geometry similar to configuration 1 ("horizontal" orientation and multiple molecule-electrode contact) was chosen to study the counterion effects as it showed the best transport properties. To accommodate the presence of the counterions, the electrodes for the junction were increased (see Fig 3.11). Benchmarking calculations, were carried out, the electrodes of the previous junction was increased and its electronic structure and transport calculated. It was found that increasing the size of the electrodes has a negligible effect on the transport properties of the system. Hence, any changes in predicted transport properties can be credited to the presence of counterions.

As described previously, the energy levels of the POM in the junction device were calculated using DFT-NEGF and zero bias in order to study the effect of counterions on the energy levels of the system. Fig 3.12 shows a comparison between the energy levels of the two counterion-containing systems and configuration 1. The Fermi energy has increased by 0.04 eV to -2.36 eV due to the increased size of electrodes. All comparisons have been adjusted for this. The orbital shape of the HOMO for the Cs^+ and TMA system is identical with the HOMO for configurations 2 and 3 and to the HOMO-2 of configuration 1.

The calculations reveal that the presence of counterions influence the positioning of the

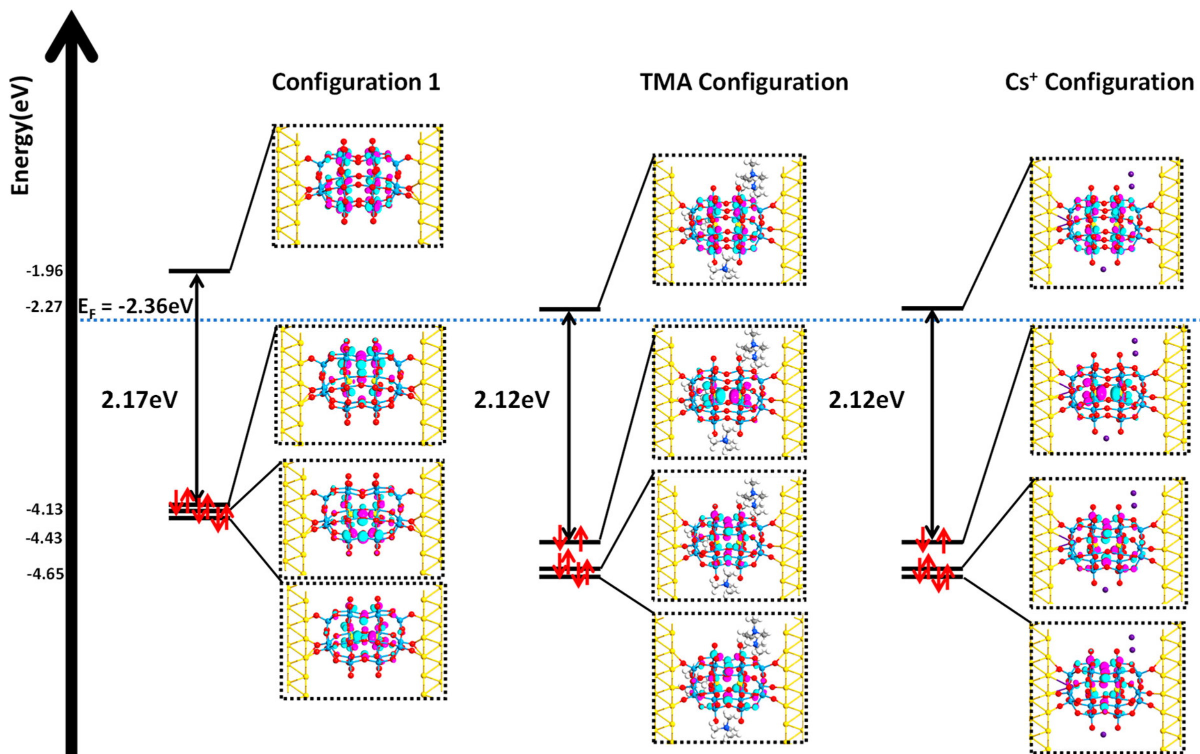

Figure 3.12: Comparison of HOMO-LUMO energies and the respective frontier Kohn-Sham molecular orbitals. The blue dotted line marks the Fermi Energy dominated by the electrodes.

energy levels, resulting in a stabilization, bringing down the energy much closer to the Fermi energy E_F in comparison to the structures without counterions. Interestingly, the results for the TMA and Cs^+ are almost identical with respect to energy level positioning and symmetry of the orbitals. The LUMO level for these systems lies much closer to the Fermi energy, while the HOMO level lies deeper. The results suggest a slight lowering of the HOMO-LUMO gap; however, the difference is insignificant.

The counterions also seem to break the degeneracy of HOMO, HOMO-1, and HOMO-2. The HOMO is clearly higher in energy than HOMO-1 and HOMO-2 for the counterion containing systems. The symmetry of the orbitals is similar, localized on several of the oxygens of the cage, but they are not identical with the HOMO and HOMO-1 of configuration 1.

The LUMO for the systems are identical with configurations 1-3 and are delocalized over the central tungsten cage. The counterions do, however, stabilize the energy with respect to the Fermi energy. As a result, it lies $\approx$ 0.08 eV above E_F. Given that, the transport of the POM has been shown to be LUMO dominated. This is significant for the transport properties of the system. From the energy levels of the junction alone, it would be expected that the presence of counterions increase the current-voltage characteristics significantly.

To further analyse the electronic structure of the counterion containing junctions the PLDOS at zero bias was calculated and is shown in Fig 3.13. The calculated PLDOS is effectively identical for Cs^+ and TMA with only slight differences in the first resonances below the Fermi

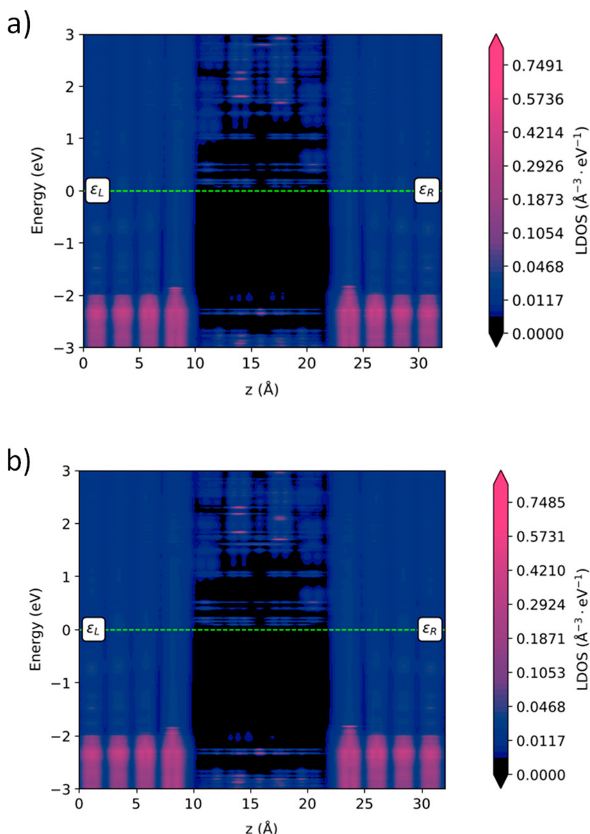

Figure 3.13: PLDOS for the counterion-containing systems: (a) TMA containing system; (b) Cs containing system.

energy. Compared to the single molecule systems, there are more available states above the Fermi energy and all lie closer to the Fermi energy. Below E_F, the density of states is found at lower energies. The calculations illustrate that the presence of counterions influence the Local Density of States of the junction, with available states being lower in energy,analogous to the effect on the energy levels.

The theoretical transmission spectra for the counterion containing junctions are shown in Fig 3.14a. Like the previous results, the spectra for TMA and Cs are almost identical. All peaks are in the same position, with only slight differences in T(E), possibly due to the respective sizes of the counterions. These results suggest that the two cations influence the transport properties of the POM in the same way or the nature of the counterion does not matter and the transport is influenced by the counterion positioning.

The calculations show that the presence of the counterion clearly affects the transport properties of the POM junctions, as highlighted by the difference in the transmission spectra compared to configuration 1 (“no counterions”). The counterions lower the energy of the transmission peaks, bringing them closer to E_F. The peaks remain narrow, as there are still only a few energy states involved in the conduction of electrons. There are significantly more peaks between 1.5 and 2 eV, likely caused due to interaction of counterions with the electrodes. However, given the high bias required to activate these channels, this influence is largely unimportant.

a)

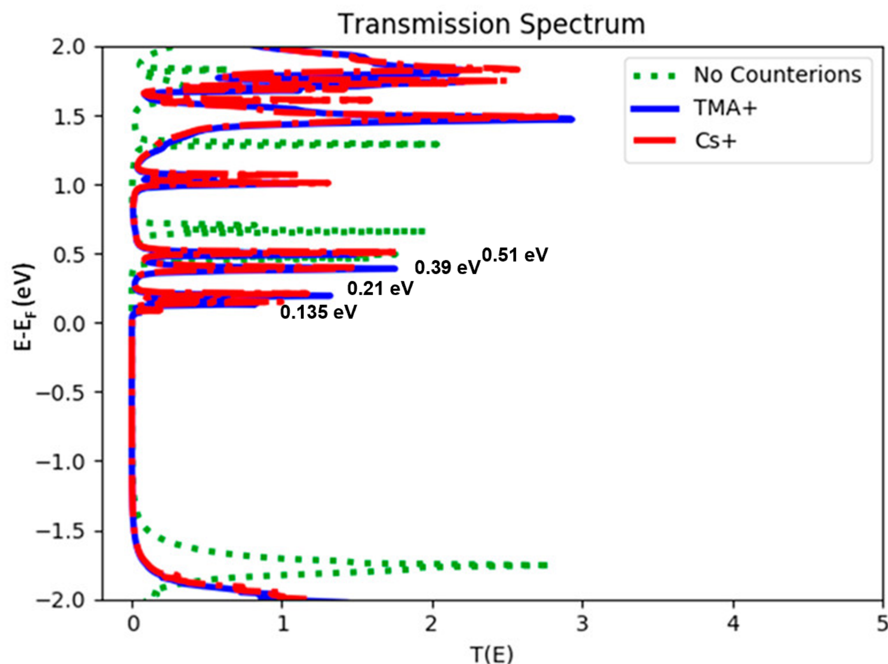

b)

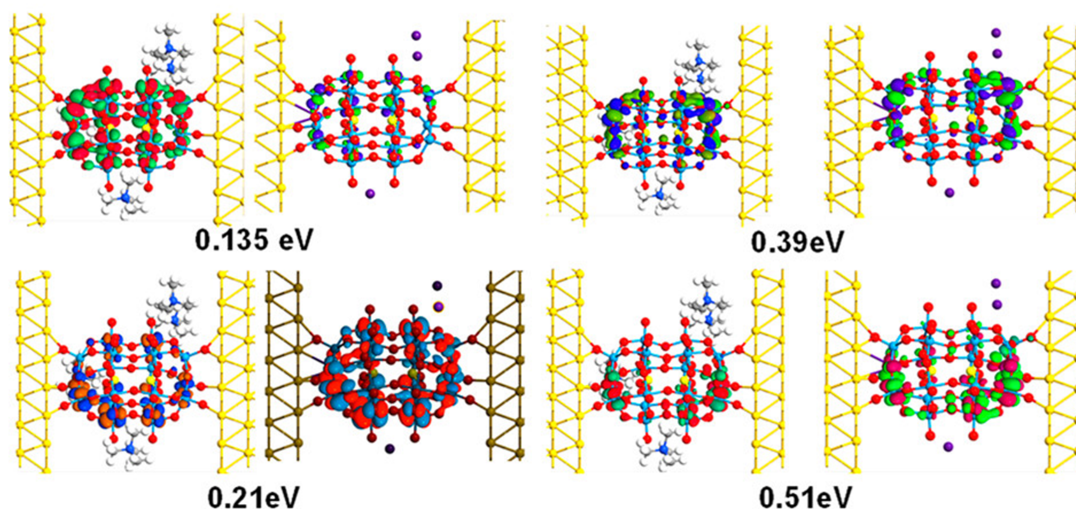

Figure 3.14: (a) Zero bias transmission spectra for configuration 1, with Cs^+ and TMA counterions. (b) Visualized transmission eigenstates for the first four peaks above the Fermi energy. Comparison of the energy states for the TMA-containing system (left) with the Cs^+-containing system (right).

To further understand how counterions influence the transport, the transmission peaks closest to the Fermi energy (0.00 eV) in the range 0-0.51 were analyzed by calculating and visualizing the dominant transmission eigenstates. These are shown in Fig 3.14b. The orbital symmetry and positioning of the eigenstates for both systems are identical. There are small differences in the size of the electron clouds when visualized at the same isovalue. Most notably, at 0.135 eV, where the Cs^+ system's orbitals are much smaller. This is consistent with the lower value of T(E). Because the transmission eigenstates for the peaks are the same for both species of counterion, it can be concluded that they influence the transport of POM junctions the same way.

The calculations also reveal that all the dominant transmission eigenstates are localized exclusively on the POM molecule and not on the counterions. They are all LUMO-like in character, with delocalization across the tungsten atoms in the cage. This implies that the presence of counterions does not create new conductance channels but makes existing ones more energetically stable, which brings them close to the Fermi level and as a result contribute significantly to transport. This reduction in energy makes the transmission modes more likely to be in the bias window and hence increasing the conductance of the system compared to the case without counterions.

When combined with the results for configurations 1-3, it provides clear evidence that the main feasible conductance pathways are focused on the tungsten d-orbitals, which are similar to the LUMO level which is delocalized over the whole tungsten cage. These conductance pathways are influenced by the contact to the electrodes, which shifts the density toward other tungsten areas. In addition, the presence of counterions changes the positioning of the energy level of the molecule with respect to the Fermi energy of the electrodes. As a result, the transmission channels are affected and moved closer to the Fermi level. The delocalization of the transmission eigenstates may offer a way to tune the transmission pathways by chemically influencing these tungsten atoms or by changing the counterions.

Fig 3.15 shows the computed I-V characteristics for the counterion-containing systems. The calculated bias range is smaller than for the POM junction where counterions have been excluded. This is due to the increased size of the systems, the computational cost for calculating transport under an applied bias is much higher. Nonetheless, the results clearly reveal a strong influence of the counterions on the transport.

The first thing to note from Fig 3.15 is that the current for counterion-containing systems rises much more quickly than for configuration 1. Additionally, the magnitude of the calculated current is much higher at lower bias than for configuration 1. Without counterions, at a bias of -1 V the current reaches $\approx 400nA$. However, for the TMA system, the current reaches this value at a bias of -0.3 V and is more than double by -0.5 V. This is a clear indication of an increase in conductance and therefore current flow for the TMA-containing system. Similarly, for the Cs^+ system, the current rises more quickly than in the absence of counterions. By a bias of 0.26 V it

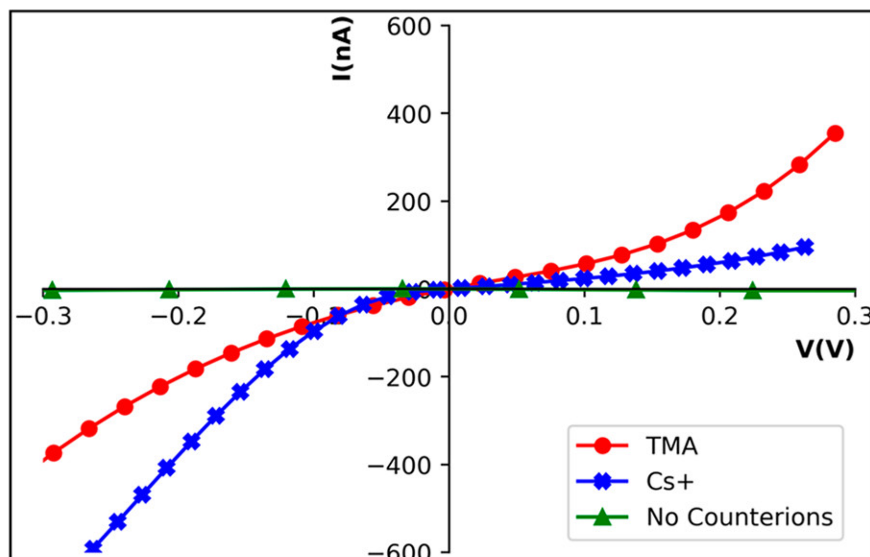

Figure 3.15: Computed I-V curves for the counterion-containing systems.

is already at around 100 nA, whereas a bias of nearly 1 V is required to reach the same current with no counterions.

The increased current at lower bias is consistent with the effects of the counterion on the transmission peaks relative to the Fermi energy. As these conductance channels have been pushed down in energy, a smaller applied bias is required for them to be within the energy window caused by an applied bias.

Given the almost identical transmission spectra for Cs and TMA system shown in Fig 3.13 a, the slight differences in the IV curve for the Cs system compared to the TMA system are surprising. In positive bias the current rises more slowly in the presence of Cs compared to TMA. This may be due to the differences in the value of the T(E) in the peaks between 0 and 0.5 eV. From Fig 3.14a the TMA spectra show peaks with higher transmission in this region.This difference being caused by the nature of the two cations and their charge transport capabilities.

The results suggest that the organic cation (TMA) provides better charge transport than the inorganic one (Cs). Although unexpected given the identical transmission curves, when considering the relative size/polarization of the two cations studied, it is not surprising that TMA would provide better charge transfer. Further experimental work would be key in confirming this prediction.

Overall, the DFT and NEGF simulations illustrate that the effect of the countercations on the transport properties of POMs is not negligible. In fact, the presence of counterions pushes the unoccupied energy levels of the POM closer to the Fermi energy. As a result, the transmission peaks are also found closer to the Fermi energy. Therefore, a lower bias is required for significant current flow in the POM molecular junction.

3.4 Conclusion

The fundamental transport properties of $[W_{18}O_{54}(SO_3)_2]^{4-}$, a POM molecule, have been explored using DFT and NEGF methods. This study has provided insight into what factors will influence the transport of this molecule and by extension other POM molecules.

The calculations show that the electronic structure of the molecule dictates the transport profile of the molecular system. However, the transport is influenced by some key aspects of the device setup. It was found that the contact strength of the molecule to the electrodes greatly influences the current flow through the molecule, with stronger contacts resulting in higher predicted currents. It was also shown that the orientation of the molecule to the electrodes has a key influence on the device's transmission spectra. The horizontal geometry results in the most favorable transmission profile for this molecule.

Lastly, the importance of the counterions on the transport has been illustrated. By exploring two potential counterions, TMA and Cs^+, the simulations suggest that the presence of these ions pushes the unoccupied energy levels closer to the Fermi level of the device. Thus, the conductance channels are more readily available at lower biases, and hence the predicted current is much greater than for systems where the counterions are ignored. The results of the calculations also indicate that TMA and Cs^+ influence the device in much the same way, with no difference in transmission spectra and PLDOS. However, TMA provides better charge transport as illustrated by the computed I-V curves.

This is a purely theoretical and computational study. Using standard experimental techniques in the field of molecular electronics it is possible to measure the POM-based junction's I-V Curves which would confirm the findings of the simulations. This theoretical exploration provides key insights into the transport behavior of this molecule which will inevitably aid device design for molecular electronic device applications. Namely, the influence of counterions on potential device operation cannot be ignored. Here, it has briefly been studied with one case, but further work could explore the details on how different counterion arrangements, number of ions, and identity of counterion influence the system's transport and whether they can be taken advantage of from a device engineering point of view.

Chapter 4

Further POM Studies

4.1 Exploring the Moiety Space of a POM

4.1.1 Introduction

In the last chapter the transport properties of $[W_{18}O_{54}(SO_3)_2]^{4-}$ were thoroughly explored as a molecular junction using first principle computational techniques. Modelling provides key insights to different material properties that can guide the development of new devices at the cutting edge. In the previous chapters, the possibility of POM-based flash memory (and other molecular memories was discussed). One of the main reasons that molecular electronics is being researched so widely is the large range of chemical systems and the capabilities for manipulating and targeting properties. Specifically, one of the main advantages of the POM-based molecular devices is that it allows use of their redox chemistry and chemical variety. In addition to the wide range of POM cage type (Keggin, Ludoquivist, etc...), there can even be significant variety within the same cage, by substituting the moiety of the cage. Changing the caged moiety leads to different, structural, electronic and energetic properties that can play a huge part in developing new molecular devices.

In this chapter, the previous work is extended by exploring different moieties (Y) of the $[W_{18}O_x(Y)]^{b-}$ POM. The aim was to explore, through simulation, how changing the nature of "Y" influences the electron transport properties and overall electronic structure of the molecule. There is a vast number of different "Y" possibilities, the list that is explored here is not exhaustive. The chosen moieties are based on molecules synthesized and reported on in the literature [75, 80, 103]. In addition, the "Empty" POM is explored i.e $[W_{18}O_{54}]$, the case where there is no caged moiety. The explored POMs are listed in the Table 4.1.

The list contains the different variety of POMs studied here, but there are further possibilities, highlighting the rich chemistry of POMs. Furthermore, even for the chosen POMs, there are two POMs studied here: $[W_{18}O_{54}(SeO_3)_2]^{2-}$ and $[W_{18}O_{54}(SeO_3)_2]^{4-}$ that differ only by redox state, this would also be feasible for the rest of the POMs given the highly active redox nature

POM Molecule	Moiety
$[W_{18}O_{54}]$	None ("Empty")
$[W_{18}O_{54}(SO_3)_2]^{4-}$	$[(SO_3)_2]^{2-}$
$[W_{18}O_{54}(SO_4)_2]^{4-}$	$[(SO_4)_2]^{2-}$
$[W_{18}O_{54}(SeO_3)_2]^{2-}$	$[(SeO_3)_2]^{1-}$
$[W_{18}O_{54}(SeO_3)_2]^{4-}$	$[(SeO_3)_2]^{2-}$
$[W_{18}O_{56}(IO_6)]^{6-}$	$[(IO_6)]^{6-}$
$[W_{18}O_{56}(WO_6)]^{6-}$	$[(WO_6)]^{6-}$

Table 4.1: List of POM molecules and the caged species explored in this chapter.

of these molecular clusters.

The ultimate aim is to incorporate this type of POM cluster as the storage element of a molecular flash memory and take advantage of their properties. As discussed before, in order to make this a reality, a fundamental understanding of the transport through these molecules is critical. The main property that requires understanding for memory application is the POMs ability to store charge, and "how much charge" it can store. Capacitance is a measure of a systems ability to store charge. Therefore, it is the natural property to explore for this application. Hence, the main aim of the work in this chapter was to estimate the atomic scale capacitance of these POM molecules and assess how the different caged atoms influence the charge storage.

4.2 Simulation Methodology

4.2.1 General Computational Settings

All calculations were carried out using the Quantum ATK software packages (version 2019-2021). The single molecule calculations were carried out using the BP86 GGA type functional, with a SG15 pseudopotential and a medium basis set which has been shown to describe the geometry and electronic structure of these non-conventional Wells Dawson POMs accurately [77, 83, 84, 104]. For the Junction calculations the gold electrodes were described by a FHI pseudopotential and a SZP basis set, a successful and efficient approximation used in molecular junction calculations [105]. A Monckhorst grid k-point sampling of 5 × 5 × 400 was used to compute the device system accurately.

4.2.2 Estimating the Atomic-Scale Capacitance

Macroscopic capacitor physics is based on the parallel plate capacitor, where two conductive plates are separated by space or a dielectric, leading to a build up of charge on the plates and an electric field between them. For this case, the capacitance is given by:

$$C = \frac{Q}{V} = \frac{Q}{Ed} = \frac{A\varepsilon}{d} \tag{4.1}$$

where C is the capacitance, Q is the charge, V is the applied bias, E is the electric field, d is the distance between the plates, A is the cross sectional area of the parallel plates and ε is the permittivity of the spacer layer.

However, the capacitance at the nanoscale may be significantly different. Calculating the capacitance of molecules and nano-scale systems is an active area of research [106–109]. For the purposes of this work, the goal was not to compute an absolute value of capacitance, but to compare the capacitance of the different caged moieties of the Au-POM-Au systems. Hence, a simpler approach was taken. To estimate the capacitance, the electrostatic energy of the device was computed as a function of the applied bias:

$$E(V) = \frac{1}{2}\int \delta v(r,V)\delta n(r,V)dr \tag{4.2}$$

where δv is the induced electrostatic potential and δn is the induced electron density and r are the atomic coordinates of the device. From this the Electrostatic energy was plotted against applied bias and Capacitance was extracted by using the relation:

$$E = \frac{CV^2}{2} \tag{4.3}$$

4.3 Results and Discussion

4.3.1 Electronic structure of the POM Single Molecules

The starting point is to calculate and analyze the electronic structure of the single molecules listed in Table 4.1 before creating the junction device. As stated in the introduction, there is a sizeable diversity of $W_{18}O_xY$ style POMs that have been or can be synthesized. The molecules were chosen as they had previously been suggested for memory based applications, however the moiety type, redox state and number of molecules need not be limited to the ones presented here.

One of the considerable advantages and reasons molecular systems are being explored for the future of electronic devices beyond Moore's law is the incredible diversity. Furthermore, the success and expertise of synthetic chemistry results in a versatility in molecular electronic systems controlled by small changes on the molecular level. In this instance, the properties of the $W_{18}O_xY$ POM cage can be changed significantly by choice of "Y", even changes in redox state can considerably influence the charge transport properties and subsequently the potential device applications.

The single molecules listed in Table 4.1 were optimized and the energy levels computed and visualised. The HOMO, LUMO and other unoccupied orbital energy levels are shown in Fig 4.1. The HOMO-LUMO gap (E_{HL}) is also shown in the figure. It is clear that changing the caged moiety significantly changes the relative energy positioning of the energy levels and also

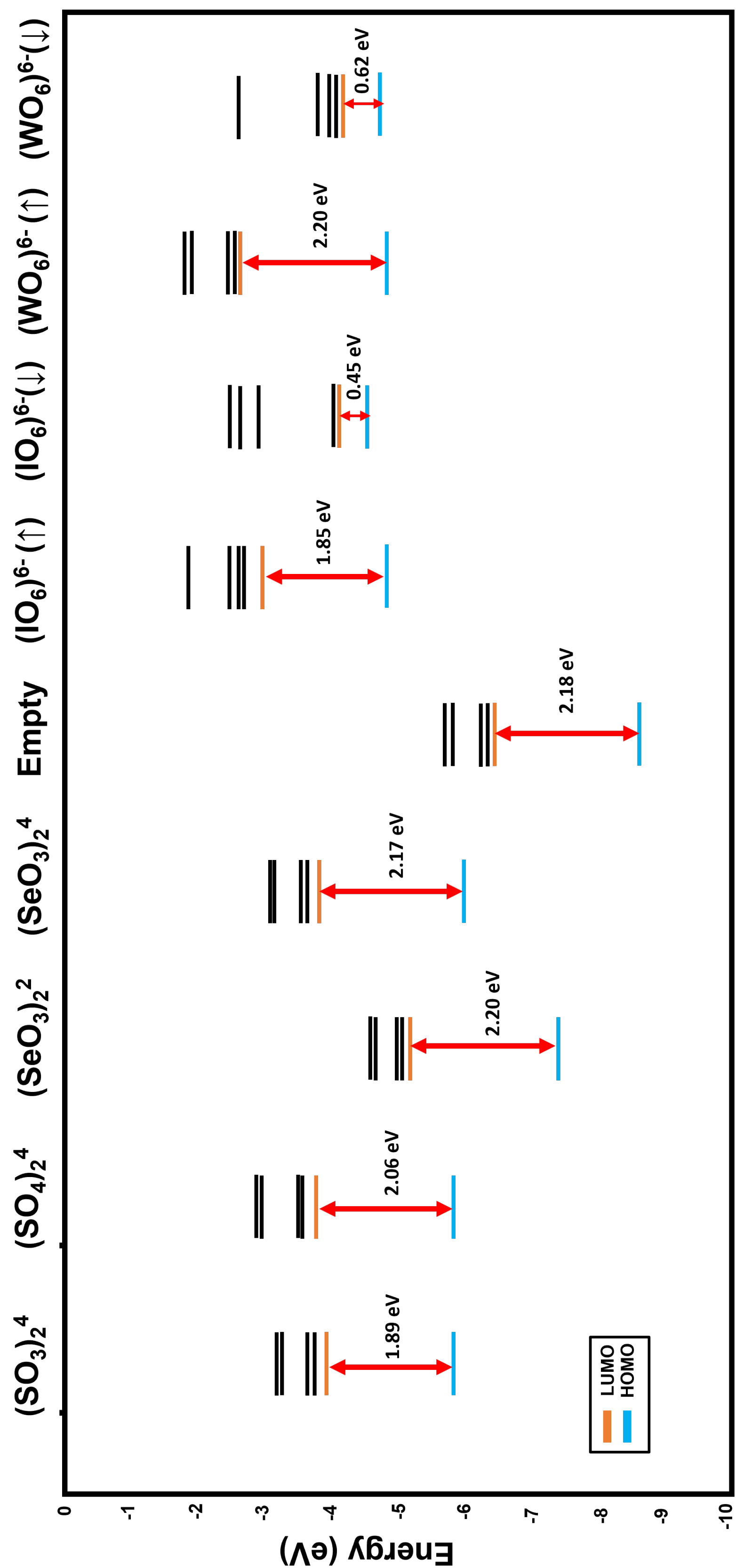

Figure 4.1: Visualisation of the respective HOMO, LUMO and other unoccupied molecular orbital energies for all the POM molecules in this study.

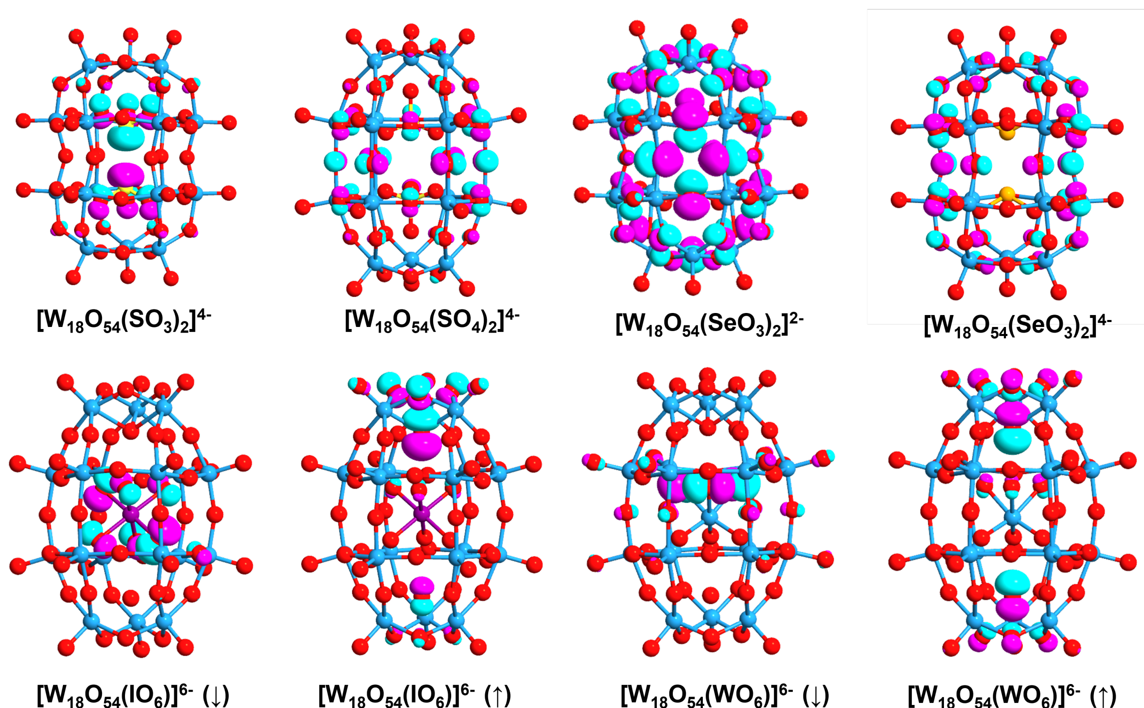

Figure 4.2: Visualisation of the HOMO levels for the POMs in this study.

the respective E_{HL}, which will significantly influence the charge transport properties. The first notable trend in Fig 4.1 is the higher the redox state of the molecule (more charged) the higher the energy of the energy levels. The "Empty" cage (i.e $W_{18}O_{54}$) has a redox state of zero and clearly has the lowest lying energy levels. The energy levels of $(SeO_3)_2{}^{2-}$ are visibly more stabilised (more negative) than the 2x reduced $(SeO_3)_2{}^{4-}$. Whilst the $IO_6{}^{6-}$ and $WO_6{}^{6-}$ have the highest energy levels due to their higher charge. This trend was expected as increasing the number of electrons in the system raises the energy of the occupied orbitals and subsequently the unoccupied orbitals leading to the clear visible trend across the $W_{18}O_xY$ species.

The E_{HL} range from 1.89 to 2.20 eV (excluding the "spin down" gaps which are 0.45eV and 0.62 eV). Simply through selection of moiety the energy gap can be engineered. By changing the caged species from SO_3 to SO_4 results in a 0.17 eV increase in the energy gap due to higher energy of unoccupied orbitals. there is very little change in the energy gap after the reduction on $(SeO_3)^{2-}$ to $(SeO_3)^{4-}$ which could be advantageous for storing multiple electrons in memory applications. In general, the presence of a moiety reduces the E_{HL} with respect to the "Empty" cage. This can be explained by looking at the orbitals given by Fig 4.2, Fig 4.3 and Fig 4.4. Since the LUMO and LUMO+ levels lie on the cage, changing the moiety doesn't influence the unoccupied energy levels. However, the HOMO is commonly localised on the moiety thus increasing the energy of the HOMO and reducing the overall gap. The case where the gap hasn't really changed can be explained by the fact the HOMO is mostly localised on the cage as shown by Fig 4.2.

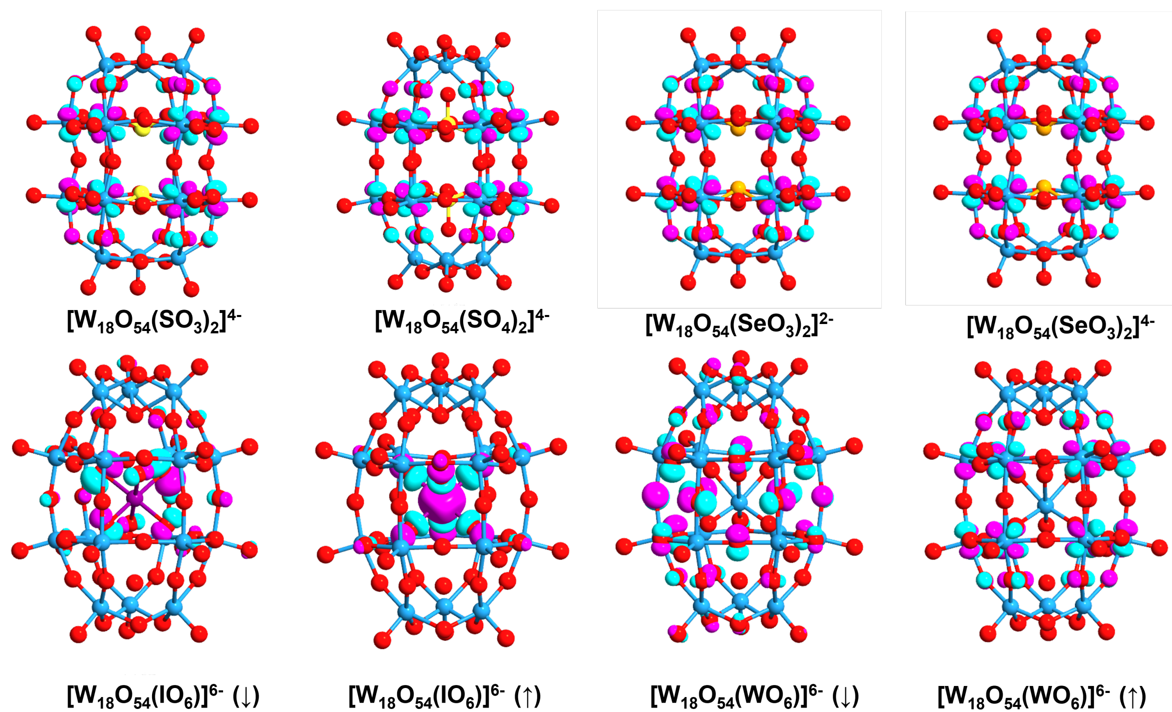

Figure 4.3: Visualisation of the LUMO levels for the POMs in this study.

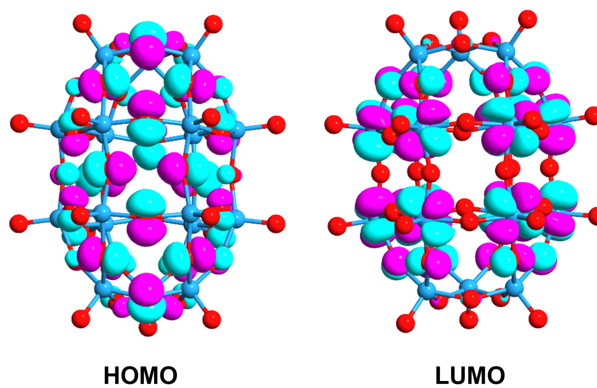

Figure 4.4: Visualisation of the HOMO-LUMO levels for $W_{18}O_{54}$ ("Empty" POM).

With the exception of the $[W_{18}O_{56}(IO_6)]^{6-}$ anion, the LUMO levels for all systems are d-like in nature and are delocalised across the central band of the tungsten cage. Interestingly, the unnocupied orbitals are dominated by the metal cage and thus the reduction of the molecule will occur across this cage in most cases. For the $[W_{18}O_{56}(IO_6)]^{6-}$ species, the LUMO levels for both spin states are localised on the central IO_6 structure. Thus the caged species is of critical importance for the reduction and subsequently the storage of electrons.

The $[W_{18}O_{56}(IO_6)]^{6-}$ and $[W_{18}O_{56}(WO_6)]^{6-}$ are interesting systems as both are affected by spin polarization, the IO_6 containing species has an unpaired electron whilst although the $[WO_6]$ containing system has fully paired electrons, the electronic structure is more complex due to the transition metal centre,W. Because of this, a difference is seen in the computed spin states (up and down) in the spin polarised DFT calculation as shown by the different energy levels in Fig. 4.1. As a consequence, in this particular redox state the system could contain interesting spin-based or magnetic properties. From the energy level perspective, the "spin up" HOMO-LUMO gap is similar to the rest of the $W_{18}O_xY$ systems. $[W_{18}O_{56}(IO_6)]^{6-}$ has the smallest HOMO-LUMO gap of all molecules studies, and is considerably smaller than that of $[W_{18}O_{56}(WO_6)]^{6-}$. Looking at the HOMO-LUMO energy levels in Figs. 4.2 and 4.3 this can be explained by the fact that both the HOMO and LUMO lie on the caged moiety compared to the LUMO typically being the d-orbitals of the tungsten cage. The "spin down" HOMO and LUMO state for the $[W_{18}O_{56}(IO_6)]^{6-}$ configuration is very similar and localised on the oxygen atoms of the $[IO_6]^{6-}$ resulting in a smaller energy gap. The "spin down" energy gap for $[W_{18}O_{56}(WO_6)]^{6-}$ is also considerably smaller due to the differences in the energy levels of "spin up" and "spin down" configurations. Due to the fact the species have an unpaired electron, it is possible this could influence the transport through the molecule and subsequently the capacitance and storage properties.

It's worth noting that in the absence of an external magnetic field, the calculated spin-up and spin-down states are typically degenerate in energy in DFT calculations. Hence there is no preference for one spin direction over the other, and the DFT calculation treats them equally. However, it gives an insight into the different spin states that could exist under an external magnetic field. In cases where an external magnetic field is applied, additional considerations may be required to account for its effects on the electronic structure. This can involve applying a Zeeman term to the Hamiltonian or considering spin-orbit coupling, depending on the specific situation and level of theory employed.

In this section, the different POM molecule configurations studied have been introduced and their electronic structure analysed. The ground-state DFT calculations indicate that although all the molecules have the same cage structure and therefore similar electronic structure, the difference in caged species and redox state has a significant influence in the nature of the HOMO, LUMO and LUMO+ levels. By extension, the HOMO-LUMO gaps all lie in similar region 1.85-2.2 eV but are influenced by the structural changes. Namely, the HOMO levels tend to be

localised on the caged species whilst the LUMO levels tend to be delocalised across the tungsten cage, with exceptions. Understanding this helps rationalise the differences in electronic structure and guide in engineering the molecular features required for electronic device applications.

4.3.2 Electronic structure of the POM Molecular Junctions

The aim of this chapter is to explore how different moieties and redox states of a similar POM cage influences the charge storage, or electron transport in general of these POMs. As explained in the last chapter, the simplest and most efficient way to study the transport of the POM molecules is as POM molecular junctions. For all these species the Au-POM-Au configurations were created and studied computationally. Of course, for POM based memory devices, the architecture would be more sophisticated, however the aim here was to compare the charge storage of these molecules by estimating the capacitance and comparing their transport. The simplest way to achieve this goal is by studying molecular junction systems.

It was shown and discussed in the last chapter that the strength/geometry of the POM-Au connection has a significant influence on the electrical response to an applied bias and thus on the electron transport. Moreover, the number of Au-POM-Au configuration possibilities are vast. It is common, that a molecular linker be used to specify the geometry and ensure more consistent connection between gold and the molecule. There are a wide range of synthetic possibilities but as yet, no examples of linkers with these specific POMs have been reported thus a linker is not considered here. A typical method for studying POM (and other) molecular junction is through C-AFM (conductive atomic force microscopy). When using this method, a molecule typically linked to a gold surface forms a junction with the C-AFM gold tip, however the link is in the Van der Waals limit [110–112]. There are also other examples of non-covalently bonded molecular junctions in the literature [113, 114].

Since the goal is to compare between different molecules and taking into account all of the above, it was decided to create the POM junction configurations where the POM is connected to the electrodes through the VDW limit. The POM is sandwiched between two gold (111) bulk electrodes at a distance of the sum of the Van Der Waals radius of the two atoms (gold and oxygen (3.32 Å)) either side. This is considered an approximation to the typical C-AFM tip to the molecule. This configuration is considered the non-ideal/ least favourable transport conditions, i.e the "worst case" scenario for transport is being investigated. This way, any effects due to contact strength or geometry between molecule and gold across the different studied molecules are not considered, and a more consistent systematic comparison between the different molecules in Table 4.1 can be carried out. Furthermore, it was shown in the last chapter that the molecule orientation (horizontal vs vertical) significantly impacts the magnitude of current through the junction. It was shown that due to the HOMO alignment, the horizontal orientation showed the best transport conditions. For this reason, all the junction configurations in this work have beem created for the case where the molecular orientation is horizontal.

The molecular junctions for all the molecules in Table 4.1 were created and studied at zero bias using DFT-NEGF method as previously described. In the last section, the electronic structure of the single molecules in vacuum were analysed. As discussed in the previous chapter, although the electronic structure of the molecule dominates the junction properties, the electronic structure is altered by the presence of the gold electrodes and the non-equilibrium distribution and can lead to changes in the energy levels and energy gaps. Therefore, to fully understand the transport behaviour of these systems, it is vital to analyse the electronic structure of the molecule in the junction configuration. The energy level diagram for all the molecular junction configurations in this study is shown in Fig 4.5, where the relative positioning of the HOMO, LUMO, LUMO+1 to +4 and respective HOMO-LUMO gaps are displayed.

Comparing Fig 4.1 with Fig 4.5, the introduction of the molecule into to the junction system influences the energy level diagram as expected. Firstly, in Fig 4.5 it is notable that the Fermi level is shown and is the same for all junctions. The Fermi level is calculated for the whole junction system, the gold electrodes are the same size for all junctions and in fact only the caged atom/redox state changes. Therefore, the Fermi level would be expected to be the same in all cases, allowing for an easier comparison of the energy levels with respect to this energy. For ease of comparison, the Fermi level is normalized to 0 and the energy levels are reported with respect to the Fermi level. The changes in alignment of the energy levels between the Fermi level and single molecule is not appropriate due to the different Fermi levels of the system. What is evident from Fig 4.5 is that excluding the empty caged POM($W_{18}O_{54}$) which is neutral, the Fermi level energy lies closer to the HOMO for all junctions compared to the LUMO.

In all cases, the HOMO-LUMO gap has changed in some way. In general the changes are small with only the $(SO_3)_2{}^{4-}$ containing POM and the "spin down" states of the $(IO_6)^{6-}$ and $(WO_6)^{6-}$ containing systems showing significant change in the energy gap. Thee change for $(SO_3)_2{}^{4-}$ from 1.89eV to 2.14 is consistent to what was reported in the last chapter and provides validation to the weak contact junction configuration. The significant change in energy gap is due to the stabilization of the HOMO due to excellent alignment between the orbitals and the electrodes as can be seen from Fig 4.6.

For the "spin down" $(IO_6)^{6-}$ and $(WO_6)^{6-}$ systems, there is a significant reduction in the HOMO-LUMO gap with it essentially disappearing for $(IO_6)^{6-}$. Although some rationalisation can be obtained from the respective orbitals,for example the HOMO and LUMO for $(WO_6)^{6-}$ being localised in the same region, the HOMO and LUMO have changed for these two systems when placed in the junction configuration. The calculation of the molecular energy spectrum predicts that the $[W_{18}O_{56}(WO_6)]^{6-}$ junction has an extra electron on the molecule compared to the isolated molecule, thus has an unpaired electron. It is possible that due to the non-equilibrium distribution of the junction configuration and the "unpaired" electron makes the electronic structure more difficult to describe. Further investigation is needed to fully understand the changes, though out of the scope of this work. Furthermore, given the small gaps, the "spin up" HOMO-

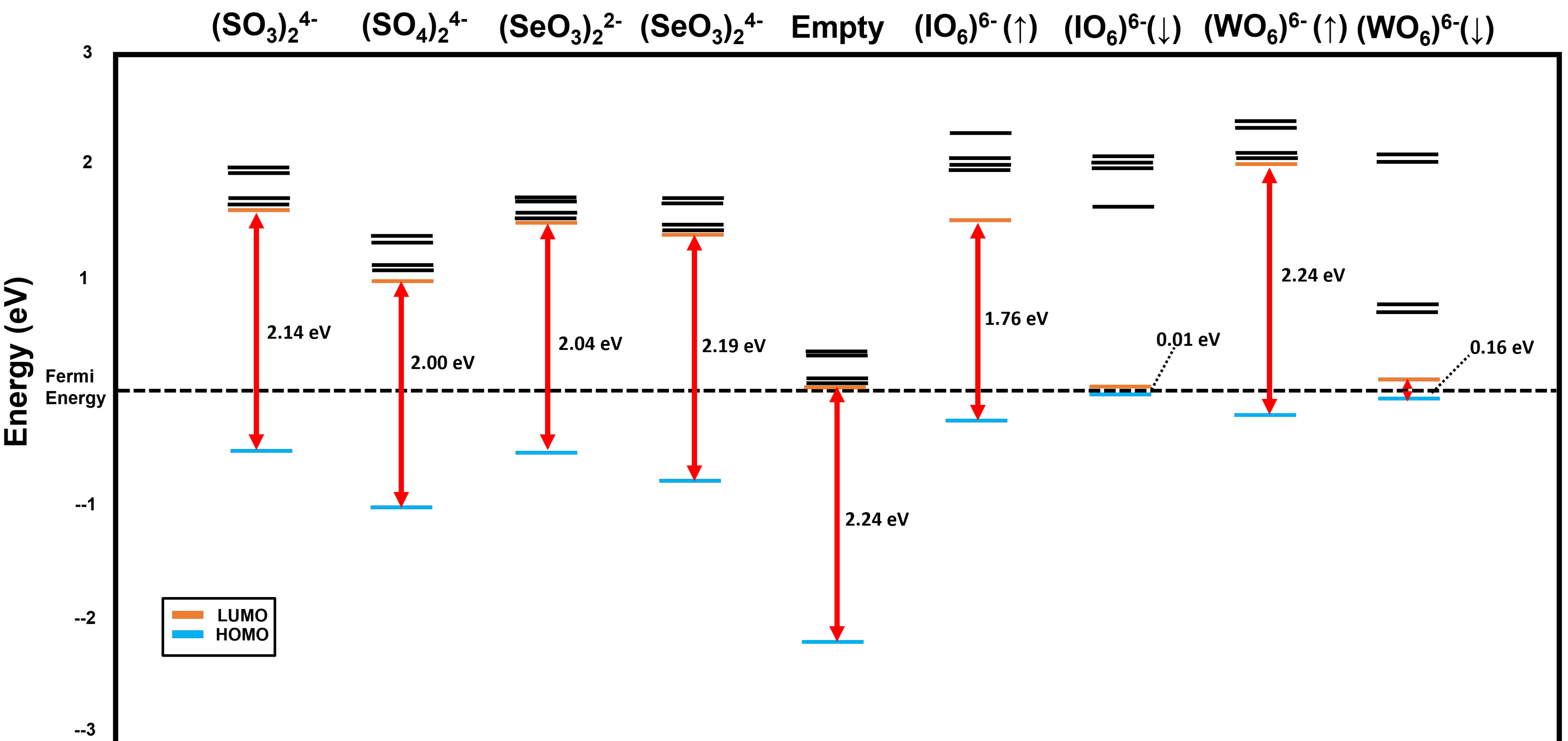

Figure 4.5: Visualisation of the respective HOMO, LUMO and other unoccupied molecular orbital energies for all the POM molecular junctions in this study.

LUMO configuration for these junctions are likely the best description for the electronic structure. Nonetheless, it is clear for the junction configurations for these two molecules, they both appear to contain an open-shell configuration (i.e an unpaired electron).

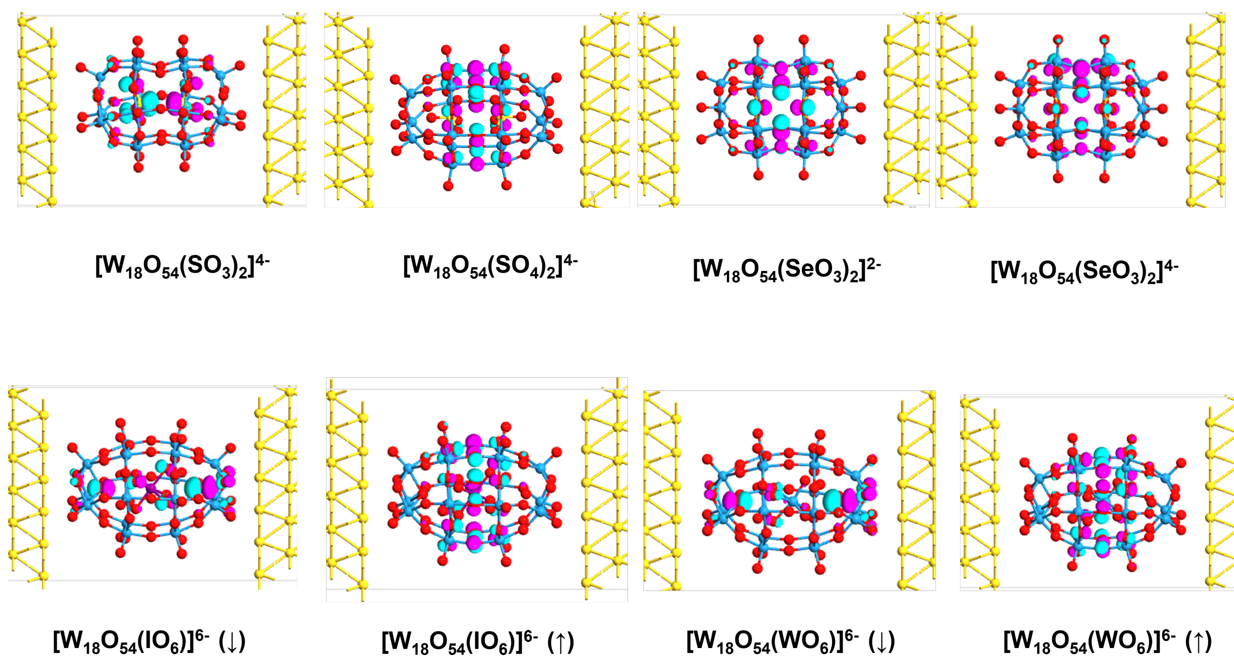

Figure 4.6: Visualisation of HOMO levels for the POM Junctions in this study.

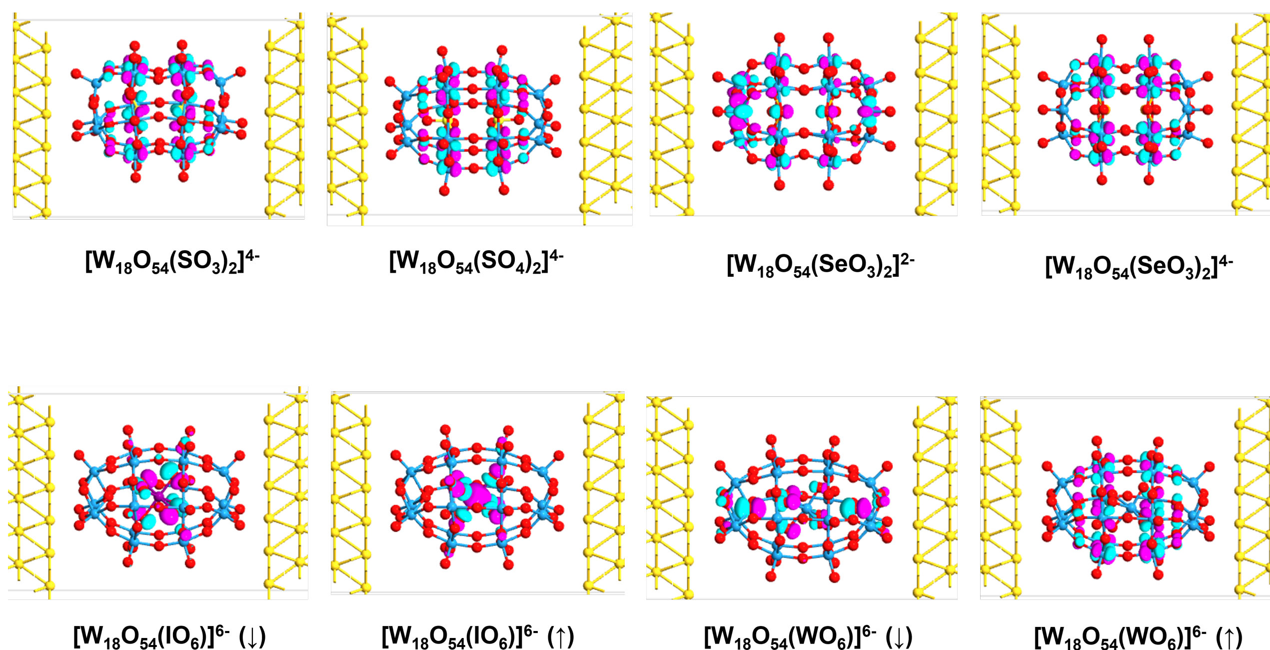

Figure 4.7: Visualisation of LUMO levels for the POM Junctions in this study.

Despite slight changes in the HOMO-LUMO energy gap and excluding the $[W_{18}O_{56}(IO_6)]^{6-}$ and $[W_{18}O_{56}(WO_6)]^{6-}$ POMs, the HOMO-LUMO orbitals and general electronic structure of

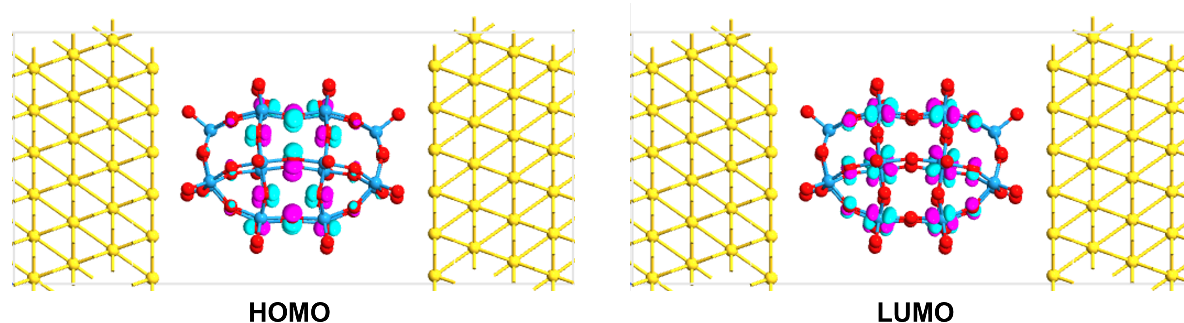

Figure 4.8: HOMO-LUMO levels for $W_{18}O_{54}$.

the molecules remain the same even when in the junction configuration. This is consistent with the findings of the previous chapter, thus the electron transport properties through the junction are dictated by the electronic structure of the molecule. Hence, studying the electron transport of through molecules as junctions is appropriate for understanding and comparing the charge storage and transport properties of the POM molecules.

4.3.3 Transport in the Molecular Junctions

The transport of the POM molecular junctions was investigated using the DFT-NEGF method. Initially, the junctions were studied under zero bias and their transmission spectra computed as shown in Fig 4.9. This gives an insight to the electron transport properties of the molecular junction.

In Fig 4.9 only the transmission spectra of the configurations that have fully paired electrons is shown. The transmission of these systems is not affected by the spin polarized states. Whereas, as will be discussed further later, the $[W_{18}O_{56}(IO_6)]^{6-}$ and $[W_{18}O_{56}(WO_6)]^{6-}$ have spin resolved transmission for the two different states (up and down). Hence these systems will be considered separately. What is clear from Fig 4.9 is that the computed transmission spectra mirrors the energy level diagram for the junctions presented in Fig 4.5. Where peaks in transmission correspond directly with the discrete energy levels of the molecule. Furthermore, the alignment of energies of transmission between the different molecules are consistent with that of the energy levels in Fig 4.5. It was shown in the previous chapter that the electron transport in POM molecular junctions are LUMO-dominated, thus the first peak in the transmission above the Fermi level (which is set to 0 in the plot) is expected to be LUMO-like in nature. The respective transmission eigenstates would demonstrate this as discussed previously. Therefore, the nature of the LUMO and LUMO+ levels is an important consideration for transport through these molecules.

Given the low conductance and discrete energy levels of these systems, the peaks in transmission shown in Fig 4.9 are very sharp. The energy range of interest for transport would be -1 to 1eV at most, as higher energy levels would require significantly higher applied bias. The

Figure 4.9: Transmission Spectrum for the POM Junctions with selected caged species (empty ($W_{18}O_{54}$), $(SO_3)_2^{-4}$, $(SO_4)_2^{-4}$, $(SeO_3)_2^{-2}$, $(SeO_3)_2^{-4}$)

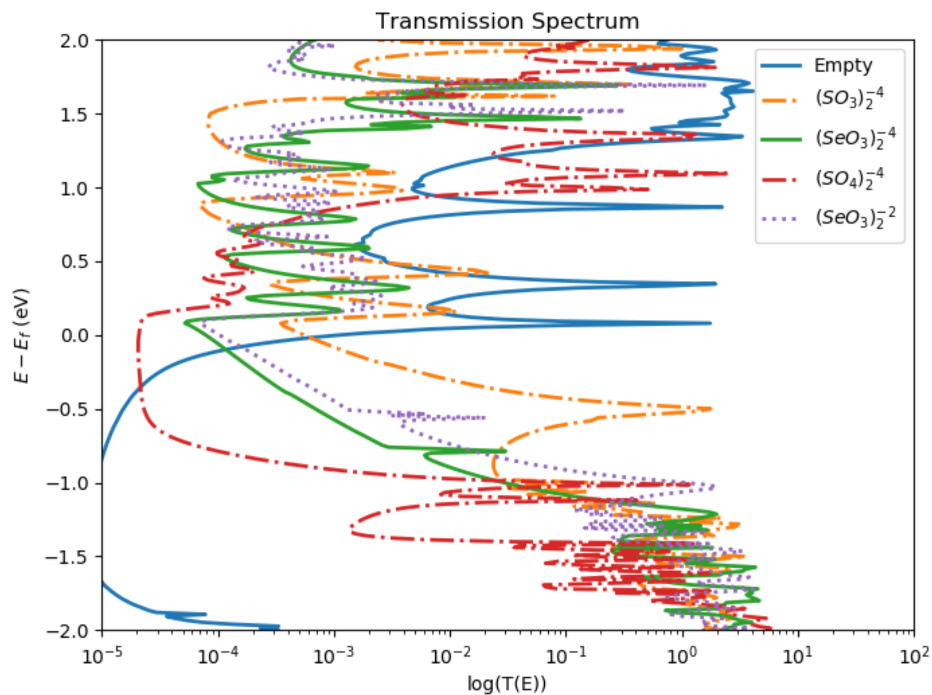

Figure 4.10: Transmission Spectrum in log scale for the POM junctions with selected caged species (Empty ($W_{18}O_{54}$), $(SO_3)_2{}^{-4}$, $(SO_4)_2{}^{-4}$, $(SeO_3)_2{}^{-2}$, $(SeO_3)_2{}^{-4}$)

peaks below -1eV correspond mostly to the filled states of the molecule and the gold electrodes. Whereas above 1 eV are the transmission states for higher level unoccupied orbitals. From this, it can be discerned that the "Empty" and the $[(SO_3)_2^{4-}]$ would show the highest magnitude of current as they are the only configurations with peaks within the bias window. It also suggests that these would be the only configuration showing significant IV characteristics. However, the linear scale Transmission spectra fails to capture subtleties in the transport profile of these junctions.

Inspecting the transmission spectra in the log scale (log (T(E)), further insight can be gained to the transport and further transmission profiles are revealed for the different caged species. Unlike in the linear scale, it can be seen that there are transmission resonances within the 0.5 to -0.5eV energy window (for a -1 to 1 V applied bias). In fact, what is made evident is that there are very similar profiles (peaks in similar positions and of similar shapes) for all POM junctions, differing primarily in intensity and area of curve which corresponds to the conductance. This is as expected, although there are some differences in the HOMO due to the nature of the caged moiety, the LUMO however is practically the same for all as shown in Fig 4.7. Additionally, the unoccupied orbitals mostly correspond to the d-orbitals of the tungsten cage and so a similar profile across all molecules are expected. However, the difference in caged species, redox state, charge distribution and E_{HL} lead to differences in the magnitude of transmission and the positioning of some transmission peaks. This highlights from a device point of view, how small changes to the molecule can have drastic changes in transport and device performance, making POM molecular electronics a versatile candidate for device engineering.

The POM molecular junctions were studied under an applied drain bias ranging from 0-1V. Initially, the junctions were studied under an applied bias of -1 to 1V. Due to computational expense and slow convergence, the bias range was focused to 0-1V. This is reasonable for the purpose of comparing between these POM configurations. It is typical that the I-V characteristics for the POM junctions to be almost symmetric under reverse bias (albeit a lower magnitude of current). This is clearly seen in the computed I-V curve for the Au-$[W_{18}O_{54}(SO_3)_2]^{4-}$-Au junction which is shown in Fig 4.11.

The I-V characteristics computed for the Au-$[W_{18}O_{54}(SO_3)_2]^{4-}$-Au studied here mirror those of the three different Au-$[W_{18}O_{54}(SO_3)_2]^{4-}$-Au configurations discussed in the previous chapter as shown in Fig 3.8. In fact, the magnitude of the current here is in the same range as to that for configuration 3 which suggests the set up of the junctions in this chapter (in the order of the Van der Waal radius) shows coupling of the molecule to the electrodes of similar strength as the direct bond for configuration C discussed in the last chapter. Further validating the junction configuration selected for this study.

It is expected from the log transmission spectra that the I-V Curves for the different moieties would be similar in shape but differ significantly in magnitude of current. The computed currents follow the trend seen in the transmission spectra, with the current at a bias of 1V being only 1.36

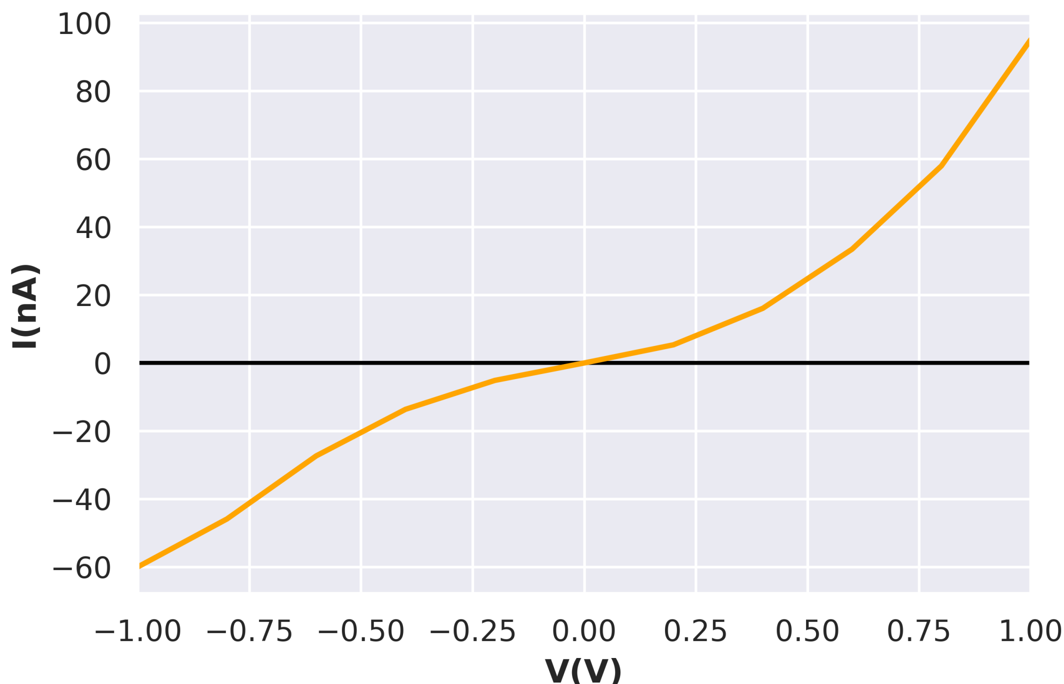

Figure 4.11: The Computed I-V curve for the Au-$[W_{18}O_{54}(SO_3)_2]^{4-}$-Au junction. The shape of the IV curve is typical for all of the POM junctions in this chapter.

nA for the $(SO_4)^{-4}$ containing POM and being 4 orders of magnitude bigger at 1883.18 nA for the case of the empty POM cage. As a result, to compare across the POM junctions, the I-V curves are plotted in log scale for the current (shown in Fig 4.12).

With regards to shape, given the "exponential type" linear scale I-V Curve, the log scale shows a linear I-V curve. Even from the log scale what is evident is that the I-V curves for all junctions are essentially the same shape but differ in magnitude of current. This is not unexpected as the only thing that changes is the caged molecule/redox state. However, the extent of difference in magnitude of current for the different moieties is interesting. It is clear that the redox state of the molecule, which is dominated by the charge of the caged moiety, influences the magnitude of current. The empty POM cage ($W_{18}O_{54}$) which has neutral charge has a much higher current than the other systems, by several orders of magnitude. Additionally comparing the I-V curve for $(SeO_3)_2{}^{-4}$ and $(SeO_3)_2{}^{-2}$ the less negative redox state (-2) produces more current. Though the difference is very small as expected given it is the same molecule with little change to electronic structure and geometry. From the energy level diagram in Fig 4.5 and the linear scale transmission spectrum in Fig 4.9 it would be expected that the $(SO_4)_2^{-4}$ would have the best transport properties after the Empty Junction. Since it has the lowest energy gap and also transmission peaks closest to the Fermi level, albeit at ≈ 1 eV. The linear scale transmission explains the variation in the relative magnitude of current for these junctions. However, the log scale transmission reveals subtle transmission peaks which explains the relative ordering of the

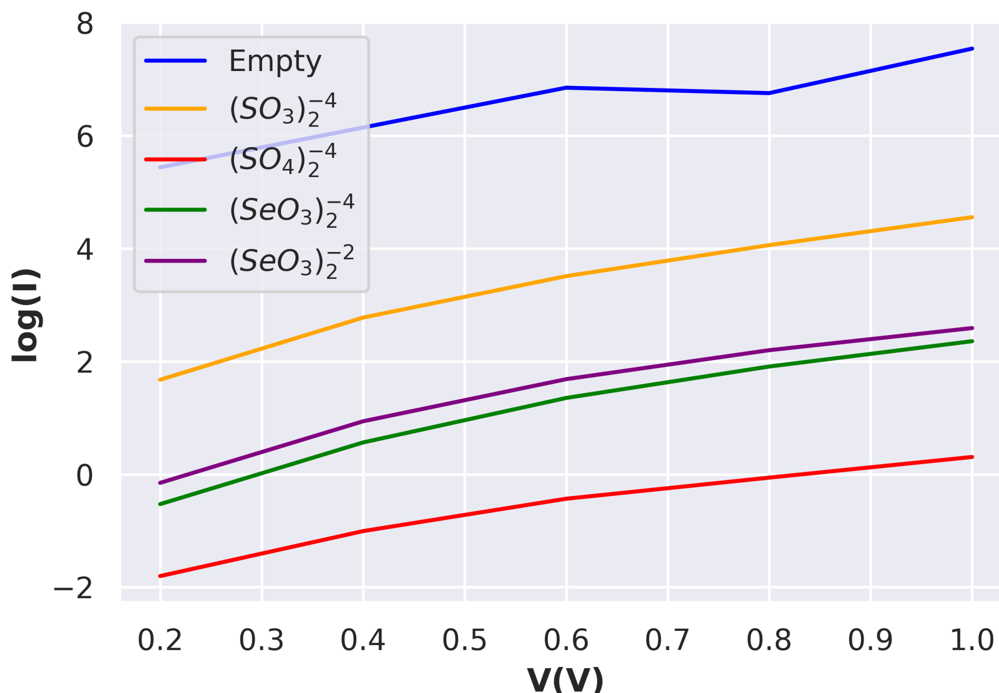

Figure 4.12: Comparison of the Current-voltage characteristics for the POM Junctions with selected caged species (empty ($W_{18}O_{54}$), $(SO_3)_2^{-4}$, $(SO_4)_2^{-4}$, $(SeO_3)_2^{-2}$, $(SeO_3)_2^{-4}$)

different POM Junctions. The transmission profile in the log scale in the region of 0-0.5 eV, is very similar for all of the studied POMs, as clearly dictated by the molecules cage. Though they differ in intensity and energy positioning, in general they are of similar profile. What is considerably different is the width and area of the profile in this region which related to the relative conductance of the different caged species. The order of increased transmission is consistent with the order of the differences in magnitude of the current for the different POMs as revealed by the Log(I)-V profile in Fig 4.12. Aside from the $(SeO_3)_2{}^{-4}$ and $(SeO_3)_2{}^{-2}$ which have very similar order of magnitude of current as explained by the transmission profile and the fact the species differ by only 2 electrons (redox state), what is highlighted by the computed spectra here is that very small changes in the molecule (the nature of the caged moiety) has a significant influence on the transport properties of the system.

Even though the differences in HOMO-LUMO gaps are reasonably small across all junctions as shown by Fig 4.5, the relative spacing of the higher unnoccupied levels, the positioning with respect to the Fermi level and positioning of the HOMO all varies due to the changed identity or state of the caged species. Subsequently, this is reflected in the transmission profile highlighted in the log scale which helps rationalise the computed I-V characteristics. Understanding why these changes are so pronounced for the change of moiety could be accomplished by a deeper study of the respective energy levels and the corresponding transmission eigenstates in the region of 0-0.5 eV. It has been revealed from the electronic structure and transport simulations, that the

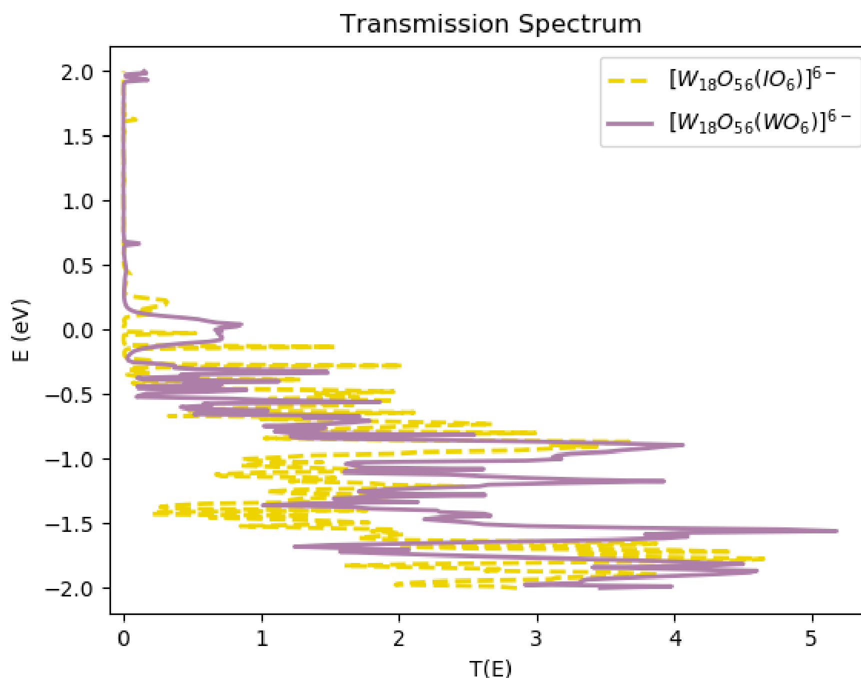

Figure 4.13: Transmission Spectra for $[W_{18}O_{56}(WO_6)]^{6-}$ and $[W_{18}O_{56}(IO_6)]^{6-}$ molecular Junctions

conductance of the molecule can be tuned significantly by the choice of caged species and the respective redox states available to the molecule.

Up to this point the focus has been on the closed shell examples. Two examples of open shell systems (containing an unpaired electron) were studied here, these are the $(IO_6)^{6-}$ and $(WO_6)^{6-}$ containing POMs. These types of molecules are known to have interesting magnetic properties due to their different possible spin states at different redox states. From a device transport perspective, this can result in spin-polarised and spin-dependant transport as has been seen reported in a wide variety of molecular junction systems [115–118]. From a memory point of view, different spin states could aid in multi-bit memory, depending on the spin-dependant nature of the transport. However, further investigation of different redox states and their spin-dependence would be required to assess spin based memory applications.

The computed transmission spectrum for $[W_{18}O_{56}(WO_6)]^{6-}$ and $[W_{18}O_{56}(IO_6)]^{6-}$ is shown in Fig 4.13. In this case, although it is known the transport is influenced by the spin polarization, the spectra for the case of sum of all spins is given. This allows a simpler comparison between the two molecular junctions. Given the only difference between the two systems is the nature of X in XO_6 being either W or I, it is unsurprising that the transmission profile is similar for these two junctions. Most notably above the Fermi level (0 eV) there are very few transmission states, whereas below, the occupied states there are several sharp peaks. However, there are subtle differences which are also expected given the differences in the Energy level spectrum reported in Fig 4.5. A significant observation and difference to the transmission spectrum of

the other POM junctions above, is the transmission states around the Fermi level (0ev), with a broad peak for the Tungsten based system and a sharp peak of the Iodine containing system. Typically there are no states at the Fermi level (but maybe slightly above the Fermi level) due to the HOMO-LUMO gap of the molecule. However, inspection of the Energy level diagram in Fig 4.5 suggests a much smaller HOMO-LUMO gap for the "spin-down" energy levels, which lie close to the Fermi level. This results in transmission eigenstates at the Fermi level energy in these systems. The main difference in spectra between the W and I containing system, is in the width of the states near the Fermi level, which can be explained by the relative positioning (and thus accessibility) of the unoccupied states of the spin-down state in W compared to in that of Iodine as shown by the energy level diagram.

To further examine the effect of the spin polarization of these two systems, the transmission spectra for each is split in spin-up and "spin down" configuration. As before, by plotting the log(T(E)) a more resolved transmission profile can be obtained that can better explain any IV characteristics. The spin-resolved transmission for $[W_{18}O_{56}(WO_6)]^{6-}$ is shown in Fig 4.14. The first thing to note is that the transmission profile below the Fermi level (0eV) in unaffected by the spin polarization, this is expected as these transmission eigenstates correspond to the occupied energy levels of the molecule. As predicted previously, the peak at the Fermi level energy corresponds to transmission of the "spin down" state which is consistent with the energy level diagram of the junction due to having an unpaired electron. The profile above this peak is very similar for both spin states, differing only in the order of magnitude of the T(E), this is due to the "spin up" state having a larger HOMO-LUMO gap than the "spin down" and thus it would be expected that the higher transmission at this energy are spin dependent and correspond to the "spin down" state. Due to the spin-dependant transmission, it would be reasonable to predict that this POM junction would have a higher conductance than the previous junctions, hence the spin properties of the caged moiety are significant to the transport of this junction.

Similarly, the $[W_{18}O_{56}(IO_6)]^{6-}$ junction has an unpaired electron and so it is expected to have spin dependant transmission channels. The transmission spectra in Fig 4.13 showed that there are sharp peaks around the Fermi level energy compared to the broader peak for the $[W_{18}O_{56}(WO_6)]^{6-}$ junction. Like in the WO_6 containing configuration the $[W_{18}O_{56}(IO_6)]^{6-}$ junction also shows spin dependant transmission profile as seen in the spin resolved transmission spectra in Fig 4.15. At the Fermi level there are multiple sharp peaks for the "spin down" state that do not exist for the "spin up" transmission spectra. This is consistent with the energy level diagram. Like in the $[W_{18}O_{56}(WO_6)]^{6-}$ case, the profile above the Fermi level is very similar for both spin states but differ in magnitude due to the respective energy gaps in the spin states (up to 1eV). Again, it can be concluded that the transport in the $[W_{18}O_{56}(IO_6)]^{6-}$ junction has spin dependent transmission channels due to the open shell. Interestingly, the main difference between the WO_6 and IO_6 containing system is that for IO_6 the "spin down" transmission eigenstates are sharp around the Fermi level, whereas for WO_6 there is a singular broad peak.

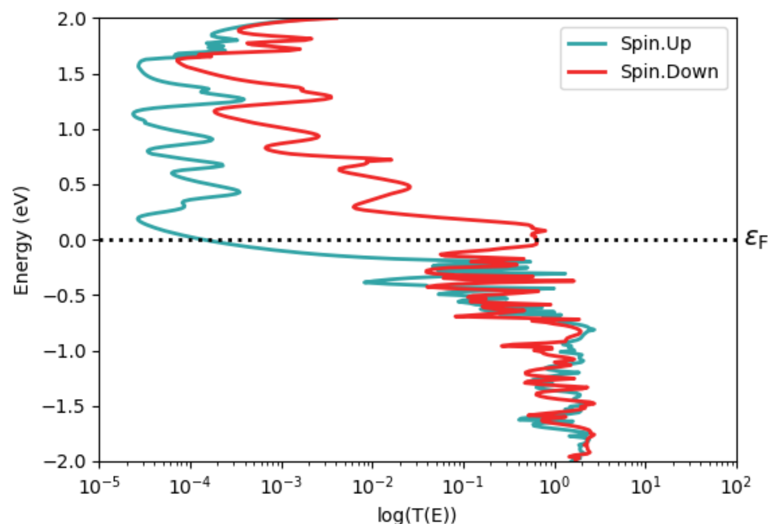

Figure 4.14: The log scale Transmision spectrum for the $[W_{18}O_{56}(WO_6)]^{6-}$ molecular junction. spin-dependence is shown.

This can be rationalised from the energy level diagram in Fig 4.5, it can be seen that for IO_6 there is an almost non existent HOMO-LUMO gap with only the LUMO lying close to the Fermi level with the further unoccupied energy levels lying at much higher energies and therefore less accessible for transmission. As a result the "spin down" transmission channels are sharp peaks. Conversely for WO_6 the energy gap is slightly larger, though still very small but more importantly the subsequent unoccupied energy states lie far lower. Therefore, it is not inconceivable that near the Fermi level there is a broader transmission channel. Moreover, by observing the nature of the LUMO as shown in Fig 4.7 for WO_6 it is less localised on the WO_6 moiety and lies on parts of the POM cage which would lead to a broader range of transmission eigenstates. Whereas for IO_6 it is more localised to the moiety leading to sharper peaks in the transmission. Regardless of the differences, both of these systems have spin dependent transport which illustrates how small changes to the POM molecule can lead to diverse properties and applications, key for device engineering.

It has been noted the transmission states at and near the Fermi level result in increased conductance of the POM junctions compared to other molecules in this study. In addition to the physical consequence of states near the Fermi level, from a simulation point of view this provides a practical challenge. Systems that have states close to the Fermi level, like in metals, small-gap semiconductors or for the molecular junctions here, can be difficult to adequately describe with the DFT-NEGF formalism. In this situation, the states shift between occupied and unoccupied leading to convergence problems. There are procedures that can mitigate this but potentially at the expense of accuracy, for example by increasing the temperature for the electron occupation function. The convergence for these two systems, due to spin polarization was very challenging to achieve at an applied bias. For the $[W_{18}O_{56}(IO_6)]^{6-}$ junction, conver-

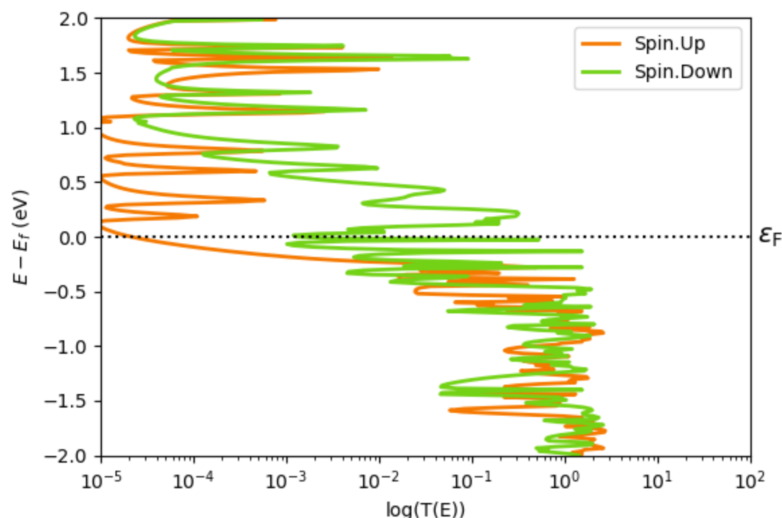

Figure 4.15: The log scale Transmission spectrum for the $[W_{18}O_{56}(IO_6)]^{6-}$ molecular junction with spin-dependence is shown.

gence at biases higher than 0.4V was not achieved in the timescale of this study. The simulation methodology employed here, struggles describing the sharp peaks near the Fermi level, and so convergence for acceptable accuracy is unfortunately not achieved. For the $[W_{18}O_{56}(WO_6)]^{6-}$ junction case increasing the number of k-points, the energy mesh for which the calculations are carried out, reducing the damping (controls how much of the electron density guess is used in the next iteration), tuning other algorithm parameters in Quantum ATK led to successful convergence for this junctions to obtain the IV curve from a bias of 0V to 0.8V. The same computational procedure failed to reach convergence for the higher bias of the $[W_{18}O_{56}(IO_6)]^{6-}$ junction, likely due to the sharper peaks, and increased number of states at the Fermi level.

Like with the Transmission Spectra, with the DFT-NEGF method the current can be split into the respective spin contributions, as a result IV curves for both the "spin up" and "spin down" states can be plotted. The IV Curves for "spin up"(left) and "spin down"(right) states of $[W_{18}O_{56}(WO_6)]^{6-}$ are shown in Fig 4.16. It must be noted that in reality, the sum of the two IV curves is what would be measured experimentally, in this case, given the difference in magnitude of the current, the IV Curve would resemble that of the "spin down" contribution. However, it is very useful as with the transmission spectra, to analyse the IV characteristics of the different spin contributions in order to fully understand the nature of this molecular junction and how significant a difference the caged species can make to the transport and charge storage of the POM cage. Inspecting the "spin up" IV Characteristics in Fig 4.16 (left) it can be seen that the IV curve is akin to the other POM junctions studied in this chapter, with similar shape and magnitude of current. The shape and magnitude of current is consistent with the transmission spectra for the "spin up" state as discussed above and also with the large HOMO-LUMO gap of 2.24 eV, which leads to very low currents at low bias, and a rise only at higher biases. Whereas

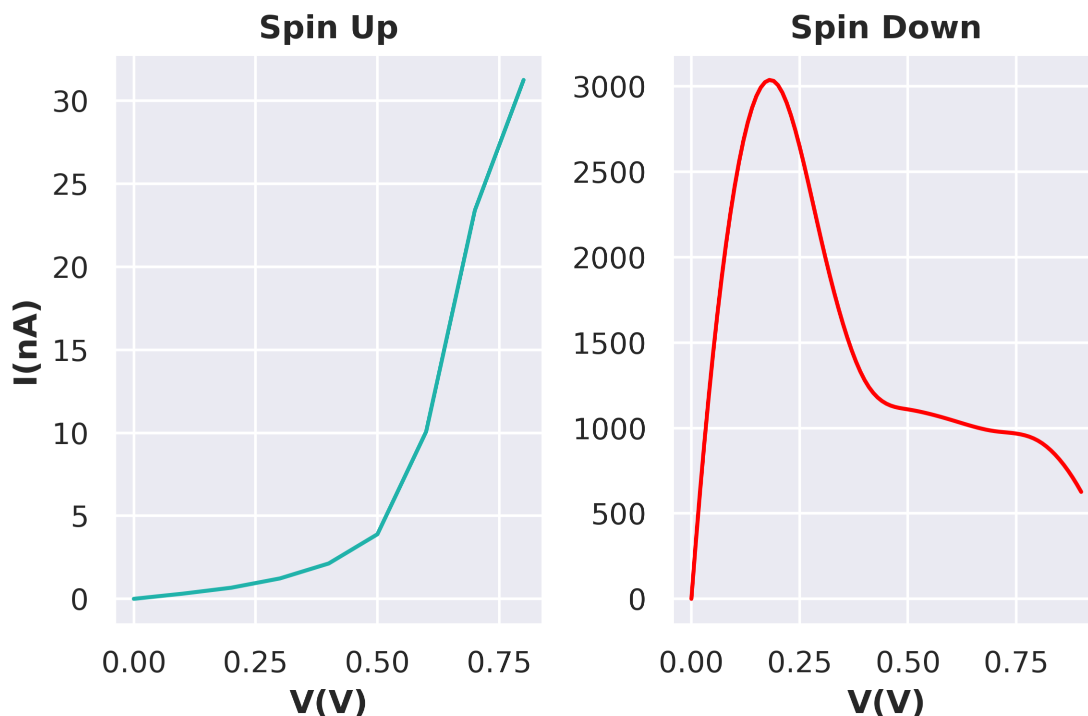

Figure 4.16: Computed IV curves for both spin states in the $[W_{18}O_{56}(WO_6)]^{6-}$ molecular junction.

the "spin down" contribution, due to the broad peak at the Fermi level, dominates the transport for this junction. As shown in Fig 4.16, the "spin down" state results in a steep rise in current at low bias reaching saturation at around 0.2V. The current is predicted to be in the microampere region compared to nanoampere for most of the POM junctions in this study. The rapid rise in current is due to the broad peak around the Fermi level of the device as shown in Fig 4.14, as the bias increases this peak reduces the in intensity and the energy window of the applied bias also increases leading to a drop of current. What these predictions show, is that simply by change of the caged species the transport of the molecule changes considerably which in turn opens a wide range of device engineering opportunities.

As previously discussed, unfortunately the IV characteristics of $[W_{18}O_{56}(IO_6)]^{6-}$ could not be computed past 0.3V due to difficulties in convergence at higher bias. The IV Curves for the successfully converged bias points are shown in Fig 4.17. Although only a small applied bias range it provides insight to the potential transport of this POM junction. Like in the case of $[W_{18}O_{56}(WO_6)]^{6-}$, due to the peak around the Fermi level the "spin down" contributes several orders of magnitude of current higher than that of the "spin up" state. The shape of the IV curves are the same for both states, consistent with the gap between the LUMO and successive energy levels as shown by Fig 4.5. Although difficult to discern with so few bias points, the shape is similar to the other POM junctions in the study. Once again, this example further illustrates how the nature of the caged species can strongly influence the electron transport properties of the

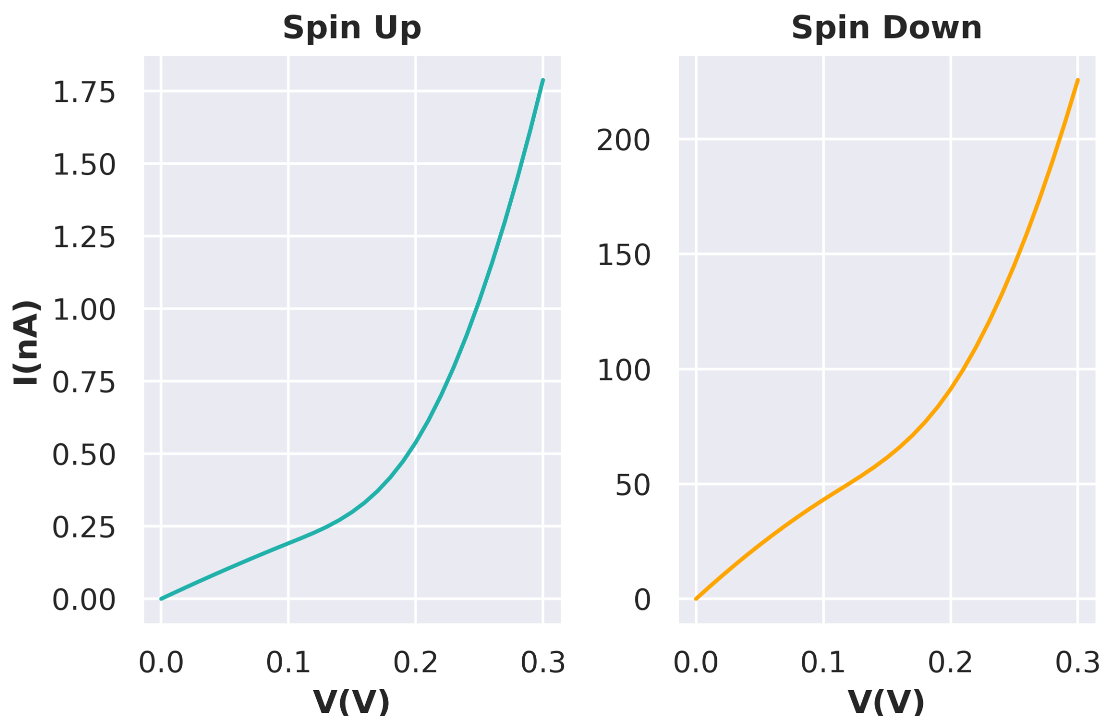

Figure 4.17: Computed IV curves for both spin states in the $[W_{18}O_{56}(IO_6)]^{6-}$ molecular junction.

molecule.

In this section, the transport characteristics for POM junctions that differed by the caged molecule in the POM was studied thoroughly using the DFT-NEGF method. The simulations show how the electronic structure of the POM cage changes considerably with the nature of the caged POM and the resultant redox state. Consequently the electron transport properties can be engineered through choice of caged moiety, resulting in a wide range of application possibilities for POM based molecular electronics.

4.3.4 Estimating the Capacitance

Until now the electron transport properties of different POM molecular junctions have been studied. However, the original motivation for studying these POMs is for flash memory applications. The important property for memory applications is their ability to store charge. To quantify and compare the ability of these Pmolecules, the capacitance was estimated following the simple approach outlined at the start of this chapter. It must be stressed, that the capacitance is being calculated for the Au-POM-Au system as a whole and not only the molecule. In order to frame the values into context, a reference value was calculated for the case of two Au electrodes separated by the same distance as in the Au-POM-Au system. Capacitance is typically calculated as macroscopic property influenced by the dielectric constant of a material. It is in fact a

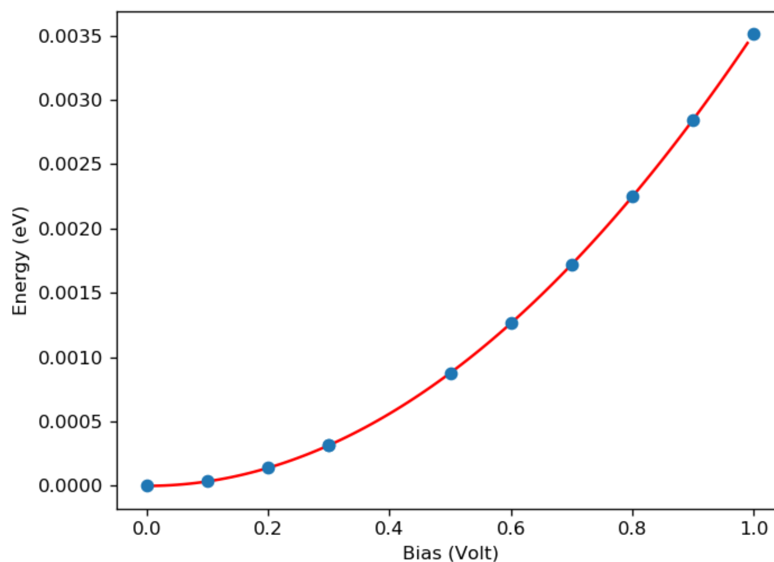

Figure 4.18: Plot of electrostatic energy vs applied bias for the $[W_{18}O_{54}(SO_3)_2]^{4-}$ molecular junction. The capacitance is then extracted from this curve, given by $C = \frac{E}{V^2}$.

complex value which at the molecular scale is influenced by many factors and is an active area of research. The aim here, was not to find an absolute value of the capacitance of these POM systems, but to compare how changing the caged moiety or redox state influences the charge storage capabilities of the molecule.

There is a drop in electrostatic potential across the junction due to the charge storage in the molecule under an applied bias. This is reflected in the electrostatic energy which is calculated as function of applied bias. The plot of electrostatic energy against applied bias is shown in Fig 4.18 for the case of $[W_{18}O_{54}(SO_3)_2]^{4-}$ junction, the other junctions in this study show the same relationship between E and V. The capacitance is then extracted from equation 4.3. The calculated capacitance for all junctions (except the $[W_{18}O_{56}(IO_6)]^{6-}$ junction due to poor convergence) from this study is reported in Table 4.2.

Caged Moiety	Capacitance (F)
Gold Reference*	1.126 x 10^{-21}
Empty	4.31 x 10^{-21}
$(SO_3)_2^{-4}$	3.19 x 10^{-21}
$(SO_4)_2^{-4}$	2.86 x 10^{-21}
$(SeO_3)_2^{-2}$	2.84 x 10^{-21}
$(SeO_3)_2^{-4}$	2.65 x 10^{-21}
$(WO_6)^{6-}$	4.69 x 10^{-21}

Table 4.2: Calculated Capacitance for the different POM Junctions in this study.

To the best knowledge of the author, there are no known studies which report the single

molecule capacitance of these or other POM molecules (Only capacitance of POM containing layers in devices have been reported in the literature [119, 120]). However, there are several studies reporting values of single molecule capacitance, including for amino acids, redox active and ferrocene containing molecules. Typical values range from 10^{-22} F to 10^{-18} F (aF) [107, 108, 121], the calculated values here in Table 4.2 lie in this range and though the absolute values are not of interest, the values themselves can be considered reasonable for these molecular junctions.

The calculated capacitance of all POM junctions are at least twice that of the reference case where there is no molecule. This highlights the charge storage capabilities of the molecules. In general, the order of highest to lowest capacitance follows the same trend in order of magnitude of current through the junctions. With the WO_6 containing system having the highest capacitance of the molecules studied and thus would be expected to store the most charge. A very similar capacitance is found for the "Empty" POM, consistent with the magnitude of current produced. The lowest capacitance is predicted to be for the $(SeO_3)_2^{-4}$, $(SeO_3)_2^{-2}$ and $(SO_4)_2^{-4}$ containing POMs which all have similar values consistent with the IV curves reported in the previous section. It is important to note, whilst the single molecule capacitances are reasonably small, in device applications there would be a layer of several molecules increasing the capacitance per unit area for reasonable charge storage density.

All the POM molecules in this study show relatively low transmission due to the HOMO-LUMO gaps, this is important for charge storage. However, it is expected that in order to "charge" the molecule it must be able to carry some current under an applied voltage. It is also not unexpected that the larger the conductance the higher the charge that can be stored across the molecule. But though there are orders of magnitude differences in the current across these POMs, the difference in capacitance (which is related to the electrostatic energy) is not so large. The charge storage occurs predominantly on the metal cage of the POM in all cases. Because of this, although the change in caged moiety influences the LUMO (and higher) energy level positioning and subsequently the current flow, it has less of an effect on the overall capacitance which describes the charge storage of the entire molecule. Notwithstanding, there are still differences in the estimated capacitance simply by changing the caged atom. This simulation study has demonstrated why these (and other) Polyoxometalates are ideal candidates for molecular electronic applications. The diversity of geometry and chemical variety opens up a wide range of opportunities for the device engineer. In this study it was shown that for a particular type of POM cluster, changing only the nature of the caged species can engineer different IV-characteristics and also charge storage capabilities.

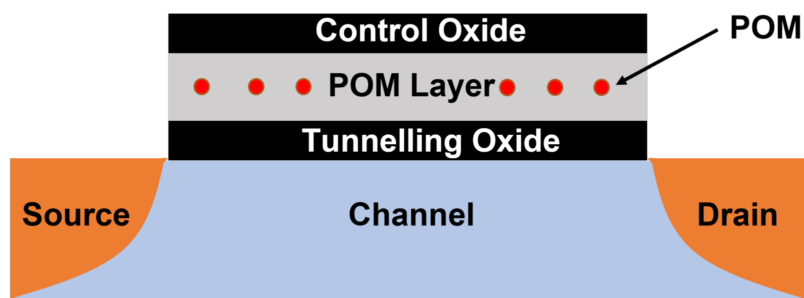

Figure 4.19: Depiction of a hypothesized flash memory device using POMs as the storage element.

4.4 POM on SiO_2 for flash memory, challenges and next steps

So far in this thesis, the focus has been on the electronic structure and transport properties of the single molecule studied from first principles in the form of a molecular junction. However, the goal was to assess if the excellent charge storage and redox capabilities could enhance current flash memory technology, leading to molecular memory. From the work in this thesis, it has been shown that current can be driven through the molecule but it is dependant on a variety of factors such as contact strength and geometry to source and drain, nature of the POM molecule itself and also the counter cations of the system. From the perspective of flash memory device operation, it is important to understand the energy level positioning of the unoccupied orbitals in the molecule with respect to the valence and conductance band of SiO_2 substrate (see device structure in Fig 4.19). The positioning of these energy levels and how they change as they store electrons is key for how the flash memory device will operate and whether or not the molecules could offer enhanced memory capabilities. Therefore, although significant understanding of the molecules charge transport properties has been gained as a molecular junction, it is key to also understand how it will behave in the floating gate architecture. The goal was to use first principle methods to calculate the energy level positioning of the POM molecules with respect to the band structure of SiO_2 and Silicon in order to carry out more accurate full scale device simulations.

An attempt was made to simulate SiO_2-POM structure in order to calculate the positioning of the molecule energy level with respect to the conduction band in SiO_2. This would more closely resemble the architecture of a flash memory device. Like in the case of molecular junction, the Molecule orientation is important and so both horizontal and vertical geometries were explored. The horizontal configuration is shown in Fig 4.20. Due to the heavy computational effort required, a slab-molecule calculation was considered the best route forward. The process was to create and relax a slab of SiO_2 large enough to encapsulate the Molecule in both orientations. Although in a molecular flash memory device, multiple molecules would be present in the memory storage layer, considered to require at least 9 for effective memory storage [81, 122], this is beyond the limitations of first principle calculations hence only one was considered. An initial calculation with a low energy mesh and k-point sampling in order to allow the molecule

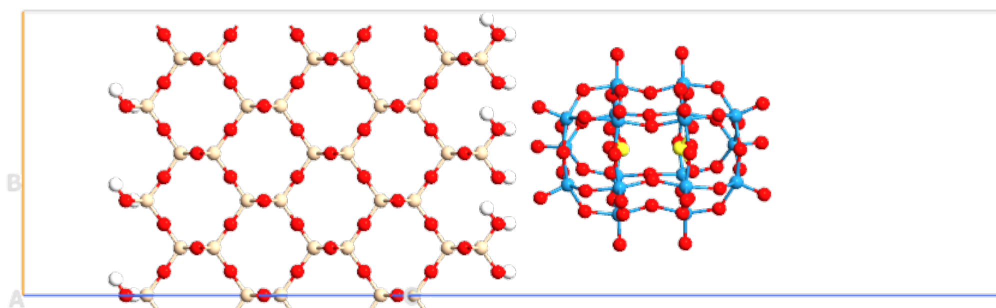

Figure 4.20: Example of SiO_2 slab and molecule configuration

DFT Functional	SiO_2 Band Gap	POM ΔE_{HL}
PBE	5.42	1.94
PBE-1/2	7.64	3.1
BP86	5.28	1.89
BP86-1/2	7.6	3.05
PBES	6.9	N/A
HSE06	9	N/A
TBO9	8.36	2.76

Table 4.3: Respective Energy Gaps for different DFT functionals for SiO_2 and POM. In all cases SG15 Pseudopotential was used with a High Basis Set.

to attach to the surface, followed by a more accurate DFT geometry relaxation. Finally from the relaxed structure the electronic structure would be computed and analysed. Unfortunately, this goal could not be completed due to several challenges. It was decided given the time and scope of the project this could not be completed without further guidance from experimental work.

The first challenge is in order to successfully calculate the energy level positioning of the molecule with respect to the SiO_2 slab, is that the HOMO-LUMO gap of molecule and band gap/ bandstructure of the oxide must be described accurately by DFT and with the same functional for both. It is well known that DFT struggles to accurately predict band gaps [123], though there are some approximations such as DFT-1/2 or the use of Hybrid functionals (that are computationally very expensive) which can better reproduce the band gap of SiO_2 which is $\approx$ 9eV [124]. These typically failed to reproduce the HOMO-LUMO gap of the molecule, as shown in Table 4.3. An approach used often is to relax the structure with a functional such as PBE which reproduces the geometry of both systems well and can be supplemented with the Grimme D3 corrections for Van der Waals interactions [125] and then calculate the energy levels with a different functional (or the half correction) which better reproduces the band structure. However, this approach may result in an artificial potential due to the mixing of functionals, additionally, a functional that satisfactory reproduces both the energy levels of the molecule and the band structure of the

slab was not found. It begs the question, which should be prioritised and how to be sure the estimation is reasonably close to the real system.

Another challenge is that the best gaps were only produced when a large basis set and pseudo potential was employed, as the SiO_2-POM system is already very large with respect to number of atoms, this results in a very slow calculation, particularly the relaxation. Moreover, even if a particular molecule-surface configuration is found, it is likely to be one of many reasonable structures, to have a good understanding, several different possible configurations should be studied. This would be far too cumbersome to complete in the timescale of this PhD project. Therefore, whatever conclusions would be drawn for the simulation, it could only be drawn for one specific surface-molecule configuration, without experimental validation of the structure it poses a challenge of accuracy given the high computational cost. In addition to the molecule-surface geometry, another computational challenge is the number of layers of the slab needed to properly screen the potential, from the initial tests carried out here, more than 6 is needed to accurate model the structure. This further increases the size of system to be simulated, which lowers the number of different geometries that can be studied in a reasonable time frame.

Furthermore, the approach here is to use a crystalline slab of SiO_2 for simplicity, in reality the oxide is a thin amorphous layer, there is significant debate about the effect of the amorphous nature on the band gap, dielectric constant and electrical properties of the insulator. Simulating the crystalline structure may not be a good approximation, this would need experimental validation. The amorphous structure, adds to the complexity of modelling the system and increases the different molecule-surface configuration possibilities further increasing the computational challenge and effort.

Despite the challenges, other approaches such as Molecular Dynamics approximations for fixing the molecule to the surface, and potentially creating DFTB parameters for the system to increase computational efficiency and better describe the energy levels/band gap could potentially make the problem more manageable. However, it was concluded that further guidance from experiment into the structure would be needed to aid in computing the energy level positioning from first principles. Without more accurately estimating the energy level positioning within the flash memory device, further simulation results would be more speculative. For this reason it was decided to change the direction of the project. Despite this, molecular electronics, specifically the potential of Polyoxometalates in electronic devices, is a very promising area of research. Further combination of simulation and experimental work can lead to further developments and down-scaling of electronic devices.

4.5 Conclusions

The simulations presented in the first half of this thesis highlight the potential and versatility of the $[W_{18}O_{56}(Y)]^{n-}$ type POMs for nanoelectronic applications. It was shown in this chapter

that the nature of "X" can considerably alter the electron transport and charge storage properties of the molecule, due to the changes in electron structure which in turn gives wider possibility for engineering new molecular electronic devices. In the previous chapter it was shown that the although the electronic structure of the molecule dominates its electron transport properties, the geometry between molecule and electrodes is highly significant. Furthermore, these molecules typically are surrounded by charge balancing anions, which are ignored when studying their transport. The work presented in this thesis highlight that the presence of these counterions are not insignificant and in fact enhance the conductivity through the molecule. Challenges remain in describing the molecule in a device architecture to accurately understand the electronic structure for device simulations. However, through further development of first principle, semi-empirical and device modelling alongside experimental progress, POM based memories and electronic devices will become a reality.

Chapter 5

Introduction to Josephson Junctions

5.1 A brief introduction to Quantum Computing

The modern world has been shaped by the continuous development of computing power due to the downward scaling of transistors. The invention of the transistor and subsequently the computer (from here on referred to as the classical computer) is the main reason for the exponential growth in technology in the twentieth and twenty first century leading to immense improvements in the quality of life, manufacturing, medicine, and science. The enhancement of performance and computing power of classical computers relies on the continuous miniaturisation of transistors, which has approximately doubled every two years as given by "Moore's law". Moore's law is known to be slowing due to the difficulty in further scaling of devices. Moreover, even if it was possible to continue the trajectory of Moore's law indefinitely, there are still problems that classical computers will probably never be able to handle in reasonable timescales. It is from this the motivation of Quantum Computing stemmed and has developed into one of the largest areas of research.

Quantum Computing was first proposed in 1980 when a quantum mechanical model of the Turing Machine was proposed by Paul Benioff [126]. It was then suggested by Richard Feynman that in order to properly simulate the quantum world, a quantum system is needed [127]. In other words "use quantum to simulate quantum". The considerable speed-up in computation has led to the goal of obtaining quantum supremacy, i.e. computation of a problem that a quantum computer can solve but would not be solvable by a classical computer in any reasonable timescale. Achieving quantum supremacy would revolutionise several areas of science and technology, including significant applications in business and economics. These possibilities drive the research into making Quantum Computing a reality.

5.1.1 What is a Qubit?

Quantum Computing has seen a rapid growth in research and there is a large variety of quantum computing architectures that have been proposed and are being actively researched for achieving quantum supremacy. Regardless of quantum computing architecture, the key component of a quantum computer is the quantum bit known as the "Qubit". Classical computers are built on binary logic, with two states of a transistor corresponding to "0" or "1". Switching between logic levels of a bit takes time as changes in electrical voltage does not occur instantly. Also, there can only ever be two states in a classical computer. For a system of N components, a complete description of the state of computer in classical physics relates to N bits. The same is not true in a quantum computer where it is 2^N.

Similar to the classical computer, a qubit is built on having two states "0" and "1". However, a quantum computer uses the phenomena of "superposition" and "entanglement" of quantum states in order to significantly enhance the computing capabilities. Although the qubit is based on having two quantum states, the superposition of states means that a quantum object can be in multiple states simultaneously, increasing the computing power. Additionally, the fact that physically separated objects can be correlated and share information through entanglement leads to increased possibilities in information processing and in the way qubits can be measured. The principles of a qubit, quantum states and superposition are best illustrated as representation on a bloch sphere as shown in Fig 5.1. In the bloch sphere representation, where two quantum states are present, it shows that the quantum state can be a superposition of the two states represented as anywhere on the surface of the bloch sphere.

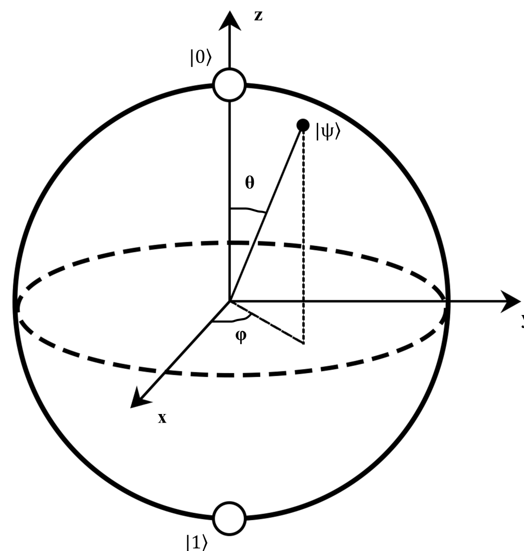

Figure 5.1: Bloch Sphere representation of quantum states of a Qubit

There are many different candidates of physical implementations of quantum computing that are being researched, primarily distinguished by the nature of the qubits. Examples in-

clude Trapped ion Qubits, Spin Qubits, Photonic Qubits and Diamond based Qubits, all with corresponding advantages and disadvantages [128–131]. One of the leading quantum computing candidates researched heavily by quantum groups and companies such as IBM, Google, Intel, IMEC is superconducting quantum computing built from superconducting electronic circuits [132, 133]. The key component of superconducting qubits is the Josephson junction (JJ), a tri-layer junction consisting of two superconductors separated by a thin insulating barrier, this will be described in detail in the next section. An understanding of the role of Josephson junctions in quantum circuits is best illustrated by considering a transmon [134]. A transmon is a type of qubit that was one of the first variants to show controlled qubit-qubit interaction with high fidelity (a measure of the closeness of two quantum states) [135], although improved JJ-based qubits have and are being developed, the simplicity of a transmon is ideal for highlighting the importance of the Josephson junction in superconducting qubit technology [136, 137].

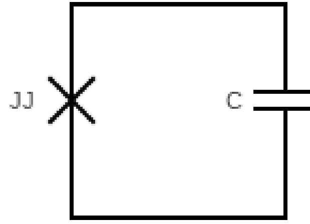

Figure 5.2: Circuit diagram of a transmon

The transmon is developed from the charge qubit (also known as the Cooper-pair box). The charge qubit is simply a small superconducting island connected to a large superconducting reservoir through a Josephson junction, the qubit frequency is tuned by a capacitively coupled gate voltage on the island. This type of qubit suffered from strong susceptibility to stray capacitance, defects and fabrication variability, to help reduce these issues, a large shunting capacitor is added to the circuit to give rise to the transmon which is illustrated in Fig 5.2. The circuit Hamiltonian of a transmon is given by:

$$\hat{H} = 4E_C(\hat{N} - n_g)^2 - E_J cos(\hat{\phi}) \tag{5.1}$$

where $\hat{N}$ is the number of excess Cooper pairs (pairs of electrons bound together at low temperatures) on the island, $\hat{\phi}$ is the phase difference across the JJ, E_c and E_J are the capacitive and Josephson energy respectively. In a transmon qubit, $E_J/E_C \approx 50$ and thus the charge sensitivity is significantly reduced and the Josephson energy dominates, this has lead to improved reproducibility and quantum coherence times [138].

The transmon is similar to a LC-Resonator circuit, however instead of a resonator, there is a Josephson junction, which adds non-linearity to the energy levels of the system, which is key for a creating a qubit. As previously mentioned, the importance for any qubit is the existence of

two quantum states. If the LC-Resonator circuit is considered,it can be modelled as a quantum harmonic oscillator, where the energy levels are the quantum states given by the superconducting phase. As the different energy levels are harmonic, the energy spacing between them is identical. For qubit applications this is problematic, as although you have two quantum states $|0\rangle$ and $|1\rangle$, the higher states of $|2\rangle$ are also easily accessible as the energy spacing is equidistant and hence the is no longer a two level system and so information can be lost. When a Josephson junction is introduced into the circuit, the harmonic energy levels become anharmonic, and there is an energy difference between $|0\rangle$ and $|1\rangle$ and $|1\rangle$ and $|2\rangle$ and so on, therefore ensuring a two level system. The higher the anharmonicity between the energy levels the better for qubits. The energy spectrum of a quantum harmonic oscillator and of a transmon is shown in Fig 5.3.The Josephson junction also acts as a valve between these two states through the tunneling of Cooper pairs. Therefore the Josephson junction is a key component of superconducting qubit technology and thus complete understanding of the physics and material properties of this system is essential for obtaining quantum supremacy and commercial quantum computers using superconducting qubits.

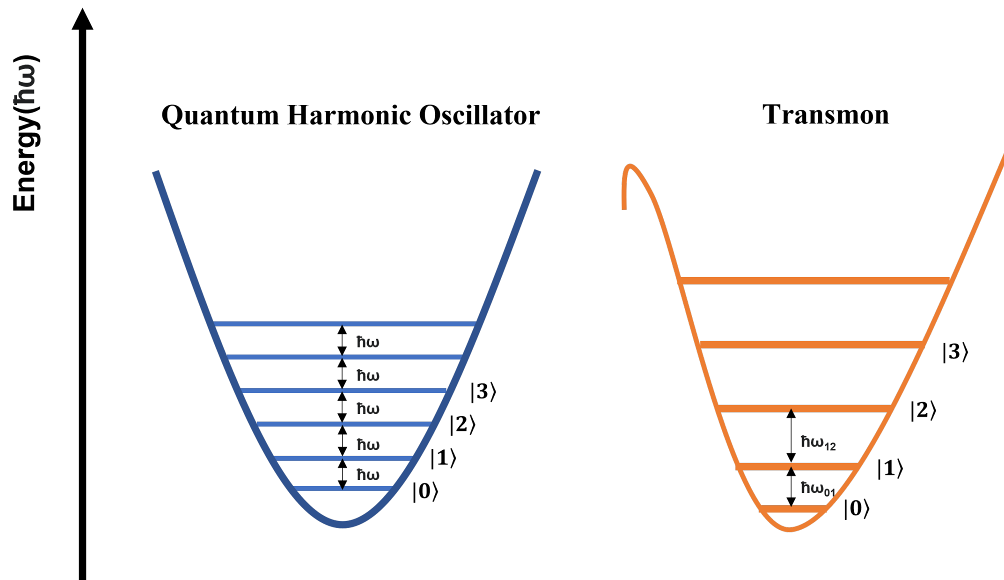

Figure 5.3: The energy diagram for a Quantum Harmonic Oscillator and Transmon illustrates the importance of anharmonicity in the Transmon circuit.

5.1.2 Josephson junction Physics

Up to now, a short introduction to quantum computing and its motivations has been given, it has been explained that superconducting qubit technology is one of the most promising architectures for achieving quantum supremacy. It was also shown that Josephson junctions are the key component of the technology providing anharmonicity to the quantum system. Although Josephson junctions have several applications, the preceding section gives the reader context to

the importance of JJ in quantum computing, one of the main motivations behind the research in this half of the thesis. So, what is a Josephson junction?

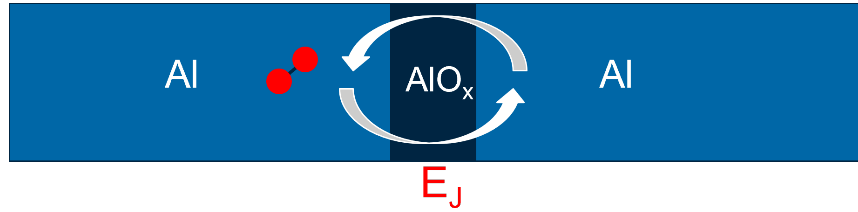

Figure 5.4: Diagram of a typical Josephson junction. In this case the archetypal Al/AlO$_x$/Al is considered. Where the two superconductors are Aluminium and the insulating barrier is Aluminium Oxide. It is shown the tunneling of a Cooper pair given by the Josephson Energy.

A Josephson junction is a tri-layer system that consists of two superconductors separated by a thin insulating barrier that is weakly coupled to the superconductors (see Fig 5.4. The archetypal Josephson junction is the Al/AlO$_x$/Al tunnel junction, but a wide range of different systems are possible. It is named after Brian Josephson, who developed the physics of the tunnelling problem through this type of system in the 1960s [139, 140]. It was discovered that these types of junctions resulted in the quantum mechanical tunneling of bound electrons (known as Cooper pairs) across the weak link (through the insulating barrier) at low temperatures. This tunneling phenomena is described by the DC and AC Josephson effects. Building on the theoretical frameworks of superconducting physics of Bardeen–Cooper–Schrieffer (BCS) theory and Ginzburg-Landau theory of superconductivitym the DC and AC Josephson effect is formulated in terms of the complex order parameter (ψ) and the superconducting phase (φ) [141, 142].

In a Josephson junction, the superconducting contacts on either side of the barrier are described by ψ_1 and ψ_2 with associated phases of φ_1 amd φ_2. A significant amount of the physics of JJ is dictated by the phase difference between the superconducting contacts given by:

$$\Delta\varphi = \varphi_1 - \varphi_2 \tag{5.2}$$

The AC Josephson effect decribes how the phase of the junction will vary linearly with time and the resulting current will be sinusoidal AC when a fixed voltage is applied across the junction. Mathematically this is given by:

$$\frac{d(\Delta\varphi)}{dt} = \frac{2eV}{\hbar} \tag{5.3}$$

where $\hbar$ is Dirac's constant and e is the electron charge. This shows that the oscillating current due to the biased voltage is driven by the phase difference between the two superconductors. Because of this effect, JJs are excellent voltage-to-frequency converters. The nature of this response is what makes JJs useful as non-linear components in superconducting qubits.

Another interesting phenomena of JJs is that at low temperatures, a supercurrent can flow

through the junction even when there is no applied voltage. This is known as the DC Josephson effect and is also underpinned by the phase difference and the resulting supercurrent is given by:

$$I_s = I_c sin\Delta\varphi \tag{5.4}$$

where the supercurrent, I_s, is dictated by the critical current (maximum possible supercurrent) ,I_c, and oscillates as a function of the phase difference $\Delta\varphi$. The critical current is an intrinsic parameter of the device which is related to its size, material properties and height of the tunnel barrier. Fine control of this parameter is important for excellent design of superconducting qubits. Low temperature exploration of JJs is challenging and expensive, a very useful link between the normal state conduction and superconducting state (at low temperatures) is given by the Ambegaokar-Baratoff relation [143]. It is an extremely useful equation for studying JJs as it connects the critical current of the junction to the resistance of the junction under normal state conduction, R_N, and is given by:

$$I_c R_N = \frac{\pi\Delta}{2e}\tanh\left(\frac{\Delta}{2K_bT}\right) \tag{5.5}$$

where Δ is the superconducting energy gap, k_B is the Boltzmann constant and T is the temperature. The superconducting energy gap parameter, Δ, can be considered as half the amount of energy required to break apart a Cooper pair of the superconducting system and is temperature dependant.

5.2 Variability and Noise in Josephson Junctions

It has been discussed how Josephson junctions are a key component of superconducting qubits. Their physics has also been described with important parameters such as the I_c being highlighted. It was mentioned above how a JJ can in principle be made of any S-I-S, and there are many examples of different material combinations used (for example Nb, Pb, Co, Ni, PdFe, NiFe, Carbon nanotubes) [144–147]. However, one of the most studied and most successful JJs is the Al/AlO$_x$/Al which will be the focus of the rest of this thesis.

Al/AlO$_x$/Al tunnel junctions can be fabricated in a variety of ways. The most common method is through double angle shadow evaporation using what is known as a "Dolan Bridge". Essentially, a thin layer of aluminium is deposited on a substrate covered by a mask through evaporative deposition. The aluminium is then oxidised at low pressures, before the second aluminium is deposited [148]. The nature of the fabrication process leads to variability junction to junction, specifically, the grown oxide is amorphous in nature which is a leading cause of the variability and also leads to defects and two level systems (TLS) which are considered a major source of decoherence in superconducting qubits.

Josephson junctions are fabricated to a design specification, typically designed around tar-

geted critical current values, which are influenced by size of the junction, specifically the barrier length. Although self-limiting, the oxidation process of aluminium oxide leads to variation in thickness of the barrier oxide due to differences in crystal orientation, grain boundaries, surface structure and other factors [149]. The barrier length tends to be limited to 1-2nm. However, it is known that the resistance (and thus critical current) varies exponentially with barrier length, thus control of this barrier length is critical. Small barrier lengths can lead to short circuits which hamper their use in device operation. There are suggestions of metallic links, gaps, pin-holing through the barrier due to the amorphous nature of the oxide making reproducible junctions more difficult to obtain [150–153]. Understanding how structural effects influence the electrical response of these junctions is key to improving reproducible fabrication. This is where atomistic simulation can be used to enhance the general understanding of what factors influence the device performance. Investigating the effect of barrier length on the junction performance is one of the main goals of this thesis.

In addition to barrier length variability, the thermal oxidation process leads to local variation in oxide stoichiometry and density through the barrier [154, 155]. Although the thermal oxidation does eventually lead to a uniform amorphous layer, the local variations during the oxidation can lead to thinner portions in the barrier and variability in atomic structure junction to junction. These variations can strongly influence the electrical response and critical current of the junctions. Understanding what atomic structure effects lead to variability in critical currents of these tunnel junctions through computational modelling is the aim of this thesis.

As mentioned above, the amorphous oxide is known to be a leading cause of defect states and so called Two level systems (TLS). The defects interact with one another and with other elements of the superconducting circuit leading to decoherence. Although they are known to exist, there is still little understanding on how they arise or what is causing them. There are several good phenomenological theories to explain on an atomic level what is causing them, however no main candidate as yet. There very good experimental and computational studies on the origin of these defects in the literature [156–159]. However, the topic of defects is out of the scope of this thesis. It is the opinion of the author that accurate and detailed modelling will be an essential tool for understanding defects and decoherence in superconducting qubits, the main aim of the research presented in this thesis is to aid in the development accurate atomistic models of the Al/AlO$_x$/Al tunnel junctions to study how the atomic structure influences junction performance. Development of accurate models of the Al/AlO$_x$/Al and other Josephson junction will lead to further studies and understanding of defects and decoherence.

5.2.1 Examples of Simulating Al/AlO$_x$/Al

A complete understanding of the Al/AlO$_x$/Al tunnel junction is vital for improving the various technologies for which this device plays a key role. Studying these junctions experimentally is expensive, slow process and very challenging [160]. Due to their small size and growth

process, thorough exploration of different junction parameters is very difficult. This is where the use of modelling and simulation can offer insights not available to experiment. Despite the "simple" structure, because of the amorphous nature of the thin insulating barrier there are several challenges in modelling this system hence there are only a handful of studies reported in the literature. In this section, these studies are reviewed to give context to the aims and simulations explored in this half of the thesis.

One of the earliest examples of modelling the Al/AlO_x/Al junction is the work by Jung and co-workers published in 2009 [161]. In their work they carry out ab initio plane wave DFT (PBE functional) simulations of the Al/Al_2O_3/Al using periodically repeated slabs of the atomic layers with fully stoichiometric aluminium oxide which is assumed to be Al_2 terminated with the Al surface. They calculate different structures, increasing the multiples of the oxide barrier. They calculate the PDOS profiles for the junction using DFT in an attempt to compare barrier heights to parameters extracted from the I-V curve measurements using the analytical and phenomenological Simmons model. They find a qualitative agreement between the potential profile from DFT and the potential barrier extracted using analytical model with experimental data. Direct comparison to the analytical results (extracted from experiment) and the DFT calculations is not straightforward and thus although related they could only present qualitative findings. In addition, this work models the Al/AlO_x/Al with a crystalline oxide, which of course differs to the real system where the grown oxide barrier is amorphous. Given the PDOS is strongly linked to local structure, the amorphous nature of the barrier is an important factor to be taken into account for understanding the potential barrier of the system.

Dieskova and co-workers published a study in 2013 where they use ab initio calculations to calculate the conductance of the Al/AlO_x/Al tunnel barriers using the Landauer formalism [162]. They also use ground state density functional calculations to extract band gap, barrier width, effective mass and used them in the Simmons model (potential barrier model), an sp-model and a tight-binding model to compare them to the previous conductance calculations. Once again, for ease of simulation, they model a periodic oxide barrier and investigate the conductance as they increase the size of the barrier (2L, 3L, 4L, 5L). They report poor agreement between their calculated conductance and experimental results they suggest an underestimation in the barrier widths in the experimental data as a main cause for the poor agreement. They show that the conductances calculated from their analytical models (using parameters from DFT) show excellent fit with the ab initio calculated conductance. This presents a possibility of more efficient and flexible modelling of the tunnel junction by only inputting parameters from ab initio and then predicting transport analytically. Although an interesting study, the studied models are considerably smaller than real junctions, due to the computational cost of ab initio calculations. The small size of the junctions would likely be a leading cause of poor agreement with experimental junctions that are considerably bigger. Moreover, the studied widths are in the range of 0.4-1 nm which are also smaller than typical tunnel junctions (1-2nm). Lastly, the use of crystalline stoi-

chiometric Al_2O_3 whilst computationally simpler to model, it is not capturing the effects of the real system where the barrier is amorphous and the nature of the disorder is hypothesized to be a leading cause for defects and variability. Nonetheless, this study illustrates how a combination of DFT and analytical models could be an efficient way of exploring the junctions.

Cyster,DuBois and co-workers have contributed considerably to the development of modelling the Al/AlO$_x$/Al tunnel junctions with studies in growth, transport and exploring defects in the oxide. In the two examples presented above a crystalline barrier was used, it has been commented that some of the shortcomings in simulation results could arise from the fact this barrier is in fact amorphous and that modelling this explicitly is important. This was addressed by Dubois et. al in their paper in 2016 [163]. They presented an efficient procedure for creating the amorphous oxide through a simulated melt-quench process using Molecular Dynamics with empirical potentials to create disorder. The resulting oxide was sandwiched with Al electrodes to make the junction and the electronic structure was calculated using DFT methods (PBE functional). They took into account the fact that the nature of the oxide is known to be oxygen deficient and studied various different Al:O ratios. Their goal was to provide a framework for creating realistic and accurate models of the junction that compare to experimental junctions. They explore how the coordination number of Al in the oxide varies with different stoichiometries, this is compared to experiment and they find good agreement in the percentage of 4, 5 and 6 coordinated Al throughout the barrier. This provides a good framework for efficient and accurate modelling of the junction system which strongly influenced the work in this thesis.

In addition to creating the junction and studying the electronic structure, Cyster et al, [164] also studied the electrical response of the Al/AlO$_x$/Al tunnel junctions and the influence of the atomic structure on their performance. They used empirical potentials and molecular dynamics simulations to create and describe the electronic structure of the junction. They then combine this with NEGF to study the electron transport through the device. The motivation for using NEGF compared to previous work is that it is a 3D transport solver that explicitly takes into account the atomic structure of the barrier, the density, local variations and stoichiometry. This gives a better understanding of the transport from an atomistic point of view. In their work they study changes in density, stoichiometry and barrier length on the Resistance $\times$ Area product (RA) as calculated from NEGF. To benchmark their RA values, they fix their Fermi level to a value of 1.35 eV found by matching their data to a representative resistance area from experiment. As the Fermi level strongly influences the current/resistance values, they accept that it limits their discussion to qualitative trends rather than quantitative match to experiment. Their simulations shown that RA increases exponentially with increased oxide stoichiometry, it suggests that oxygen deficiency leads to conductive hotspots through the barrier. Their NEGF calculations show an exponential relationship between RA and thickness of the barrier (ranging from 1-3 nm) as expected. It is also reported that the overall density of the barrier (as there may be local variations) is also significant for the resistance of the junction with higher densities

reducing the conductance. Intriguingly, they report the charge and current density calculations of the junctions which point to localized conduction channels. These can be linked to changes in the stoichiometry and density of the oxide. It suggests that highly oxygen deficient structures have metallic conduction channels for which the current flow is concentrated, this is consistent with some microscopy studies in the literature. These results show how atomistic modelling and transport simulation could be used to understand this junction system and aid in the eradication of defects and variability. Although the approach of using NEGF to study the transport is very effective, but it is combined with the empirical potentials to study the electronic structure, which may struggle to fully describe the quantum effects of the system. Classical potentials opens the possibility for a larger structure to be studied. Alhough this approach could benefit from an additional ab initio description of the electronic structure and to improve the accuracy of the transport calculations, this approach is computationally more intensive.

Until now, all the Al/AlO_x/Al tunnel junctions studied computationally have been created from a "plug and slice" technique of creating the oxide and then sandwiching between the Al electrodes. But in reality, the oxide is surface grown and the nature of the local structure of the oxide is known to be strongly linked to its growth process. Therefore, to fully describe the junction computationally accurate growth simulations would ideally be employed to mimic the real structure. However, not just for Al/AlO_x/Al tunnel junctions, growth simulations in general are very challenging.

Cyster and colleagues reported in 2020 a study that simulates the fabrication of aluminium oxide tunnel junctions [165]. They use an iterative growth procedure for growing the oxide with sequential calculations using Molecular Dynamics, they test two different empirical potentials ReaxFF and Streitz and Mintmire (S-M potential). They also study the influence the Al surface plane has on the growth by studying both Al(100) and Al(111). Their work suggests that ReaxFF is better at reproducing the density of the oxide compared to S-M and also shows the self-limiting behaviour seen experimentally. Though an interesting study that offers an in depth growth procedure that can be applied to various other oxidation processes, there are still several challenges. Firstly, this procedure consists of depositing atom by atom for at least 300 atoms for a 16 by 16 substrate, a larger surface would require more atoms. This is very time consuming and computationally intensive. If the goal is to study the transport of the Al/AlO_x/Al junctions and several different properties, it is a very inefficient way to do so. The pressures in the simulation are unrealistically high which will affect the growth procedure. More importantly, despite the time intensive procedure, the calculation can only handle $\approx$ 5 ns simulation time, which is orders of magnitude shorter than real oxidation experiments. So though the structure is being grown there is no guarantee that the structure is indeed more accurate than the melt-quench-sandwich procedure nor that any important physics is omitted. Given these limitations, it is hard to be convinced that the computational effort is worth it for simply studying the transport of the junctions compared to more efficient creation methods. But if the oxidation process is the topic

of interest it is a good framework to investigate further.

Kim et al. [166] combine ab initio MD, DFT electronic structure calculations and the 3D single particle *Schrödinger* equation to study computationally the Al/AlO_x/Al tunnel junction. The aim of their work was to test if atomistic simulations can be use to inform improved fabrication processes and JJ performance. They also endeavoured to discover what characteristics of the electronic structure of the barrier influences the JJ parameters and performance. In order to obtain a framework completely free of parameters, they use plane wave DFT at PBE level for all processes. Similar to the work by Cyster, they simulate the growth as they highlight the importance of the fact the oxide is a surface oxide and that this should be taken into account when modelling the system. They use ab initio MD to simulate the growth over several picoseconds. Unlike in the previous example, the oxygen atoms aren't deposited one at a time, instead 25 oxygen molecules are places above the surface. Due to the expense of DFT calculations, the size of the junction is much smaller than that possible with empirical potentials. The grown structures are studied and the critical current computed using transmission coefficients calculated with the 3D single particle schrodinger equation. It is astutely pointed out that measuring the barrier length of the junctions is not trivial, as due to the amorphous nature deciding where it starts and ends can be arbitrary, in this work they trained a neural network to calculate the mean barrier thickness of the barrier from ELF (electron localization functions). The computed critical currents are overestimated compared to experiments, the authors suggests its due to their barriers being much thinner than real junctions. They also compare the grown structures to hypothetical crystalline barriers which they find considerably more transparent with a critical current an order of magnitude higher. This study is a good showcase of parameter free investigation of the Al/AlO_x/Al junction. Given the fully ab initio nature, the size of the junction studied is limited and the entire calculation framework would be resource intensive. Like above, the growth process is limited to a much smaller range than experimental timescales (ps in this case) which leaves the question of how successful is the growth process at capturing the real physics of growth? Although they attribute the overestimation of the critical current to the relative thickness of the junction there is considerable variation seen junction to junction. Though the work does highlight how important the local structure is the junction performance, the fully ab initio nature of the work perhaps limits the investigative possibilities.

5.2.2 Conclusions

In this chapter a brief introduction to quantum computing and its motivations was given. It was discussed how superconducting qubits are one of the leading proposed technologies for achieving quantum supremacy and that the Josephson junction is key component of these circuits. Josephson junctions are Superconductor-Insulator-Superconductor systems that provide the non-linearity to superconducting circuits for qubit applications. It was discussed how the amorphous nature of the barrier is known to cause decoherence and variability issues in JJ per-

formance and subsequent qubit applications. In order to improve this it is vital to fundamentally understand the performance of JJs and modelling and simulation is an indispensable tool in helping achieve this. In this section the best simulation studies of the Al/AlO$_x$/Al in the literature have been presented and critically reviewed. There are several challenges involved in studying this system, but accurate and efficient computational frameworks are critical for understanding fully this junction which is key for several important technologies, such as superconducting qubits. The rest of this thesis aims at building upon the works presented in this chapter to use atomistic simulation methods to study the Al/AlO$_x$/Al structure in order to understand how the atomic and electronic structure of the barrier influences the junction performance.

Chapter 6

Studying the Oxide Stoichiometry of Al/AlO$_x$/Al

6.1 Introduction

As discussed in the previous chapter, Josephson junctions are superconducting tunnel junctions that consist of two superconductors separated by a thin insulating layer. They are key to several different device technologies, most notably SQUIDs (Superconducting Quantum Interference Devices) and superconducting qubits [167, 168]. Superconducting qubits are a favourite among many qubit technologies in the race for quantum supremacy [169]. Josephson junctions(JJ) are key to the superconducting qubits as they create non-linearity in an otherwise harmonic potential. [134]. One of the main challenges faced in quantum computing is decoherence of qubits. Most improvements to decoherence times thus far has been achieved through circuit design and engineering. The amorphous nature of the barrier leads to considerable variability in junction performance and poor control of the critical current, I_c, which is a key parameter for controlling the qubit energy levels and operating frequencies [156, 170, 171]. Despite their wide use experimentally and the fact the physics has been well understood since the 1960s, there is still a poor fundamental understanding from an atomic perspective of how the structure of the thin insulating barrier of the junction affects the performance and variability of the device and by extension the qubit applications [140, 172].

The experimental exploration of junctions is expensive, painstaking and very time consuming [160, 173, 174]. Through the use of modelling different junction types, properties and effects can be created and studied more easily. Using accurate and efficient computational models the understanding of these systems can be improved and aid the fabrication and design of Josephson junctions for qubit and other applications. The main goal of this work, through simulation, is to explore how the nature of the amorphous barrier influences key junction parameters and the electron transport of model Josephson junctions. Ultimately, the aim is to link atomic and electronic structure to device variability and tranport behaviour and gain a thorough understanding

of transport across the barrier, in order to gain better control of the critical currents of fabricated JJ devices.

As was discussed at length in the previous chapter, modelling the Al/AlO$_x$/Al system computationally has several challenges, hence there are relatively few studies in the literature. One of the first challenges is the size of realistic junctions for qubit applications. These junctions are in the range of 100 nm $\times$ 100 nm (and can range to several μm^2). These dimensions are very computationally demanding for atomistic simulations. Applying periodic boundary conditions can be a good approximation by artificially increasing the size of the model junction, however not all issues are alleviated. Moreover, the amorphous nature of the barrier means periodic boundary conditions may remove some of the amorphousness. Another major challenge is that the oxide is usually grown, but experimental timescales and pressures are still beyond the capabilities of current Molecular Dynamics (MD) simulation methods. Growth simulations are possible and actively researched, however they are cumbersome and do not guarantee that the amorphous nature of the simulated grown oxide is realistic with respect to the grown oxides in the lab. Finally, the amorphous barrier itself, is subject to significant debate in terms of structure, electronic properties and oxide stoichiometry [175–177]. Typical crystalline aluminium oxide has the formula Al_2O_3 (or $AlO_{1.5}$), but experimental evidence suggests the disordered barrier in Al/AlO$_x$/Al is actually oxygen deficient and its stoichiometry ranges in values from 0.8-1.5, with typical values of 1.1-1.3 in regular junctions [178]. As reviewed in the previous chapter, it has been shown by Cyster et al. [179] in their simulation study that barrier stoichiometry has a sensitive effect on the atomic and electronic structure of the junction and subsequently the transport properties and thus device performance.In this chapter this is explored further through simulation of junctions with different oxide stoichiometries using more accurate atomistic semi-emipirical simulation methodology for the electronic structure over classical force fields, whilst also employing the 3D numerical transport method, Non Equilibrium Greens Function (NEGF). Many of the results presented in this chapter were published in the Journal of Nanotechnology and thus is referenced here in advance [180].

6.2 Simulation Methodology

6.2.1 Computational Details

All calculations were carried out using the QuantumATK-2021 software [25]. The NVT (conserving Number of atoms, Volume and Temperature) Molecular Dynamics simulations were calculated using classical force fields. The "ReaxFF" parameter set was chosen as it shows the limiting behaviour of oxidation in other studies and a good qualitative description of amorphous aluminium oxide [165, 181].The electronic structure of all junction models were calculated with DFTB using the "magsil-1-1" parameter set [182–184]. A Monckhorst-Pack grid k-point sam-

pling of 5×5×300 was used whilst the density mesh cut off was set to 100 Hartree. All transport simulations were done using NEGF as implemented in Quantum ATK. The zero bias transmission is calculated with 9x9 k-point sampling grid as is the Projected Local Density of States (PLDOS) to analyze the electronic structure of the junction device. The junctions were studied under applied bias of -1 to 1V, to simulate the current-voltage (IV) characteristics in normal state conduction (i.e. not superconducting).

6.2.2 Creating the Junctions models using Molecular Dynamics

To accurately study the Al/AlO$_x$/Al tunnel junction it is of critical importance to ensure the barrier is indeed amorphous. As stated in the introduction although it is possible to grow structures through Molecular Dynamics, replicating experimental times and pressures is still beyond the computational capabilities. Therefore, the barriers in this work are created using a more efficient approximation through simulated annealing method. This method has been successfully applied to create realistic amorphous structures, including Al_2O_3 [163, 185].

NVT Molecular Dynamics is a method to simulate a canonical ensemble where Number of atoms (N), Volume (V) and Temperature (T) is conserved. As with all Molecular Dynamics simulations, Newton's equations of motion are solved for a configuration of atoms with the atomic interactions determined by classical potentials, semi-empirical or ab-initio techniques under a set of conditions. In NVT Molecular Dynamics the energy of endothermic and exothermic processes is exchanged with a thermostat. The temperature of the system is related to the average kinetic energy of the system through:

$$\langle E_{kin}|\rangle = \frac{3}{2} N k_B T \tag{6.1}$$

There are a variety of thermostat algorithms available to realistically replicate the canonical ensemble. In this work, the Nose-Hoover thermostat is mostly employed. In this approach, a Hamiltonian for the system has the form:

$$H(P,R,p_s,s) = \sum_i \frac{p_i^2}{2ms^2} + \frac{1}{2} \sum_{ij,i \neq j} U(r_i - r_j) + \frac{p_s^2}{2Q} + gkTln(s) \tag{6.2}$$

where R and P are representative of all coordinates, r_i and p_i; s is the degree of freedom for the heat bath; Q is an imaginary mass chosen carefully, g is the number of independent momentum degrees of freedom. The starting point is a fully optimized 3×3× 1 slab of Corundum (crystalline form of aluminium oxide). The amorphous aluminium oxide created experimentally has a reduced density of 3.18 gcm^{-3} (which is 0.8 times the density of Corundum (3.97gcm^{-3})). To ensure this density is replicated, the size of the z coordinate of the simulation box is increased by a required multiple dependent on the stoichiometry of the structure. As the goal is to study different stoichiometries, oxygen atoms are manually removed to create the desired stoichiometry

for the sample. The z coordinate is adjusted relative to the change in mass from the stoichiometry to ensure a density of 3.18 gcm^{-3} for all model junctions to be comparable. An NVT Molecular Dynamics simulation is run to heat the structure to 3000K for 4 ps, creating disorder in the structure. The next step is to cool the structure over 6 ps to 300K, these timescales were chosen based on the work by Cyster et al. [165, 179].

The final disordered configuration is geometry optimized using DFTB to ensure bond distances and Coordination Numbers are close to the experimental values, the optimization proceeds until the forces are below 0.05 eV/ÅÅs discussed in Chapter 1, DFTB is a parameterized version of DFT that shows good transferability and accuracy whilst being computationally less expensive and more efficient. DFTB was selected as the simulation method over DFT, as 1) it can more accurately reproduce the band gap of crystalline and amorphous Al_2O_3, 2) to explore the stoichiometry a significant number of junction models need to be created and studied, given the several-step process for creating the model structures, standard ab-initio DFT is too computationally demanding and thus DFTB offers a considerable speedup and 3) again as DFTB is more efficient it is possible to study larger junction dimensions (with more atoms) without losing significant accuracy. The final structure is then assessed by analysing the Al-O Coordination Number and radial distribution function to ensure the oxide is truly amorphous. The radial distribution function is calculated using the following equation:

$$g(r) = \frac{1}{4\pi r^2}\frac{1}{N\rho}\sum_{i=1}^{N}\sum_{j\neq i} < \delta(r - |r_i - r_j|) > \tag{6.3}$$

The junction is created by sandwiching the amorphous oxide between two 5x5x1 layers of bulk Al(111), the structure is optimized using DFTB once again, to describe the bonding at the interface. This optimization creates disorder to the aluminium layers at the surface as described in other studies before returning to the bulk Al structure [163, 165, 186]. The final junction structure for all the models presented in this chapter have a oxide barrier length of 18-19Å which is within the experimental range of 10-20 Å [149]. Due to computational cost, the lateral dimensions of the junctions are considerably smaller than the experimentally fabricated JJs for qubits applications. Hence, periodic boundary conditions are applied in the x and y directions for the simulation. A typical Junction model in this work is illustrated in Figure 6.1.

6.2.3 Transport Simulations

The charge transport through the junction is calculated by combining DFTB (for the electronic structure) with NEGF method. A considerable advantage of this method is it allows the computation of transmission probability, charge density, current, local bond contribution to current and how they relate to the electronic structure of the system. NEGF is implemented as described in the Theoretica Foundations chapter where calculating the retarded green's function allows for the further estimation of transmission probability, IV characteristics (through the Landauer

formalism) and conductance.

The Resitance-Area product (RA) is commonly reported for experimental junctions under normal conditions (non-superconducting), the resistance of the junction is a key parameter for estimating the critical current (maximum superconduncting current) of the junction from the Ambegaokar-Baratoff equation [143]. Therefore, this is one of the main parameters computed in this work. To calculate resistance of the junction, first the zero bias conductance of the system is computed as given by:

$$G = -\frac{2e^2}{h}\int T(\varepsilon)\frac{\delta f_0(\varepsilon)}{\delta\varepsilon}d\varepsilon \tag{6.4}$$

where f_0 is the equilibrium Fermi-Dirac distribution function. The resistance is then simply:

$$R_N = \frac{1}{G} \tag{6.5}$$

From the Ambegaokar-Baratoff equation it can be related to the critical current [143].

$$I_c R_N = \frac{\pi\Delta}{2e}\tanh\left(\frac{\Delta}{2K_b T}\right) \tag{6.6}$$

Where I_c is the critical current, R_N is the normal state resistance, Δ is the superconducting parameter, which is taken as 190 μV at 100mK [187].

6.3 Results and Discussion

6.3.1 Creating the Junction Models

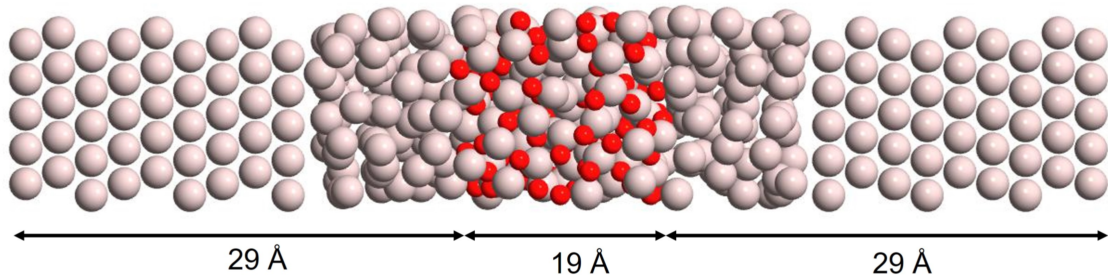

Figure 6.1: Illustration of the Al/AlO$_x$/Al Junction Model.

A typical junction model is illustrated in Fig 6.1. It is important that the models are validated to be sure the barriers are actually amorphous. This is done by comparing the radial distribution of the amorphous barrier with that of crystalline corundum. In crystalline corundum there is

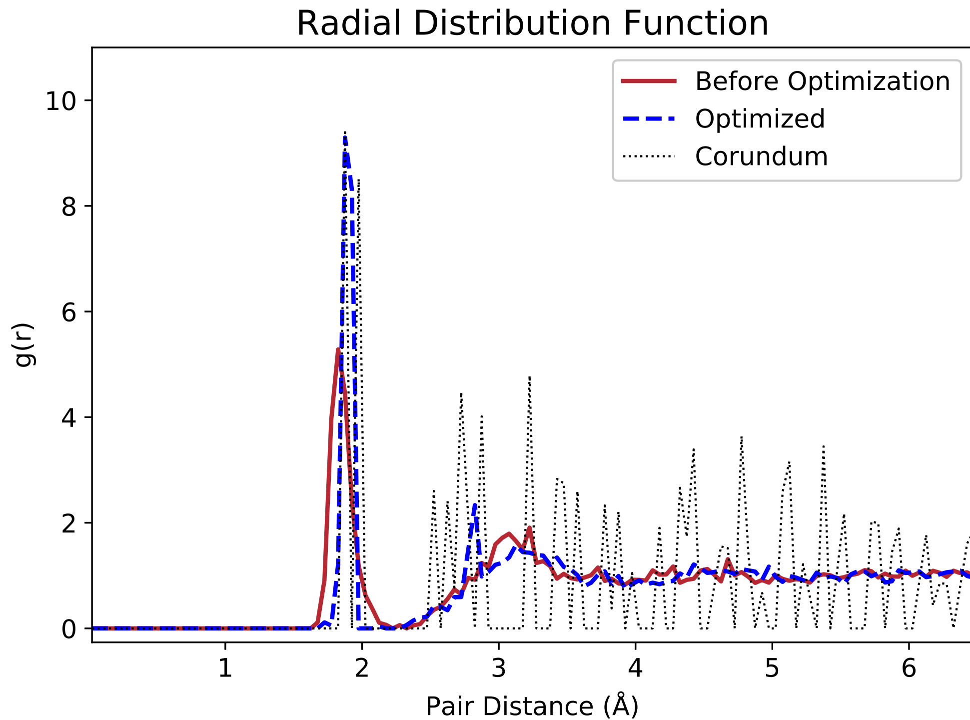

Figure 6.2: Radial Distribution comparing corundum (Crystalline Al_2O_3) and amorphous Al_2O_3 before and after optimization.

long range and short range order shown by clear peaks as seen in Fig 6.2. For amorphous aluminium oxide, short range order is expected and is observed with a clear peak $\approx$ 1.8-2 Å accounting for the Al-O bond distance, but there should be no long range order and therefore no distinctive peaks at larger distances [185, 188]. Hence the RDF shows that the models created by the simulated annealing method are actually amorphous. Moreover, there are no peaks below 1.8 Å confirming that there are no unrealistically short Al-O bonds within the barrier. All of the junction models reported in this thesis show similar radial distribution plots as the one in Fig 6.2 but have been excluded for brevity.

The aim of the work in this chapter was to study how the stoichiometry affects the atomic structure, and in turn how it affects the charge transport properties. However, Al:O ratio does not give any insight into the actual structure of the barriers. Instead, analysing the Al-O Coordination Number gives a quantitative understanding and allows for the comparison of the differences between barriers. This measure gives an insight into the relative metallicity of the barriers and an understanding of the amorphous nature. Typical crystalline aluminium oxide would have no distribution of Coordination Numbers (CN) with all values being 6. In amorphous aluminium oxide a distribution is expected, with higher number of highly coordinated Al expected for higher stoichiometries. Although the simulated annealing method is an approximate method that has been shown to give good qualitative amorphous structures. But it can sometimes give unrealistic structures, which have to be circumvented through observation of any unreasonable Al-O bond

distances and coordinations. This is why the geometry optimization step after the annealing, carried out with DFTB, is important to model realistic barriers. The importance of this step is highlighted in Fig 6.3 which reports the CN distribution before optimization, after optimization and after junction formation for a barrier with $AlO_{1.1}$ stoichioimetry.

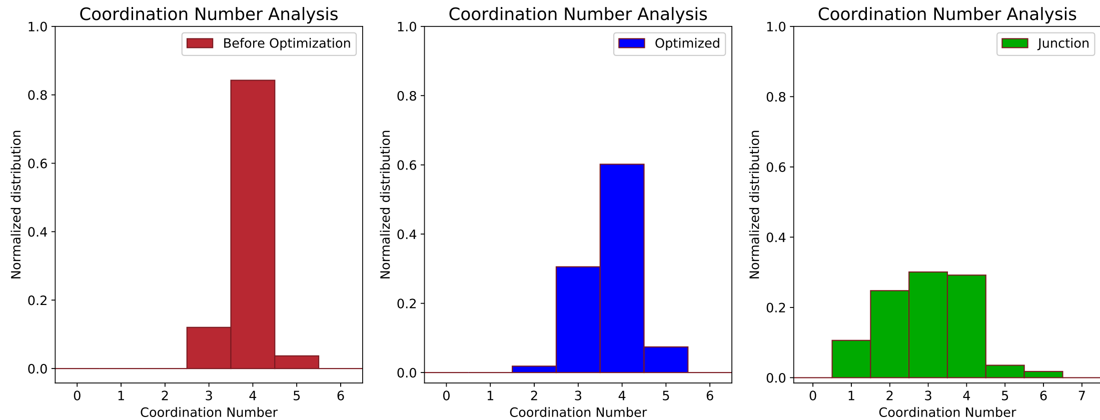

Figure 6.3: Comparison of Coordination Number and atomic structure for the different steps in junction creation.

Fig 6.3 shows the geometry optimization improves the distribution across 2,3,4,5 coordinated Al, namely the increase in 5 coordination, as the ideal Al coordination is to six oxygens. This wider distribution is evidence of a fixing of unrealistic bond distances leading to change in coordination distribution. This can also be seen in Fig 6.2, where the peak at ≈ 1.9 Å is much bigger after optimization. The Coordination Number distribution for all the junction models studied is in good agreement with experiment and other theoretical studies reported previously [159, 163, 189].

Fig 6.3, also shows the typical changes expected when the barrier is inserted into the junction structure. The distribution of 1 and 2 coordinated Al increases significantly as the barrier bonds to the surface Aluminium. Low coordinated Al is at the interface is typical which influences the effective stoichiometry and barrier length, one of the main sources of variability in Al/AlOx/Al.

6.3.2 Studying the Influence of Oxide Stoichiometry on Current-Voltage Characteristics of Al/AlO$_x$/Al

In this section, the transport simulations with NEGF are reported and compared across Junction models with barrier stoichioimetry ranging from 0.8 to 1.5. The zero bias transmission spectra and PLDOS was calculated for all junction models. The PLDOS highlights the electronic structure in the junction, specifically the metallicity of the barrier as oxygen concentration increases. The electronic structure of amorphous aluminium oxide and thin barriers in general is poorly understood and subject to debate. Unlike crystalline aluminium oxide with a clear bandstructure and an accepted bandgap of around 9 eV, the "bandgap" of amorphous aluminium oxide is not

so clear and depends on a variety of factors such as atomic structure, density, oxygen concentration, fabrication method [190]. There have been several experimental studies reported that have shown that amorphous aluminium oxide structures have a significantly reduced "bandgap" ranging between 2.8-3.2 eV [191–193]. The bandgap calculated here for the fully stoichiometric (Al_2O_3) amorphous aluminium oxide lies between 2.3-3 eV, in good agreement with experiment.

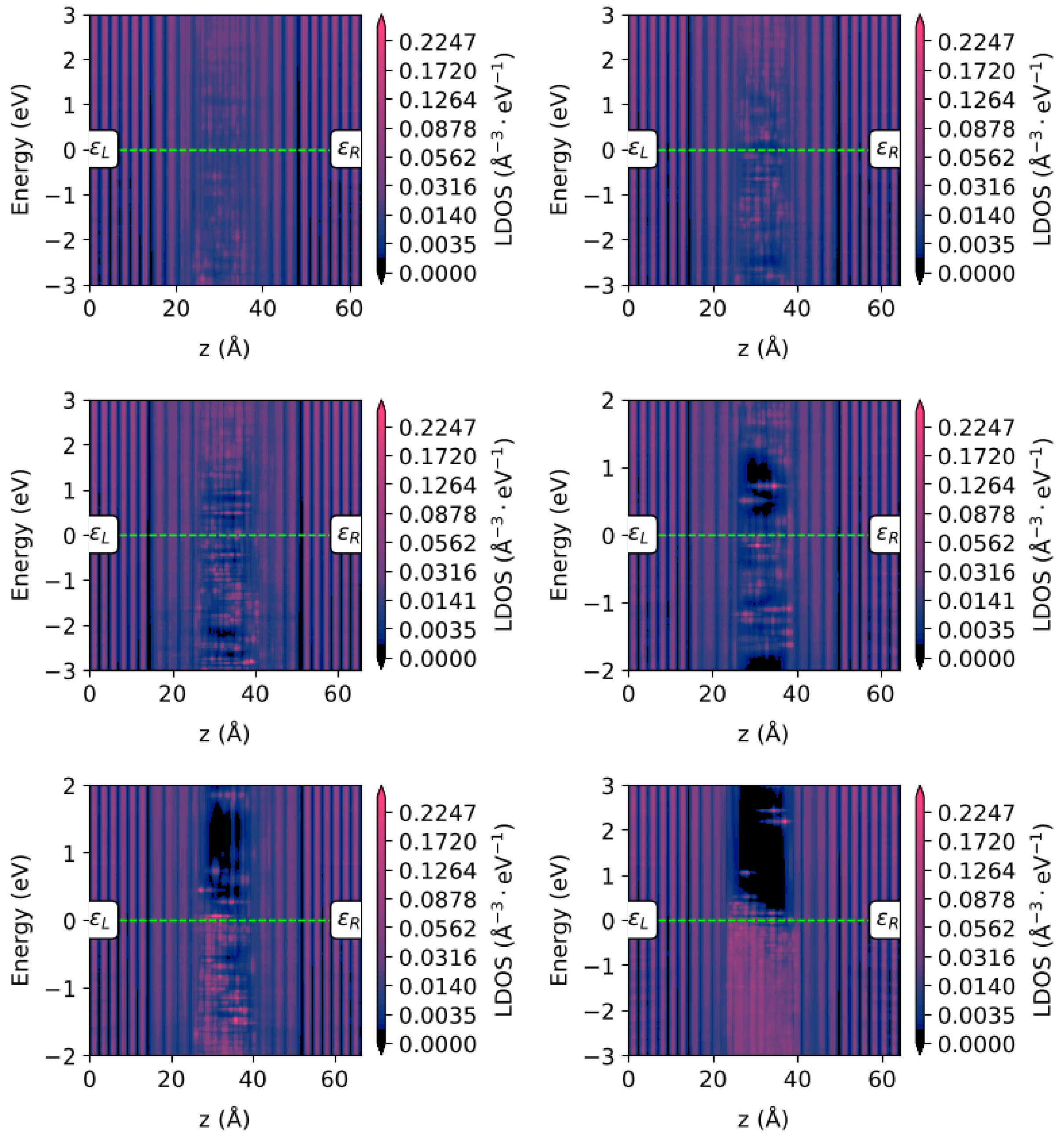

Figure 6.4: PLDOS for the different oxide stoichioimetries; top left=0.8, top right= 1.1, centre left =1.2, centre right = 1.3, bottom left = 1.4, bottom right = 1.5.

The PLDOS highlights the electronic structure of the device as a function of the Z coordinate (the transport direction). In the junction models reported here, the barrier lies approximately between 20-25 Å to 40-45 ÅThe metallicity of the insulating barrier can be gauged by

The PLDOS shown in Fig 6.4, where continuous DOS in the insulating region indicates metallic character. The calculations show, as expected, that bandgaps appear only in models with increased stoichiometry of the aluminium oxide barrier. The DFT study by Kim et.al (which was reviewed in the previous chapter) reports that bandgaps only open up for highly coordinated Al (CN $\geq$4) [186]. This is consistent with the results reported here, and is sensible as higher stoichiometries have a much higher distribution of highly coordinated Al and hence gaps open up in the barrier as observed.

The electronic structure of the barrier plays a significant role in the predicted transport of the entire junction. The $AlO_{0.8}$, $AlO_{1.1}$ barriers have continuous density of states in the barrier, so can be expected to be metallic in nature. It is evident, particularly below the Fermi level that gaps are appearing for the $AlO_{1.2}$ barrier. The $AlO_{1.3}$ shows a more prominent gap above the Fermi level albeit with resonances disrupting the gap. Finally $AlO_{1.4}$ and fully stoichiometric $AlO_{1.5}$, show clear bandgaps due to highly coordinated Al. From these structures, it would be expected that with increased Al:O ratio, there would be significant increase of junction resistance.

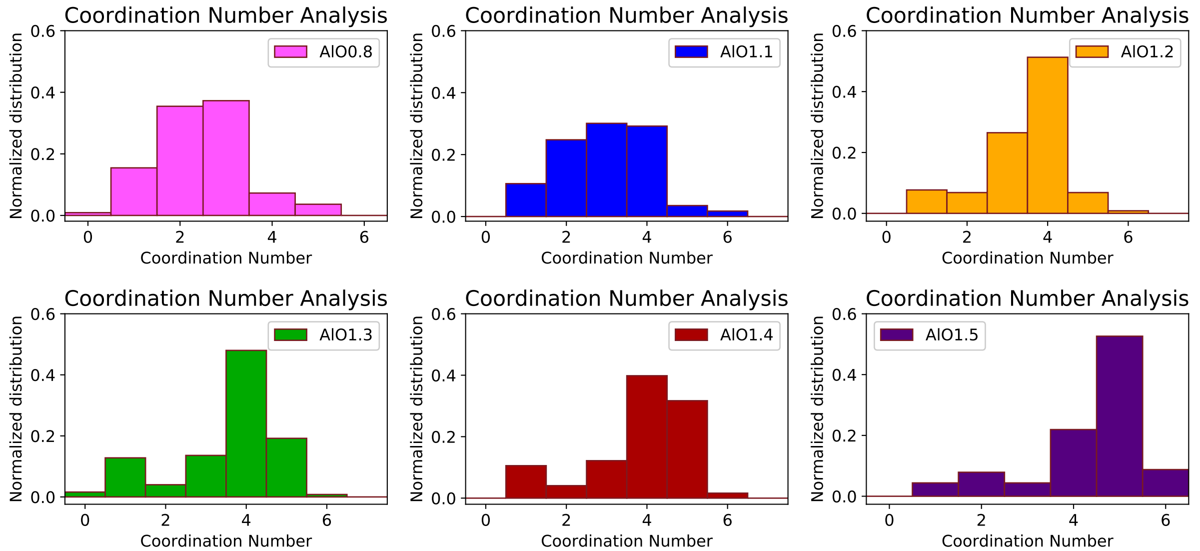

Figure 6.5: Coordination Number Analysis to quantify difference in atomic structure across different aluminium oxide stoichiometries.

In addition to the electronic structure, Al:O ratio has a significant influence on the atomic structure of the barrier as shown in Fig 6.5. Generally, low stoichiometries (0.8,1.1) lead to low distribution of 5 and 6 coordinated Al. There is a high distribution of 1,2 and 3 coordinated Al, due to oxygen deficiency, this would be prevalent throughout the barrier and not just at the Al-aluminium oxide interface. Increase in oxygen content increases significantly the distribution of the four coordinated aluminium, whilst reducing the low coordinated Al. There is also a clear increase of 5 coordinated Al which becomes more abundant until it dominates in fully stoichiometric barriers.

The current flow through the junctions reported above were computed. All the models were

studied under an applied bias (-1V to 1V) and the IV characteristics computed as shown shown in Fig 6.6 and Fig 6.7. Due to the small size of the junctions (compared to experimental junctions), only qualitative comparison is appropriate. Nonetheless, microampere currents are reasonable and the IV characteristic is typical of that of a Josephson junction (linear at low bias), which suggests the essential physics is being captured by the chosen simulation methods.

Fig 6.6 shows the IV curves for junction models with stoichiometries ranging from 0.8-1.5. As expected from the discussion on atomic and electronic structure, the current is significantly higher for $AlO_{0.8}$ than for the other barriers. The barrier is oxygen deficient and so is significantly metallic in nature and has a much higher conductance, with currents more than 2 times that of $AlO_{1.1}$. In order to more easily compare the junctions 1.1-1.5, Fig 6.7 shows the IV curves without the $AlO_{0.8}$ structure.

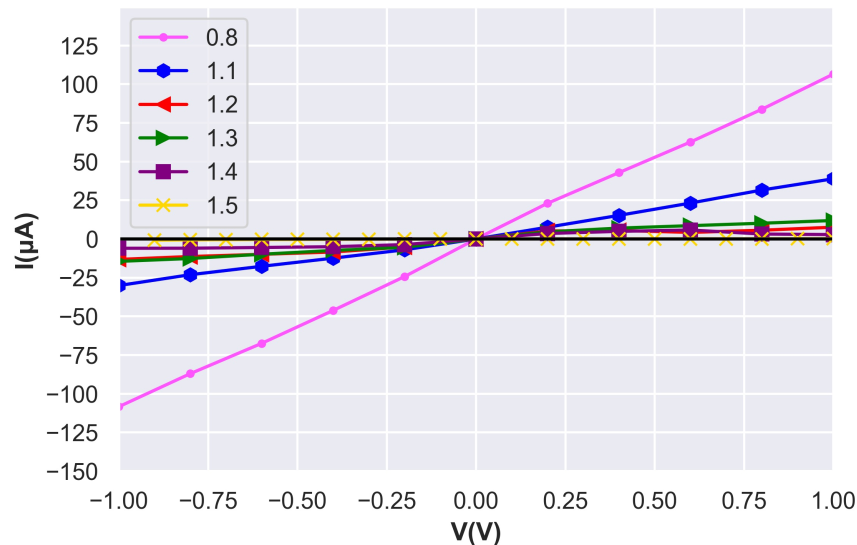

Figure 6.6: Current-Voltage (I-V) Curves for different oxide stoichiometries (0.8-1.5).

The expected trend of higher Al:O resulting in lower current is observed in the IV-Characteristics with only slight deviations. Firstly, $AlO_{1.1}$ barrier is significantly more conducting than the rest, with currents 3-4 times larger. This is in line with the analysis of the electronic structure and PLDOS as there are no gaps seen around the Fermi level. As a result, the barrier behaves more metallic and as expected is more conductive. Slight differences in the magnitude of current can be seen for the other junctions. Surprisingly $AlO_{1.3}$ is more conducting than $AlO_{1.2}$ in the positive bias regime, and have similar magnitude of current in the negative bias regime. From the electronic structure, it may be expected that $AlO_{1.3}$ would show more resistance, due to the clearer bandgap. However, analysis of the atomic structure in the barrier, it can be seen that $AlO_{1.2}$ shows a higher 4 coordinated distribution and a lower 1 and 2 coordinated Al than expected for this stoichiometry. As a result, the barrier may be more insulating than expected. Hence, it shows similar characteristics to $AlO_{1.3}$. This example illustrates why Al:O ratio alone

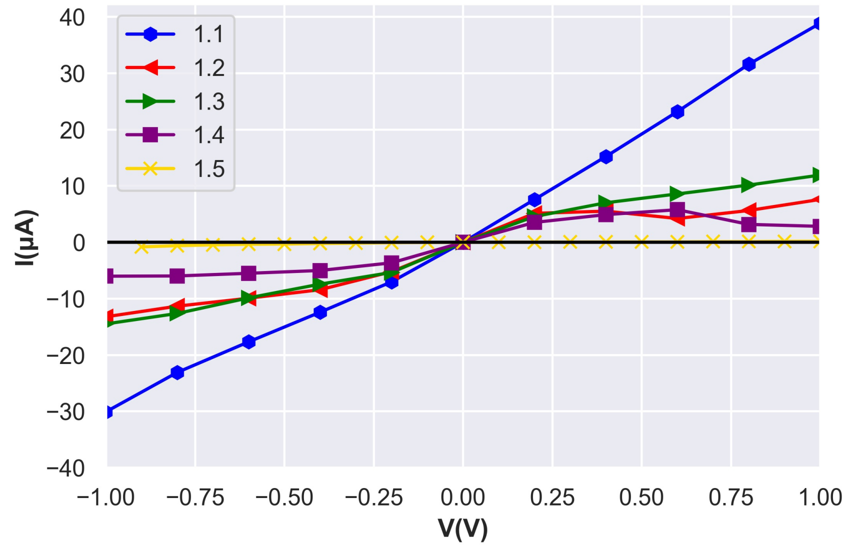

Figure 6.7: Current-Voltage (I-V) Curves for different oxide stoichiometries (excluding 0.8).

is not a good metric for understanding differences in junction performance, in fact it is the local atomic structure, better described by the Coordination Number that gives insight into how the atomic structure affects performance.

Whilst this analysis is valid for these two junctions, it is worth noting that another barrier, also $AlO_{1.3}$, could have a different local atomic structure and thus different device performance. This is discussed in detail in the next section for a range of $AlO_{1.1}$ barriers. Finally, Fig 6.7 show that the fully stochiometric barrier has significantly lower currents (nA range) than the rest of the barriers. This is easily explained through the fact this barrier has a much higher distribution of highly coordinated Al as well as a clear bandgap in the PLDOS. Though the PLDOS at zero bias shows the gap formation above the Fermi-level, under bias, the resonances shift and this gap is firmly within the bias window, consequently affecting the IV curves. This is illustrated at the bottom part of Fig 6.8. As a result, this barrier would be more insulating and hence have higher resistance/produce lower currents as revealed by the IV curve simulations.

In addition to the IV characteristics, the Resistance-Area (RA) product is computed as it is how the Junction resistance is commonly reported experimentally. Normal state resistance is an important junction parameter as using the Ambegaokar-Baratoff relation, it allows the estimation of the critical current of the device when it is superconducting. Control of the critical current I_c is key for the fabrication of high quality qubits. By studying how the resistance of junctions varies, the superconducting properties can be probed and how they relate to the atomic structure of the junction can be analysed.

Fig 6.9 shows how the RA varies with stoichiometry for the simulated junction models. The $AlO_{1.5}$ model has been excluded for clarity as its RA is two orders of magnitude higher. This way how RA changes between 0.8 - 1.4 can more reasonably be compared. The RA values are also

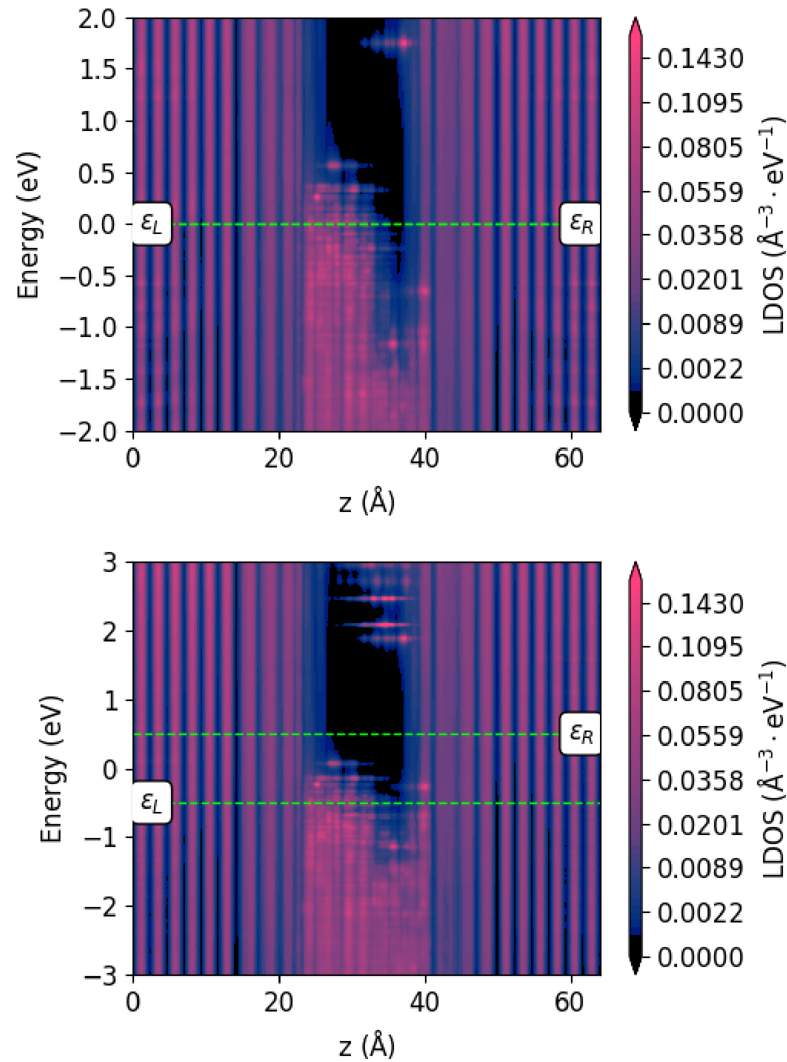

Figure 6.8: PLDOS of $AlO_{1.5}$ at zero bias (top) and a bias of 1V (below).

reported along with the computed Critical Current Density, J_c, in Table 6.1. The simulated values of RA are underestimated compared to experimentally observed junctions. The model junctions have RA in the range of 1 mΩ μ m^2 to 10 $\Omega\mu m^2$ compared to the experimentally expected range of 250 $\Omega\mu m^2$ to 25 k$\Omega\mu m^2$. This is unsurprising for a variety of reasons. Firstly, the size of the model junctions cannot meet the experimental range, the cross sectional area of the junctions are $\approx$ 1.4 nm $\times$ 1.4 nm whereas for experimental junctions are typically $\approx$ 100 nm x 100 nm. Although periodic boundary conditions are applied, this is still an approximation to artificially increase the size of the junction, though cannot fully account for effects of junction size and so the resistance is underestimated. Secondly,these model junctions represent the most ideal structure with no impurities, no effects from measurement techniques and no discernible defects. As a result it is expected that the resistance will be underestimated. However, a qualitative comparison between the models is still valid, and so the computational methods employed here can explore the atomistic effects on the electrical response of the junctions.

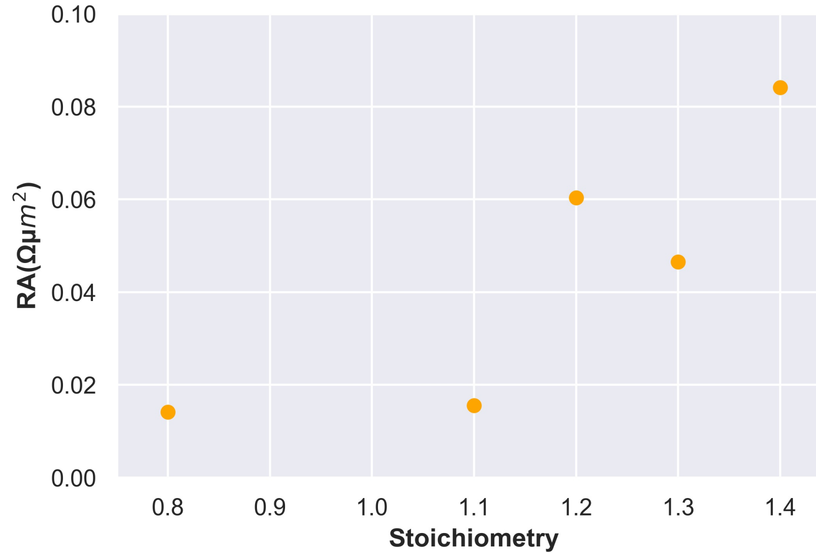

Figure 6.9: RA vs Stoichiometry.

The variation of RA with stoichiometry is consistent with the computed IV curves. The RA for $AlO_{0.8}$ and $AlO_{1.1}$ is the lowest and close in value. The RA of $AlO_{1.2}$ is more than three times the RA of $AlO_{1.1}$. The anomaly of $AlO_{1.2}$ producing less current than $AlO_{1.3}$ is supported here by the drop in RA for the $AlO_{1.3}$ barrier of more than 1 m$\Omega\mu m^2$. As discussed above, this is due to a highly coordinated barrier for $AlO_{1.2}$ leading to a more insulating gap than expected. Finally $AlO_{1.4}$ has a RA more than 8 times that of $AlO_{0.8}$, as seen from table 6.1 $AlO_{1.5}$ is even bigger with RA $\approx 7\Omega\mu m^2$. These results show a clear but complex relationship between Al:O ratio and junction resistance, where increased oxygen content leads to significant increases in the resistance. Though Al:O alone cannot be relied on, as local atomic structure can strongly influence the "effective stoichiometry" of the barrier and lead to larger than expected resistances as seen in $AlO_{1.2}$.

In the work by Cyster and co workers (reviewed in the last chapter), the effect of stoichiometry on Al/AlO$_x$/Al models using NEGF is also explored [179]. They report RA values that range between 10^{-2} to 10^3 $\Omega\mu m^2$. This is a similar range of values to what has been calculated here. They also find considerable increases in resistance with increasing oxygen content. They report a transition from metallic to insulating at stoichiometries of 0.9. In the simulations presented in this work, a similar transition at ≈ 1.1 is observed. The difference in transition stoichiometry from these models and those reported by Cyster et.al is most likely due to differences in the local atomic structure of the oxide barrier, emphasising that this is a better measure than Al:O ratio. Direct comparison between their reported RA values and the results here is not straightforward due to different electronic structure models employed. Furthermore, the models by Cyster and co workers have an oxide barrier length of 14 Å compared to the 19 Å barrier lengths of the models in this work. In the work by Cyster and co-workers there is a drop of resistance at

Stoichiometry	RA ($\Omega\mu$m^2)	$J_c(A/cm^2)$
1.5	6.948	4.28 x 10^3
1.4	0.084	3.54 x 10^5
1.3	0.046	6.41 x 10^5
1.2	0.060	4.93 x 10^5
1.1	0.016	1.91 x 10^6
0.8	0.014	2.10 x 10^6

Table 6.1: Calculated Resistance-Area Values (RA) and Critical Current density for the different aluminium oxide stoichiometries.

higher stoichiometries, which they attribute to the oxygen distribution within the barrier. The simulations here predict a continued increase in resistance with increasing oxygen content with no similar drop. These discrepancies highlight the sensitivity of the local Al-O structure on the electrical response,compared to the Al:O ratio itself.

The critical current density has been computed by dividing the critical current computed from equation 6.5 by the cross sectional area of the junction, shown in Table 6.1. As the resistances have been underestimated, it can be expected that the critical currents for the junction models are overestimated. Experimentally, high quality Al JJs for qubit applications can expect a critical current density, J_c, of 1- 10^3 A/cm^2, whereas these model junctions range from 1 to 10^6 A/cm^2. The calculations demonstrate that the J_c is sensitive to the atomic structure of the barrier and not just the Al:O ratio, density, barrier length, junction size, hence the difficulty in consistent reproducible junctions. Controlling the barrier structure, either by epitaxial growth, or otherwise should lead to more favourable control of critical current.

6.3.3 Junction to Junction Variability of Al/AlO$_x$/Al models

A main challenge in using Josephson junction devices in qubit circuits is the lack of control of the critical current of the junction, the critical current is a key parameter for controlling qubits an their reproducibility. Due to the amorphous nature of the barrier there is often significant variability in the critical current values from junction to junction even if they are fabricated in the same wafer. In this section, multiple junction models where all device and material parameters are the same were studied with the aim to replicate the variability in the critical current from Junction to Junction. Additionally, the goal was to understand how this variability arises in order to help overcome it and guide the fabrication process.

Five different Al/$AlO_{1.1}$/Al junctions were studied, all generated the same way as described above. The stoichiometry of the junctions was chosen to be AlO$_{1.1}$ as it is suggested by literature and experimental data to be the most common stoichiometry from most junction material growth processes.

Fig 6.10 shows the IV characteristics for 5 different Al/AlO$_{1.1}$/Al samples. All Junctions

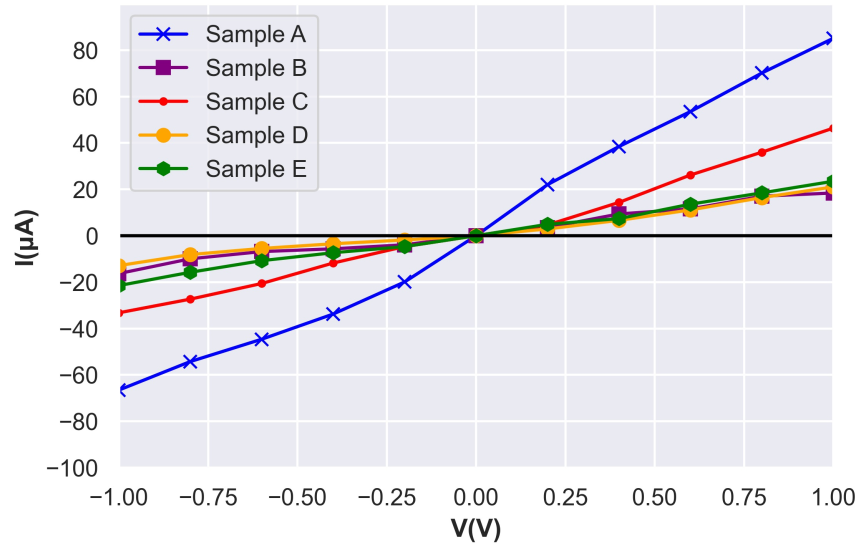

Figure 6.10: Comparison of the IV Curves 5 different $AlO_{1.1}$ Junction samples.

qualitatively replicate the expected IV curve of a typical Josephson junction. As is evident, there is variability across the devices. In particular Sample A is the most conductive, with currents 2-4 times that of the other samples. Sample C is more conductive by 1.5 to 2 times that of B,D and E. Whilst samples B,D,E show remarkable consistency, with almost inseparable IV curves. Fig 6.11 reports the variation in RA across the 5 samples. The RA values range from 0.016 - 0.156 $\Omega \mu m^2$.These are also reported along with the Critical Current densities in Table 6.2. Sample A has the lowest RA, which is consistent with the IV curve in Fig 6.10, Sample D appears to have the lowest current and hence the fact it has the highest RA is expected.

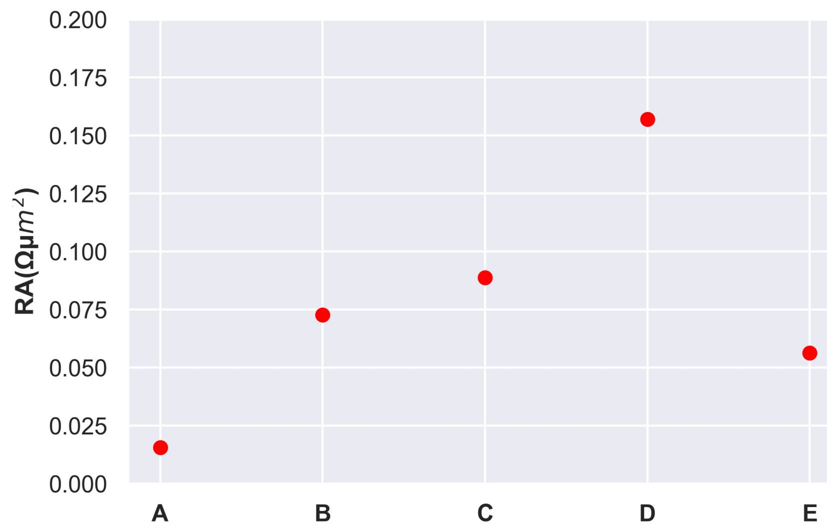

Figure 6.11: RA comparison across the five different samples.

Junction	RA ($\Omega\mu$m^2)	$J_c(A/cm^2)$
Sample A	0.016	1.91 x 10^6
Sample B	0.072	4.11 x 10^5
Sample C	0.087	3.43 x 10^5
Sample D	0.156	1.90 x 10^5
Sample E	0.056	5.30 x 10^5

Table 6.2: Calculated Resistance-Area Values (RA) and Critical Current density for the different Junction Samples.

The calculated critical current densities are in the range of 10^5 to 10^6 A/cm^2. The differences between samples follow the inverse of the RA trend, as expected as the critical current is calculated from the resistance values. Excluding Sample A, the values for B, C, D, E are all within the same order of magnitude, and are close in value though clear variability remains. This is similar to the results reported by Kim et.al, in their DFT study of Al/AlO$_x$/Al barriers they find variability in the computed critical current density even when the stoichiometry and length of the barriers are similar [186]. Specifically, Kim et al. report that for two barriers with a mean thickness of 7.1-7.2 Å the critical current varies by factor of more than 2.6. The variation in samples B, C, D, E here ranges by a factor between 1.8-2.8.

In all cases the density, barrier length, oxide stoichiometry and preparation method are all the same, yet differences in resistance and transport remain. Sample A produces the highest current in normal conduction,has the lowest calculated RA and its superconducting critical current is an order of magnitude higher than the other samples. This can be explained by contrasting the atomic structure through the distribution of aluminium coordination Number as reported in Fig 6.5.

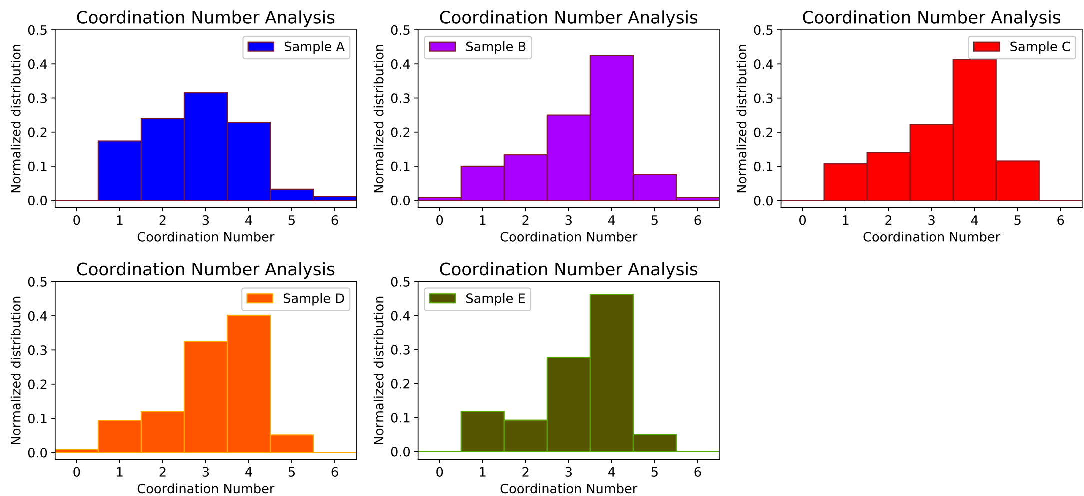

Figure 6.12: Coordination Number Analysis across 5 samples of Al/AlO$_{1.1}$/Al.

The low resistance of Sample A is consistent with the high distribution of low coordinated Al (CN = 1,2,3) compared to the other samples. Equally, there is a lower distribution of highly co-

ordinated Al (CN=4,5,6). As a result, the barrier would be expected to be more metallic. Hence more conductive, as predicted. The distribution of Coordination Number (CN) for samples B-D are very similar with only subtle differences.

In addition to local atomic structure, it is important to compare the electronic structure of the junctions for understanding differences. Comparing the PLDOS of Samples B,D,E in Fig 6.13 it can be seen that for Sample D, there is an opening of a small energy gap just above the Fermi level. This leads to a break in the metallicity of the barrier and helps explain why the RA for this junction is higher than the others. This gap may arise due to a higher distribution in highly coordinated Al, particularly Al(3). Once more demonstrating that small differences in the structure of the amorphous barrier can lead to significant variability in performance of the junctions.

Despite the atomic structure of B,C, D and E being only subtly different, the IV characteristics show C produces more current than B,D and E. Variability structure to structure is emphasised by the transmission spectra which shows the different energies (relative to the Fermi level) at which the electrons can scatter through the device, and the relative probability (T(E)) of the electron being transmitted. The area under the curve gives the conductance of the device system.

The transmission spectra at zero bias is shown in Fig 6.14, only peaks between the energies of -0.5 to 0.5 eV are shown as these are the only ones relevant within the -1 and 1V bias range. Under bias the peaks will change slightly in intensity and can shift further apart. However, the zero bias spectra gives good insight to the conductance of the junction. Samples B and C have a thicker linewidth for easier comparison. The intensity (given by T(E)) for the different samples is consistent with the IV characteristics shown in Fig 6.10.

The peaks in the transmission spectra relate to conduction pathways through the oxide barrier. These conduction pathways depend on the local atomic structure of the barrier. As seen from the spectra, despite the density, stoichiometry, length and material type all being identical, the amorphous nature of the barrier leads to significant variability in electronic structure, resistance and charge transport. The sensitivity to atomic structure is a challenge for consistent fabrication of Al/AlO$_x$/Al and other Josephson junctions, for controlling the I_c and reducing decoherence in superconducting qubits.

6.3.4 Analysis of Transmission Pathways

Tunnelling through the oxide is hypothesized to occur through metallic pathways. It has been suggested that oxygen deficiency increases the metallic pathways within the oxide and thus increases the conductance across the barrier. It can also lead to leakage of cooper pairs, leading to increased noise and decoherence in superconducting qubits. As discussed above, the peaks in the transmission spectra correspond to transmission pathways in the device. The transmission coefficient at specific energies can be split into local bond contributions, as described by [194,

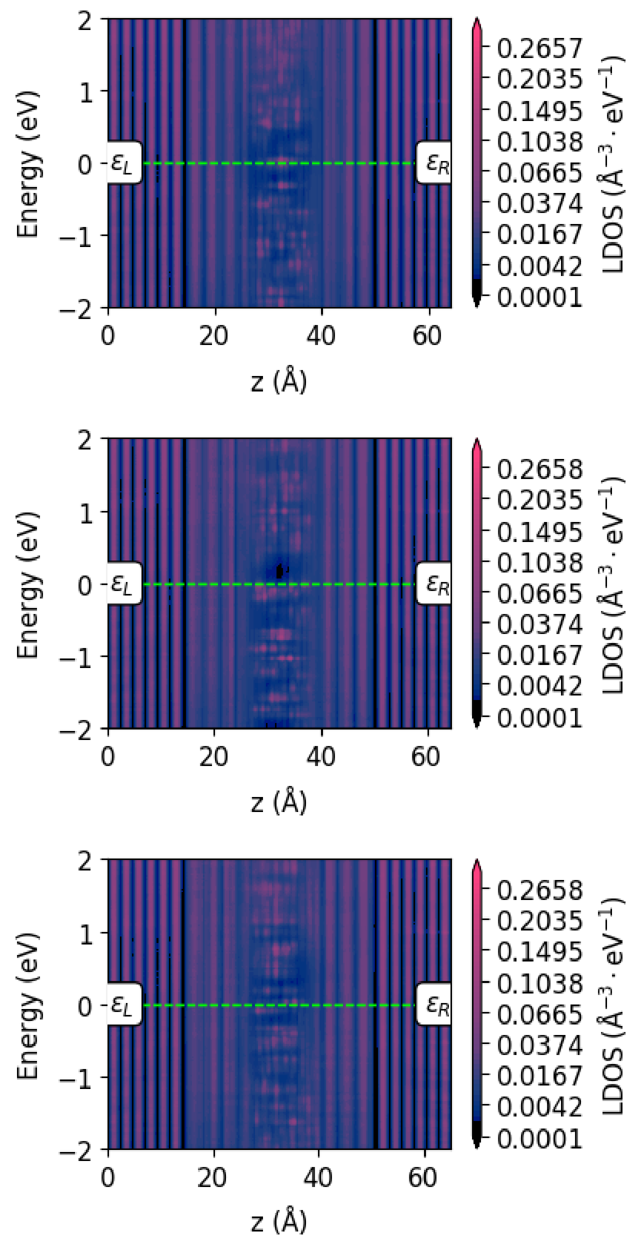

Figure 6.13: PLDOS comparison for Sample B(top), D(middle), E(bottom).

195]:

$$T(E) = \sum_{i \in A, j \in B} T_{ij}(E) \tag{6.7}$$

The local bond contributions can be visualised in the barrier, and can show positive pathways i to j or negative j to i (back scattering). Predicting this flow of electrons can give further insight to how the amorphous nature of the barrier influences the properties of the junction.

Analysis has been carried out on all $AlO_{1.1}$ junctions, only peaks within the applied bias range were examined. Fig 6.15 shows the transmission spectra for Sample B with the relevant peaks highlighted by the dotted box. The transmission peaks in this region show the most

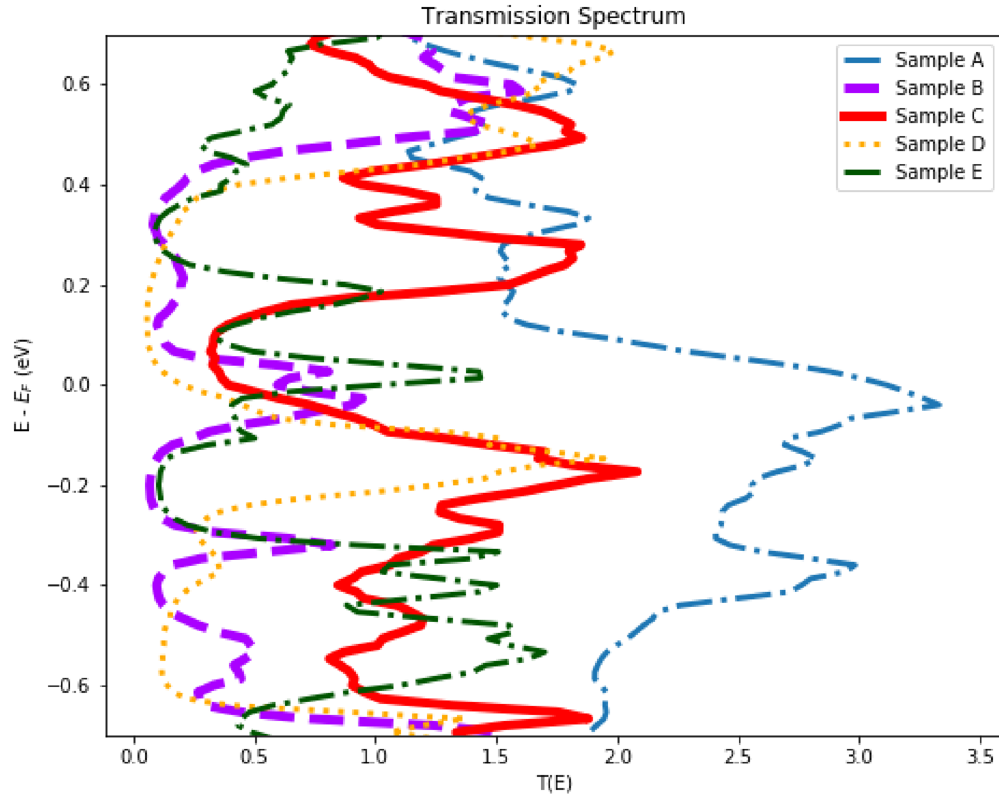

Figure 6.14: Transmission Spectrum for the five different $AlO_{1.1}$ samples.

prevalent conduction pathways in the barrier. Fig 6.16visualises of the conduction pathway at 0.03 eV for Sample B, very close to the Fermi level. Only bond contributions higher than 20% of the T(E) at that peak are shown.

From the pathway in Fig 6.16, it can be seen that predominantly electrons flow from Al to Al, consistent with the transport being dominated by metallic conduction pathways. The transmission of electrons doesn't necessarily flow between directly bonded Al atoms, therefore longer range tunneling occurs. From this pathway, several "routes" can be identified. There is a group of Al atoms that contribute the highest weight to T(E) (highlighted by the purple arrows) this group identifies a "hot-spot" within the barrier.This is consistent with the findings in ref [179] which report "hot spots" corresponding to metallic conduction pathways. Finally, it can also be seen some arrows travelling in the opposite direction, which shows back scattering, which would decrease the conductance and hence can give an insight to rises in resistance within the barrier.

Further analysis of the transmission pathways in sample B found similar results. Namely, transmission is dominated by metallic pathways Al to Al. Peaks at 0.21 eV, -0.03 eV, all contain, in addition to others, the same atoms as those that dominate the pathway in 0.03eV, this high-

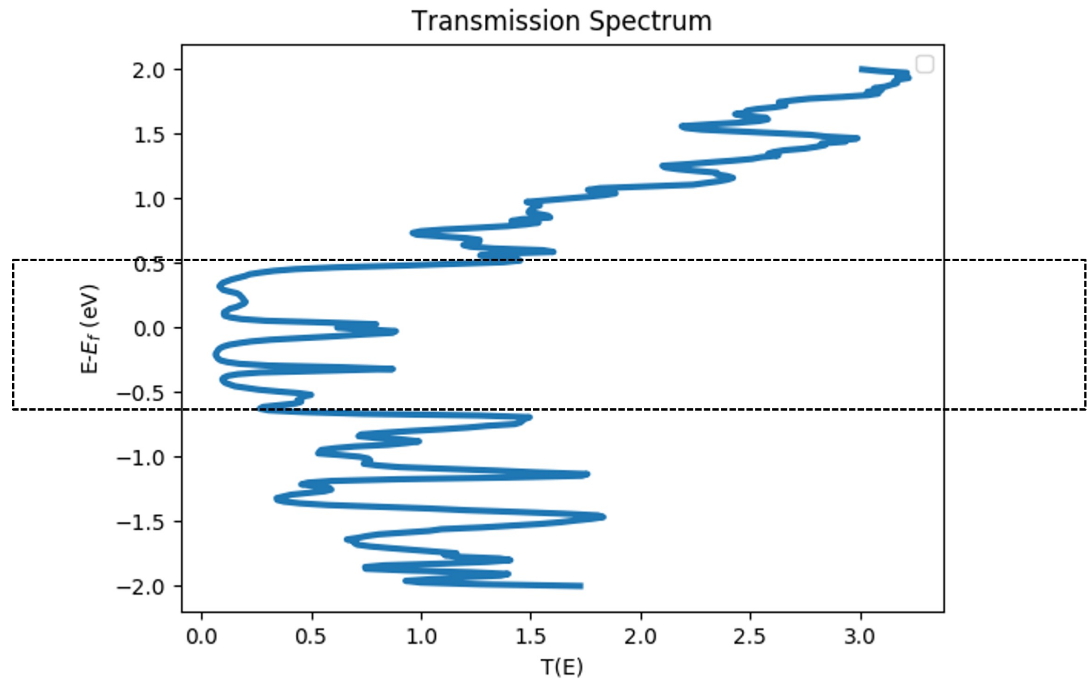

Figure 6.15: Sample B transmission spectra. Dotted box highlights the peaks associated with the IV curves.

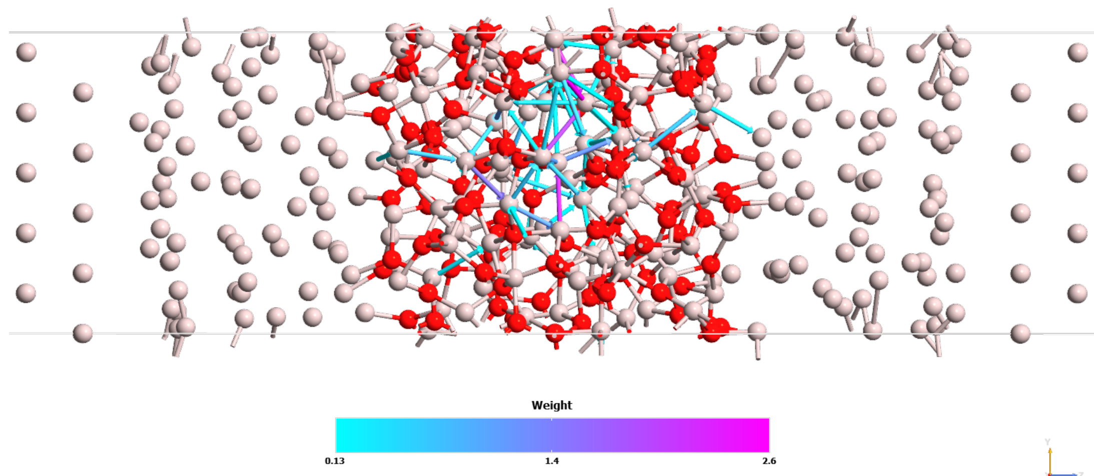

Figure 6.16: Transmission Pathway for the peak at 0.03 eV in the transmission spectra for Sample B.

lights the strong influence of local atomic structure, that creates "hotspots" which contribute to the conductance at various different energies. Although, there are examples of Al-O bond contributions to the transmission, transport through the oxygen atoms is much less common,

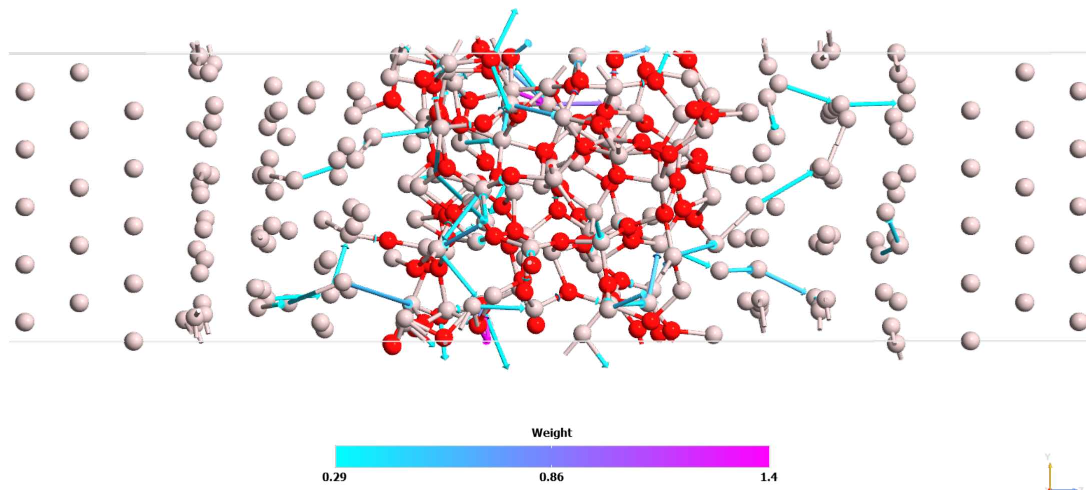

Figure 6.17: Transmission Pathway for Junction A at -0.04eV.

and suggests increasing oxygen concentration increases the resistance (decreases the I_c) of the junction.

Examples of transmission pathways through the different junction barriers from A-E is shown in Fig 6.17- 6.21 at specific energies corresponding to transmission peaks of the respective transmission spectra. In order to maintain brevity, only an example for each is shown here.

From the analysis of pathways through other junctions at several different T(E) peaks, it was found that they had common atoms in the dominant pathways even at different energies, hence "hotspot" areas in the amorphous barrier. The pathways are also dominated by Al-Al contributions, including long range order, suggesting metallic pathways through the barrier are key to transport in the junction. Moreover, though similar trends are observed for all junctions, the actual transmission pathways vary considerably from junction to junction, demonstrating the impact of local atomic structure and how differences can sensitively influence the electron transport.

6.3.5 Transmission Pathway Experiments

In the previous section the idea of transmission pathways was introduced as a major advantage of the simulation framework used in this work for studying the atomic structure effects of the oxide barrier on the resulting electron transport properties. From thorough analysis of the transmission analysis it was concluded that 1) within a barrier there are recurring atoms that are involved in all major transmission peaks, suggestive of "hotspots" that dominate the transport of the entire

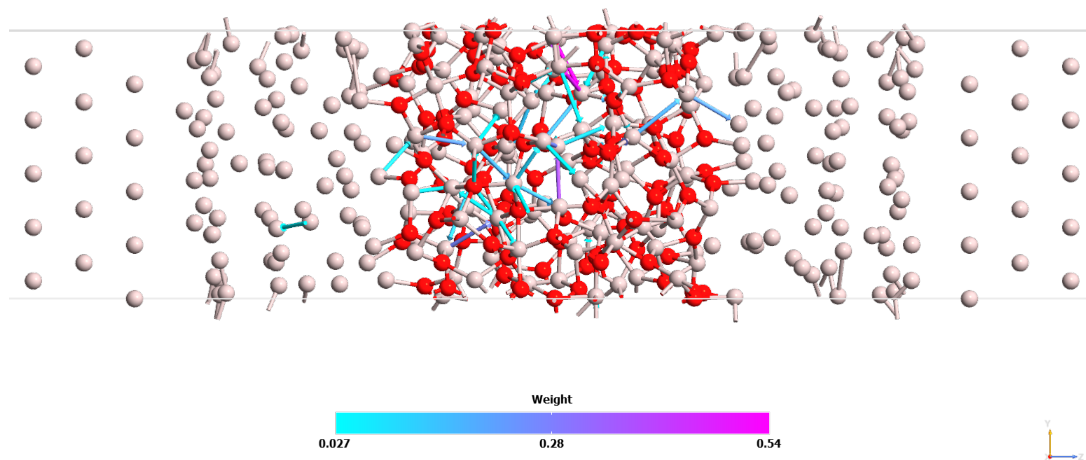

Figure 6.18: Transmission Pathway for Junction B at -0.03eV.

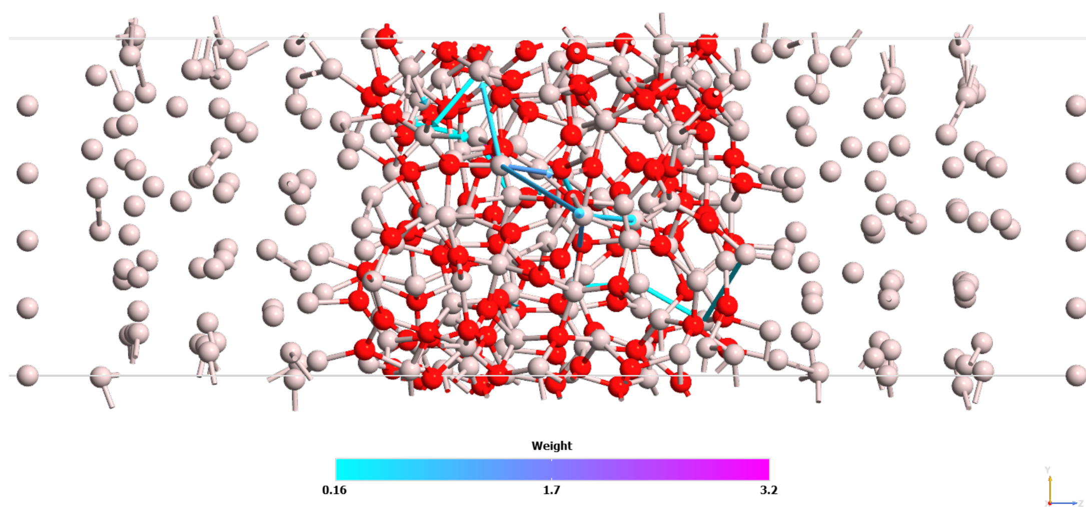

Figure 6.19: Transmission Pathway for Junction C at -0.17eV.

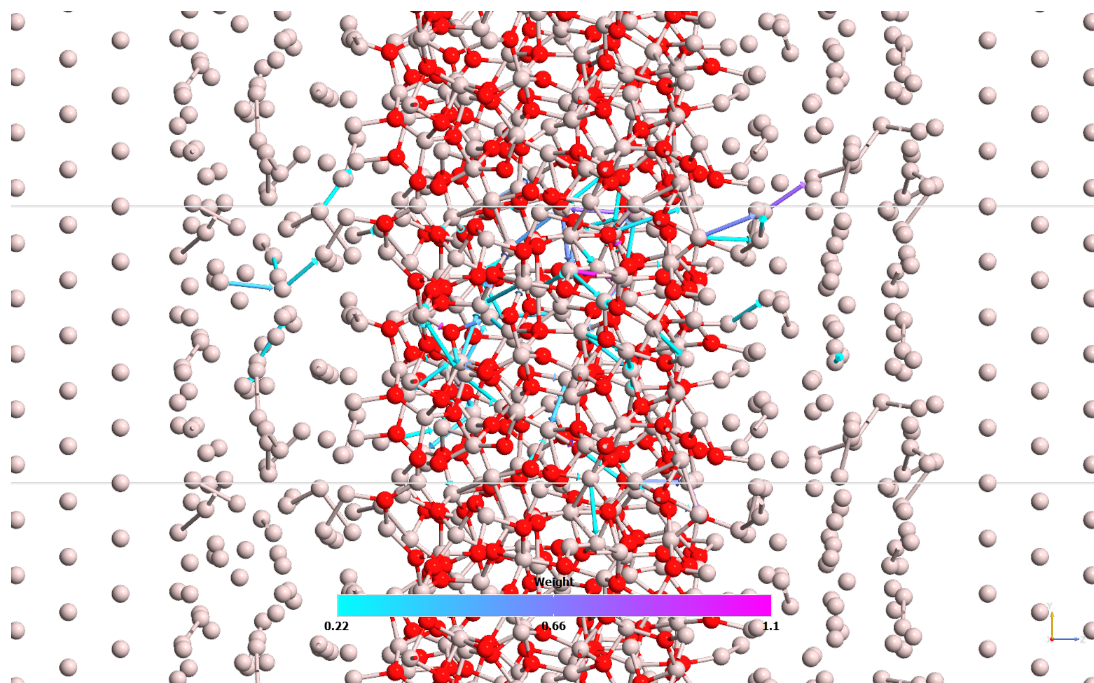

Figure 6.20: Transmission Pathway for Junction D at -0.15eV.

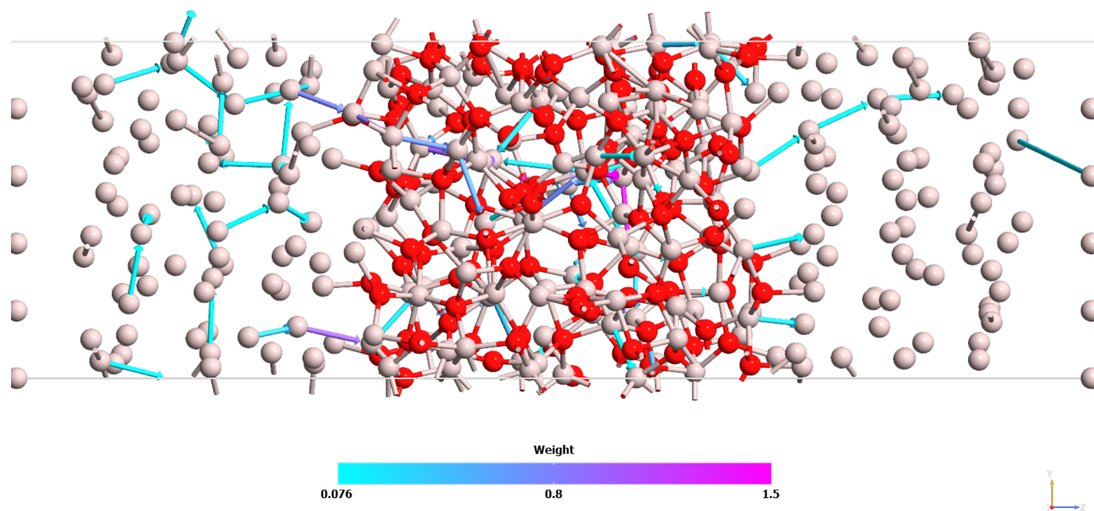

Figure 6.21: Transmission Pathway for Junction E at 0.013eV.

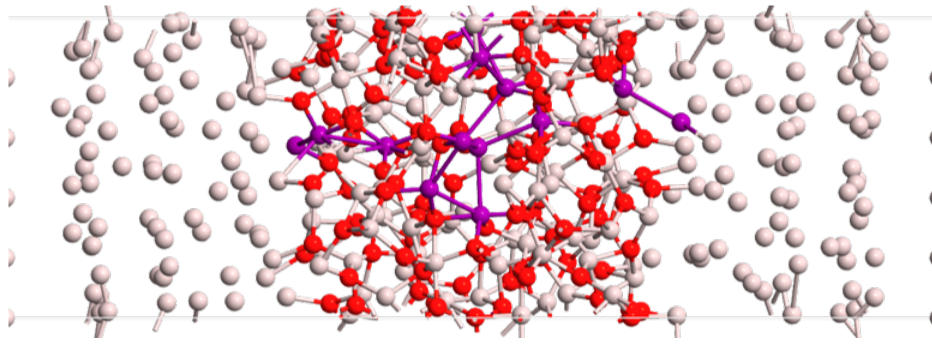

Figure 6.22: Highlighted atoms (in purple) for which the Transmission is concentrated at 0.03eV for Junction B.

junction 2) the majority of transport happens through Al-Al (not necessarily directly bonded) 3) pathways are strongly dependant on local structure and vary junction to junction, appear to concentrate in areas of low oxygen density.

In this section, the aim is to build on these observations and provide better understanding through a series of simulation tests. A key advantage of simulation is that "hypothetical structure variations" can be easily modelled and explored to gain understanding of the fundamental physics. Focusing on the transmission pathway at 0.03eV for Junction B, several different modifications were made to explore the transport in cases of where the transmission pathway of this junction is altered. The effect of the changes is quantified through the change in resistance.

These changes represent an entirely hypothetical structure, and it is noted that in reality, these changes would change the nature of the barrier, it is also noted that these changes influence the density, stoichiometry and other parameters of the junction which could influence the results. However, these tests can still provide a valuable insight into the nature of the transmission through the barrier and how local atomic structure affects the resistance and by extension the critical current and superconducting properties.

Starting from the transmission pathway at 0.03eV for Junction B as shown in Fig 6.16 the main atoms involved in transmission (over 20% contribution) can be highlighted. As previously discussed it is also found that many of these atoms are involved in the transmission at other energies, therefore any changes would affect the transmission at these energies too, thus affecting the transport of the whole junction. The transmission pathway atoms is highlighted in "purple" in Fig 6.22.

The first test was to remove this entire transmission pathway leaving a gap in the oxide and removing the main pathways for the transmission. This is shown in Fig 6.23.

The "complete removal" structure was simulated at zero bias and its Transmission Spectrum was computed along with the resistance of the junction. These are shown in Fig 6.24 and compared to Junction B. It can be seen that the predicted resistance shows significant increase for the barrier where the pathway has been removed. The resistance rises from 40 kΩ to 67 kΩ. The first caveat that needs to be taken into account is that the "hotspot" of atoms deleted primarily

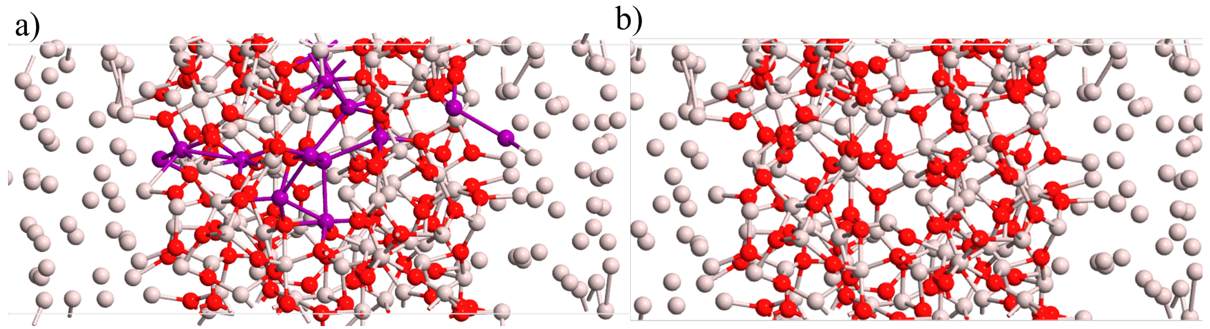

Figure 6.23: a) Transmission Pathway at 0.03eV b) Complete Removal test structure.

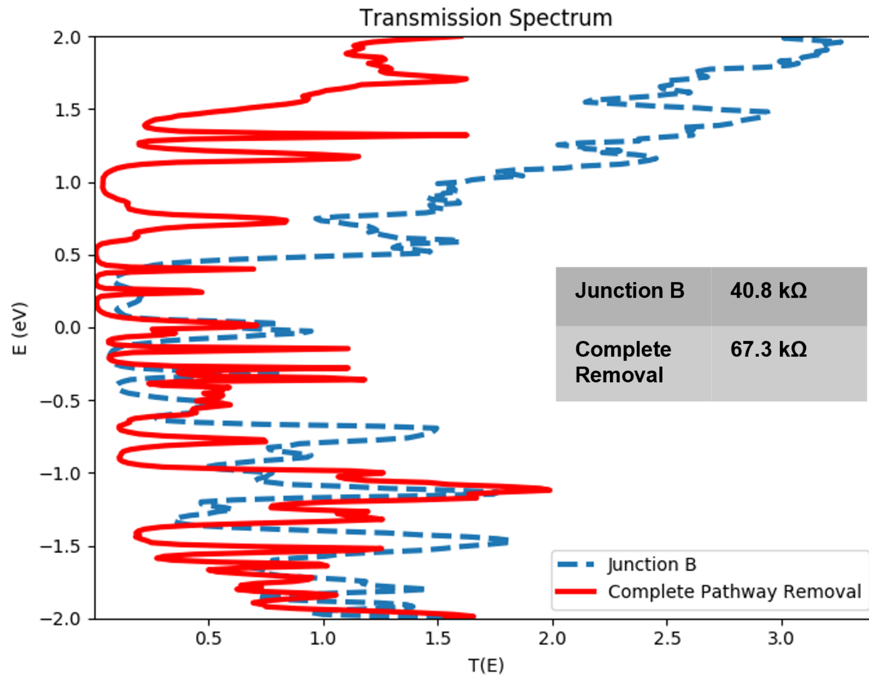

Figure 6.24: Complete removal test transmission spectra. The respective resistances are also shown in the table.

consist of Al, thus deleting all these atoms will result in an increase of oxygen stoichiometry in the aluminium oxide barrier. As reported in the previous section, increasing oxygen content increases resistance. So this can be an explanation for the resulting increase in resistance. In spite of that, it would also be reasonable to suggest that, deleting the main pathways for transmission through the barrier results in less favourable transmission pathways and thus the conductance drops.

Analysing changes in transmission spectra gives an insight to the loss of the hotspots. A few observations can be made. The spectra seems to have shifted up slightly, with peaks at higher energies. Peaks around the Fermi Energy (0 eV) are similar in appearance but have lower T(E), due to the loss of transmission pathway reducing the conductance. Above 0.5 eV where the

peaks were broad and showed high conductance, become sharp after the removal. This is further evidence that the loss of the "hotspot" atoms cause a drop in conductance, and consequently evidence for the existence of hotspot regions for transport in the barrier.

The peak at 0.21eV in Junction B appears to split into two intense peaks after the removal of atoms. Comparing 0.24eV in complete pathway removal to 0.21eV offers insight to the importance of hotspots. Comparing the two transmission pathways in Fig 6.25 it is clear to see the removal of the pathway vastly reduces the number of pathways. Evidently, the region of a high concentration of pathways in Fig 6.25 a) is not present in Fig 6.25 b), instead there are fewer pathways but with a larger weight, concentrated in other areas of the barriers, not in the region of the deleted hotspot. This suggests, that the removal of the atoms has concentrated the transmission through other atoms in the barrier at this energy resulting in an increase in T(E), but with a more intense peak resulting in lower overall conductance.

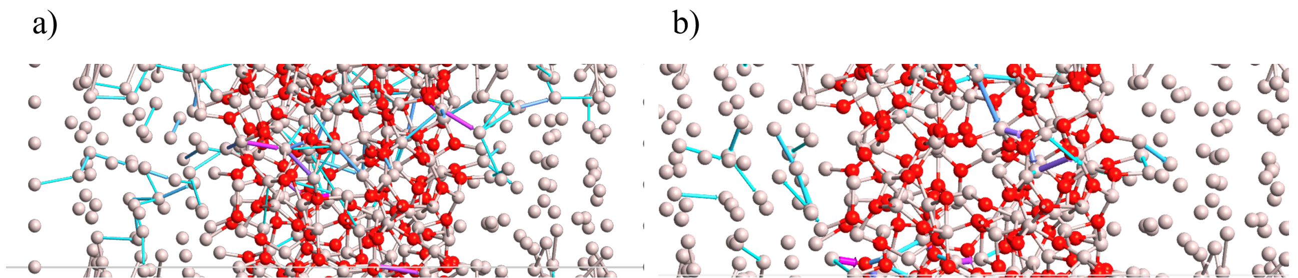

Figure 6.25: a) Transmission Pathways at 0.21 eV for Junction B b) Transmission Pathways at 0.24eV for Junction B after removal of "hotspot"

The peak at 0.4eV which also seems to have split from the broader peak at 0.21eV of Junction B shows the same as 0.24eV with transmission pathways being concentrated through different atoms, this pathway is very similar to that of 0.24eV and is shown in Fig 6.26.

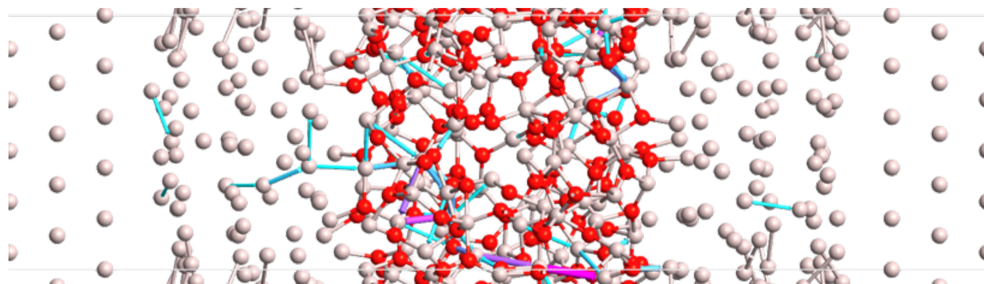

Figure 6.26: Transmission Pathway at 0.4eV for Junction with removed hotspots

Similar analysis can be done at all peaks, from this it is evident is that removal of these dominant atoms reduces the conductance and causes changes in the transmission spectra due to disruption to the dominant pathways through the barrier.

In contrast to completely removing all of the "hotspot" atoms, a test was carried out where two atoms were removed. By looking at the original dominant atoms, it could be argued there are

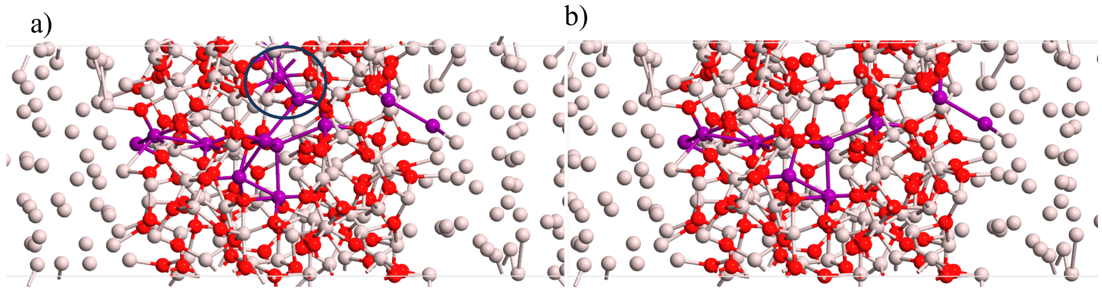

Figure 6.27: a)Junction B Pathway at 0.03eV with Al atoms circled that are to be removed b) The Pathway removal structure studied with the remaining dominant atoms highlighted in purple

"two main pathways" one leading upwards and one downwards and along z-direction. Fig 6.27 illustrates the Pathway removal structure, where the two atoms have been removed. It is expected that by removing these atoms, a major pathway for transmission will be removed leading to a drop in conductance. To verify this, the zero-bias transmission spectra was computed.

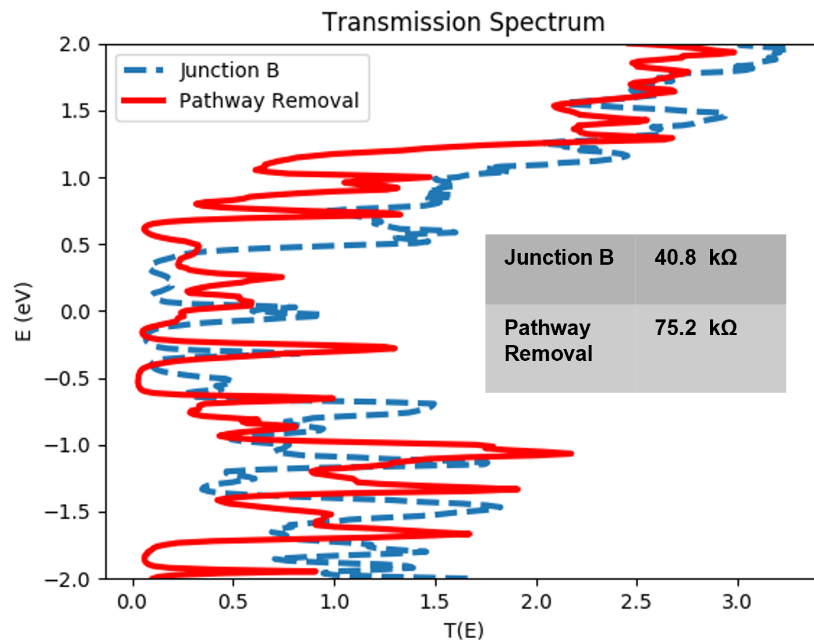

Figure 6.28: transmission spectra for the Pathway Removal structure compared to Junction B with resistance values in the table insert

The computed resistance values from the calculated transmission spectra in Fig 6.28 show that removing these two Al atoms increases the resistance significantly, by almost double, from 40 to 75kΩ. The deletion of atoms causes slight changes to the transmission spectra. Most notably there's a slight shift upwards in the positioning of the peaks. The intensity of the peaks around the Fermi has reduced and the overall broadening of the peaks throughout the Spectra has decreased, consistent with the reduction in conductance. This change is more significant than for the complete removal test where the peaks above 0.5eV were the most affected, with

peak narrowing clear elsewhere too. Overall the loss of two atoms has as big (from these results bigger) effect on the resistance of the junction than deleting all the dominant atoms. The difference may be due to the reduction in density of the barrier offsetting the increased resistance slightly.

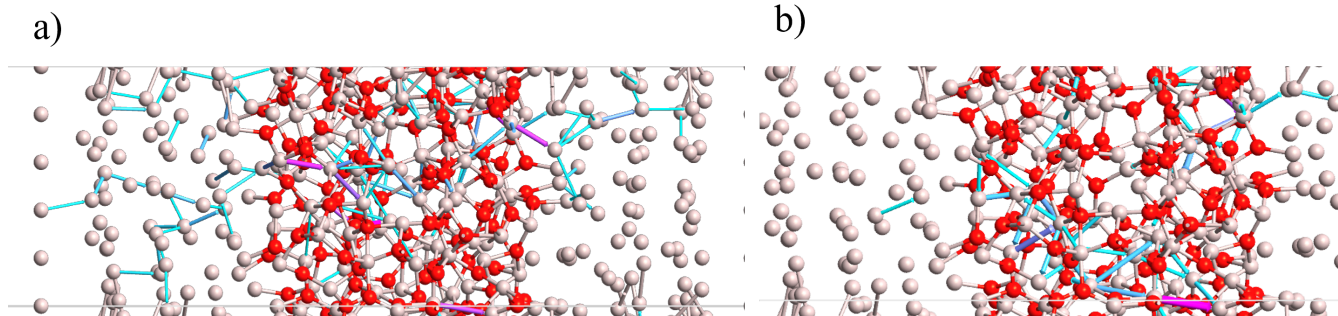

Figure 6.29: a) Transmission Pathway at 0.21eV for Junction B b) 0.25eV for the modified Junction

To further analyse the influence of removing the two atoms highlighted in Fig 6.27 the Transmission pathway for the peak at 0.25 eV was visualised and compared to the corresponding peak 0.21 eV in Junction B. The two pathways are shown in Fig 6.29. It is clear that the removal of the atoms causes significant changes to the main Transmission pathway at this energy. It can be seen that the transmission no longer goes through the areas of these atoms, it also is diverted away from some other pathways that aren't directly through these atoms (but through the centre of the barrier). The transmission for the modified barrier is now concentrated through atoms at the bottom of the barrier. (Bottom relative to Fig 6.29, as with periodic boundary conditions this is not "bottom of the barrier"). This shift in Pathways to be concentrated through different atoms at a "thinner area of the barrier", as well as a reduction in the number of pathways leads to considerable change in conductance as computed by the resistance.

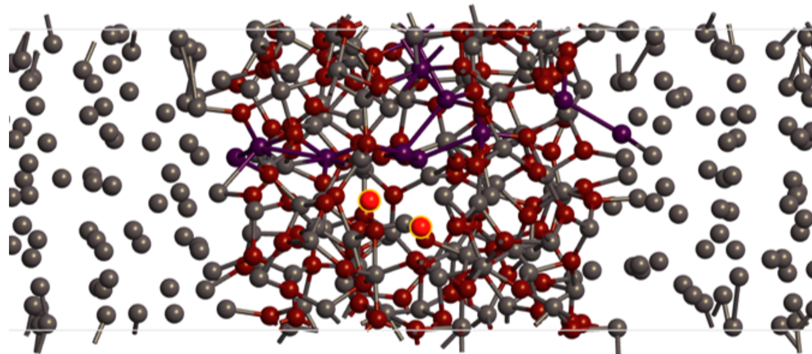

Figure 6.30: The transmission pathway from the disruption test. The highlighted atoms are oxygen atoms that have been converted from Al.

Another test carried out was to disrupt rather than remove the transmission pathway as before. In this test, two aluminium atoms involved in the "dominant atoms" for transmission

through the barrier were converted to oxygen and the transmission spectra at zero bias was computed. The two atoms that have been converted are highlighted in Fig 6.30

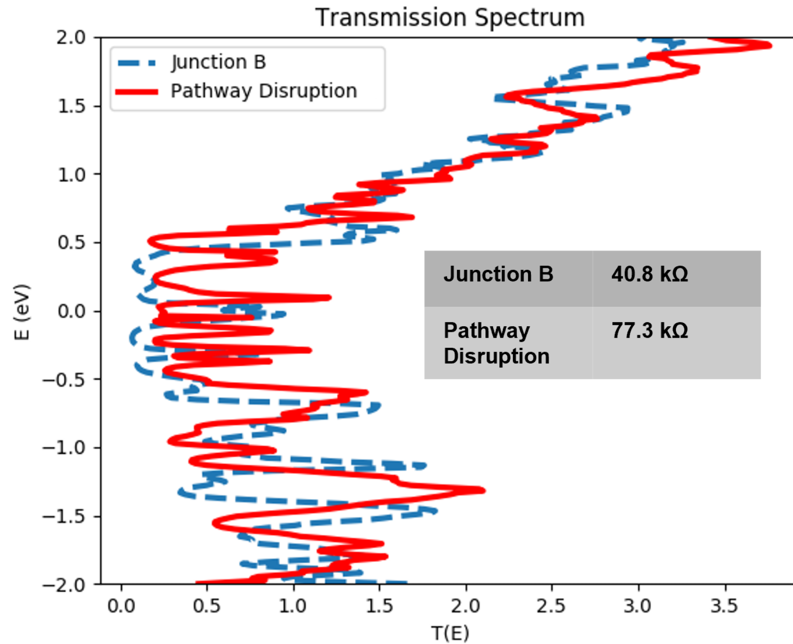

Figure 6.31: transmission spectra for Junction B and the disrupted pathway model.

The transmission spectra for the disrupted pathway model has shifted downwards slightly, there are some subtle changes (certain peaks broadening and changing in intensity) but overall similar shape and peak distribution to model B. The change of these two atoms results in a predicted resistance of almost twice the amount as Junction B as shown in Fig 6.31. This significant gain in resistance can be rationalised by two main observations. First the increase in oxide concentration and thus barrier stoichiometry will naturally lead to an increase in resistance as the barrier becomes more insulating (even if this is only an increase of two oxygen atoms / a four atom change). Secondly, the two atoms that were converted are involved in several of the main transmission pathways, thus by this change the pathways have been disrupted and the overall conductance of the junction decreases, leading to increased resistance.

To analyse further, the transmission pathway at 0.09eV for the disrupted model was computed and visualised and compared to the pathway at 0.21eV for Junction B, given the shift in transmission spectra, these two peaks are the most comparable. Both pathways are shown in Fig 6.32. In the figure the two Al atoms that are converted are highlighted in the circle. What is clearly illustrated by this tests is the change in Al atoms, leads to a "block" of pathways in this region, and seems to also reduce the number of pathways overall. This observation is consistent with the increased resistance.

The tests presented here are not exhaustive and there are a wide range of different test through the barrier that could be carried out using this atomistic simulation methodology. Addition-

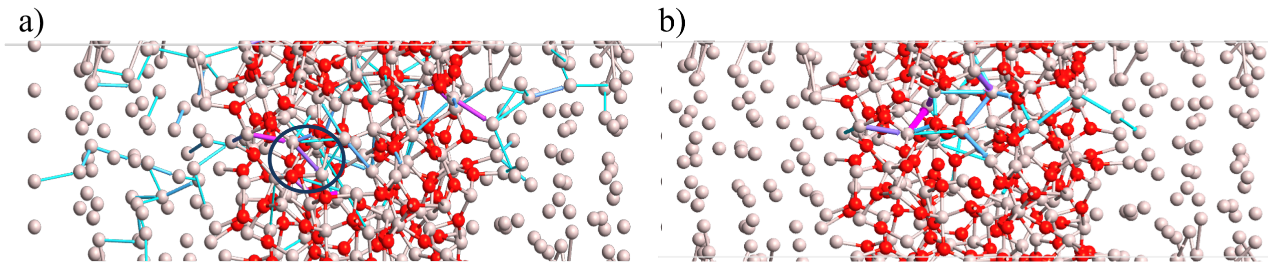

Figure 6.32: a)Transmission Pathway for Junction B at 0.21eV, the circled atoms are the Al atoms that have been converted to oxygen b) Pathway after the change.

ally,the analysis need not be limited to the transmission peaks presented here, only an example for each is reported here for brevity. Overall, computing the transmission pathways and altering the barrier structure highlights the importance of the local atomic structure of the barrier on the electrical response of the junctions. Hence, reducing variability in the amorphous structure of the oxide would lead to better control of the electrical properties of this device and devices built with Josephson junctions.

6.4 Conclusions

Atomistic understanding of Al/AlO$_x$/Al and other Josephson junctions is key to improving their fabrication process and achieving control of critical current and other parameters. Developing and employing efficient and accurate modelling techniques can significantly boost progress and understanding of the Al/AlOx/Al. In this chapter the atomic and electronic structure of the archetypal Josephson junction: Al/AlO$_x$/Al have been thoroughly studied using a combination of Molecular Dynamics, DFTB and NEGF methods.

It has been shown that the stoichiometry of the barrier sensitively affects the critical current of the Al/AlOx/Al, the effects can be rationalised through the opening of a energy gap in the barrier with increasing oxygen concentration, linked to the local atomic structure studied by Al-O Coordination Number. The amorphous nature of the barrier leads to unavoidable variability within the junction, this has been studied here computationally across different samples created in the same way. It was found that differences in local structure arise naturally which strongly influences the electronic structure of the barrier leading to variability in the IV characteristics, junction resistance and critical currents. Though some consistency between samples was observed, small differences in structure resulted in significant variation in the simulated current values and hence the device performance.

Finally, within this computational framework the nature of tunnelling through the barrier has been explored. Analysis of the transmission pathways provides further evidence that metallic pathways dominate the transport in the junction. As a result, increased oxygen concentration (higher stoichiometry) reduces the metallic pathways in the barrier and lead to increased resis-

tance. This is further evidence that local atomic structure is vitally important for controlling critical currents.

Exploration of dominant atoms in the transmission pathways of a Junction model illustrated the appearence of metallic hotspots. Changing the structure of these atoms in particular has a significant effect onthe overall resistance properties of the junction and alters the transmission. This is further evidence that changes in the barrier structure due to the amorphous nature can lead to unwanted variability in the electrical response characteristics.

Chapter 7

Exploring the barrier length of Al/AlO$_x$/Al

7.1 Introduction

In the last chapter the influence of the atomic structure of the amorphous barrier, specifically the Al:O ratio, was studied computationally. It was shown that local structure can have a significant influence on the transport properties of the Al/AlOx/Al tunnel junction and could subsequently lead to variability between junctions.

One of the key parameters that requires control when fabricating Josephson junctions is the amorphous aluminium oxide barrier length. Since the electron tunneling scales exponentially with increasing barrier length (i.e with increasing barrier length, junction resistance increases exponentially) [3,196]. In typical Josephson junctions the barrier length is 10-20 Å, however can vary significantly depending on the quality of the fabrication. Due to the scale of the junctions; measuring the physical barrier length experimentally is challenging and unreliable. . Typically the barrier length is estimated by fitting the measured I-V characteristics to the Simmons model for tunneling and extracting the length as a parameter [197]. However, the Simmons model is one dimensional model with approximations which are not not suitable to capture the atomistic nature of the tunneling barrier. For this reason in this chapter, the approach is to use atomistic material simulations.

The aim of the work presented in this chapter was to use atomistic simulation methods to probe the relationship between barrier length and resistance of the Al/AlO$_x$/Al tunnel junction. Furthermore, to understand how the local atomic nature of the barrier changes with increasing length and its influence on the electron tunneling through the device.

7.2 Creating the Junctions Models

The junction models were created following the same procedure described in the previous chapter. Oxygen is removed from the crystalline junction to obtain the desired stoichiometry. In this section $AlO_{1.1}$ and $AlO_{1.5}$ have been explored. The amorphous oxide was created from the

crystalline model through simulated annealing following a similar procedure reported by Cyster and colleagues and the one described in the previous chapter [165]. The different barrier lengths were controlled by slicing or repeating an already amorphous oxide and repeating the simulated annealing molecular dynamics simulations. The different sizes were generated from an amorphous oxide in order to preserve the stoichiometry and density. Although there are variations in stoichiometry through the amorphous structure, if the size was to be adjusted for a crystalline junction, the removed oxygen atoms would have to be carefully selected so that the slicing does not increase or reduce the required stoichiometry. By slicing from the already amorphous sample there is less opportunity for human error and better consistency across the model amorphous barriers. The amorphous barriers are then sandwiched between bulk aluminium electrodes and allowed to relax using DFTB. The full details of procedure were given in the previous chapter.

The barrier length is controlled as a multiple of a standard $3 \times 3 \times 1$ unit cell of corundum(0001) adjusted for the reduced density. However, the actual physical barrier length is difficult to predict and measure. The multiple relaxation steps during the junction creation procedure inevitably leads to variation in the physical barrier length even when the same initial size of oxide is used. For studying the relationship between barrier length and resistance, a consistent and accurate measure of barrier length is vital. Measuring directly from the generated models (with a virtual ruler) is difficult since deciding where the oxide barrier starts and ends is arbitrary and subject to debate. For consistency, the barrier length is measured from the Electrostatic Difference Potential (EDP) profile of the junctions. The potential drops and rises significantly at the Al-AlO$_x$ interfaces. Measuring the distance between these two points gives a consistent method for measuring the barrier length of all the created junction models. This is illustrated in Fig 7.1.

The final Junction model is then studied at zero bias and then under bias using DFTB-NEGF simulation methodology. The resistance is calculated from the inverse of conductance. For both the analysis and measuring the physical barrier length an important computed value is the electrostatic difference potential of junction device which is calculated using the DFTB-NEGF method. The electrostatic difference potential is the solution of the Poisson equation which takes into account the electron difference density, mathematically:

$$\nabla^2 \delta V_e = \frac{e}{4\pi\varepsilon_0} \delta n(r) \tag{7.1}$$

The electron density difference, $\delta n(r)$, is the difference in total electron density of the system and the neutral non-interacting atoms (before the system is calculated self-consistently). Thus the electrostatic potential difference shows regions where significant charge redistribution has occurred in the system.

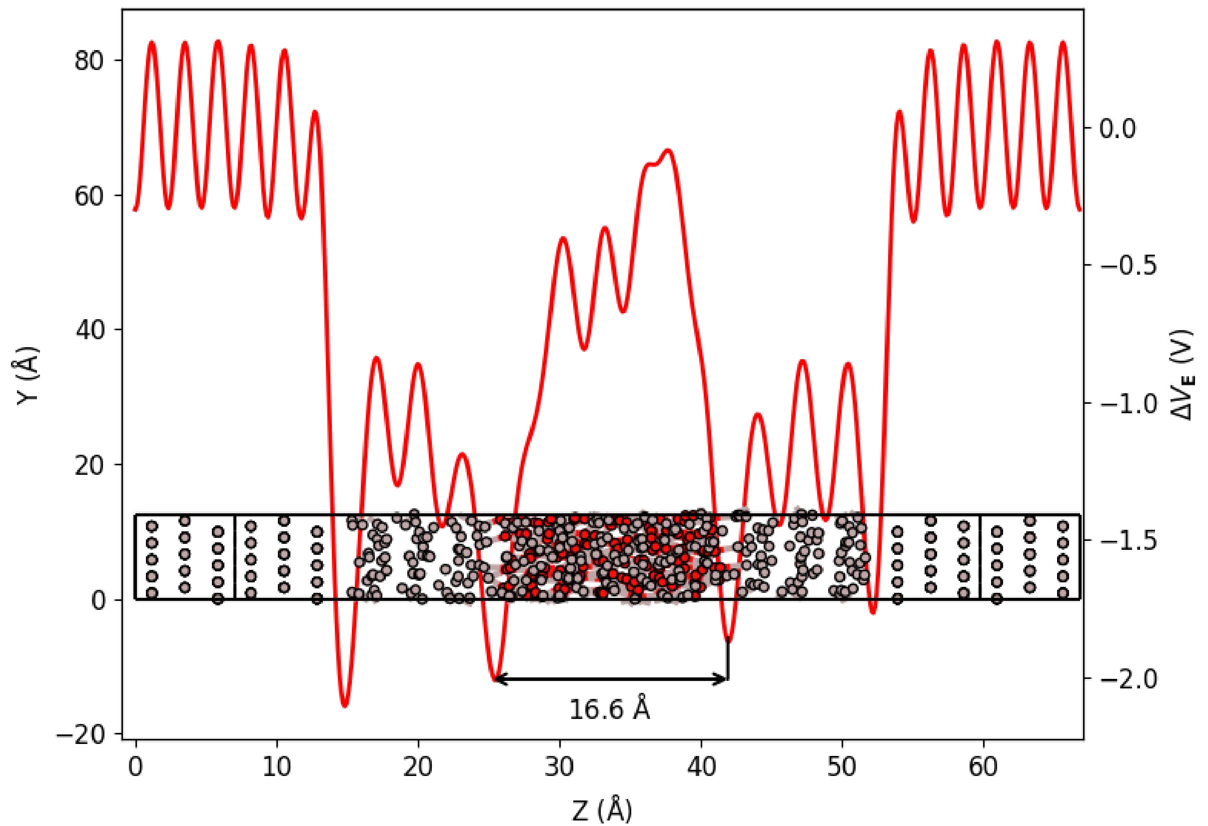

Figure 7.1: Illustration of how barrier length was measured in this work. Overlay of the Electrostatic difference potential with the junction configuration's YZ coordinates.

7.3 Initial Exploration of the barrier length

As a starting point, junctions were created (as described in the previous section) for both $AlO_{1.1}$ and $AlO_{1.5}$, due to computational expense 5 junctions for each stoichiometry were created and studied. The amorphous barrier was designed as a multiple of "corundum size" denoted as L. The actual barrier length was then measured from the potential as discussed in the previous section.

Sample	Corundum Size (Å)	Amorphous Size (Å)	Density (g/cm^3)	Physical Length
L	13	16.25	3.18	
0.5L	6.5	8.13	3.18	8.19
0.6L	7.8	9.75	3.07	9.15
0.7L	9.1	11.38	3.03	11.8,
0.8L	10.4	13	3.14	12.5
0.9L	11.7	14.63	3.22	14.6

Table 7.1: Size and density parameters for the $AlO_{1.5}$ model barriers

Table 7.1 shows the parameters for the creation of the model barriers for $AlO_{1.5}$. The "corundum size" is the size of the corundum unit cell used before adjusting the size for the required

lower density of amorphous aluminium oxide. The "amorphous size" refers to the size of the simulation cell used for the simulated annealing, it has been calculated to allow for the density of the resulting amorphous oxide to be approximately 0.8 times the density of corundum. In the table, the final density is reported for the amorphous oxide after the simulated annealing and DFTB geometry optimization. The last column in the table reports the "physical length" of the barrier. This is the length measured from the electrostatic difference potential. This is the most accurate length for the barrier that will be used for analysis of the junctions and their transport properties.

The density data in Table 7.1 shows that there is variation in density in the samples. Although the aim was to keep the density constant, there were unavoidable changes in order to allow for geometry relaxation for accurate bond lengths and distances. There are two samples, 0.6L and 0.7L, with a lower density than desired whilst the rest are close to the desired $3.18 g/cm^3$. This shortfall arises due to the geometry optimization and the way the corundum was sliced resulted in lower than expected mass. This lower density could influence the local atomic structure of the barrier and thus the electron transport properties. However, difference in density is reasonably small and so it is not expected to have a significant influence on the local atomic structure compared and thus its influence on the analysis should be small.

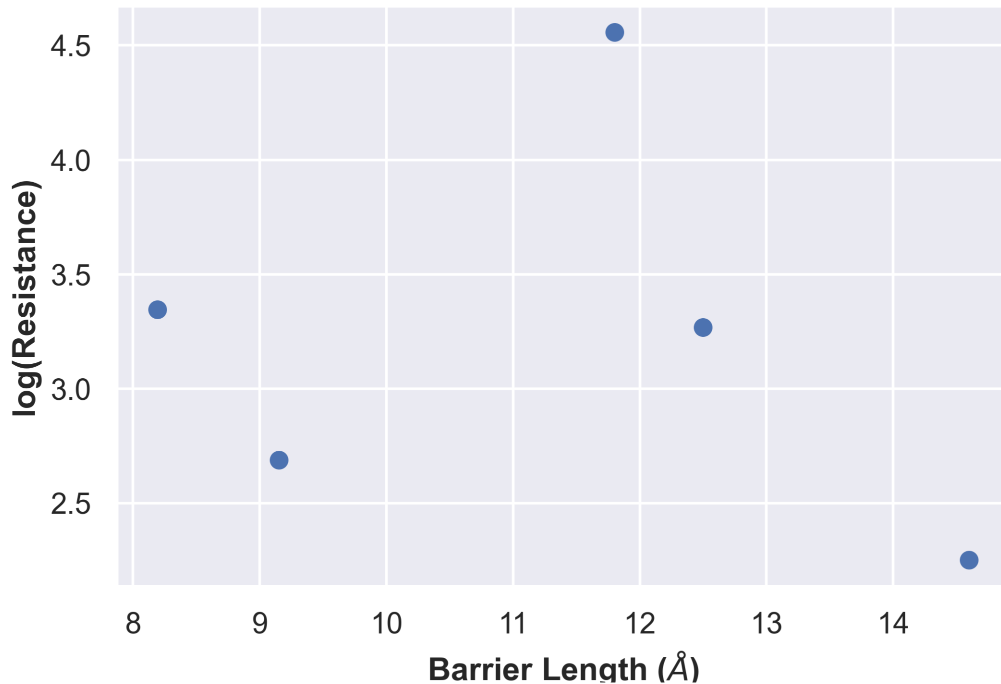

Figure 7.2: Log of Resistance vs barrier length Data for $AlO_{1.5}$ Junctions.

The computed resistance vs physical barrier length for the five $Al)_{1.5}$ junction models is shown in Fig 7.2. The resistance is reported in log scale so that all values can be compared. The value of resistance for the junction with barrier length at 11.8 Å(0.7L) is significantly larger

(an order of magnitude) than the other models. The data is unexpected, although there is some variation in resistance with increasing barrier length, it is not exponential nor consistent. In fact, the computed values show little evidence of a relationship with a stochastic spread of data points. However, a conclusion cannot be drawn as there are too few data points to establish this relationship. Nonetheless, variation in the order of magnitude of the computed resistance was expected and that is not observed here.

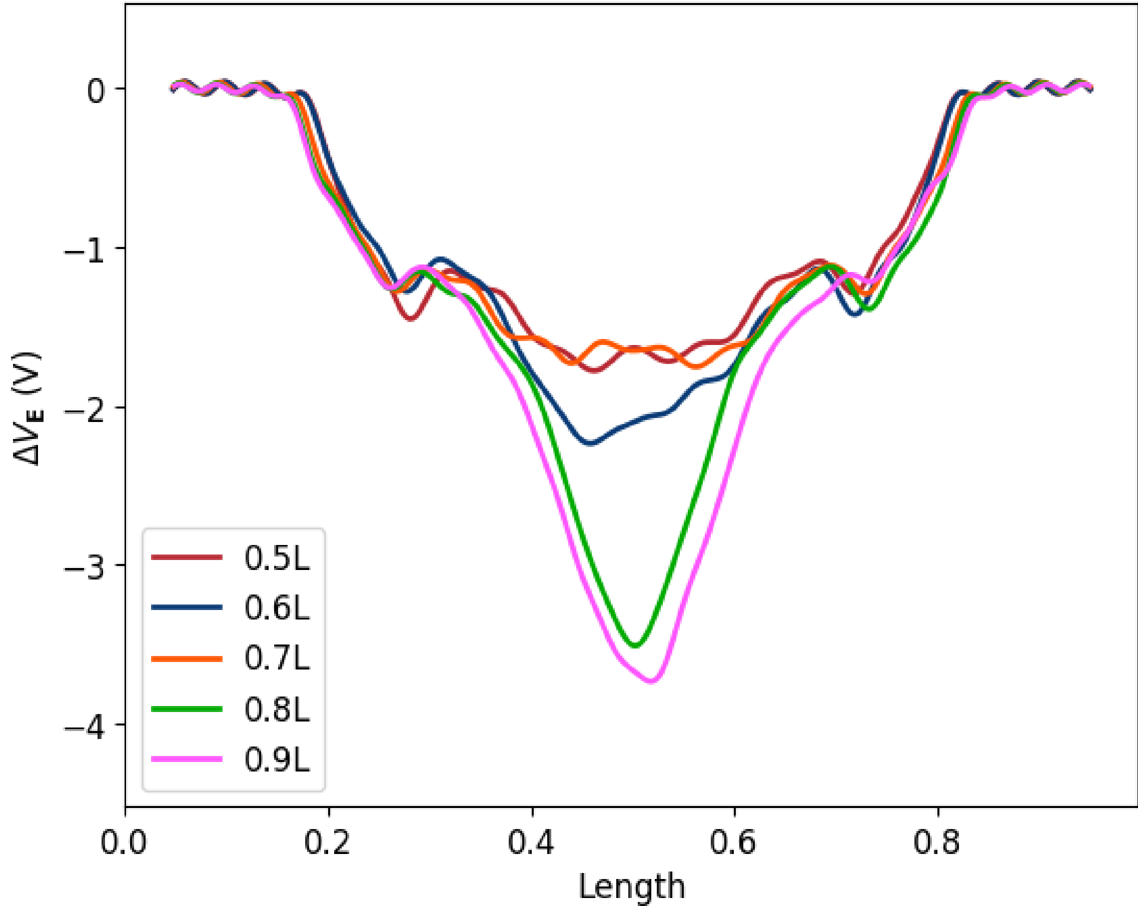

Figure 7.3: Comparison of the Electrostatic Difference Potential for the $AlO_{1.5}$ barriers. The length is given as a multiple of the lenght in the "Z" coordinate.

As part of the analysis of these junctions, the electrostatic difference potential (EDP) is computed and compared, at zero drain bias. In the region of the barrier it is expected that the EDP drops. In addition, the larger the barrier length the deeper the potential drop (valley) profile. This could be explained by the increase in oxygen content in the junction, which leads to an increased potential (more negative) due to the electronegativity of oxygen. Fig 7.3 shows the EDP for all the junction models from Table 7.1. In general, the figure reveals that the trend of larger barrier length leads to a more negative potential as expected. The only exception is 0.7L shows a similar EDP to 0.5L which may be due to its lower density leading to a lower than expected electron difference potential. It can be seen that shorter barriers have significantly smaller EDP than the longer barriers 0.8 and 0.9L, this is due to considerably different oxygen

concentrations leading to a larger potential.

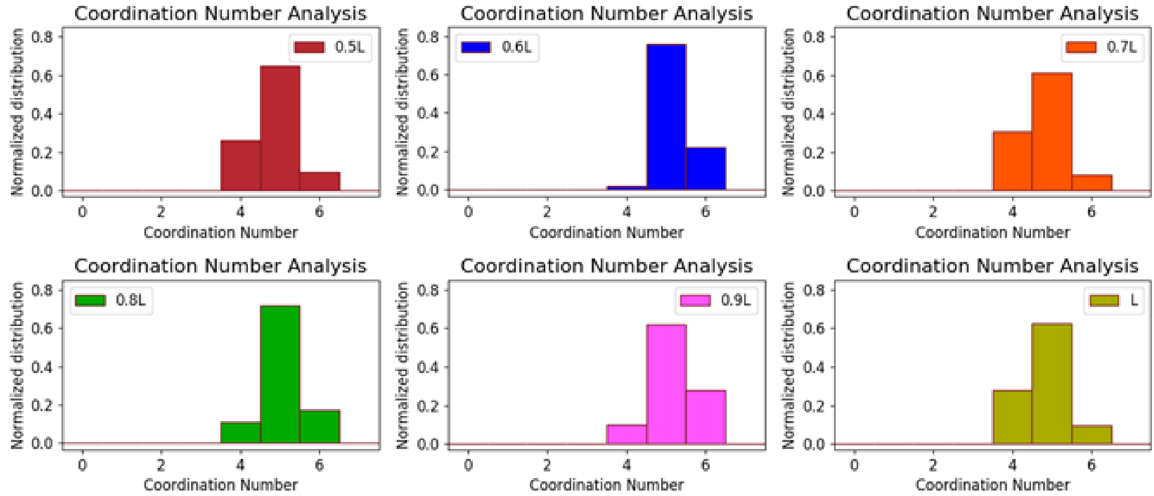

Figure 7.4: Al-O Coordination Number comparison for the $AlO_{1.5}$ Junctions with different barrier lengths.

In an attempt to understand the unexpected relationship between resistance and barrier length in this data set, the Al-O Coordination number (CN) was computed for each of the barrier in the model junctions. Computing the CN allows comparison of the local atomic structure of the barrier. In this case it would be expected for there to be very little difference in the distribution due to having same/similar density and stoichiometry despite the differences in length. The CN for all the barriers in this set are shown in Fig 7.4.

In general the distribution of coordination number is similar across all lengths. The most common CN is 5 since the amorphous barrier is fully stoichiometric. The 0.5L model has a lower CN(6) than the rest, likely due to there being less oxygen in the barrier for this size. In general there are differences in the distribution of CN(6) which is lower in 0.7L and L. These differences will arise from the stochastic nature of the molecular dynamics simulations in the simulated annealing. However, the minor differences in CN across these junctions do not correlate to the differences in computed resistance.

As previously discussed in the last chapter, the amorphous barrier in fabricated Al/AlOx/Al tunnel junctions is known to be oxygen deficient. With usual stoichiometries in the range of 1.1-1.3. Because of this, as part of the intial study, several barriers with $AlO_{1.1}$ stoichiometry were modelled. The parameters of these barriers are reported in Table 7.2.

The created oxygen deficient barriers have lengths that range between 7-13.5 Å, the density is in general quite consistent and close to the 0.8 times the density of crystalline aluminium oxide despite the multiple geometrical relaxation processes. The resistance was computed from the zero bias transmission spectra for all junction models and plotted against the measure barrier length and is shown in Fig 7.5.

Similar to the preliminary results for the $AlO_{1.5}$ resistance, the resistance results for $AlO_{1.1}$

Sample	Amorphous Size (Å)	Density (g/cm^3)	Physical Length (Å)
L	14.05	3.18	
0.5L	7.03	3.22	7.2
0.6L	8.43	3.28	9.38
0.7L	9.835	3.17	10.7
0.8L	11.24	3.25	12.3
0.9L	12.645	3.18	13.5

Table 7.2: Size and density parameters for the $AlO_{1.1}$ model barriers.

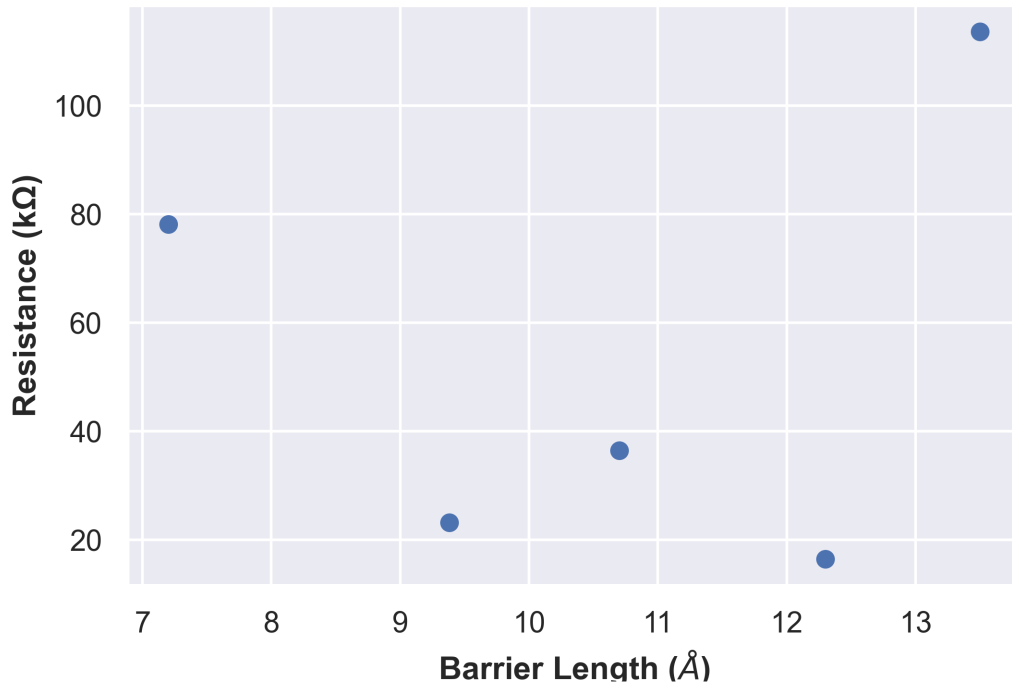

Figure 7.5: Resistance vs barrier length for the $AlO_{1.1}$ Junction models in this initial study.

also do not show an exponential relationship with increasing barrier length. From the five data points, there is no clear relationship between the barrier and length and resistance. The resistance for the smallest barrier (7.2 Å) is unexpectedly high, whilst the largest barrier in this case shows the highest resistance as expected. Nonetheless, the range of resistances for increasing barrier lengths do not show a strong correlation between resistance and length.

The electron difference potential for the junction models are shown in Fig 7.6. Compared to the EDP for the fully stoichiometric barriers, an obvious difference is that the ΔV becomes less negative in the barrier region (between 0.4-0.6 times the length), whereas for the Al_2O_3 it becomes more negative. This highlights the effect of oxygen deficiency on the charge distribution in the barrier. Aside from the 0.6L sample, the trend is as expected, with larger peak for larger barrier length. The 0.6L is larger than expected, but that seems to correlate with the

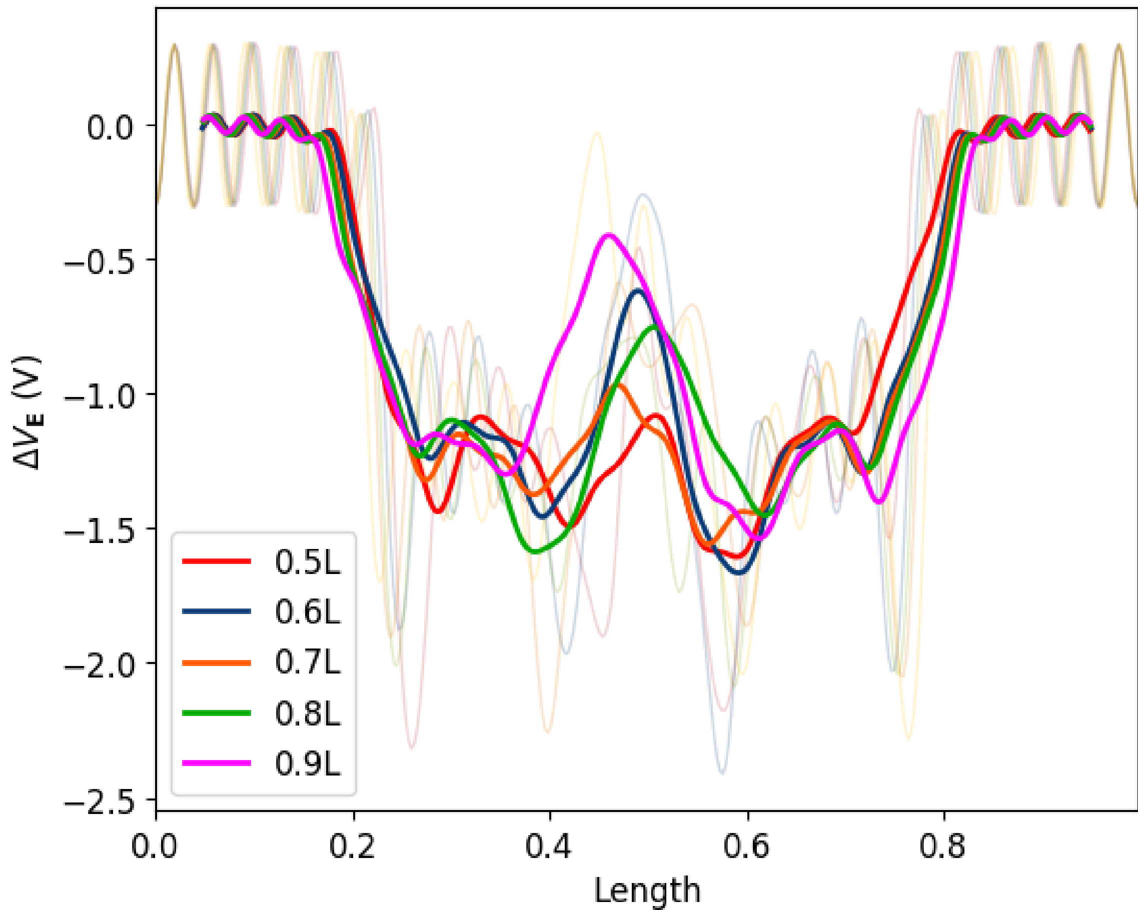

Figure 7.6: Electrostatic difference potential for the 5 created barriers 0.5-0.9L with $AlO_{1.1}$.

larger density value for the sample. A higher density results in a larger than expected charge distributed compared to the rest of the barriers.

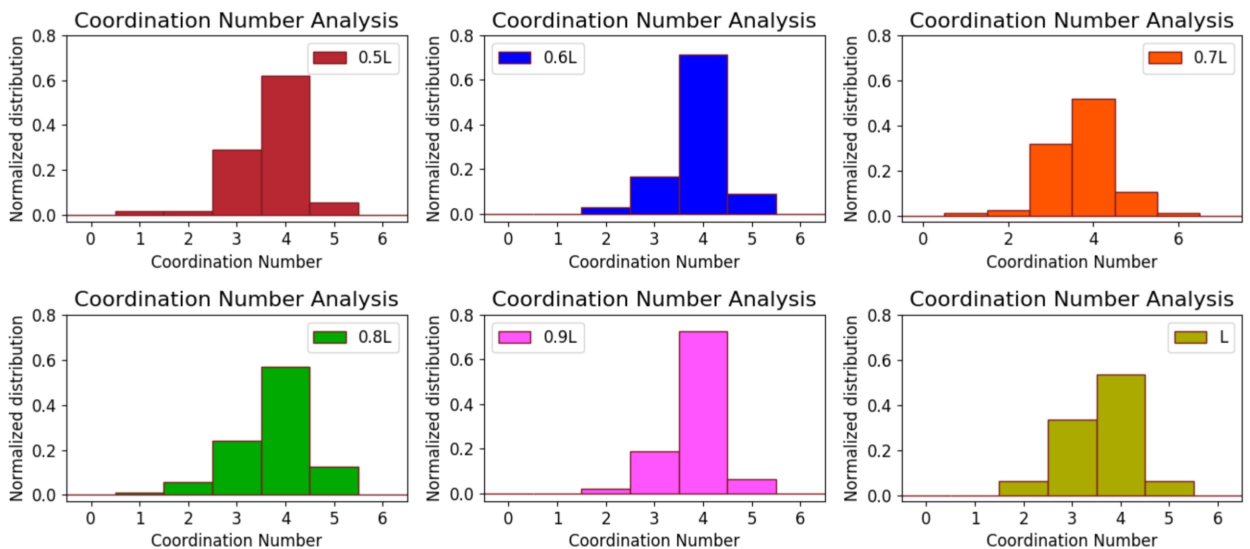

Figure 7.7: Al-O Coordination Number for the amorphous barrier in the different $AlO_{1.1}$ junction models giving an insight to the local atomic structure in the barrier.

The local atomic structure of the barriers are compared by computing the Al-O coordination number distribution. This is shown in Fig 7.7. The Coordination distribution is dominated mostly by stoichiometry and density more than barrier length. As can be seen from the figure, in general there are only small subtle differences between the coordination distributions. In all cases the CN(4) is the most common. The differences in local structure does not account for the considerable differences in resistance.

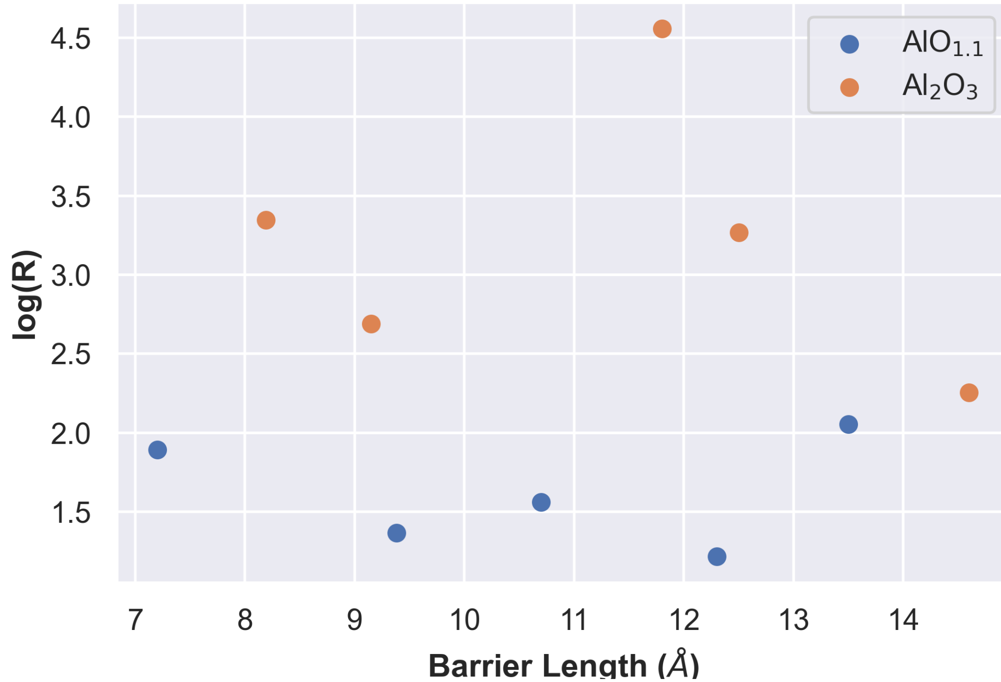

Figure 7.8: Comparison between log(Resistance) of $AlO_{1.1}$ and $AlO_{1.5}$ vs barrier length.

From the initial study there are too few data points to draw any meaningful conclusions. However, the resistance vs length results were unexpected. Previous published work in the literature shows that resistance increases exponentially with increasing barrier length in tunnel barriers such as Al/AlO$_x$/Al. Fig 7.8 shows clearly that for both sets there is randomness to the data. The difference in magnitude of resistance is solely due to the stoichiometry as expected from the results of the last chapter. The results from these simulation suggest either 1) an issue with the simulation model (NEGF-DFTB), 2) an issue with the Al/AlO$_x$/Al model junction and the way it has been created or 3) high variability due to some physical phenomena. In order to explain the data here and further investigate the influence of barrier length, many more data points are required.

7.4 Further Study of the barrier length in Al/AlO$_{1.1}$/Al Josephson Junctions

The initial results explored in the last section produced unexpected results with no clear link between barrier length and resistance. In order to investigate this further it was very important to gather many more data points. Due to the computational burden, it was decided to explore further the AlO$_{1.1}$ barriers as experimentally grown barriers are known to be oxygen deficient. A total of 23 model junctions were simulated with barrier lengths ranging from 5-22.2 Å . Ideally, data would be gathered from hundreds of simulations, however at this level of theory it is not achievable in a realistic time frame.

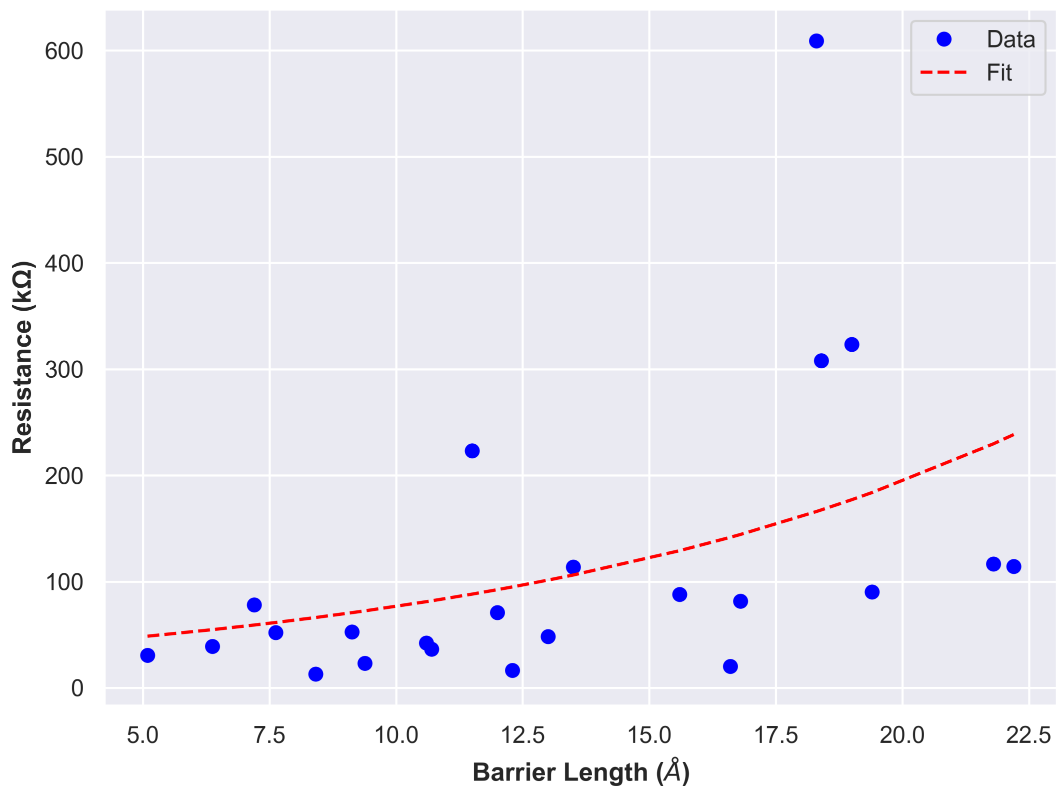

Figure 7.9: Resistance vs barrier length for simulated Al/AlO$_{1.1}$/Al model junctions.The red line is a fit to the exponential function $y = ae^{bx}$.

The computed resistance was plotted against measured barrier length for all junctions and is shown in Fig 7.9. To assess the existence or not of an exponential relationship, the data is fit to an exponential function ($y = ae^{bx}$) which is the red dotted line as a guide to the eye. The calculated data does not show an exponential relationship between barrier length and resistance. In fact, it would be difficult to argue that there is a strong link between these two variables. In general,

the data suggests an increase in resistance with increasing barrier length but not exponentially. In actuality, below 150 kΩ the data is weakly linear, almost flat with considerable variability. There are a few data points higher than 200 kΩ but these appear to be anomalies (outliers) rather than part of the trend.

The results of the simulations here do not show the expected experimental observation. Hence, it raises the question to how physical representative the model junctions are with respect to a real system, it questions the validity of DFTB-NEGF method employed to explore the transport of the system or the method for which resistance is computed. Before analysing in depth the model junctions it was important to explore the validity of the methodology used in the simulations.

It is possible that the unexpected results are a result of the amorphous nature of the aluminium oxide barrier. Though experimental oxide is amorphous, it is grown and will maintain some epitaxy/ crystallinity. Direct comparison between the simulated annealing structure and an experimentally grown thin barrier is difficult. But the results here may suggest that the barriers in this study have a higher degree of amorphousness compared to real junctions. In addition, it is predicted that the amorphous nature is the cause of variability in the electrical response of Josephson junctions [163, 198]. It is possible that due to the amorphous barrier there is an "effective barrier length"/ "effective conduction area" much smaller than the physical length which would explain the data in Fig 7.9. This will be discussed in more detail later in the chapter.

If the amorphous nature was the cause of the unexpected relationship observed in the calculations and also if the simulation methodology used here is in fact sound, then simulating crystalline AlO_x tunnel junctions would show a clear exponential relationship between resistance and barrier length. To test these two proposals, several hypothetical crystalline model Al/Al_2O_3/Al tunnel junctions were created and simulated using DFTB-NEGF. The crystalline models differed in length of the barrier. The barriers were created by placing 3x3x1 slices crystalline corundum (0001) of different lengths (Z-vector) between bulk Al to create Al/Al_2O_3/Al devices. The Al was placed at appropriate bond lengths for for Al-O (1.8-1.9 Å) and Al-Al (2.55-2.70 Å). An example of the crystalline model junctions is shown in Fig 7.10. The devices were studied at zero bias using DFTB-NEGF methodology. The transmission spectra was computed and the conductance calculated in order to calculate the resistance of the barriers as described previously.

Seven hypothetical junctions were modelled with crystalline barrier lengths ranging from 6-26 Å. The computed Resistance increased exponentially with increasing barrier length. The log plot of R vs barrier length is shown in Fig 7.11. The straight line fit illustrates the exponential relationship between the Al_2O_3 crystalline barrier length and the resistance as calculated from DFTB-NEGF. This shows that the DFTB-NEGF methodology is appropriate and capable of reproducing the expected exponential relationship between barrier length and resistance as seen experimentally, albeit only when the barrier is crystalline.

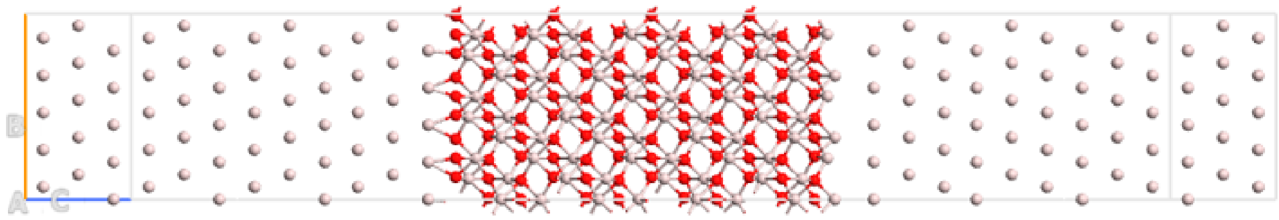

Figure 7.10: Example of a hypothetical Crystalline Al/Al_2O_3/Al tunnel barrier studied in this work.

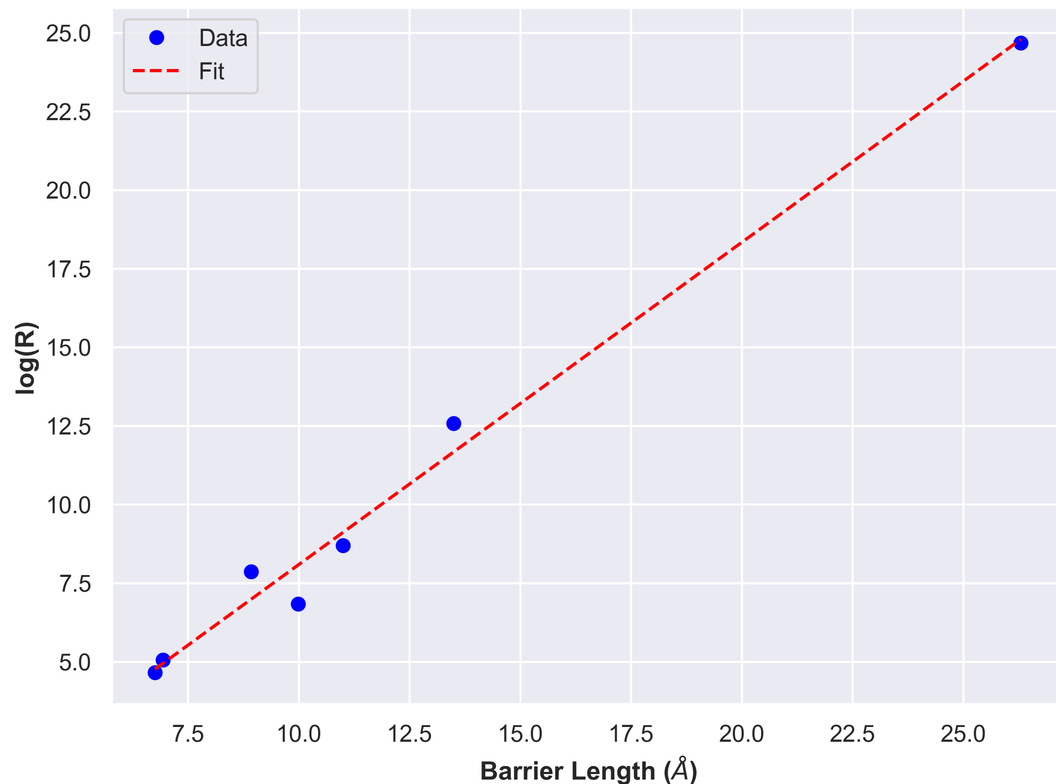

Figure 7.11: Plot of log(R) vs barrier length for the Al/Crystalline Al_2O_3/Al model junctions. The data shows a straight line fit (red dotted line) showing exponential relationship between R (resistance) and barrier length.

The results of these simulations gives confidence in the chosen methodology. The DFTB-NEGF methodology should reproduce the exponential relationship between the amorphous barrier length and resistance of the junctions. The fact that it is not observed and there is significant variability suggests a problem with the amorphous barrier containing $Al/AlO_{1.1}/Al$ model junctions. Of course, experimentally the amorphous oxide barrier is grown and thus will follow the morphology of the Al surface. Although through the simulated DFTB relaxation there is disorder at the Al/AlO_x interface and "surface" oxide is created in the models here, it is only an approximation to the actual structure. However, there have been studies of Al/AlO$_x$/Al junction

created in this way that don't report the same variability/lack of exponential relationship [165]. Hence, this shouldn't be the main cause of the data here. Another possibility is that the barrier is far more amorphous than in reality, as the grown structure would show some epitaxy and crystallinity. The barriers here may have a higher degree of disorder leading to more variability.

It is hypothesized that the amorphous nature of the barrier results in an "effective barrier length" which is smaller than the physically measured barrier. Hence the barrier has thinner regions where the tunneling occurs [149, 197]. As a result, from the data shown in Fig 7.9 it is possible that even though the physical barrier length ranges from 5-22.5 Å, the effective barrier length (from thinner region of the barrier) is similar in all cases resulting in non-exponential differences in resistance across all the modelled junctions. This is consistent with the idea of conduction hot spots in the barrier that were reported in the previous chapter. If the tunneling is dominated by smaller portions of the barrier then the effective length of the barrier is reduced. This is a possible hypothesis to explain the results from the simulations reported here.

Due to the smaller size of the model junctions compared to experimental junctions, it is plausible that the hot spots from the simulation are more pronounced and localised to smaller regions. In addition, the use of periodic boundary conditions in the lateral directions, may amplify any amorphous effects leading to a much smaller effective barrier length/conduction area. Thus the effective barrier length, though still smaller than the physical one, will vary more significantly than what is observed here leading to an exponential increase in resistance.

The idea of an effective barrier length smaller than the physical barrier length has been reported in the literature. Zeng and co-workers directly measured the thickness distribution of state of the art Al/AlO$_x$/Al tunnel junctions using STEM imaging (scanning transmission electron microscopy) [149]. Their results showed that in every junction barrier thickness has a distribution ranging from 1nm to 2nm. From their measurements and tunnel probability calculations they report that less than 10% of the total barrier area is active in the tunneling process. This finding supports the hypothesis that in the model junctions only a small portion of similar size is involved in the tunneling for all the different barrier lengths leading to the trend observed in Fig 7.9. In other words there are similar thickness distributions and tunneling areas for all the different junctions. The goal was then to find evidence that the conduction is concentrated into smaller regions through the barrier.

7.4.1 Analysis of the Electron Density and Transmission Pathways Through the Barrier

In order to explore the idea of thinner regions through the amorphous oxide barrier the electron density was visualised for slices in the XY plane of the amorphous barrier in the transport direction. The advantage of atomistic simulation methods is the structural properties can be visualised on the atomic scale easily. Fig 7.12 is intended to guide the reader as to the direc-

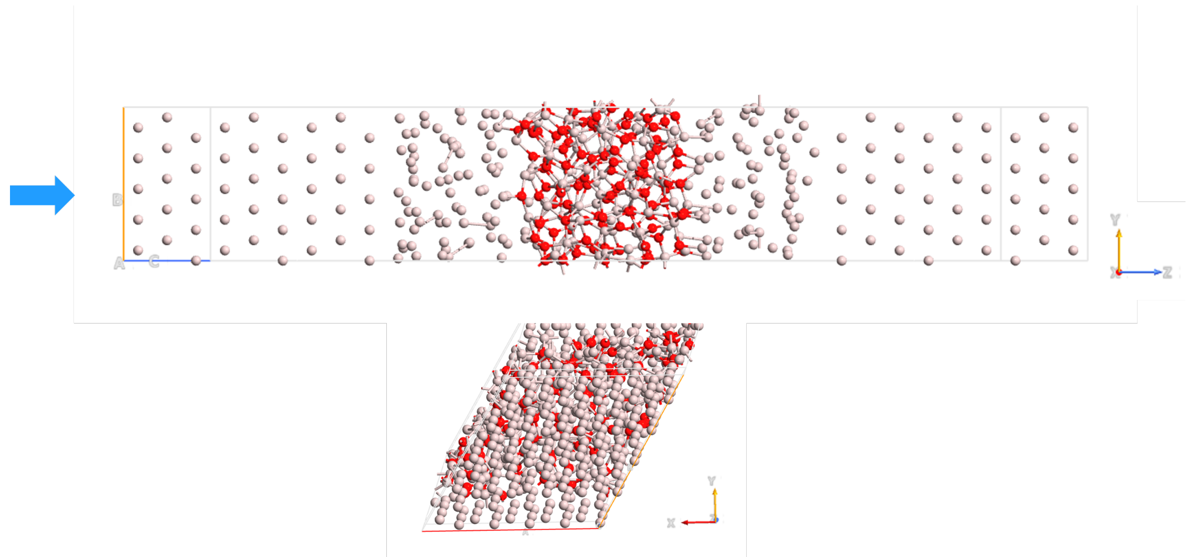

Figure 7.12: A Al/AlO$_x$/Al model studied here with a physical barrier length of 13.5 Å, with the direction of visualization of the XY cut planes clearly indicated (above). XY plane view is shown below.

tion and orientation of the XY plane cuts of electron density that are shown in Fig 7.13. This particular Junction being studied has a measured barrier length of 13.5 Å.

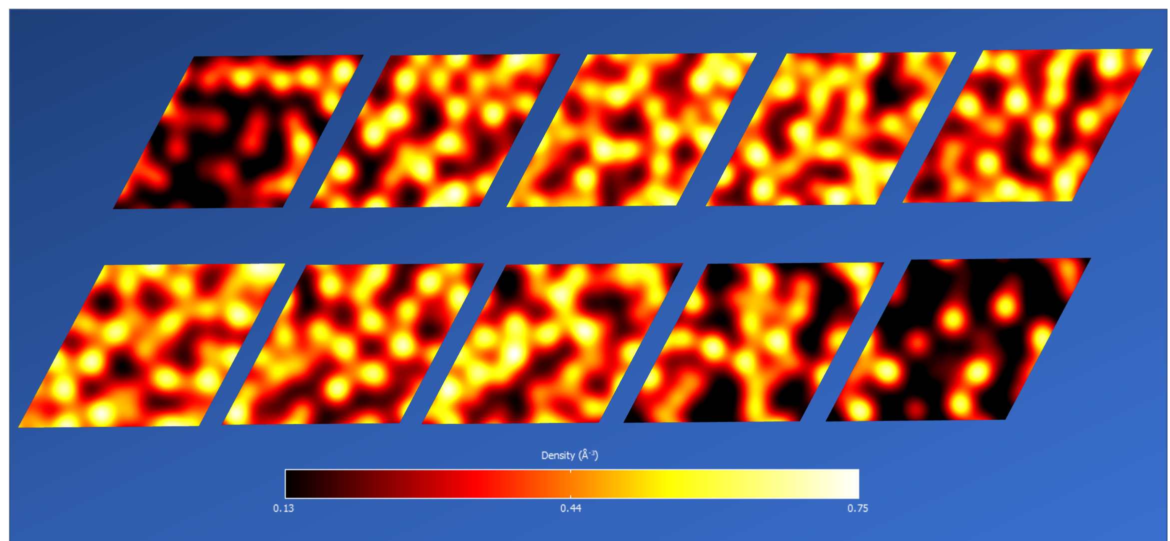

Figure 7.13: Electron density cuts illustrating thinner regions in the barrier. Going across the barrier it is split evenly in 10 segments in the XY plane. Top left is the beginning of the barrier, bottom right is the end of the barrier.

Fig 7.13 plots the electron density distribution in the XY plane for 10 segments evenly distributed across the transport direction for the AlO_x barrier. The high regions of electron density (yellow regions) correspond to areas of high oxygen concentration, whereas the darker regions are areas of low electron density and subsequently thinner regions of the amorphous barrier.

From Fig 7.13 it could be argued that the low regions of electron density are primarily found on the bottom half of the XY cuts. This is in particular more pronounced in the last 4 cuts(bottom right of the figure) as the end of the barrier is reached in the transport direction. As discussed previously, using the DFTB-NEGF method the bond contributions of the electron transmission at different energies of the transmission spectrum can be computed and visualised (the transmission pathways). This allows a qualitative picture for where the transmission is concentrated through the barrier and if it does indeed appear to concentrate in thinner regions of the amorphous barrier. The transmission pathway for the model shown in Figures 7.12 and 7.13 at the Fermi energy is shown in Fig 7.14. Fig 7.16 and 7.17 show the transmission pathways for the two peaks closest to the Fermi energy as shown in the transmission spectra in Fig 7.14. It is clear that the simulation predicts that the electron transport is concentrated at the lower (arbitrary description due to periodic boundary conditions) part of the barrier. All three major transmission peaks show that the transmission is primarily concentrated in this region.

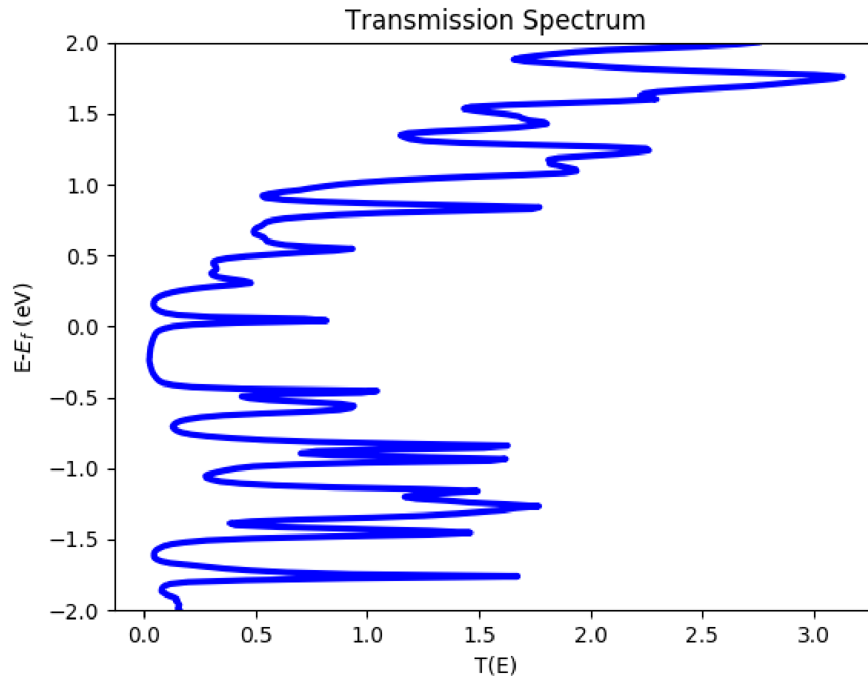

Figure 7.14: Transmission Spectrum for the Al/AlO$_x$/Al model with 13.5Å barrier length.

The pathways are in good qualitative agreement to the electron density plots in Fig 7.13 which suggest the thinner regions of the barrier are located at the "bottom" part of this barrier. Thus, the simulations predict that tunneling is concentrated in thinner portions that result due to the amorphous nature of the barrier. Which in turn leads to an effective barrier length smaller than the physical one (the measured barrier length).

This qualitative evidence here has been shown for one particular Al/AlO$_x$/Al tunnel junction, but indeed similar patterns emerge for all junctions reported in this chapter. A further example is

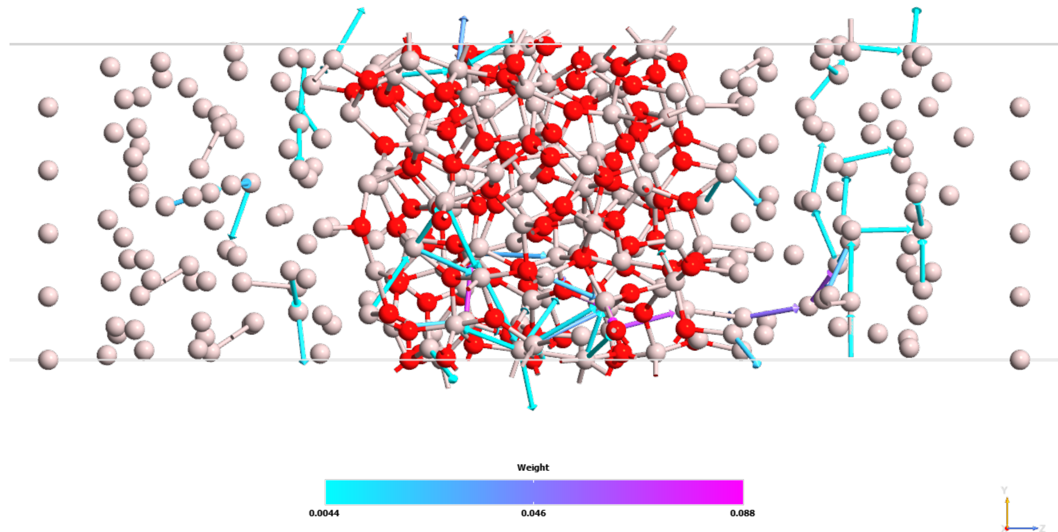

Figure 7.15: Transmission Pathway at Fermi Level for Junction Model with 13.5 Å barrier length.

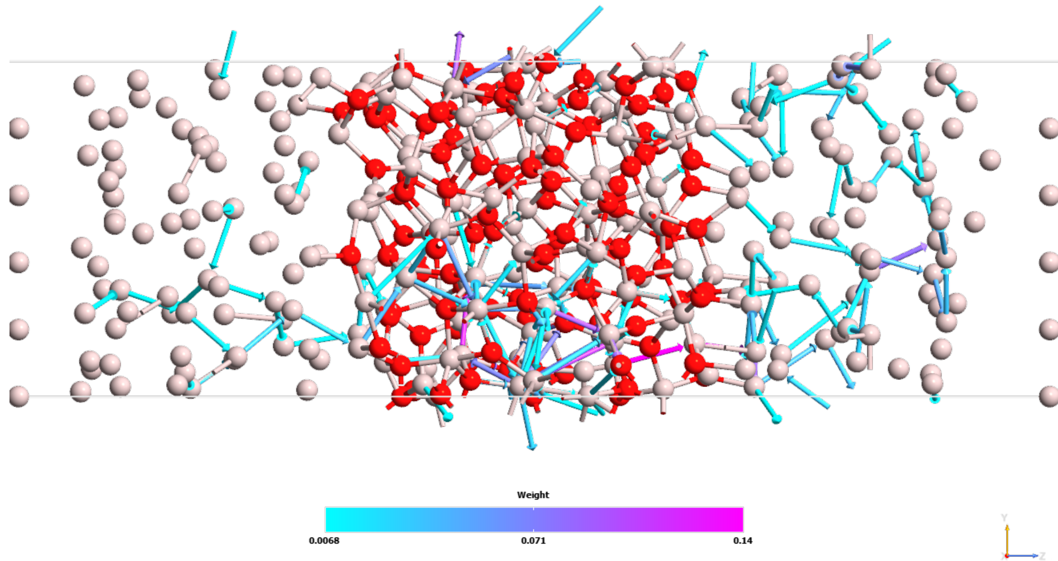

Figure 7.16: Transmission Pathway at 0.2eV above Fermi for Junction Model with 13.5 Å barrier length.

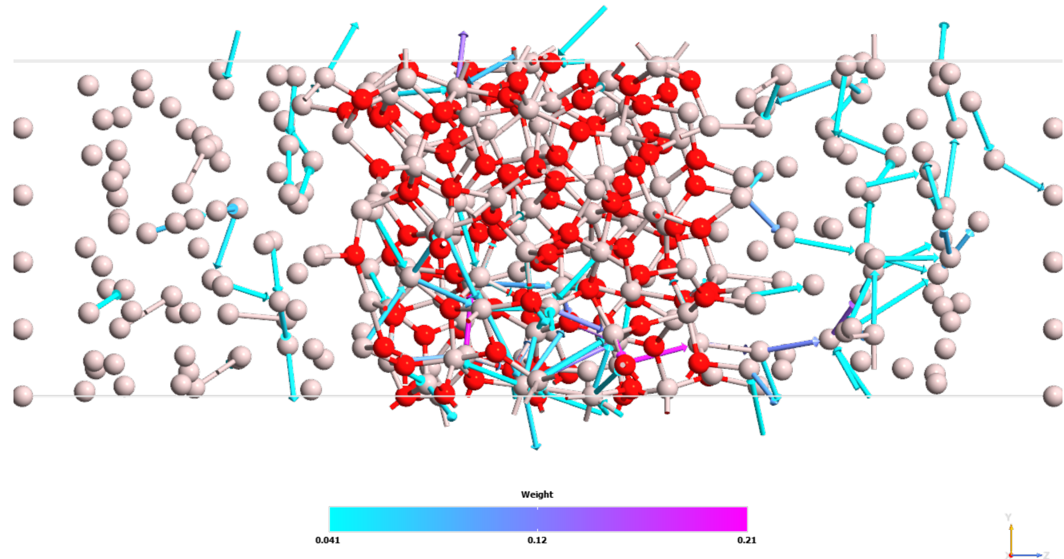

Figure 7.17: Transmission Pathway at 0.31eV above Fermi for Junction Model with 13.5 Å barrier length.

for the tunnel junction with a physical barrier length of 7.6 Å. The electron density is computed and visualised as described for the previous model. The electron density XY cut planes evenly distributed across the barrier is shown in Fig 7.18.

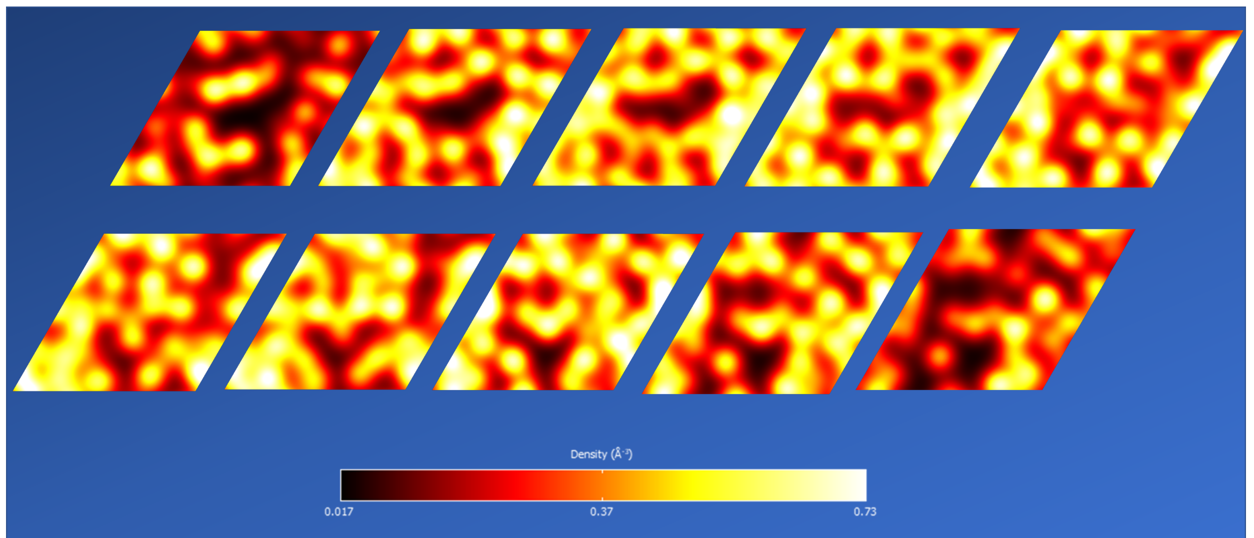

Figure 7.18: Electon Density XY cuts evenly distributed across the 7.6 Å barrier model.

The electron density plots in Fig 7.18 suggest a region of low density near the centre of the barrier, in particular in the first half (in the transport direction) of the barrier (top row in Fig

7.18) as shown by the large gap (dark regions). As the end of the barrier is reached the thinner region moves further down the cut plane. But overall, the thinnest region appears to be through the centre.

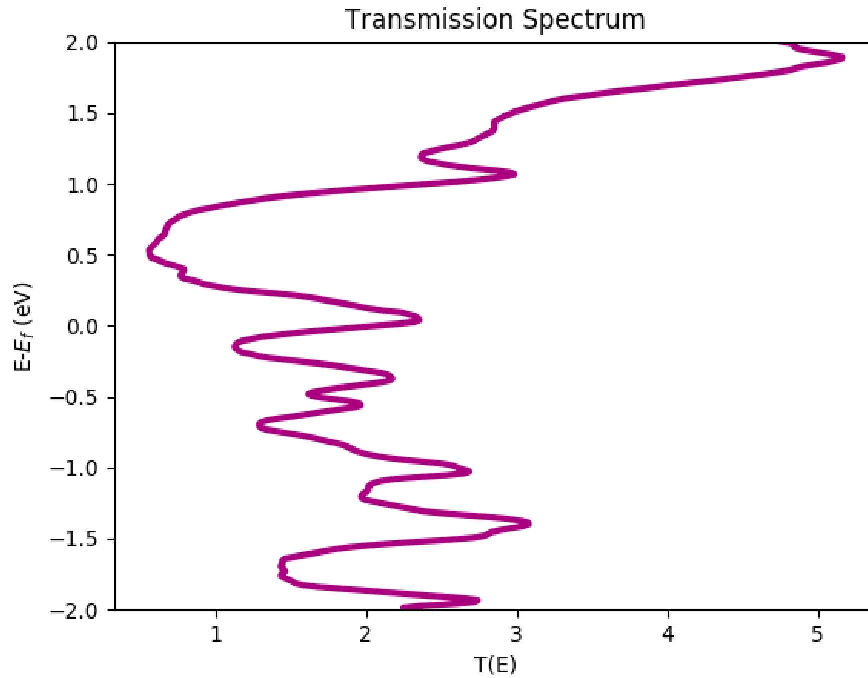

Figure 7.19: Transmission Spectrum for the Al/AlO$_x$/Al model with 13.5 Å barrier length.

The transmission pathways for this barrier were also computed at the Fermi energy and the two closest transmission peaks as predicted by the transmission spectrum in Fig 7.19. The pathways are shown in Fig 7.20, 7.21 and 7.22. It is evident, that the pathways at all three energies are primarily concentrated in the same region of the barrier. This region of transmission concentration is in the same region as the low electron density reported in Fig 7.18. This indicates that this is the thinnest region of this particular barrier and that the tunneling primarily occurs here. Which like with the previous barrier, indicates that in these models there is an effective barrier length smaller than the physical(measured) one. In the interest of brevity, only two model junctions has been presented here, however similar patterns are observed for all model junctions in this chapter.

Even if the data is qualitatively explained by an effective barrier length which is smaller than the physical barrier length of the model junctions studied, the challenge that remains is to quantify this in some way in order to understand the data. In a study by Dorneles et al. [197], J-V (Current Density-Voltage) characteristics of Al/AlOx/Al were fitted to the Simmons equation for electron tunneling to extract the barrier height and length. It was found that the when the area was kept as a constant, the fit of the J-V characteristics to the model was only reasonable. However, they repeated the fit by leaving the Area as a free parameter. They found

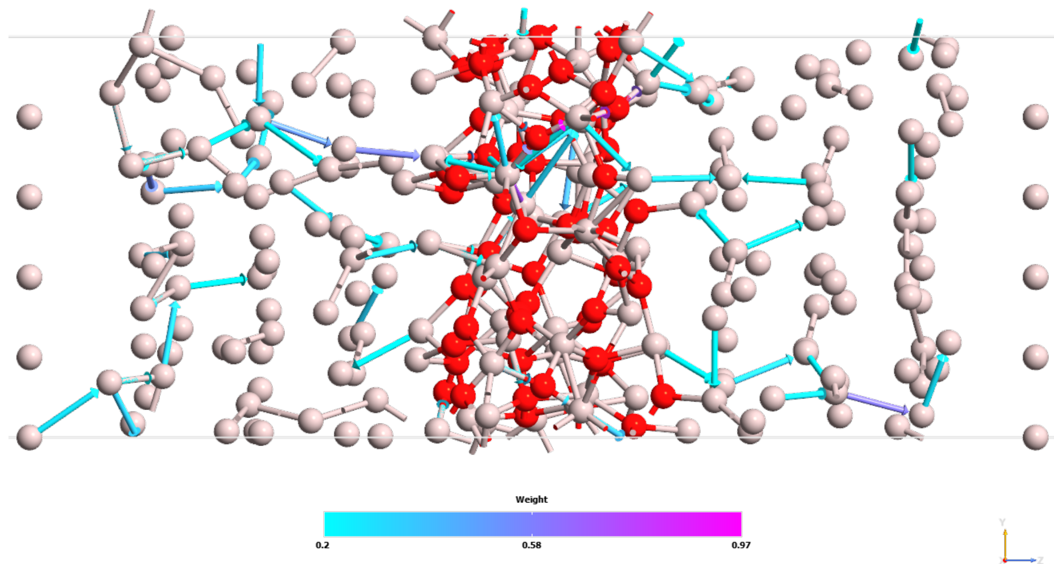

Figure 7.20: Transmission Pathway at Fermi Level for Junction Model with 7.6 Å barrier length.

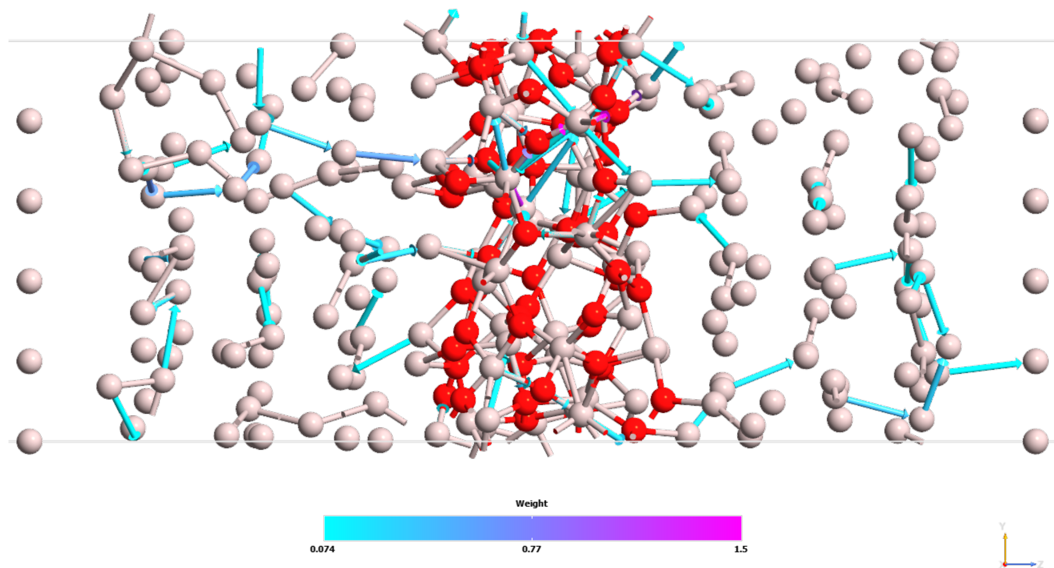

Figure 7.21: Transmission Pathway at 0.04eV above Fermi for Junction Model with 7.6 Å barrier length.

that the effective area was significantly smaller than the physical area suggesting hot spot regions through the barrier.

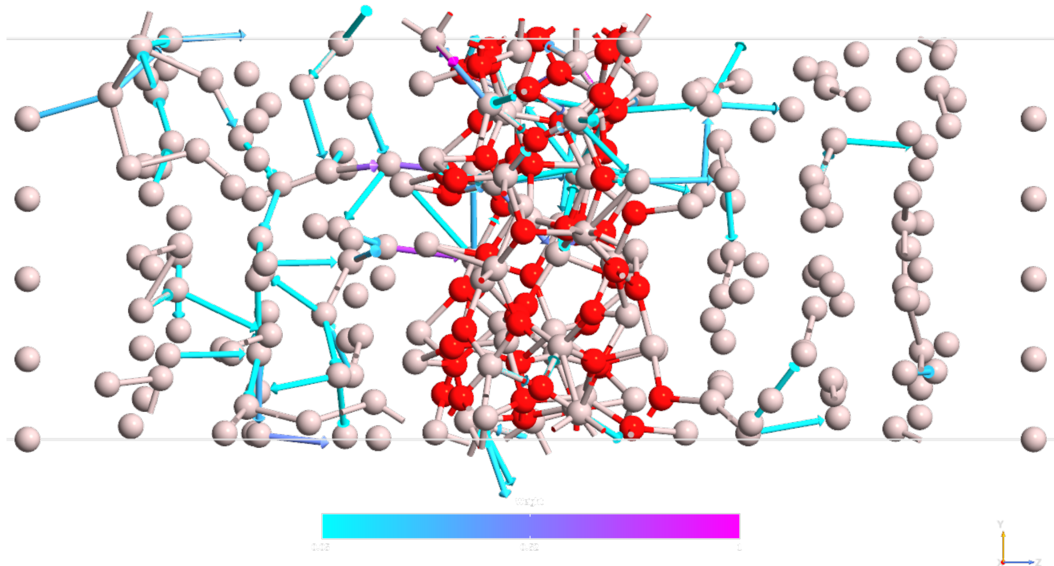

Figure 7.22: Transmission Pathway at 0.37eV below Fermi for Junction Model with 7.6 Å barrier length.

The Simmons model is typically used to fit experimental I-V curves and extract parameters such as the barrier length as part of the typical analysis. Although it is a 1D model it has been successful at describing electron tunneling in junction systems containing a thin insulating barrier, such as the Al/AlO$_x$/Al tunnel barrier. Given the success of this model for estimating junction parameters it begged the question, could the simulated I-V curves from the junction models in this study be fitted to the Simmons model? In doing so the "effective" barrier length and area can potentially be estimated. Even if not "physically correct" in terms of actual number, it could still be a way of quantifying the effective barrier length of the model systems in this work and predict how much smaller it is compared to the physically measured length and area. In the next section, the Simmons model will be introduced and discussed.

7.4.2 The Simmons model for The Electron Tunnel effect.

In 1963 and 1964, John G Simmons published three papers which derived a generalized formula for electron tunneling between two electrodes separated by a thin insulating film [3, 199, 200]. Although a relatively simple 1D model with several underlying assumptions it has been very successful at explaining several experiments. Fitting experimental data to this model allows for the extraction of parameters for a wide range of junction structures including Josephson junctions, magnetic tunnel Junctions and even molecular junctions [201–203].

The model as derived by Simmons deals with a general case of a thin insulating barrier be-

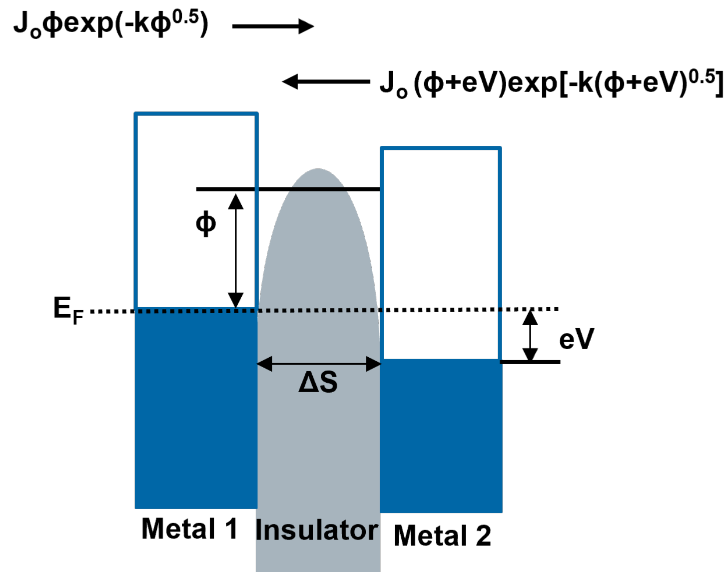

Figure 7.23: Pictorial representation of a general case of a thin insulating barrier between two electrodes as described by Simmons [3].

tween two electrodes as shown by Fig 7.23. The starting point for the derivation of the model is the probability of an electron penetrating a potential barrier of height $V(x) which is given by the WKB approx$

$$D(E_x) = exp[-\frac{4\pi}{h}\int_{s_1}^{s_2}[2m(V(x)-E_x)]^{\frac{1}{2}}dx] \tag{7.2}$$

The full derivation is avoided here as it is not necessary for understanding the model and its applications. Interested readers are directed to Simmons' papers for the full derivation. The derived generalized formula for current density through a thin insulating barrier is given by:

$$J = \frac{e}{2\pi h(\beta\Delta s)^2}\{\varphi e^{-A\varphi^{\frac{1}{2}}} - (\varphi+eV)e^{-A(\varphi+eV)^{\frac{1}{2}}}\} \tag{7.3}$$

and

$$A = \frac{4\pi\beta\Delta s}{h^3}(2m)^{\frac{1}{2}} \tag{7.4}$$

Where J is the current density, h is Planck's constant, β is a correction parameter (usually ≈ 1),Δs is the barrier length, φ is the mean barrier height, m is effective mass and V is voltage.

This equation is general and can be applied to any shape of potential barrier if the barrier height is known. Alternatively, the barrier height can be determined from the IV-Characteristics. The generalized model is based on the underlying assumptions that the potential in the barrier is spatially averaged and varies linearly with both space and applied bias. Both of these assumptions are questionable and may only apply under a range of conditions. However, the Simmons model continues to be used due to its simplicity and success at estimating parameters.

The original model was expanded by Simmons to include image forces to better match ex-

periments, the model was also improved to include temperature dependence and thermal effects. In addition, Brinkman, Dynes and Rowell revised the model in 1970 to describe junctions with asymmetrical fermi functions in the electrodes, i.e different electrodes [196]. Therefore supplying a considerable toolkit for analysing metal-insulator-metal systems. In the work presented here, the simulations (aside from broadening effects) are done at 0K temperature and thus thermal effects can be ignored, in the Al/AlO$_x$/Al tunnel junction, asymmetry is also not a concern. This simplifies the analysis for quantifying an effective barrier length.

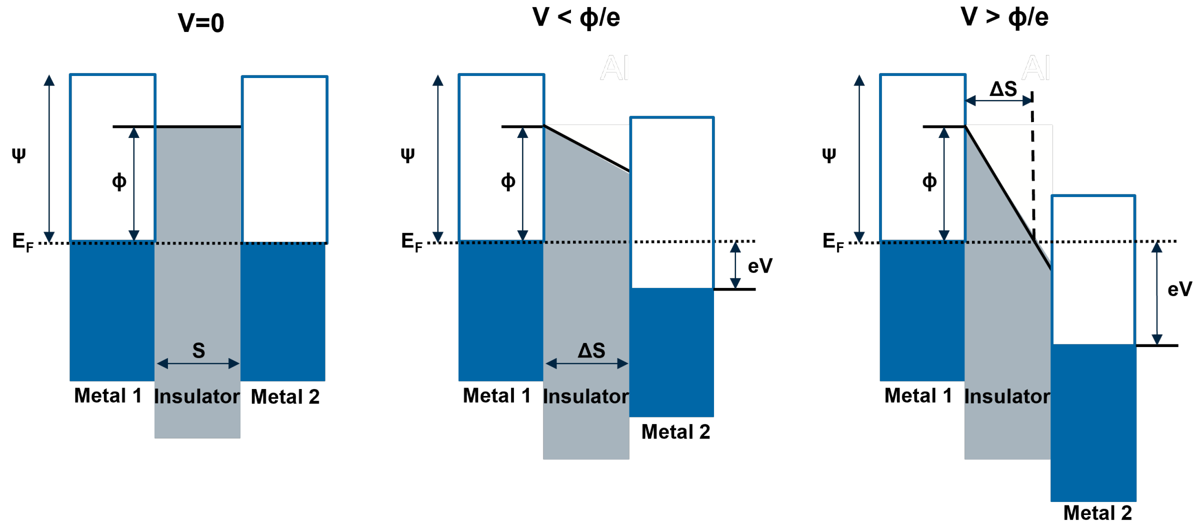

Figure 7.24: Diagrams for the rectangular barrier model under different bias conditions.

In addition to the generalized barrier, Simmons presents a rectangular barrier model. This model is presented pictorially in Fig 7.24. Although an idealized and crude approximation it has been remarkably successful at describing the physics of electron tunneling through a thin insulating barrier. Adjusted for a rectangular barrier and the case where $0<V<\varphi$, the current density is given by:

$$J = (\frac{6.2x10^{10}}{s^2})\{(\varphi - \frac{V}{2})e^{-1.025s(\varphi-\frac{V}{2})^{\frac{1}{2}}} - (\varphi + \frac{V}{2})e^{-1.025s(\varphi+\frac{V}{2})^{\frac{1}{2}}}\} \tag{7.5}$$

where for numerical convenience J is in A/cm^2, φ is in V and s is in Å.

Typically measured J-V characteristics are fit to this equation, the generalized above, the thermal equation in [199] or the Brinkman et al. version. For the fitting procedure, the barrier height and length (φ ΔS) are left as free parameters and estimated from the curve fitting. As discussed previously, Dorneles et al. showed a better fit if the junction area is not kept as a constant parameter and is in fact also left as a free parameter to describe the effective area of conduction which has been shown to be smaller than actual area. In addition, the junctions in this study are dealt with periodic boundary conditions in the cross-section to inflate the size of the junction. Therefore, it is more appropriate to leave the area as a free fitting parameter.

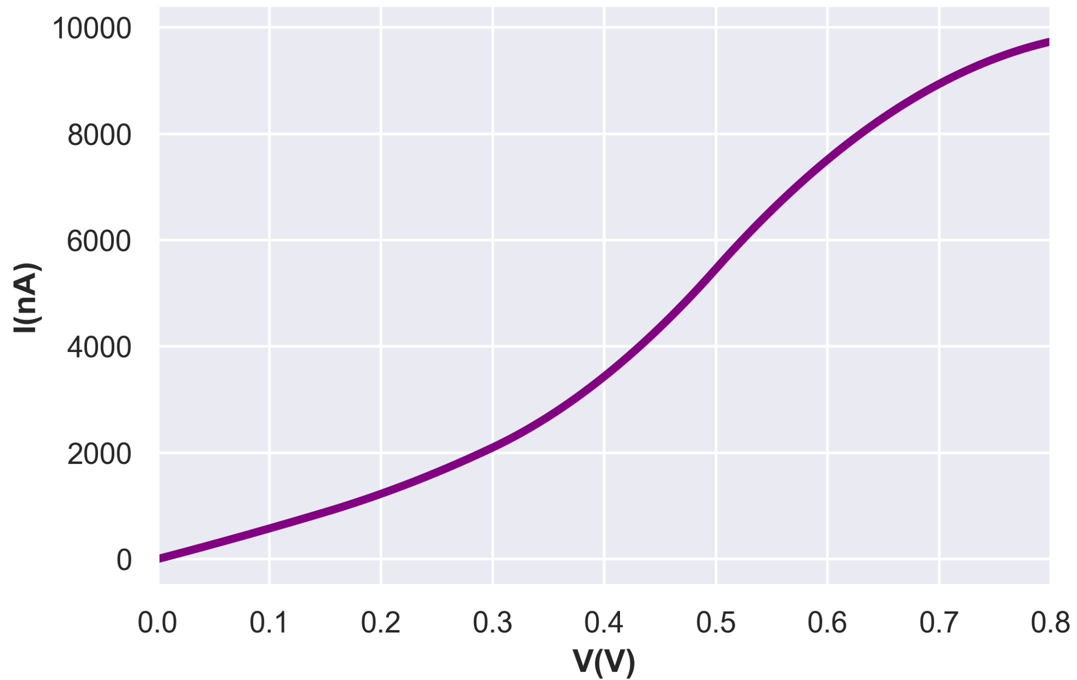

Figure 7.25: Typical computed IV curve for one of the model junctions studied in this work. This example is for a Junction with a 10.7 Å barrier length.

7.4.3 Fitting to the Simmons model

In order to use the Simmons model to quantify the effective barrier length of the model junctions, it is necessary to calculate the Current-Voltage characteristics for all the junctions in the data set. Although computationally expensive, it is very useful as it also verifies that the computed resistance data from the zero bias transmission spectra is accurate and validates the method for comparing junction resistances.

A typical IV-Curve for a Al/AlO$_{1.1}$/Al device in this data set is shown in Fig 7.25. In JJ devices the IV curves tend to be linear at low bias and show a similar shape to that in Fig 7.25, this non-linearity is typical in the higher bias range. Not all junctions in this data set have such non-linearity some show a more linear IV-curve, nonetheless the DFTB-NEGF method qualitatively reproduces the IV-Curves of the Al/AlO$_{1.1}$/Al junction. The computed IV curves correlate exactly with the Resistance-barrier length data reported in Fig 7.9, with junctions with the highest resistance showing the lowest I-V curves. Validating the normal state resistance calculations at zero bias.

All the IV Curves in the data set were fit to the Generalized and Rectangular Simmons model, leaving Area (A_{eff}), barrier length (Δs) and barrier height (φ) as free parameters. In general, a reasonable fit was achieved with the generalized model, with some IV curves showing a poor fit. All IV-Curves showed good fit with the rectangular model with R-Squared values larger than

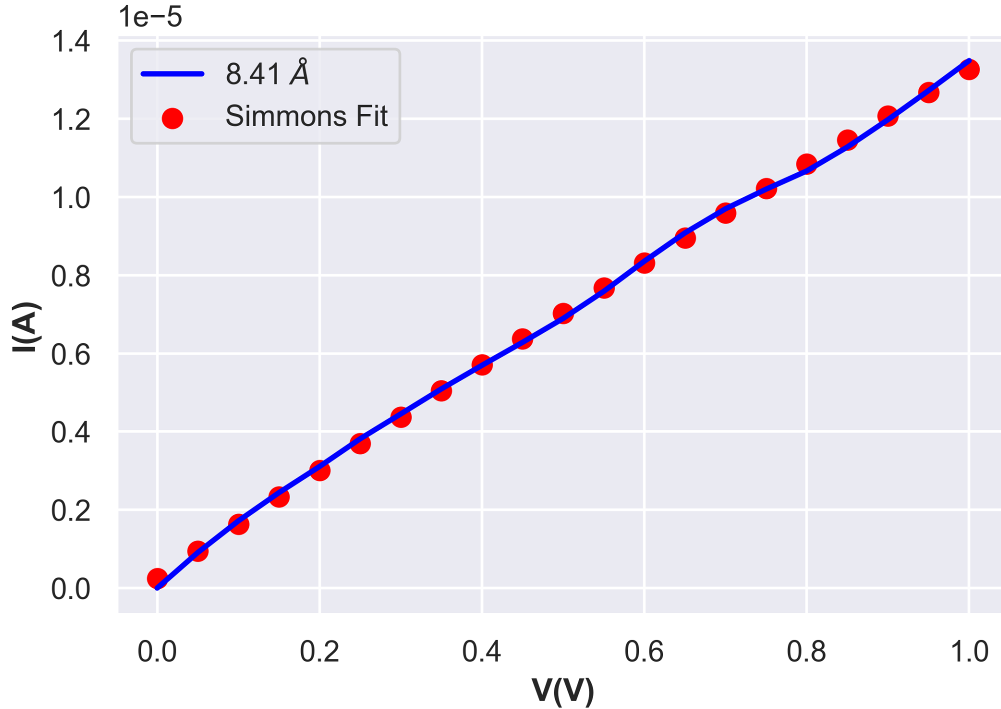

Figure 7.26: Simmons Fit IV Curve for a barrier with 8.41 Åphysical barrier length fitted to the Rectangular Simmons model.

0.90 in all cases. An example of an IV-Curve fit to the rectangular model is shown in Fig 7.26. The IV curve is linear and shows an excellent fit to the rectangular Simmons model. For the rest of the chapter, any discussion of Simmons fit refers to the rectangular model as this showed the best fit across all curves in this work.

One of the key parameters extracted from the model is the potential barrier height (φ). The fitted height is reported in the literature to lie in the range of 0.8-3 eV [204–210]. Though given different contact materials, such as copper, cobalt, gallium are used its difficult to compare between studies [211–213]. A barrier height of 2eV is considered typical. However, given the wide range found, a barrier height within the range of 0.8-3 eV is considered acceptable and suggests that the IV curves in this data set are characteristic of Al/AlOx/Al tunnel junctions. The barrier height is used to benchmark the models in this study and determine whether the models are representative.

The barrier height describes a one dimensional potential that implicitly includes effects from the dielectric constant, band gap, amorphousness and other material properties of the barrier. Table 7.3 lists the extracted barrier heights for the fitted models denoted by their measured physical barrier length. Although the qualitative fit between the Simmons model and the calculated IV curve is good, the values for some of the extracted barrier heights are unexpected. Twelve of the barriers have an extracted barrier height of 2.8-2.93 eV, within the 0.75-3 eV range reported in the literature. These barriers cover a range of resistances from 13-113 kΩ. Six of the

Physical barrier length (Å)	barrier height (eV)
5.05	2.89
6.37	0.5
7.2	8.56
7.6	2.86
8.41	2.85
9.13	2.83
9.38	2.83
10.7	2.80
11.5	0.5
12	5.86
13	2.83
13.5	2.87
16.6	2.85
16.8	2.84
18.3	0.5
18.4	0.5
19.4	9.18
21.8	0.5
22.2	0.5

Table 7.3: Fitted barrier heights (eV) for the model junctions in this study given by their physical barrier lengths.

barriers have an extracted barrier height lower than the range of around 0.5eV, these primarily correspond to the barriers with highest resistances (114-609 kΩ) but also with a resistance of only 39 kΩ. Although significantly smaller than the 0.75eV, it may still be a reasonable value caused by anomalies in the barrier models producing non typical IV-curves. Finally, there are three extracted values that are far higher than 3eV and these barriers are not considered to be representative of typical Al/AlO$_x$/Al barriers (with barrier heights of 5.86, 8.56, 9.18 eV).

In addition to the barrier height, fitting the IV curves to the Simmons model allowed the extraction of the barrier length and the effective conduction area of the model devices. Fig 7.27 shows the RA vs Length for all the junctions, where the area(A) is taken from the Simmons fit as is the Length. The plot shows two clusters of data points which correspond to the models with a barrier height of 2.8-2.93 eV showing unphysical lengths very close to 0, whilst the barriers of height 0.5 eV show larger, but still small lengths of ≈ 1 Å.

In general, the extracted lengths for the barriers in the range of 2.8-2.93 Å are unphysically small, indicating essentially no barrier present, with more variation in the effective area. The figure does suggest an exponential increase in RA with increased length, however it is difficult to discern as the extracted lengths range in 0.0002-0.003 Åand several at ≈ 1 Å. However, on closer inspection to the junctions with barrier height 2.8-2.9 eV, although clearly nonphysical barrier length, the RA does appear to increase exponentially with increasing lengths as shown in Fig 7.28.

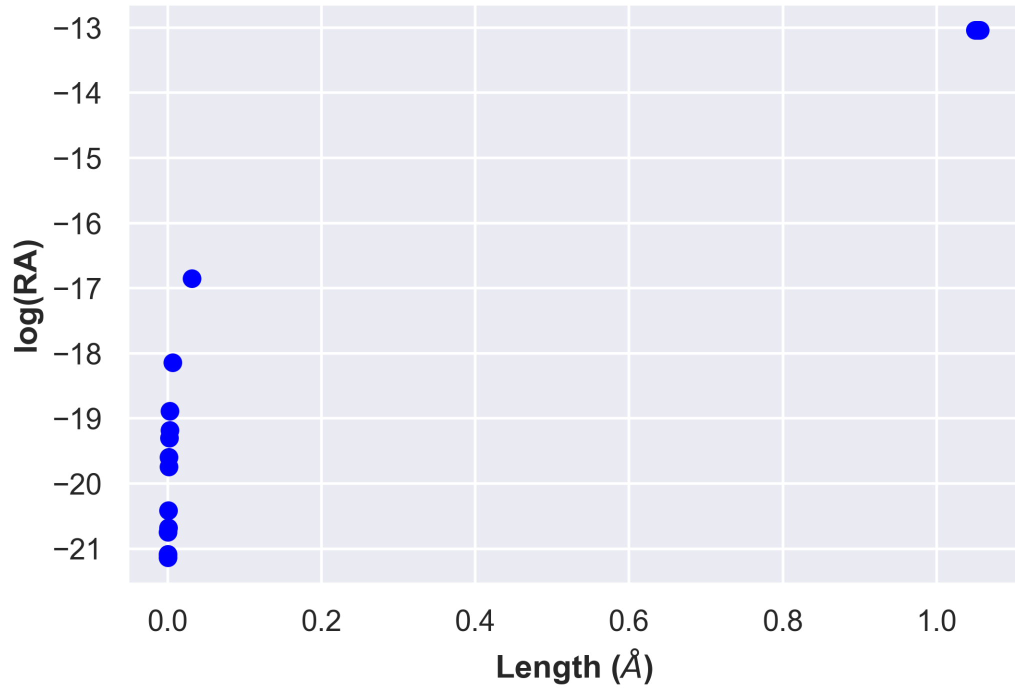

Figure 7.27: Plot of log(RA) vs Length for Resistance and Area values extracted from Simmons model fitting.

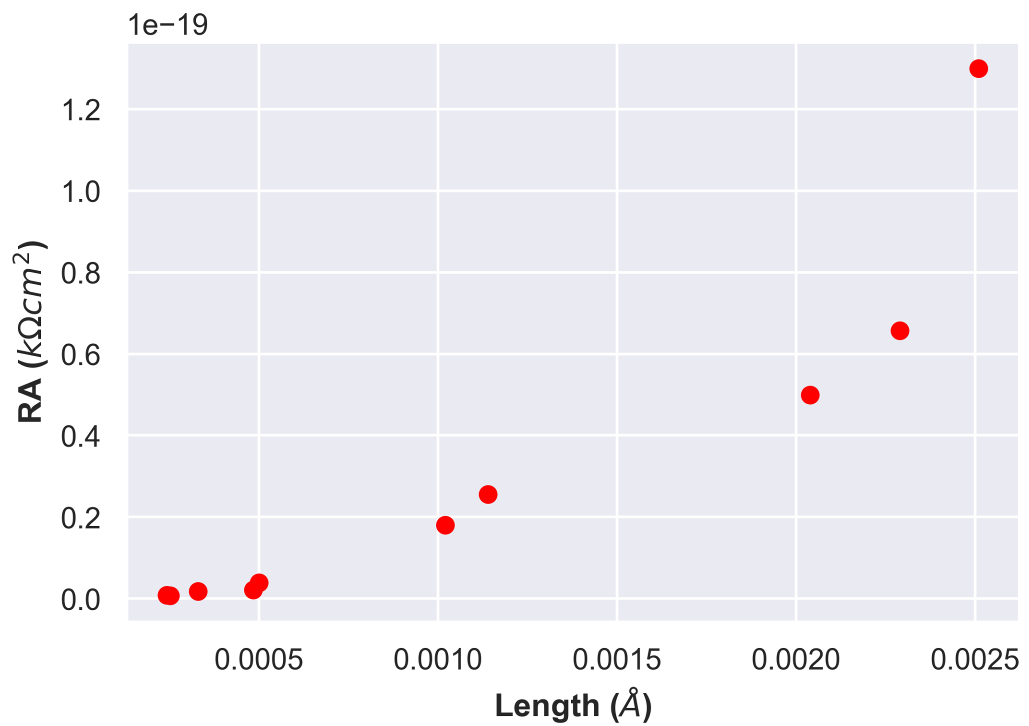

Figure 7.28: Plot of RA vs Length for model Junctions with barrier height 2.8-2.93 eV.

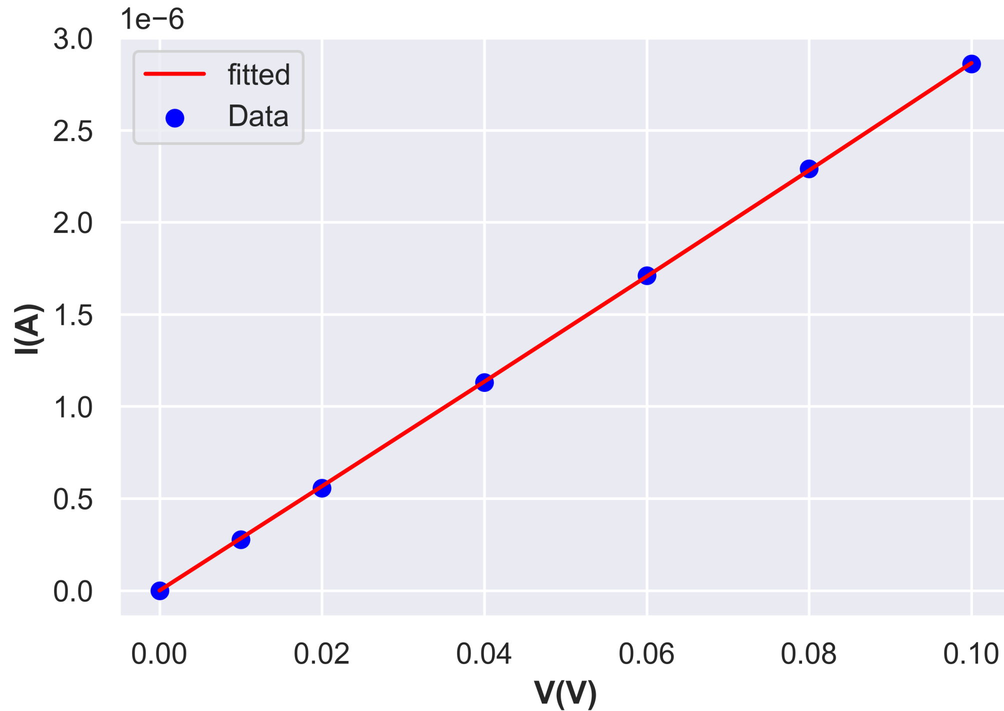

Figure 7.29: Fitting of IV Curve from small voltage range to Simmons model.

In Simmons' original paper, the derived model is reported to be suitable for voltages below the barrier height. Thus the data from extracted barrier heights of 0.5eV is problematic, not to mention the uncharacteristically small barrier lengths. In the previous chapter it was reasoned that the current in our models is overestimated, resistance underestimated, leading to critical current densities higher than expected. This is mainly attributed to the size of the model junctions and the lack of discernible defects. This could partially explain the extremely small barrier lengths extracted from the Simmons fit. However, the Simmons model is known to be problematic at higher applied biases and is typically only deemed applicable for small voltages, far lower than the barrier height (typically in the millivolt range). Moreover the fit is dependant on the non-linearity of the IV characteristics of the junction and sensitive to the fitting range which can impact the results significantly.

Given the model size of the junctions and also this sensitivity to fittings range, fitting the IV curves for the bias range of 0-100 mV is a more sensible guide to exploring the barrier length of the junctions in this study. Hence, the IV curves were re-calculated within this range for all junction models and were fitted to the Simmons model as described above. At this low bias all junctions show the typical linear form as expected in Josephson junctions. An example of the low bias IV Curve fitting is shown in Fig 7.29.

Table 7.4 reports the extracted barrier height for the junctions after re-fitting under an applied bias of 0-100mV. Although the majority of junctions still have a barrier height of $\approx$ 2.9eV as before, there has been a change in all extracted barrier lengths. This highlights the sensitivity

Physical Barrier Length (Å)	Barrier Height (eV)
5.05	0.05
6.37	2.91
7.2	0.05
7.6	0.55
8.41	2.92
9.13	2.92
9.38	0.84
10.7	0.86
11.5	2.91
12	0.89
13	2.90
13.5	2.92
16.6	2.91
16.8	0.88
18.3	2.91
18.4	2.91
19.4	2.92
21.8	0.05
22.2	0.05

Table 7.4: Fitted barrier heights (eV) for the model junctions in this study given by their physical barrier lengths.

of the fitting range on the extracted parameters. In addition, the extracted barrier lengths and effective areas have all increased significantly after re-fitting, as will be shown later in the chapter. Hence, the model is shown to be sensitive to the fitting range and its validity has to be carefully considered.

Compared to the previous fit, there are no uncharacteristically high (larger than 3eV) barrier heights found in the data set. However, there are four Junctions with an extracted barrier height of 0.05eV which clearly lies outwith the expected range. These are considered to not be representative junctions and thus are excluded from the analysis of barrier length. There are 5 models which have barrier heights in the region of 0.5-0.9 eV whilst the rest are closer to 2.9 eV. Moreover, the extracted barrier height is independent of the physical barrier length or calculated resistance of the junction models. The non-linearity of the computed IV Curves varies considerably for the bias 0-1V, hence the differences in extracted barrier height when fitted at lower bias, for which all IV curves are linear. In general, the re-fitting at low values improved the extracted barrier height with more models lying within the range of 0.5-3eV. However, the results do show the sensitivity of the range at which the IV curves are fit to the model, with the model only valid at small bias range focusing on the linear region. This is also the region at which the resistance is estimated and thus the best fitting procedure.

The extracted barrier lengths range from 0.02-2.12 Å, this is a two orders of magnitude increase in the extracted length compared to the full bias fitting, further validation of the lower

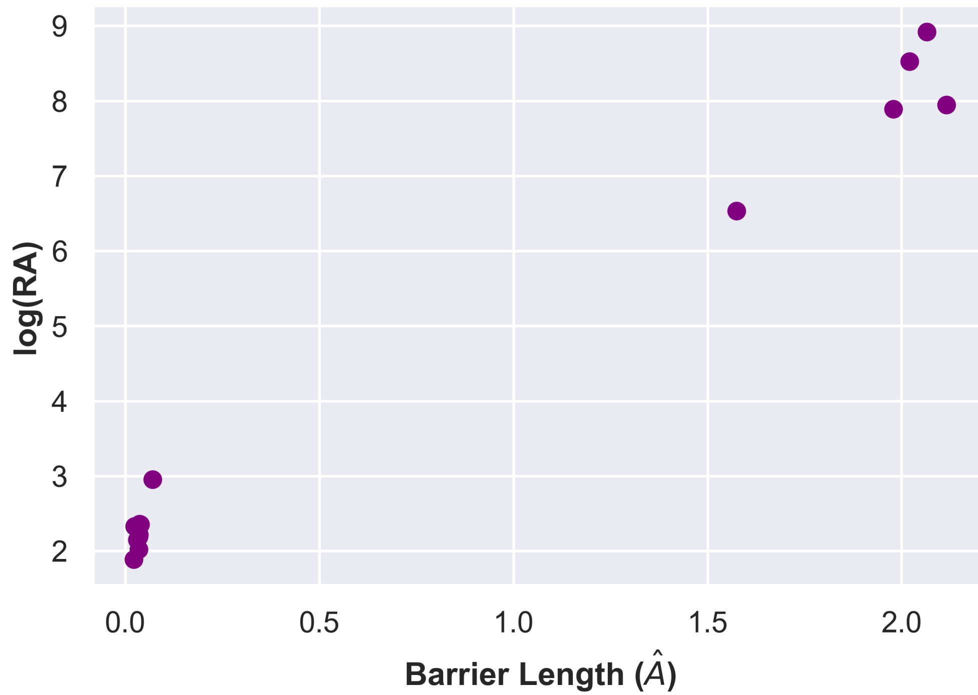

Figure 7.30: Computed RA vs barrier length, using the extracted values for area and length from the small voltage Simmons fit.

bias fit. However, the extracted lengths are still significantly smaller than what is physically expected. The extracted area values are even smaller than expected for the barrier heights $\approx$ 2.90 eV, whereas for the barrier heights $\approx$ 0.5-0.9eV the lengths, though still small, are not completely unreasonable, whilst the extracted areas are bigger than expected. Given the smaller barrier height it would be expected that the effective conduction area be significantly bigger than for the larger barrier heights. To investigate the effective barrier length and conduction area, the extracted area value was multiplied with the computed resistance reported above, to give an effective RA for the junctions. This is plotted (in log scale for RA) against the extracted length values from the Simmons model in Fig 7.30 to explore the relationship between resistance and barrier length.

From Fig 7.30 it is clear that there are two clusters of data points pertaining to the junctions. The data points close to 0 Å are for all the junctions with barrier height $\approx$ 2.9eV, with barrier lengths of 0.02-0.07 Å. The other cluster of data points lie between 1.5-2.2 Å and are the five junctions with barrier heights ranging from $\approx$ 0.5-0.9 eV. From the figure, an exponential relationship between RA and barrier length is observed even for such small range. The difference between RA at 0.02 Åand 1.6 is four orders of magnitude. While care must be taken in analysing across the data given the barrier height changes, as the change in RA will be influenced by the different barrier height, but even within the clusters of data with same barrier height show exponential increase in RA with increasing barrier length, for example 0.03 to 0.07 Å shows an order of magnitude increase, as does the difference between 1.6 and 2 Å. Further investigation

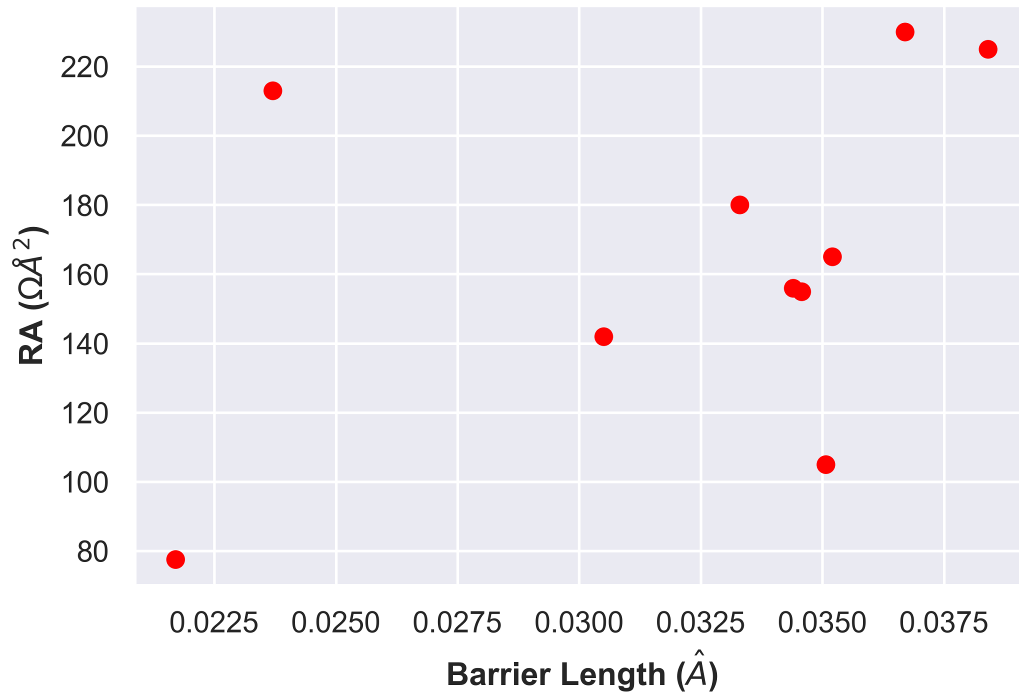

Figure 7.31: Computed RA_{eff} vs barrier length for the Junctions with barrier height $\approx$ 2.9 eV.

of the influence of changing barrier height on the resistance of the junction would be required. There is nothing to suggest that the potential barrier height does not change with changing barrier length. So although analysing the extracted length vs RA can lead to valid conclusions, more research is need to further understand the relationship between barrier height and barrier length. From the extracted parameters, an exponential relationship between effective barrier length and RA is confirmed, despite the small lengths.

Due to the the two sets of barrier heights, it is useful to also explore the data separately. The RA_{eff} vs barrier length extracted for the junctions with barrier heights $\approx$ 2.9 eV is shown in Fig 7.31. The data point at length 0.07Å is excluded to facilitate the analysis as this has a considerably higher RA. RA is typically expressed in units of Ωcm^2, however for numerical convenience given the smaller values, here it is reported as Ω Å^2 . The data is scattered with RA values ranging from 77.6 to 224 Ω Å^2 for lengths of 0.02 to 0.038 Å. Fitting to the Simmons model has not improved the scattered nature of these data points. However, it can help explain the data. To explain scattered R vs physical length data in Fig 7.9 it is hypothesized that the physical barrier length is not in fact the effective barrier length and in actuality the effective barrier length for most of the junctions is the same or very close in value hence no exponential change in resistance. From the extracted fit for the junctions in Fig 7.31, the length is predicted to be unphysically small, nonetheless, for all these junctions it is predicted to be in the range of 0.02-0.04 Åwith very small changes in length in the range of 0.001Å. In other words the model predicts essentially the same length for all junctions.

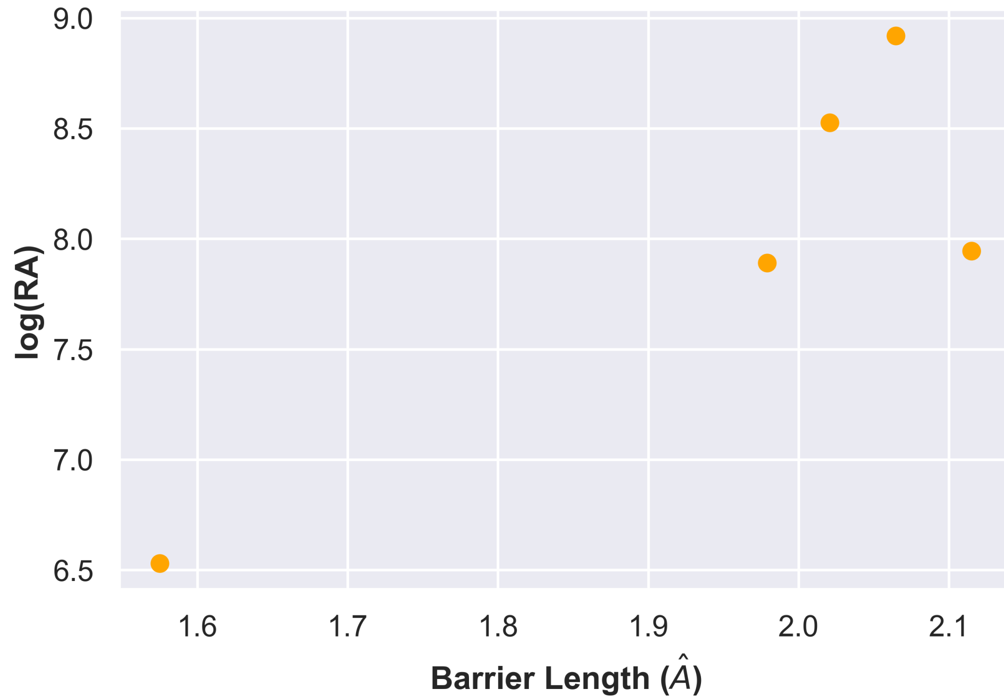

Figure 7.32: logRA vs barrier length for Junctions with barrier heights ranging between 0.5-0.9eV.

Although, the RA varies (hence the scattered nature of the plot), the RA value is sensitive to small changes in the area as well as inherent variability in the computation of resistance due to the amorphous nature of the barrier. Therefore, the Simmons fit overall suggests despite the ranging physical barrier lengths all junctions have similar effective barrier lengths much smaller than the measure length, due to thinner regions in the amorphous barrier. Whilst the Simmons fit fails to predict reasonable values for length, for reasons that will be discussed later in the thesis, it usefully extracts reasonable barrier heights due to the shape of the computed IV curves and also predicts similar lengths/areas for all barriers which provides evidence of an effective length and helps explain the original simulation data.

The RA (in log scale) against extracted barrier length for the Junctions with barrier heights ranging 0.55-0.9eV is shown in Fig 7.32. For the junctions in this set, the barrier lengths are significantly higher at 1.5-2.2 Å. Nonetheless, the values are still smaller than expected, the fit predicts barrier lengths close to the length of an Al-O bond. The extracted area parameters also range of 2.6-37 nm^2 which are closer to physical areas, however an overestimation given the small simulation cell size (despite the inflation through periodic boundary conditions). It is possible that the smaller barrier height of these junctions lead to larger conduction and thus the extracted area is much bigger than expected. Though a small number of data points, the RA values change exponentially with increasing length best demonstrated by the difference between the point at 1.57 Å and 1.98 Å showing more than order of magnitude difference. As before there is still some variability inherent in the values (e.g the point at 2.11 Å). Notwithstanding, the

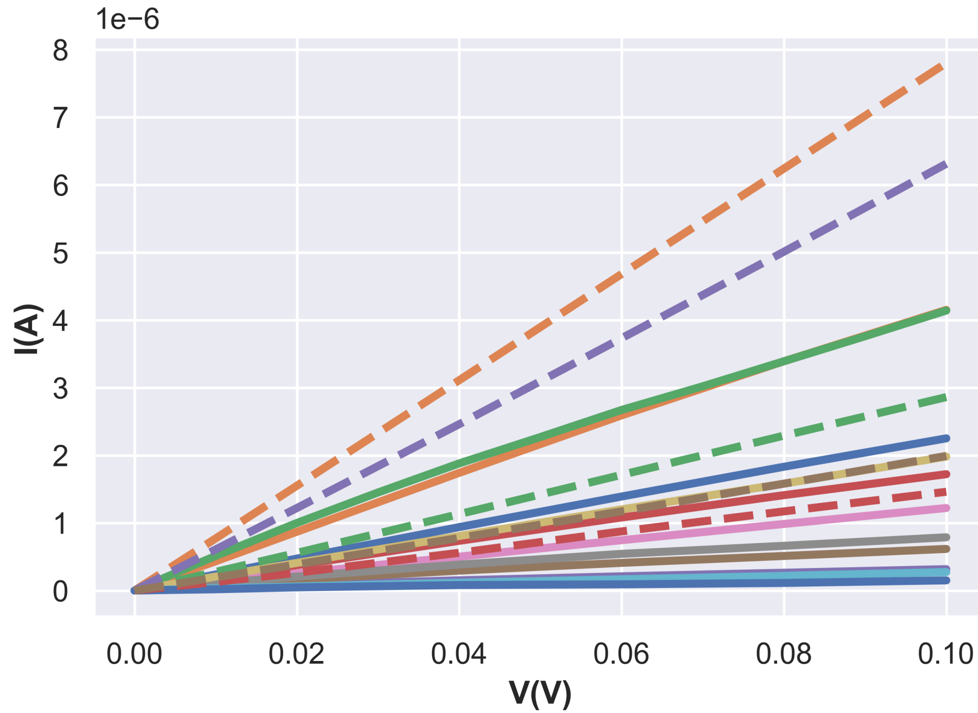

Figure 7.33: IV Curves for voltages 0-100mV for all the junctions in this study. The dashed lines correspond to the junctions with barrier heights of 0.5-0.9eV.

exponential relationship is more clear. there is also a consistent picture being built as discussed previously, which helps explain the scattered R (resistance) vs Physical Length data. Fitting to the Simmons model for these five points also suggests barrier lengths very similar in size with 4 junctions varying 1.9-2.1 Å despite considerably different measured physical lengths. This gives a consistent possible explanation for the lack of exponential relationship in the resistance vs length data from the DFTB-NEGF simulations being due to effective barrier lengths of very similar size across junctions (of similar barrier heights). The larger difference in RA in this set (compared to the barrier height $\approx$ 2.9eV) is also due to the sensitivity of Area on the computation in RA. In this set, the area varies more significantly between junctions thus a wider variation of RA even at similar length values.

For further analysis of the extracted parameters and resulting two clusters of barrier height data, it is useful to analyse the small voltage IV curves. As reported previously in the chapter, the IV curves for all the junctions, at full bias and small bias regime, follow the expected order of the computed resistance, with highest current for lowest resistance as expected. Fig 7.33 shows the IV Characteristics under an applied bias range of 0-100 mV for all the junctions reported in Fig 7.30. The 'dashed lines' correspond to the computed current-voltage data for the junctions with barrier height of 0.5-0.9 eV. As expected the junction with the smallest barrier height 0.55 eV has the highest current at 0.1V. Whilst, the lower barrier height curves are higher currents in the range of 0-0.1V than most, they don't have higher currents than all. This is due to the

IV curves being influenced by multiple parameters and not just barrier height. In addition, the sensitivity to fitting range can lead to noise and variability in the extracted parameters. The IV Curves show that for the majority of the model junctions the predicted current is in a very similar range (0-3 μA).This is a further indication that despite different physical lengths in the models, the electrical response points to the fact that they all have similar barrier length/conduction areas as predicted by the fittings.

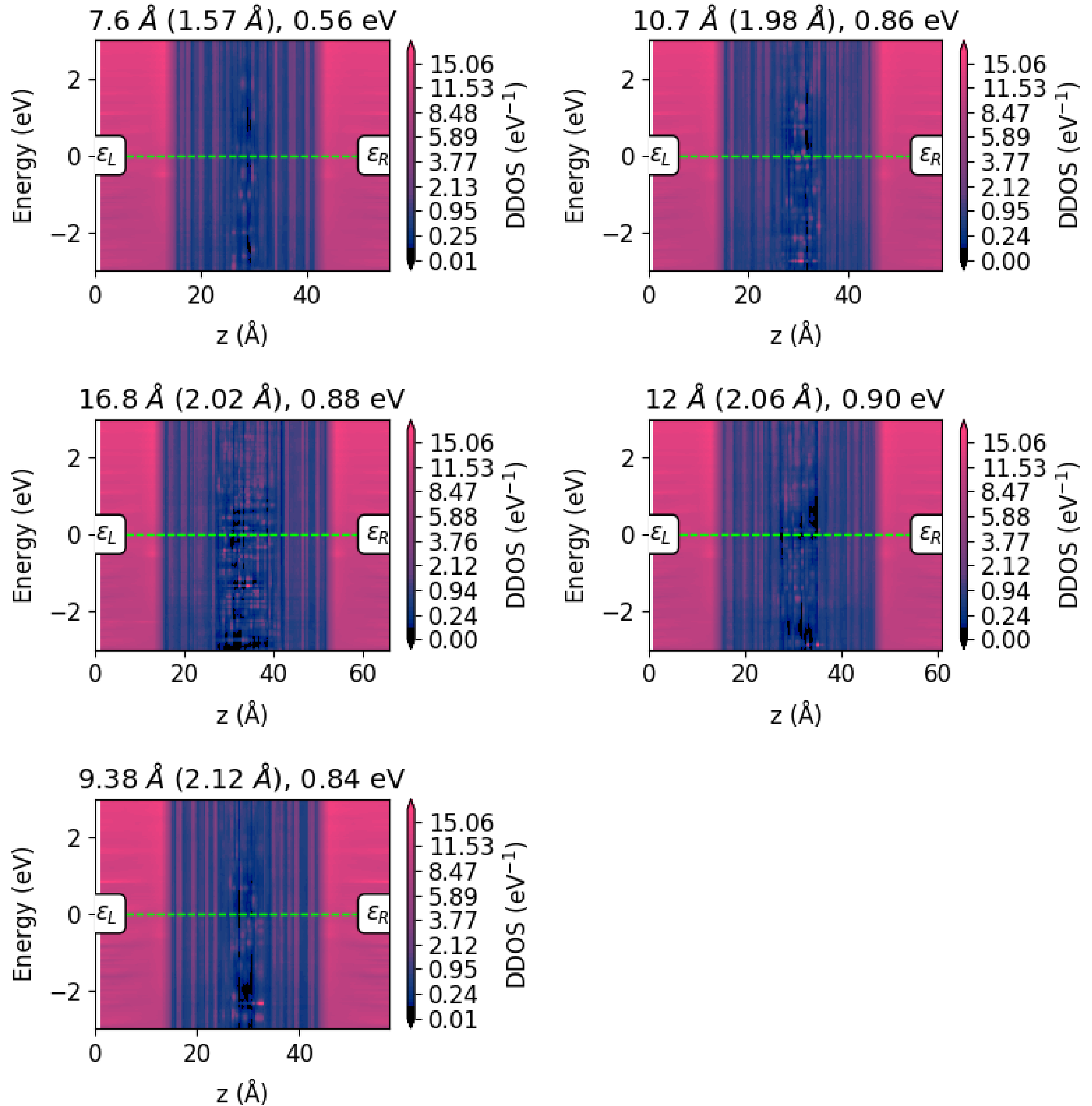

Figure 7.34: Projected Density of States for all Junction models with barrier heights ranging from 0.56-0.90 eV. The Physical length (and length from Simmons fit) is also indicated in the title of the subplots.

An advantage of the atomistic NEGF-DFTB method employed to study the model junctions is the electronic structure can be studied and linked to the electrical response. The device density

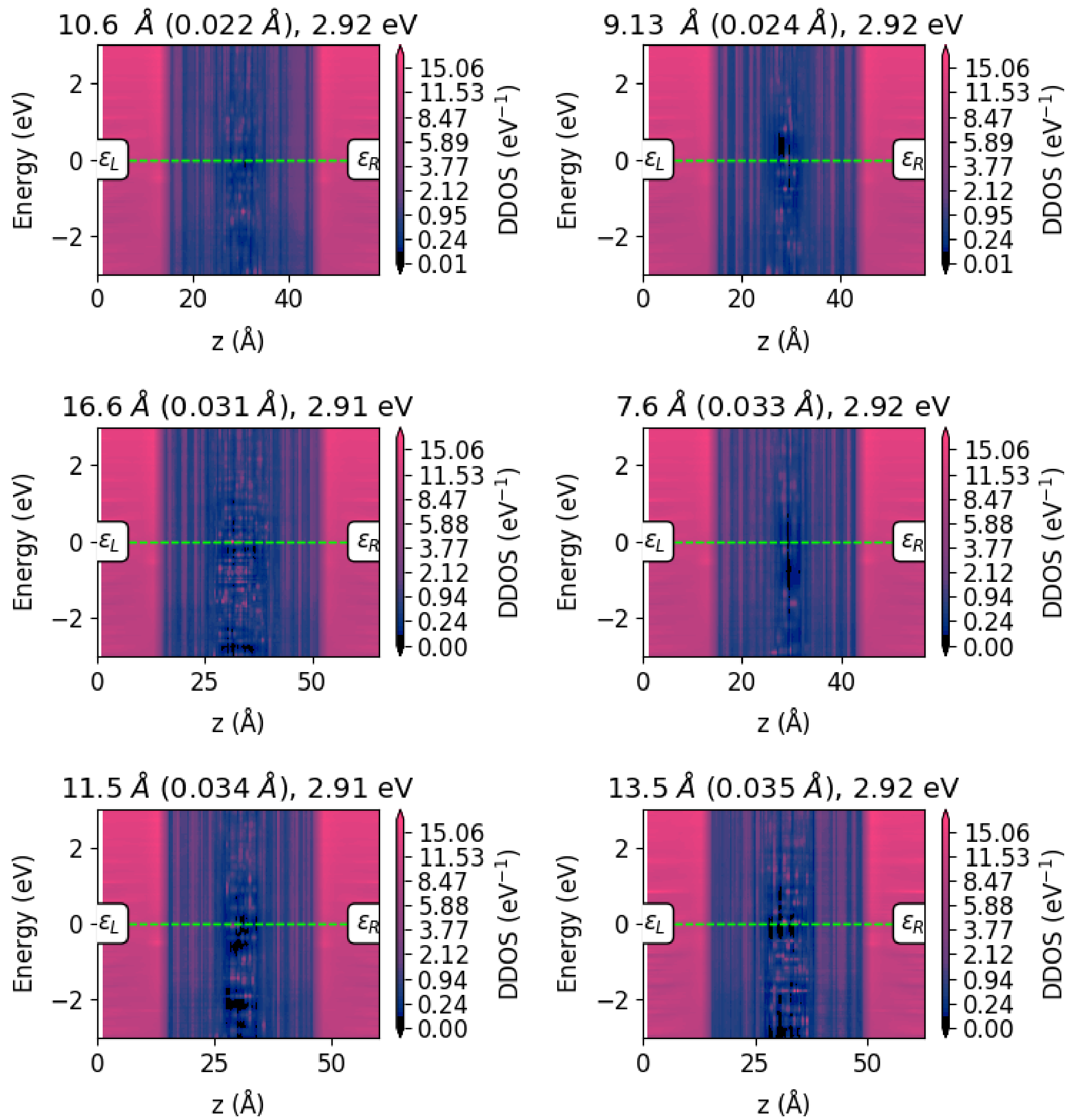

Figure 7.35: Projected Density of States for Junction models with barrier heights ≈ 2.9 eV. The Physical length (and length from Simmons fit) is also indicated in the title of the subplots.

of states (DDOS) was computed and projected onto the z coordinate (transport direction) of the junctions reported in Fig 7.33. These are shown in Fig 7.34 for the junctions with barrier height 0.55 eV - 0.90 eV and Fig 7.35 and 7.36 shows the DOS for the barrier heights ≈ 2.90 eV. The title of each DDOS list the measured physical barrier length (extracted effective barrier length) and the extracted barrier height. The DDOS are ordered in terms of increasing RA for ease of comparison.

All junction models show regions of low density of states, i.e insulating spots within the oxide. The amorphous nature barrier results in these "dark spots" being localised due to the local structure and not just an energy gap in the region of the barrier. The barrier height parameter

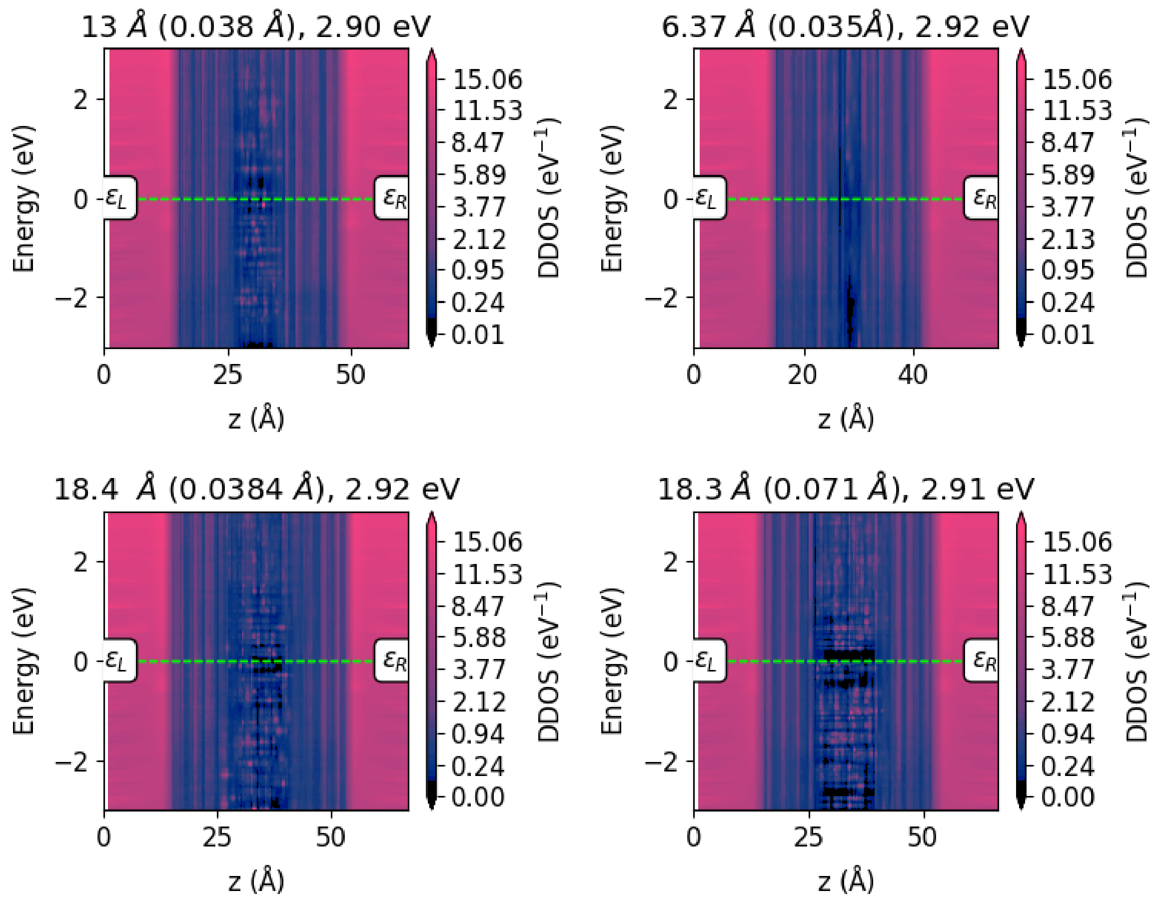

Figure 7.36: Projected Density of States for Junction models with barrier heights ≈ 2.9 eV. The Physical length (and length from Simmons fit) is also indicated in the title of the subplots.

implicitly includes the bandgap, dielectric constant of the material, density effects etc... but it is a 1D potential barrier and so fails to encapsulate entirely the electronic structure of the junction. Therefore a direct correlation between DDOS and barrier height is not expected. With respect to the transport properties only a lack of statesin the DOS close to the Fermi level will have a strong influence on the junction resistance.

Comparing the two clusters of data based on barrier heights, though subtle, the DDOS for the higher barrier heights do appear to contain more regions of low DOS. With the main exception being for 0.88 eV model. As the electronic structure influences the IV characteristics and the barrier height is extracted from this, these differences are not surprising. In general, in all three figures, the differences are only subtle is in keeping with the hypothesis that the model junctions, despite differing in physical barrier length, have similar sized effective lengths and area. There are models with more pronounced gaps in the DOS leading to a higher computed Resistance; however, the gaps are prevalent in all models and the similar DDOS profile highlights the similarity of the model junctions.

As the DOS is plotted on the physical barrier, the effective length is, of course, not visible as it is extracted from the IV curves, however, as the RA increases exponentially with the effective

length, it becomes evident that with increasing effective length, there appears to be more gaps in the DOS in general, which fits with the behaviour of the model junctions and the extracted data. The analysis of the electronic structure, computed resistance and current-voltage characteristics form a consistent picture of only subtle differences and hint to the amorphous barrier changing the effective size of the physical barrier in the model junctions.

Physical barrier length (Å)	Effective Area (cm^{-2})	Effective Length (as % of physical length)
6.37	2.68 x 10^{-19}	0.55
7.6	2.61 x 10^{-14}	20.72
8.41	3.45 x 10^{-19}	0.39
9.13	4.07 x 10^{-19}	0.26
9.38	3.79 x 10^{-13}	22.55
10.7	2.13 x 10^{-13}	18.49
11.5	6.97 x 10^{-20}	0.30
12	1.17 x 10^{-12}	17.2
13	4.76 x 10^{-19}	0.28
13.5	1.36 x 10^{-19}	0.26
16.6	7.02 x 10^{-19}	0.18
16.8	4.12 x 10^{-13}	12.02
18.3	1.48 x 10^{-19}	0.39
18.4	7.25 x 10^{-20}	0.21
19.4	1.83 x 10^{-19}	0.18

Table 7.5: The extracted area and length parameters from the Simmons fitting.

The size of the model junctions (despite periodic boundary conditions being applied to artificially inflate the cross sectional area) is a major limitation in accurately estimating resistance/ current-voltage characteristics using the DFTB-NEGF method. Albeit the physics can be described well and qualitative trends can be studied. This has an inhibiting effect to the values of the area and length that can be extracted from the Simmons model fitting in addition to the shortcomings of the 1D Simmons model itself as will be discussed. The extracted effective area and length values are reported in Table 7.5. As it has been reported in previous studies that the effective area can be as small as 10% of the actual physical area and the length considerably smaller than the measured length. Because the values are grossly underestimated, for analysis it is more sensible to report the effective length as a percentage of the actual length. Ideally, the area would be reported this way. However, due to the periodic boundary conditions, although the original simulation cell has a defined cross sectional area, once this is inflated by the boundary conditions the area is more difficult to define. Hence, when the effective area is given as a percentage, there are some values that are more than 100% of the original area. But this is misleading as area is inflated by the boundary conditions in X,Y. For this reason the Effective Area is reported in cm^{-2}, for reference the original simulation cell is $1.75x10^{-14}cm^{-2}$, in the study by Dorneles et al. [197] the effective area extracted up to the order of $10^{-19}cm^{-2}$ is reported for physical area of $4X10^{-4}cm^{-2}$.

If the small size of the simulation cell is considered, the very small effective area is not inconceivable, with four and five orders of magnitude differences reported previously. More importantly for explaining the R vs L data set shown in Fig 7.9, the values for many of the junctions are very close suggesting similar behaviour in the different models despite the physical barrier length being considerably different. There are area values in the range of $10^{-19} - 10^{-20}$ $cm^{-}2$ which primarily correspond to the junctions with barrier height (≈ 2.9). Whilst the larger areas are for the smaller barrier heights as discussed in detail above. If the simulation cell size is taken as reference, then the majority of the effective areas are orders of magnitude smaller due to thinner regions across the barrier. If it is accepted that the periodic boundary conditions successfully inflates the area of the junction considerably then all junctions show an even smaller effective conduction area.

For the barrier length data, it has already been shown that there are several junctions of similar size extracted length which helps explain the similar resistances predicted. However, to gauge how much the amorphous barrier reduces the physical length analysing the extracted length as a percentage of physical length gives an insight to how the different local structure junction to junction is effective as an insulating barrier. From the data in Table 7.5 the model clearly underestimates the effective length considerably, predicting 22.5% as the largest size of barrier, whilst some are predicted to be only 0.18% of the physical barrier, which of course is far too small to be physical. Nevertheless, the relative differences are interesting. For instance the two junctions with physical barrier length of 16.6 and 16.8 Å, the amorphous nature of the local structure clearly differs considerably, from this fit, for one junction the effective length according to the Simmons model is 0.18% of the length, in other words 99.82 % smaller. Whereas despite only being 0.2 Å bigger, the 16.8 Å junction is predicted to be 12.02% of its barrier length or 88% different. In another case however, the percentage reduction of the barrier length is very similar, for the junctions of length 13 and 13.5 Å, they have an effective length of 0.28% and 0.26% respectively suggesting a more consistent amorphous barrier for these two samples and a similar length as predicted from the fitting. Though the reduction in length may be overestimated by the fitting, it is clear is that the local structure and the inherent variability due to the amorphous oxide dictates the nature of the effective barrier length which is generally smaller than the physical barrier.

An attempt has been made to quantify the theorized effective barrier length which may explain the simulated R vs L data of the models in this study. Although there is some evidence for the existence of an effective barrier length and the effect of the amorphous nature of the barrier on the device performance has been investigated, there are several issues that need to be critically discussed in order to conclude the findings of this study. The RA values are underestimated compared to experiment, the extracted Simmons heights are acceptable but the lengths are far too small. But the question of why the values are so small remains unanswered? Is the variability junction to junction too big compared to experiment and are the findings of this study

useful or insightful despite the differences from trends? Several critical issues will be discussed in the next section with the aim of answering these questions.

7.5 Critical Discussion of the Findings of this Study

The first issue that needs to be considered is the nature of the amorphous barrier in the model Al/AlO_x/Al junctions in this study. The simulated annealing method is widely used but it is a crude approximation to the amorphous barrier. Though the amorphous barriers in this study are validated with respect to energy gaps lying with experimental range, the radial distribution function confirming that the structure is amorphous, reasonable coordination distribution and optimized bond lengths. However, given the significantly smaller size of the simulation cell and a lack of comparison to experiment, the structure whilst amorphous, may be too crude an approximation compared to a representative structure. In addition, the molecular dynamics simulations could be further optimized, as the interest in this thesis was to gain an efficient model structure and study many junctions with different structure parameters (barrier length, stoichiometry, density) an in depth study of simulation times, structure sizes and level of theory (different force fields, DFTB or even ab-initio) could be carried out to improve the consistency of amorphous barriers and reduce variability in similar sized oxide structures. Even though some initial testing was carried out, the parameters used were guided by the literature, namely those used by Cyster et al. [179, 186] and validated as previously stated, however it is accepted that improvements could potentially be made.

Even though the method for creating the amorphous model could potentially improved, it also has to be noted that further limitations arise from the "sandwich method" used to generate the model. As presented in the previous chapter the amorphous oxide model is placed between two bulk Al structures and allowed to relax to create the Al/AlO$_x$/Al structure and create an Al/AlO_x interface. Even if the oxide is improved this relaxation may produce further variability within the structure. The DFTB relaxation creates considerable disorder in the Al structure, even though some disorder is seen from experiment and other simulation studies, it is possible that the bulk Al at the interface has more disordered layers in the model than in reality and thus influencing the final structure. Additionally, the actual oxide structure is grown on Al surface, subsequently the structure of bulk Al has a considerable influence on the nature of the growth and the resulting thickness distributions [149]. By not replicating growth, some of the essential structure issues and natural defects may be missed in the model junctions. The results in this thesis are suggestive of the amorphous nature of the barrier being more disordered than experimentally. It is likely that the grown structure, even though extremely thin, maintains some epitaxy which is not replicated in the models here. The alternative method, would be to grow the structure with molecular dynamics. However, growth simulations at the atomistic level are very difficult to achieve, with very few successful examples in the literature for amorphous

materials including aluminium oxide. Current state of the art molecular dynamics simulations cannot replicate experimental timescales or pressures. Although a grown structure may result in an amorphous oxide that maintains some crystalline order and follows the Al morphology, the artificial pressures and much smaller timescales may result in missing important physics and the resulting structure be no better than the simulated annealing method applied here or an optimized version.

The aim of the work reported in this chapter and the last is to link the properties of the atomic structure of the amorphous barrier to the transport of the junction itself. Hence, an atomistic approach was required. The use of DFTB to describe the electronic structure of the junction was chosen as it has good accuracy at the atomistic level whilst being computationally efficient. In addition it allows for the handling of much larger number of atoms on a reasonable timescale so that multiple junctions and parameters can be studied. Although, experimental scales $10nm^2$ to $100\mu m^2$ is not possible, a sample space significantly bigger than ab-initio methods is possible. A potential drawback of the DFTB method is the quality of the parameterization, although tests were carried out and reported on its efficacy at replicating the AlO_x band gaps (better than DFT), geometries and bond lengths, the parameterization used was not developed for this particular application. The parameterization is based on AlO_x nanoparticles and bulk alumina and corundum. An improved parameter set for amorphous aluminium oxide or for Al/AlO$_x$/Al may better describe the electronic structure and improve results, at the expense of significant development time. Alternatively, use of DFT removes the need for parameters, however, band-gap replication is known to be worse and the number and scale of the models is more limited for perhaps modest improvement in results. It is worth noting as previously stated, DFTB parameter sets have been shown to capture the physics of a wide range of materials and show good transferability for systems for which the parameters were not developed. Therefore, given the success at replicating the geometry and energy gap of the oxide, the accuracy of the DFTB parameter set employed can be considered good enough for the purpose of the study.

The size of the simulation cell for realistic parameter-light atomistic simulations will always be a significant limitation. To alleviate this, periodic boundary conditions in X,Y (non-transport direction) are applied. However, this is problematic given the oxide is not periodic but amorphous. Because the initial simulation cell is much smaller than a real structure, any effect due the local atomic structure (i.e local stoichiometry, defects, density differences, thinner regions, energy gaps etc..) will be repeated periodically. The result is potentially an amplification of these structure effects leading to the shortcomings of the computed values and potentially the non-physical extracted lengths. The larger the simulation cell the more "diluted" these structure effects might be within the periodicity, however, the effects will still be more pronounced than in the actual structure. This is a major drawback of the simulation methodology employed here. In spite of this, even if the effects are amplified and lead to a poor quantitative match to experiment, it still allows the exploration of physical effects within the barrier and how it influences the op-

eration of the junction, as the same method is applied consistently to all models in this work allowing for investigating the effects of structural properties. Even if the exact current-voltage characteristics, or the exact value for effective area/ barrier length is difficult to compute, the simulations still provide evidence of its existence, its potential causes and can compliment experimental findings to gain an insight to the effects of the amorphous barrier. The results could also be calibrated with experimental data.

The last issue to be addressed is the use of the Simmons model to quantify the effective barrier length and the potential barrier height of the model junctions in this study. As explained above, the Simmons model is widely used to analyse IV-Curves of a variety of junction systems, including Josephson junctions hence applied here to attempt to quantify the barrier length of the simulated junctions in this study. The Simmons model is widely used largely due to its simplicity, but how well can this 1D analytical model capture the physical effects of the Al/AlOx/Al tunnel junctions? It was previously shown and discussed how the range of voltages for which the fitting is performed significantly influences the extracted parameters, so care needs to be taken. The results reported here show that the in general the barrier heights extracted from fitting the simulated I-V Curves are within the range of values reported from experimental curve fittings typically in the range of 0.8-3 eV. This is a good indication that the simulated curves are effective at replicating the IV-characteristics of experimental junctions.

However, there is a failure to extract sensible barrier lengths with the model. This shortcoming will be affected by the issues discussed above (model size, the current/conductance not matching experiment) but also will be influenced significantly by the inherent limitations of the Simmons model itself. Firstly, the curves were fit to the rectangular model as it is 1) the simplest and 2) showed the best fit to the simulated data, but a rectangular barrier model is likely too simplistic in 1D for the Al/AlOx/Al tunnel junction and will result in deviation from sensible values [164, 166]. The model is based on the WKB approximation, and so it is assumed that there is a spatially averaged potential and that the potential varies linearly in space and with applied bias. How valid are these assumptions, even for a rectangular barrier model? The WKB model is problematic in approximating the exact solution of the *Schrödinger* equation and so the Simmons model unlikely captures the subtleties of the quantum mechanical tunneling through the oxide barrier to correctly estimate parameters. The assumption of linearly varying potential under applied bias is valid at small voltage range at best but is still questionable. Furthermore, the amorphous nature of the barrier and its local structure can have significant impact on the potential of the barrier and so a linearly varying potential is difficult to confirm and is likely to be a poor approximation. Of course there are improved versions of Simmons original rectangular barrier model, where image forces are accounted for, or asymmetry such as in the Brinkman-Dowles version which could be used to improve the fit at the expense of a more complicated equation. However,they are still 1D models and suffer similar limitations as the original version.

Despite the fact that fitting the simulated curves to the rectangular Simmons model fails to

predict sensible effective barrier lengths, what is shown is despite different IV curves across the samples, the extracted lengths (within the two barrier height clusters) are predicted to be essentially the same/similar. Providing quantitative evidence that despite wider variations in "physical" barrier lengths, the effective barrier length across the junctions vary much less and are similar in value. It is hypothesized to be due to thinner portions of the amorphous barrier which may be amplified as discussed above. This is also consistent with the electron density plots and transmission pathways results presented earlier in this chapter. Notwithstanding, it is still a physical effect that is prevalent in the amorphous oxide containing tunnel junctions. The effective barrier being very close in value for all models explains very well the scattered R vs L data presented above in Fig 7.9. What the fitting also demonstrates, is even though there is smaller variation in L (0.02 -2.2 Å) an exponential relationship between RA vs Effective Length is indeed observed. Despite its limitations and failures, like in experiment, there are useful learnings to be obtained from fitting to the Simmons model, but to accurately quantify the effective barrier length a more sophisticated method is required.

7.6 Conclusions

In this chapter the relationship between oxide barrier length and the resistance of the Al/AlO$_x$/Al tunnel junction was studied using atomistic methods. The resistance is known to increase exponentially with increasing barrier length. The DFTB-NEGF calculations carried out here on more than 20 junctions do not show an exponential relationship. It was argued here that there is an effective barrier length which is much smaller than the physical length which consistent with experimental studies on the nature of the amorphous length. An effective barrier length would explain the non-exponential trend from the simulations, due to thinner regions in the barrier the effective length is similar in all cases. An attempt was made to quantify this effective barrier length by fitting to the Simmons model, a common practice experimentally. The fits provide some qualitative evidence to explain the length-resistance data, however the extracted barrier lengths are unphysically small. There are several limitations to the Simmons model which can lead to the unphysically small extracted lengths, there are also limitations from the way the junctions are modelled here which have been critically discussed. It is also suggested that the periodic boundary conditions artificially inflate the thinner portions leading to a far smaller effective barrier than would be the case in reality. Improved junction models and a more accurate way for quantifying the barrier length is necessary for further probing into the effect of the barrier length. Nonetheless, it has shown that the barrier length-electrical response relationship in the Al/AlO$_x$/Al tunnel is complex but important for high quality junctions for qubit applications. The simulations results presented in this chapter suggest the electron transport is concentrated in thinner regions across the barrier and thus control of the amorphous nature will be key in producing high quality, reproducible junctions. The work presented in this PhD thesis demon-

strates the importance of first principle and atomistic simulation techniques for aiding in the understanding and development of the next generation of electronic devices at the nanoscale.

Conclusion

Computational methods have been employed to study the properties of Polyoxometalate (POM) molecular junctions and aluminium tunnel junctions (Josephson junctions) in order to gain a deeper understanding of these material systems. The combination of Density Functional Theory (DFT) and Non-Equilibrium Green's Function (NEGF) framework allows for a comprehensive atomistic and quantum description of the junctions, which is crucial for unraveling their behavior and electron transport.

The first part of this thesis focuses on the investigation of a POM molecular junction, specifically $[W_{18}O_{54}(SO_3)_2]^{4-}$, utilizing DFT and NEGF. The simulations revealed that electron transport through this junction is dominated by the Lowest Unoccupied Molecular Orbital (LUMO) and is strongly influenced by molecular orientation and the electrode-molecule contact. The simulations predicted that a horizontal geometry exhibits higher overall conductance for this molecule. The study also considered the presence of counterions in the molecular junction system, and the calculations suggested that counterions have a stabilizing effect on the unoccupied energy levels of the molecule, resulting in a significant increase in conduction. Therefore, when designing devices that incorporate these anionic molecular clusters, the effects of accompanying charge balancing counterions need to be taken into account. One significant advantage of POM molecules is their rich diversity, as demonstrated by the simulations in this work, where changing the caged atom in $[W_{18}O_{54}]$ enabled engineering of the HOMO-LUMO gap and caused significant alterations in electron transport through the molecule.

Although DFT can successfully describe these molecules and, when combined with NEGF, can investigate their transport properties, several challenges still remain. As explained in the "Theoretical Foundations Chapter," while the formulation of DFT is exact, the exact exchange-correlation (XC) functional remains unknown. The success of DFT calculations relies on employing the appropriate functional and basis set for the specific problem at hand. To understand how these molecules can be incorporated into devices, such as flash memory, it is crucial to employ a functional and basis set that can accurately describe the properties of both the molecule and its surroundings. However, for a POM embedded in an oxide, DFT fails to accurately describe the band gap of SiO_2. Any functional that reasonably succeeds in describing its electronic structure fails to capture the properties of the molecule. This specificity of functionals in DFT represents a major limitation in describing complex, multi-material systems. Additionally, due

to its ab initio nature that explicitly treats each atom (and all its electrons), DFT calculations are computationally expensive, posing a scalability issue when studying large systems.

The second part of this thesis focuses on the study of Al/AlO$_x$/Al using DFTB combined with NEGF for transport calculations. The influence of AlO$_x$ (barrier) stoichiometry and length was investigated. The amorphous barrier was modeled using simulated annealing methods with classical force fields and Molecular Dynamics. The simulation results presented in this thesis suggest that the local atomic structure varies considerably with stoichiometry, and a higher oxygen concentration makes the barrier more insulating. However, inherent variability arises due to the amorphous nature of the barrier, leading to differences in local atomic structure, even in barriers with the same Al:O ratio. These structural variations strongly influence electron transport through the barrier, resulting in variability in IV characteristics, junction resistance, and critical currents.

The relationship between barrier length and junction resistance, which is expected to be exponential, was computationally investigated in these junction systems. However, the results did not demonstrate an exponential relationship. It is argued that there is evidence for an "effective barrier" length due to thinner regions within the amorphous barrier. Some studies suggest that only 10% of the barrier actively participates in tunneling, leading to the concept of an "effective" barrier length. The simulations conducted in this work may have overemphasized the effects of the effective barrier due to a simplistic modeling of the amorphous barrier, which is likely different from the experimentally grown structure. Additionally, in order to overcome size limitations of the junction models, periodic boundaries were applied in the X and Y directions, which potentially enhanced the presence of defects and caused variations in the effective barrier length observed in the results.

While the simulation method employed here can be useful for probing electron transport through Al/AlO$_x$/Al and aiding in the understanding of this material system, an accurate description of the amorphous nature of the barrier is crucial to replicate the behavior and defects observed in the real system. The author believes that efficient and accurate growth simulations of the amorphous oxide, combined with a correct description of its electronic structure, are key to understanding the emergence and interaction of defect systems with other materials in Josephson junction (JJ) based applications, such as qubits.

Bibliography

[1] Q. Li, G. Mathur, S. Gowda, S. Surthi, Q. Zhao, L. Yu, J.S. Lindsey, D.F. Bocian, and V. Misra. Multibit memory using self-assembly of mixed ferrocene/porphyrin monolayers on silicon. *Advanced Materials*, 16(2):133–137, 2004.

[2] Hao Zhu, Sujitra J. Pookpanratana, John E. Bonevich, Sean N. Natoli, Christina A. Hacker, Tong Ren, John S. Suehle, Curt A. Richter, and Qiliang Li. Redox-active molecular nanowire flash memory for high-endurance and high-density nonvolatile memory applications. *ACS Applied Materials & Interfaces*, 7(49):27306–27313, 2015. PMID: 26600234.

[3] John G. Simmons. Generalized Formula for the Electric Tunnel Effect between Similar Electrodes Separated by a Thin Insulating Film. *J. Appl. Phys.*, 34(6):1793–1803, 1963.

[4] Adi Fuchs and David Wentzlaff. The accelerator wall: Limits of chip specialization. In *2019 IEEE International Symposium on High Performance Computer Architecture (HPCA)*, pages 1–14, 2019.

[5] Jeff Dean, David Patterson, and Cliff Young. A new golden age in computer architecture: Empowering the machine-learning revolution. *IEEE Micro*, 38(2):21–29, 2018.

[6] E. Schrödinger. An undulatory theory of the mechanics of atoms and molecules. *Phys. Rev.*, 28(6):1049–1070, 1926.

[7] Christopher J Cramer. *Essentials of Computational Chemistry, Theories and Models. Second Edition*. Wiley, 2004.

[8] D R Hartree. The Wave Mechanics of an Atom with a Non-Coulomb Central Field. Part II. Some Results and Discussion. *Math. Proc. Cambridge Philos. Soc.*, 24(1):111–132, 1928.

[9] C C J Roothaan. New Developments in Molecular Orbital Theory. *Rev. Mod. Phys.*, 23(2):69–89, apr 1951.

[10] E Fermi. Eine statistische Methode zur Bestimmung einiger Eigenschaften des Atoms und ihre Anwendung auf die Theorie des periodischen Systems der Elemente. *Zeitschrift für Phys.*, 48(1):73–79, 1928.

[11] P Hohenberg and W Kohn. Inhomogeneous Electron Gas. *Phys. Rev.*, 136(3B):B864—-B871, nov 1964.

[12] W Kohn and L J Sham. Self-Consistent Equations Including Exchange and Correlation Effects. *Phys. Rev.*, 140(4A):A1133—-A1138, nov 1965.

[13] Kieron Burke and Lucas O. Wagner. DFT in a nutshell. *Int. J. Quantum Chem.*, 113(2):96–101, 2013.

[14] Peter Kratzer and Jörg Neugebauer. The basics of electronic structure theory for periodic systems. *Front. Chem.*, 7(MAR):1–18, 2019.

[15] Narbe Mardirossian and Martin Head-Gordon. Thirty years of density functional theory in computational chemistry: An overview and extensive assessment of 200 density functionals. *Mol. Phys.*, 115(19):2315–2372, 2017.

[16] Pierpaolo Morgante and Roberto Peverati. The devil in the details : A tutorial review on some undervalued aspects of density functional theory calculations. (April):1–11, 2020.

[17] J P Perdew and Alex Zunger. Self-interaction correction to density-functional approximations for many-electron systems. *Phys. Rev. B*, 23(10):5048–5079, may 1981.

[18] Yan Zhao and Donald G Truhlar. Density Functional for Spectroscopy: No Long-Range Self-Interaction Error, Good Performance for Rydberg and Charge-Transfer States, and Better Performance on Average than B3LYP for Ground States. *J. Phys. Chem. A*, 110(49):13126–13130, 2006.

[19] Yan Zhao and Donald G Truhlar. The M06 suite of density functionals for main group thermochemistry, thermochemical kinetics, noncovalent interactions, excited states, and transition elements: two new functionals and systematic testing of four M06-class functionals and 12 other function. *Theor. Chem. Acc.*, 120(1):215–241, 2008.

[20] John P Perdew, Kieron Burke, and Matthias Ernzerhof. Generalized Gradient Approximation Made Simple. *Phys. Rev. Lett.*, 77(18):3865–3868, oct 1996.

[21] Jochen Heyd, Gustavo E. Scuseria, and Matthias Ernzerhof. Hybrid functionals based on a screened Coulomb potential. *J. Chem. Phys.*, 118(18):8207–8215, 2003.

[22] Carlo Adamo and Vincenzo Barone. Toward reliable density functional methods without adjustable parameters: The PBE0 model. *J. Chem. Phys.*, 110(13):6158–6170, 1999.

[23] John P. Perdew, Matthias Ernzerhof, and Kieron Burke. Rationale for mixing exact exchange with density functional approximations. *J. Chem. Phys.*, 105(22):9982–9985, 1996.

[24] A D Becke. Density-functional exchange-energy approximation with correct asymptotic behavior. *Phys. Rev. A*, 38(6):3098–3100, sep 1988.

[25] Søren Smidstrup, Troels Markussen, Pieter Vancraeyveld, Jess Wellendorff, Julian Schneider, Tue Gunst, Brecht Verstichel, Daniele Stradi, Petr A. Khomyakov, Ulrik G. Vej-Hansen, Maeng Eun Lee, Samuel T. Chill, Filip Rasmussen, Gabriele Penazzi, Fabiano Corsetti, Ari Ojanperä, Kristian Jensen, Mattias L.N. Palsgaard, Umberto Martinez, Anders Blom, Mads Brandbyge, and Kurt Stokbro. QuantumATK: An integrated platform of electronic and atomic-scale modelling tools. *J. Phys. Condens. Matter*, 32(1), 2020.

[26] Kevin F Garrity, Joseph W Bennett, Karin M Rabe, and David Vanderbilt. Pseudopotentials for high-throughput DFT calculations. *Comput. Mater. Sci.*, 81:446–452, 2014.

[27] T Ozaki. Variationally optimized atomic orbitals for large-scale electronic structures. pages 1–5, 2003.

[28] T Ozaki and H Kino. Numerical atomic basis orbitals from H to Kr. pages 1–19, 2004.

[29] Martin Schlipf and François Gygi. Optimization algorithm for the generation of ONCV pseudopotentials. *Comput. Phys. Commun.*, 196:36–44, 2015.

[30] Pekka Koskinen and Ville Mäkinen. Density-functional tight-binding for beginners. *Comput. Mater. Sci.*, 47(1):237–253, nov 2009.

[31] Fernand Spiegelman, Nathalie Tarrat, Jérôme Cuny, Leo Dontot, Evgeny Posenitskiy, Carles Martí, Aude Simon, and Mathias Rapacioli. Density-functional tight-binding: basic concepts and applications to molecules and clusters. *Adv. Phys. X*, 5(1), 2020.

[32] Kurt Stokbro, Dan Erik Petersen, Søren Smidstrup, Anders Blom, Mads Ipsen, and Kristen Kaasbjerg. Semiempirical model for nanoscale device simulations. *Phys. Rev. B - Condens. Matter Mater. Phys.*, 82(7):1–7, 2010.

[33] G. Elstner, M. and Porezag, D. and Jungnickel, G. and Elsner, J. and Haugk, M. and Frauenheim, Th. and Suhai, S. and Seifert. Self-consistent-charge density-functional tight-binding method for simulations of complex materials properties. *Phys. Rev. B*, 58(11):7260—-7268, 1998.

[34] M Elstner, D Porezag, G Jungnickel, J Elsner, M Haugk, Th. Frauenheim, S Suhai, and G Seifert. Self-consistent-charge density-functional tight-binding method for simulations of complex materials properties. *Phys. Rev. B*, 58(11):7260–7268, sep 1998.

[35] Marcus Elstner and Gotthard Seifert. Density functional tight binding. 2014.

[36] Supriya Ghosal, Kajari Dutta, Suman Chowdhury, and Debnarayan Jana. Importance of the hubbard u parameter to explore accurate electronic and optical behaviour of bifeo3. *Journal of Physics D: Applied Physics*, 55(37):375303, jul 2022.

[37] Supriyo Datta. *Lessons from Nanoelectronics*. World Scientific, 2nd edition, 2018.

[38] S Datta. *Quantum Transport: Atom to Transistor*. Cambridge Univ. Press, New York, 2005.

[39] Dong Xiang, Xiaolong Wang, Chuancheng Jia, Takhee Lee, and Xuefeng Guo. Molecular-Scale Electronics: From Concept to Function. *Chem. Rev.*, 116(7):4318–4440, 2016.

[40] Yongqiang Xue and Mark A. Ratner. Theoretical principles of single-molecule electronics: A chemical and mesoscopic view. *Int. J. Quantum Chem.*, 102(5 SPEC. ISS.):911–924, 2005.

[41] Christian Joachim and Mark A. Ratner. Molecular electronics: Some views on transport junctions and beyond. *Proc. Natl. Acad. Sci. U. S. A.*, 102(25):8801–8808, 2005.

[42] Jesse Maassen, Mohammed Harb, Vincent Michaud-Rioux, Yu Zhu, and Hong Guo. Quantum transport modeling from first principles. *Proc. IEEE*, 101(2):518–530, 2013.

[43] Guy Cohen and Michael Galperin. Green's function methods for single molecule junctions. *J. Chem. Phys.*, 152(9), 2020.

[44] Rolf Landauer. Spatial variation of currents and fields due to localized scatterers in metallic conduction. *IBM J. Res. Dev.*, 44(1):251–259, 2000.

[45] M. Bttiker. Role of quantum coherence in series resistors. *Phys. Rev. B*, 33(5):3020–3026, 1986.

[46] Kerem Y. Camsari, Shuvro Chowdhury, and Supriyo Datta. *The Nonequilibrium Green Function (NEGF) Method*, pages 1583–1599. Springer International Publishing, Cham, 2023.

[47] Jeetendra Singh and Chhaya Verma. Modeling methods for nanoscale semiconductor devices. *Silicon*, 14(10):5125–5132, Jul 2022.

[48] Supriyo Datta. Nanoscale device modeling: the Green's function method. *Superlattices Microstruct.*, 28(4):253–278, 2000.

[49] Richard O'Donnell. Modeling of nanoscale devices. *Proc. IEEE*, 96(9):1509–1510, 2008.

[50] Daniele Stradi, Umberto Martinez, Anders Blom, Mads Brandbyge, and Kurt Stokbro. General atomistic approach for modeling metal-semiconductor interfaces using density functional theory and nonequilibrium Green's function. *Phys. Rev. B*, 93(15):28–38, 2016.

[51] Mads Brandbyge, José Luis Mozos, Pablo Ordejón, Jeremy Taylor, and Kurt Stokbro. Density-functional method for nonequilibrium electron transport. *Phys. Rev. B - Condens. Matter Mater. Phys.*, 65(16):1654011–16540117, 2002.

[52] Académie royale des sciences (France). *Mémoires de l'Académie (royale) des sciences de l'Institut (imperial) de France*, volume T.6(1827). Paris,, 1827.

[53] Jinn-liang Liu. Poisson ' s Equation in Electrostatics. 2017(March):1–7, 2011.

[54] James M. Tour. Introduction to molecular electronics edited by m. c. petty, m. r. bryce, and d. bloor (university of durham, u.k.). oxford university press: New york. 1995. xiv + 387 pp. $42.50. isbn 0-19-521156-1. *Journal of the American Chemical Society*, 118:2309–2310, 1996.

[55] Lapo Bogani. Quantum nanoelectronics—an introduction to electronic nanotechnology and quantum computing. by e. l. wolf. *ChemPhysChem*, 11(6):1316–1317, 2010.

[56] Paven Thomas Mathew and Fengzhou Fang. Advances in molecular electronics: A brief review. *Engineering*, 4(6):760–771, 2018.

[57] R. Lloyd Carroll and Christopher B. Gorman. The genesis of molecular electronics. *Angewandte Chemie International Edition*, 41(23):4378–4400, 2002.

[58] Xinmiao Xie, Peihui Li, Yanxia Xu, Li Zhou, Yong Yan, Linghai Xie, Chuancheng Jia, and Xuefeng Guo. Single-molecule junction: A reliable platform for monitoring molecular physical and chemical processes. *ACS Nano*, 16(3):3476–3505, Mar 2022.

[59] Lu Wang, Ling Wang, Lei Zhang, and Dong Xiang. Advance of mechanically controllable break junction for molecular electronics. *Topics in Current Chemistry*, 375(3):61, May 2017.

[60] Dong Xiang, Xiaolong Wang, Chuancheng Jia, Takhee Lee, and Xuefeng Guo. Molecular-scale electronics: From concept to function. *Chemical Reviews*, 116(7):4318–4440, 2016. PMID: 26979510.

[61] Rupan Preet Kaur, Ravinder Singh Sawhney, and Derick Engles. Quantum tunneling through aromatic molecular junctions for molecular devices: A review. *Chinese Journal of Physics*, 56(5):2226–2234, 2018.

[62] Jae-Gab Lim, Seung-Dong Yang, Ho-Jin Yun, Jun-Kyo Jung, Jung-Hyun Park, Chan Lim, Gyu seok Cho, Seong gye Park, Chul Huh, Hi-Deok Lee, and Ga-Won Lee. High performance sonos flash memory with in-situ silicon nanocrystals embedded in silicon nitride charge trapping layer. *Solid-State Electronics*, 140:134–138, 2018. Selected papers from The 24th Korean Conference on Semiconductors 2017.

[63] Front matter. In Blanka Magyari-Köpe and Yoshio Nishi, editors, *Advances in Non-Volatile Memory and Storage Technology (Second Edition)*, Woodhead Publishing Series in Electronic and Optical Materials, pages i–ii. Woodhead Publishing, second edition edition, 2019.

[64] Jagan Singh Meena, Simon Min Sze, Umesh Chand, and Tseung-Yuen Tseng. Overview of emerging nonvolatile memory technologies. *Nanoscale Research Letters*, 9(1):526, Sep 2014.

[65] Sparsh Mittal. A survey of soft-error mitigation techniques for non-volatile memories. *Computers*, 6(1), 2017.

[66] Barbara De Salvo, C. Gerardi, R. van Schaijk, S.A. Lombardo, D. Corso, C. Plantamura, S. Serafino, G. Ammendola, M. van Duuren, P. Goarin, W.Y. Mei, K. van der Jeugd, T. Baron, M. Gely, P. Mur, and S. Deleonibus. Performance and reliability features of advanced nonvolatile memories based on discrete traps (silicon nanocrystals, sonos). *IEEE Transactions on Device and Materials Reliability*, 4(3):377–389, 2004.

[67] A. Allan, D. Edenfeld, W.H. Joyner, A.B. Kahng, M. Rodgers, and Y. Zorian. 2001 technology roadmap for semiconductors. *Computer*, 35(1):42–53, 2002.

[68] M. L. Ostraat, J. W. De Blauwe, M. L. Green, L. D. Bell, M. L. Brongersma, J. Casperson, R. C. Flagan, and H. A. Atwater. Synthesis and characterization of aerosol silicon nanocrystal nonvolatile floating-gate memory devices. *Applied Physics Letters*, 79(3):433–435, 2001.

[69] Jong-Ho Lee and Sang-Goo Jung. Nand flash memory technology utilizing fringing electric field. *Microelectronics Reliability*, 52(4):662–669, 2012. Advances in non-volatile memory technology.

[70] Christian Monzio Compagnoni and Alessandro S. Spinelli. Reliability of nand flash arrays: A review of what the 2-d–to–3-d transition meant. *IEEE Transactions on Electron Devices*, 66(11):4504–4516, 2019.

[71] Christian Monzio Compagnoni, Akira Goda, Alessandro S. Spinelli, Peter Feeley, Andrea L. Lacaita, and Angelo Visconti. Reviewing the evolution of the nand flash technology. *Proceedings of the IEEE*, 105(9):1609–1633, 2017.

[72] Hao Zhu and Qiliang Li. Novel molecular non-volatile memory: Application of redox-active molecules. *Applied Sciences*, 6(1), 2016.

[73] Yaping Li, J. D. Tygar, and Joseph M. Hellerstein. Private Matching. *Comput. Secur. 21st Century*, 58(11):25–50, 2005.

[74] E. Papaconstantinou. Photochemistry of polyoxometallates of molybdenum and tungsten and/or vanadium. *Chem. Soc. Rev.*, 18:1–31, 1989.

[75] De Liang Long and Leroy Cronin. Towards polyoxometalate-integrated nanosystems. *Chem. - A Eur. J.*, 12(14):3698–3706, 2006.

[76] Ghénadie Novitchi, Sergiu Shova, and Cyrille Train. Investigation by chemical substitution within 2p-3d-4f clusters of the cobalt(ii) role in the magnetic behavior of [vdcoln]2 (vd = verdazyl radical). *Inorganic Chemistry*, 0(0):null, 0. PMID: 36240010.

[77] Laia Vilà-Nadal, Scott G. Mitchell, Stanislav Markov, Christoph Busche, Vihar Georgiev, Asen Asenov, and Leroy Cronin. Towards polyoxometalate-cluster-based nano-electronics. *Chem. - A Eur. J.*, 19(49):16502–16511, 2013.

[78] Tiziana Pro, Julien Buckley, Kai Huang, Adrian Calborean, Marc GÉly, G. Delapierre, GÉrard Ghibaudo, Florence Duclairoir, Jean-Claude Marchon, E. Jalaguier, P. Maldivi, Barbara De Salvo, and Simon Deleonibus. Investigation of hybrid molecular/silicon memories with redox-active molecules acting as storage media. *IEEE Transactions on Nanotechnology*, 8(2):204–213, 2009.

[79] Vihar P. Georgiev, Stanislav Markov, Laia Vilà-Nadal, Christoph Busche, Leroy Cronin, and Asen Asenov. Optimization and evaluation of variability in the programming window of a flash cell with molecular metal-oxide storage. *IEEE Trans. Electron Devices*, 61(6):2019–2026, 2014.

[80] Leroy Cronin and Achim Müller. From serendipity to design of polyoxometalates at the nanoscale, aesthetic beauty and applications. *Chem. Soc. Rev.*, 41(22):7333–7334, 2012.

[81] Christoph Busche, Laia Vilà-Nadal, Jun Yan, Haralampos N. Miras, De Liang Long, Vihar P. Georgiev, Asen Asenov, Rasmus H. Pedersen, Nikolaj Gadegaard, Muhammad M. Mirza, Douglas J. Paul, Josep M. Poblet, and Leroy Cronin. Design and fabrication of memory devices based on nanoscale polyoxometalate clusters. *Nature*, 515(7528):545–549, 2014.

[82] Paul Lapham, Laia Vilà-Nadal, Leroy Cronin, and Vihar P. Georgiev. Influence of the contact geometry and counterions on the current flow and charge transfer in polyoxometalate molecular junctions: A density functional theory study. *J. Phys. Chem. C*, 125(6):3599–3610, 2021.

[83] Xavier López, Jorge J. Carbó, Carles Bo, and Josep M. Poblet. Structure, properties and reactivity of polyoxometalates: A theoretical perspective. *Chem. Soc. Rev.*, 41(22):7537–7571, 2012.

[84] Martin Schlipf and François Gygi. Optimization algorithm for the generation of ONCV pseudopotentials. *Comput. Phys. Commun.*, 196:36–44, 2015.

[85] De-Liang Long, Hamera Abbas, Paul Kögerler, and Leroy Cronin. Confined electron-transfer reactions within a molecular metal oxide "trojan horse". *Angewandte Chemie International Edition*, 44(22):3415–3419, 2005.

[86] Zixiao Wang, Bo Jiang, Hui Wang, and Wei Wang. Studying single molecule electrochemistry with scanning tunneling microscope break-junction technique. *Current Opinion in Electrochemistry*, 34:100997, 2022.

[87] Linda A Zotti, Beatrice Bednarz, Juan Hurtado-gallego, Damien Cabosart, Gabino Rubio-bollinger, Nicolas Agrait, and Herre S J Van Der Zant. Can One Define the Conductance of Amino Acids ? pages 1–13.

[88] Joshua Hihath and Nongjian Tao. The role of molecule – electrode contact in single-molecule electronics. 2014.

[89] Gang Zhang and Charles B. Musgrave. Comparison of DFT methods for molecular orbital eigenvalue calculations. *J. Phys. Chem. A*, 111(8):1554–1561, 2007.

[90] Yingmei Han and Christian A. Nijhuis. Functional Redox-Active Molecular Tunnel Junctions. *Chem. - An Asian J.*, 15(22):3752–3770, 2020.

[91] Yingmei Han, Maria Serena Maglione, Valentin Diez Cabanes, Javier Casado-Montenegro, Xiaojiang Yu, Senthil Kumar Karuppannan, Ziyu Zhang, Núria Crivillers, Marta Mas-Torrent, Concepció Rovira, Jérôme Cornil, Jaume Veciana, and Christian A. Nijhuis. Reversal of the Direction of Rectification Induced by Fermi Level Pinning at Molecule–Electrode Interfaces in Redox-Active Tunneling Junctions. *ACS Appl. Mater. Interfaces*, pages 0–11, 2020.

[92] Albert C. Aragonès, Nadim Darwish, Simone Ciampi, Li Jiang, Raphael Roesch, Eliseo Ruiz, Christian A. Nijhuis, and Ismael Díez-Pérez. Control over Near-Ballistic Electron Transport through Formation of Parallel Pathways in a Single-Molecule Wire. *J. Am. Chem. Soc.*, 141(1):240–250, 2019.

[93] A. Balliou, A. M. Douvas, P. Normand, D. Tsikritzis, S. Kennou, P. Argitis, and N. Glezos. Tungsten polyoxometalate molecules as active nodes for dynamic carrier exchange in hybrid molecular/semiconductor capacitors. *J. Appl. Phys.*, 116(14), 2014.

[94] Maxime Laurans, Kevin Dalla Francesca, Florence Volatron, Guillaume Izzet, David Guerin, Dominique Vuillaume, Stéphane Lenfant, and Anna Proust. Molecular signature of polyoxometalates in electron transport of silicon-based molecular junctions. *Nanoscale*, 10(36):17156–17165, 2018.

[95] Archismita Misra, Karoly Kozma, Carsten Streb, and May Nyman. Beyond Charge Balance: Counter-Cations in Polyoxometalate Chemistry. *Angew. Chemie - Int. Ed.*, 59(2):596–612, 2020.

[96] Marta Blasco-Ahicart, Joaquin Soriano-Lopez, Jorge J. Carbo, Josep M. Poblet, and J. R. Galan-Mascaros. Polyoxometalate electrocatalysts based on earthabundant metals for efficient water oxidation in acidic media. *Nat. Chem.*, 10(1):24–30, 2018.

[97] Yingmei Han, Cameron Nickle, Ziyu Zhang, Hippolyte P.A.G. Astier, Thorin J. Duffin, Dongchen Qi, Zhe Wang, Enrique del Barco, Damien Thompson, and Christian A. Nijhuis. Electric-field-driven dual-functional molecular switches in tunnel junctions. *Nat. Mater.*, 19(8):843–848, 2020.

[98] Sreetosh Goswami, Santi P. Rath, Damien Thompson, Svante Hedström, Meenakshi Annamalai, Rajib Pramanick, B. Robert Ilic, Soumya Sarkar, Sonu Hooda, Christian A. Nijhuis, Jens Martin, R. Stanley Williams, Sreebrata Goswami, and T. Venkatesan. Charge disproportionate molecular redox for discrete memristive and memcapacitive switching. *Nat. Nanotechnol.*, 15(5):380–389, 2020.

[99] Nigel Fay, Alan M. Bond, Carole Baffert, John F. Boas, John R. Pilbrow, De-Liang Long, and Leroy Cronin. Structural, Electrochemical, and Spectroscopic Characterization of a Redox Pair of Sulfite-Based Polyoxotungstates: α-[W 18 O 54 (SO 3) 2] 4 - and α-[W 18 O 54 (SO 3) 2] 5 -. *Inorg. Chem.*, 46(9):3502–3510, apr 2007.

[100] Peter F. Lang and Barry C. Smith. Ionic radii for Group 1 and Group 2 halide, hydride, fluoride, oxide, sulfide, selenide and telluride crystals. *Dalt. Trans.*, 39(33):7786–7791, 2010.

[101] Yu Hou, Lev N. Zakharov, and May Nyman. Observing assembly of complex inorganic materials from polyoxometalate building blocks. *J. Am. Chem. Soc.*, 135(44):16651–16657, 2013.

[102] Michael Thoss and Ferdinand Evers. Perspective: Theory of quantum transport in molecular junctions. *J. Chem. Phys.*, 148(3), 2018.

[103] De-Liang Long, Yu-Fei Song, ElizabethF. Wilson, Paul Kögerler, Si-Xuan Guo, AlanM. Bond, JustinS.J. Hargreaves, and Leroy Cronin. Capture of periodate in a W18O54 cluster cage yielding a catalytically active polyoxometalate [h3w18o56(io6)]6 embedded with high-valent iodine. *Angewandte Chemie International Edition*, 47(23):4384–4387, 2008.

[104] Aleksandar Kondinski and Mahdi Ghorbani-Asl. Polyoxoplatinates as covalently dynamic electron sponges and molecular electronics materials. *Nanoscale Adv.*, 3:5663–5675, 2021.

[105] Almudena Notario-Estévez, Xavier López, and Coen de Graaf. Computational study of the staircase molecular conductivity of polyoxovanadates adsorbed on au(111). *Dalton Trans.*, 50:5540–5551, 2021.

[106] V. V. Shorokhov, E. S. Soldatov, and V. G. Elenskiy. The method for the determination of electrical self-capacitance of the atomic and molecular scale objects. In Kamil A. Valiev and Alexander A. Orlikovsky, editors, *Micro- and Nanoelectronics 2007*, volume 7025, page 70250N. International Society for Optics and Photonics, SPIE, 2008.

[107] Paulo R. Bueno and Jason J. Davis. Charge transport and energy storage at the molecular scale: from nanoelectronics to electrochemical sensing. *Chem. Soc. Rev.*, 49:7505–7515, 2020.

[108] Paulo R. Bueno and Jason J. Davis. Measuring quantum capacitance in energetically addressable molecular layers. *Analytical Chemistry*, 86(3):1337–1341, 2014. PMID: 24405523.

[109] Suman Chandra, Debarati Roy Chowdhury, Matthew Addicoat, Thomas Heine, Amit Paul, and Rahul Banerjee. Molecular level control of the capacitance of two-dimensional covalent organic frameworks: Role of hydrogen bonding in energy storage materials. *Chemistry of Materials*, 29(5):2074–2080, 2017.

[110] Jacopo Oswald, Davide Beretta, Michael Stiefel, Roman Furrer, Alessia Romio, Michel Daher Mansour, Dominique Vuillaume, and Michel Calame. Charge transport across au–p3ht–graphene van der waals vertical heterostructures. *ACS Applied Materials & Interfaces*, 14(42):48240–48249, 2022. PMID: 36239396.

[111] Jeffrey M. Mativetsky, Yueh-Lin Loo, and Paolo Samorì. Elucidating the nanoscale origins of organic electronic function by conductive atomic force microscopy. *J. Mater. Chem. C*, 2:3118–3128, 2014.

[112] Dominique Vuillaume. Molecular electronics: From single-molecule to large-area devices. *ChemPlusChem*, 84(9):1215–1221, 2019.

[113] Ganna Gryn'Ova, Kun Han Lin, and Clémence Corminboeuf. Read between the Molecules: Computational Insights into Organic Semiconductors. *J. Am. Chem. Soc.*, 140(48):16370–16386, 2018.

[114] Yanxia Yu, Ling Yang, Chunhua Liu, Wei Quan Tian, Yan Wang, and Shengbin Lei. The hierarchical construction of cross-junctions of molecular wires with covalent and noncovalent interactions at the liquid/solid interface. *Chem. Commun.*, 52:8317–8320, 2016.

[115] Eliseo Ruiz, Jordi Cirera, and Santiago Alvarez. Spin density distribution in transition metal complexes. *Coordination Chemistry Reviews*, 249(23):2649–2660, 2005. Magnetism - Molecular and Supramolecular Perspectives.

[116] Vihar P. Georgiev and John E. McGrady. Influence of low-symmetry distortions on electron transport through metal atom chains: When is a molecular wire really "broken"? *Journal of the American Chemical Society*, 133(32):12590–12599, 2011. PMID: 21749033.

[117] Shundong Yuan, Shiyan Wang, Zhaoyang Kong, Zhijie Xu, Long Yang, Diansheng Wang, Qidan Ling, and Yudou Wang. Theoretical studies of the spin-dependent electronic transport properties in ethynyl-terminated ferrocene molecular junctions. *Micromachines*, 9(3), 2018.

[118] Woo Youn Kim and Kwang S. Kim. Tuning molecular orbitals in molecular electronics and spintronics. *Accounts of Chemical Research*, 43(1):111–120, 2010. PMID: 19769353.

[119] Dongfeng Chai, Carlos J. Gómez-García, Bonan Li, Haijun Pang, Huiyuan Ma, Xinming Wang, and Lichao Tan. Polyoxometalate-based metal-organic frameworks for boosting electrochemical capacitor performance. *Chemical Engineering Journal*, 373:587–597, 2019.

[120] Matthew Genovese, Yee Wei Foong, and Keryn Lian. Designing polyoxometalate based layer-by-layer thin films on carbon nanomaterials for pseudocapacitive electrodes. *Journal of The Electrochemical Society*, 162(5):A5041, jan 2015.

[121] Paulo R. Bueno, Tiago A. Benites, and Jason J. Davis. The mesoscopic electrochemistry of molecular junctions. *Scientific Reports*, 6(1):18400, Jan 2016.

[122] Oves Badami, Toufik Sadi, Fikru Adamu-Lema, Paul Lapham, Dejiang Mu, Daniel Nagy, Vihar Georgiev, Jie Ding, and Asen Asenov. A Kinetic Monte Carlo study of retention time in a POM molecule-based flash memory. *IEEE Trans. Nanotechnol.*, 14(8):1–1, 2020.

[123] John P. Perdew, Weitao Yang, Kieron Burke, Zenghui Yang, Eberhard K. U. Gross, Matthias Scheffler, Gustavo E. Scuseria, Thomas M. Henderson, Igor Ying Zhang, Adrienn Ruzsinszky, Haowei Peng, Jianwei Sun, Egor Trushin, and Andreas Görling. Understanding band gaps of solids in generalized kohn–sham theory. *Proceedings of the National Academy of Sciences*, 114(11):2801–2806, 2017.

[124] Guo-Long Tan, Michael F. Lemon, and Roger H. French. Optical properties and london dispersion forces of amorphous silica determined by vacuum ultraviolet spectroscopy and spectroscopic ellipsometry. *Journal of the American Ceramic Society*, 86(11):1885–1892, 2003.

[125] Stefan Grimme, Jens Antony, Stephan Ehrlich, and Helge Krieg. A consistent and accurate ab initio parametrization of density functional dispersion correction (dft-d) for the 94 elements h-pu. *The Journal of Chemical Physics*, 132(15):154104, 2010.

[126] Paul Benioff. The computer as a physical system: A microscopic quantum mechanical hamiltonian model of computers as represented by turing machines. *Journal of Statistical Physics*, 22(5):563–591, May 1980.

[127] Richard P. Feynman. Simulating physics with computers. *International Journal of Theoretical Physics*, 21(6):467–488, Jun 1982.

[128] Colin D. Bruzewicz, John Chiaverini, Robert McConnell, and Jeremy M. Sage. Trapped-ion quantum computing: Progress and challenges. *Applied Physics Reviews*, 6(2):021314, 2019.

[129] L. M. K. Vandersypen, H. Bluhm, J. S. Clarke, A. S. Dzurak, R. Ishihara, A. Morello, D. J. Reilly, L. R. Schreiber, and M. Veldhorst. Interfacing spin qubits in quantum dots and donors—hot, dense, and coherent. *npj Quantum Information*, 3(1):34, Sep 2017.

[130] Stefanie Barz. Quantum computing with photons: introduction to the circuit model, the one-way quantum computer, and the fundamental principles of photonic experiments. *Journal of Physics B: Atomic, Molecular and Optical Physics*, 48(8):083001, mar 2015.

[131] Sébastien Pezzagna and Jan Meijer. Quantum computer based on color centers in diamond. *Applied Physics Reviews*, 8(1):011308, 2021.

[132] Davide Castelvecchi. Quantum computers ready to leap out of the lab in 2017. *Nature*, 541(7635):9–10, Jan 2017.

[133] Frank Arute, Kunal Arya, Ryan Babbush, Dave Bacon, Joseph C. Bardin, Rami Barends, Rupak Biswas, Sergio Boixo, Fernando G. S. L. Brandao, David A. Buell, Brian

Burkett, Yu Chen, Zijun Chen, Ben Chiaro, Roberto Collins, William Courtney, Andrew Dunsworth, Edward Farhi, Brooks Foxen, Austin Fowler, Craig Gidney, Marissa Giustina, Rob Graff, Keith Guerin, Steve Habegger, Matthew P. Harrigan, Michael J. Hartmann, Alan Ho, Markus Hoffmann, Trent Huang, Travis S. Humble, Sergei V. Isakov, Evan Jeffrey, Zhang Jiang, Dvir Kafri, Kostyantyn Kechedzhi, Julian Kelly, Paul V. Klimov, Sergey Knysh, Alexander Korotkov, Fedor Kostritsa, David Landhuis, Mike Lindmark, Erik Lucero, Dmitry Lyakh, Salvatore Mandrà, Jarrod R. McClean, Matthew McEwen, Anthony Megrant, Xiao Mi, Kristel Michielsen, Masoud Mohseni, Josh Mutus, Ofer Naaman, Matthew Neeley, Charles Neill, Murphy Yuezhen Niu, Eric Ostby, Andre Petukhov, John C. Platt, Chris Quintana, Eleanor G. Rieffel, Pedram Roushan, Nicholas C. Rubin, Daniel Sank, Kevin J. Satzinger, Vadim Smelyanskiy, Kevin J. Sung, Matthew D. Trevithick, Amit Vainsencher, Benjamin Villalonga, Theodore White, Z. Jamie Yao, Ping Yeh, Adam Zalcman, Hartmut Neven, and John M. Martinis. Quantum supremacy using a programmable superconducting processor. *Nature*, 574(7779):505–510, Oct 2019.

[134] Jens Koch, Terri M. Yu, Jay Gambetta, A. A. Houck, D. I. Schuster, J. Majer, Alexandre Blais, M. H. Devoret, S. M. Girvin, and R. J. Schoelkopf. Charge-insensitive qubit design derived from the cooper pair box. *Phys. Rev. A*, 76:042319, Oct 2007.

[135] R. Barends, J. Kelly, A. Megrant, A. Veitia, D. Sank, E. Jeffrey, T. C. White, J. Mutus, A. G. Fowler, B. Campbell, Y. Chen, Z. Chen, B. Chiaro, A. Dunsworth, C. Neill, P. O'Malley, P. Roushan, A. Vainsencher, J. Wenner, A. N. Korotkov, A. N. Cleland, and John M. Martinis. Superconducting quantum circuits at the surface code threshold for fault tolerance. *Nature*, 508(7497):500–503, Apr 2014.

[136] Sarah Sheldon, Easwar Magesan, Jerry M. Chow, and Jay M. Gambetta. Procedure for systematically tuning up cross-talk in the cross-resonance gate. *Phys. Rev. A*, 93:060302, Jun 2016.

[137] Sabrina S. Hong, Alexander T. Papageorge, Prasahnt Sivarajah, Genya Crossman, Nicolas Didier, Anthony M. Polloreno, Eyob A. Sete, Stefan W. Turkowski, Marcus P. da Silva, and Blake R. Johnson. Demonstration of a parametrically activated entangling gate protected from flux noise. *Phys. Rev. A*, 101:012302, Jan 2020.

[138] William D. Oliver and Paul B. Welander. Materials in superconducting quantum bits. *MRS Bulletin*, 38(10):816–825, Oct 2013.

[139] B.D. Josephson. Possible new effects in superconductive tunnelling. *Physics Letters*, 1(7):251–253, 1962.

[140] Brian David Josephson. The Discovery of Tunnelling Supercurrents. *Proc. IEEE*, 62(6):838–841, 1974.

[141] Leon N. Cooper. Bound electron pairs in a degenerate fermi gas. *Phys. Rev.*, 104:1189–1190, Nov 1956.

[142] V. L. Ginzburg. On the theory of superconductivity. *Il Nuovo Cimento (1955-1965)*, 2(6):1234–1250, Dec 1955.

[143] Vinay Ambegaokar and Alexis Baratoff. Tunneling between superconductors. *Phys. Rev. Lett.*, 10:486–489, Jun 1963.

[144] J.-P. Cleuziou, W. Wernsdorfer, V. Bouchiat, T. Ondarçuhu, and M. Monthioux. Carbon nanotube superconducting quantum interference device. *Nature Nanotechnology*, 1(1):53–59, Oct 2006.

[145] A. A. Bannykh, J. Pfeiffer, V. S. Stolyarov, I. E. Batov, V. V. Ryazanov, and M. Weides. Josephson tunnel junctions with a strong ferromagnetic interlayer. *Phys. Rev. B*, 79:054501, Feb 2009.

[146] J. W. A. Robinson, S. Piano, G. Burnell, C. Bell, and M. G. Blamire. Critical current oscillations in strong ferromagnetic π junctions. *Phys. Rev. Lett.*, 97:177003, Oct 2006.

[147] O. Vávra, S. Gaži, D. S. Golubović, I. Vávra, J. Dérer, J. Verbeeck, G. Van Tendeloo, and V. V. Moshchalkov. 0 and π phase josephson coupling through an insulating barrier with magnetic impurities. *Phys. Rev. B*, 74:020502, Jul 2006.

[148] G. J. Dolan. Offset masks for lift-off photoprocessing. *Applied Physics Letters*, 31(5):337–339, 1977.

[149] L J Zeng, S Nik, T Greibe, P Krantz, C M Wilson, P Delsing, and E Olsson. Direct observation of the thickness distribution of ultra thin AlOxbarriers in al/AlOx/al josephson junctions. *Journal of Physics D: Applied Physics*, 48(39):395308, sep 2015.

[150] T. Aref, A. Averin, S. van Dijken, A. Ferring, M. Koberidze, V. F. Maisi, H. Q. Nguyend, R. M. Nieminen, J. P. Pekola, and L. D. Yao. Characterization of aluminum oxide tunnel barriers by combining transport measurements and transmission electron microscopy imaging. *Journal of Applied Physics*, 116(7):073702, 2014.

[151] J. R. Schrieffer and J. W. Wilkins. Two-particle tunneling processes between superconductors. *Phys. Rev. Lett.*, 10:17–20, Jan 1963.

[152] Tine Greibe, Markku P. V. Stenberg, C. M. Wilson, Thilo Bauch, Vitaly S. Shumeiko, and Per Delsing. Are “pinholes” the cause of excess current in superconducting tunnel

junctions? a study of andreev current in highly resistive junctions. *Phys. Rev. Lett.*, 106:097001, Feb 2011.

[153] V Lacquaniti, M Belogolovskii, C Cassiago, N De Leo, M Fretto, and A Sosso. Universality of transport properties of ultrathin oxide films. *New Journal of Physics*, 14(2):023025, feb 2012.

[154] X.W. Zhou, H.N.G. Wadley, and D.X. Wang. Transient hole formation during the growth of thin metal oxide layers. *Computational Materials Science*, 39(4):794–802, 2007.

[155] Lunjie Zeng, Dung Trung Tran, Cheuk Wai Tai, Gunnar Svensson, and Eva Olsson. Atomic structure and oxygen deficiency of the ultrathin aluminium oxide barrier in Al/AlOx/Al Josephson junctions. *Sci. Rep.*, 6(March):1–8, 2016.

[156] Clemens Müller, Jared H Cole, and Jürgen Lisenfeld. Towards understanding two-level-systems in amorphous solids: insights from quantum circuits. *Reports on Progress in Physics*, 82(12):124501, oct 2019.

[157] P. Dutta and P. M. Horn. Low-frequency fluctuations in solids: $\frac{1}{f}$ noise. *Rev. Mod. Phys.*, 53:497–516, Jul 1981.

[158] Timothy C. Dubois, Salvy P. Russo, and Jared H. Cole. Atomic delocalization as a microscopic origin of two-level defects in Josephson junctions. *New J. Phys.*, 17, 2015.

[159] Hiroyoshi Momida, Seisuke Nigo, Giyuu Kido, and Takahisa Ohno. Effect of vacancy-type oxygen deficiency on electronic structure in amorphous alumina. *Appl. Phys. Lett.*, 98(4):2–5, 2011.

[160] Konstantinos D. Vogiatzis, Mikhail V. Polynski, Justin K. Kirkland, Jacob Townsend, Ali Hashemi, Chong Liu, and Evgeny A. Pidko. Computational Approach to Molecular Catalysis by 3d Transition Metals: Challenges and Opportunities. *Chem. Rev.*, 119(4):2453–2523, 2019.

[161] Hyuntae Jung, Yongmin Kim, Kyooho Jung, Hyunsik Im, Yu. A. Pashkin, O. Astafiev, Y. Nakamura, Hosik Lee, Y. Miyamoto, and J. S. Tsai. Potential barrier modification and interface states formation in metal-oxide-metal tunnel junctions. *Phys. Rev. B*, 80:125413, Sep 2009.

[162] M. Zemanova Dieskova, A. Ferretti, and P. Bokes. Tunneling through Al/AlOx/Al junction: Analytical models and first-principles simulations. *Phys. Rev. B - Condens. Matter Mater. Phys.*, 87(19):1–8, 2013.

[163] T. C. DuBois, M. J. Cyster, G. Opletal, S. P. Russo, and J. H. Cole. Constructing ab initio models of ultra-thin Al-AlOx-Al barriers. *Mol. Simul.*, 42(6-7):542–548, 2016.

[164] M. J. Cyster, J. S. Smith, J. A. Vaitkus, N. Vogt, S. P. Russo, and J. H. Cole. Effect of atomic structure on the electrical response of aluminum oxide tunnel junctions. *Phys. Rev. Research*, 2:013110, Jan 2020.

[165] M. J. Cyster, J. S. Smith, N. Vogt, G. Opletal, S. P. Russo, and J. H. Cole. Simulating the fabrication of aluminium oxide tunnel junctions. *npj Quantum Inf*, 7, 2021.

[166] Chang Eun Kim, Keith G. Ray, and Vincenzo Lordi. A density-functional theory study of the Al/AlOx/Al tunnel junction. *J. Appl. Phys.*, 128(15), 2020.

[167] John Clarke and Frank K. Wilhelm. Superconducting quantum bits. *Nature*, 453(7198):1031–1042, 2008.

[168] R. C. Jaklevic, John Lambe, A. H. Silver, and J. E. Mercereau. Quantum interference effects in Josephson tunneling. *Phys. Rev. Lett.*, 12(7):159–160, 1964.

[169] Morten Kjaergaard, Mollie E. Schwartz, Jochen Braumüller, Philip Krantz, Joel I.J. Wang, Simon Gustavsson, and William D. Oliver. Superconducting Qubits: Current State of Play. *Annu. Rev. Condens. Matter Phys.*, 11:369–395, 2020.

[170] John M. Martinis, Michel H. Devoret, and John Clarke. Quantum Josephson junction circuits and the dawn of artificial atoms. *Nat. Phys.*, 16(3):234–237, 2020.

[171] P. Krantz, M. Kjaergaard, F. Yan, T. P. Orlando, S. Gustavsson, and W. D. Oliver. A quantum engineer's guide to superconducting qubits. *Appl. Phys. Rev.*, 6(2):1–66, 2019.

[172] Jennifer Gosner, Björn Kubala, and Joachim Ankerhold. Quantum properties of a strongly driven Josephson junction. *Phys. Rev. B*, 99(14):7–9, 2019.

[173] Chi Chen, Yunxing Zuo, Weike Ye, Xiangguo Li, Zhi Deng, and Shyue Ping Ong. A Critical Review of Machine Learning of Energy Materials. *Adv. Energy Mater.*, 10(8):1–36, 2020.

[174] Charles Yang, Youngsoo Kim, Seunghwa Ryu, and Grace X. Gu. Using convolutional neural networks to predict composite properties beyond the elastic limit. *MRS Commun.*, 9(2):609–617, 2019.

[175] Maria Bendova, Zdenek Pytlicek, Jan Prasek, and Alexander Mozalev. The growth and unique electronic properties of the porous-alumina-assisted hafnium-oxide nanostructured films. *Electrochim. Acta*, 327:135029, 2019.

[176] Yillin Fan He, Dongzhi Yang Chu, and Zhensheng Zhuo. Cycle Stability of Dual-Phase Lithium Titanate (LTO)/TiO2 Nanowires as Lithium Battery Anode. *J. Multidiscip. Appl. Nat. Sci.*, 1(1):54–61, 2021.

[177] Nushrat Jahan, Salim Hussain, Huzef Ur Rahman, Insha Manzoor, Shashank Pandey, Kamran Habib, Syed Kaabir Ali, Reetika Pandita, and Chandramani Upadhyay. Structural, Morphological and Elemental Analysis of Selectively Etched and Exfoliated Ti3AlC2 MAX Phase. *J. Multidiscip. Appl. Nat. Sci.*, 1(1):13–17, 2021.

[178] E. Tan, P. G. Mather, A. C. Perrella, J. C. Read, and R. A. Buhrman. Oxygen stoichiometry and instability in aluminum oxide tunnel barrier layers. *Phys. Rev. B*, 71:161401, Apr 2005.

[179] M. J. Cyster, J. S. Smith, J. A. Vaitkus, N. Vogt, S. P. Russo, and J. H. Cole. Effect of atomic structure on the electrical response of aluminum oxide tunnel junctions. *Phys. Rev. Research*, 2:013110, Jan 2020.

[180] Paul Lapham and Vihar P Georgiev. Computational study of oxide stoichiometry and variability in the al/alox/al tunnel junction. *Nanotechnology*, 33(26):265201, apr 2022.

[181] Sungwook Hong and Adri C.T. Van Duin. Atomistic-scale analysis of carbon coating and its effect on the oxidation of aluminum nanoparticles by ReaxFF-molecular dynamics simulations. *J. Phys. Chem. C*, 120(17):9464–9474, 2016.

[182] T.Heine & G Seifert J. Frenzel, A. F. Oliveira N. Jardillier. Semi-relativistic, self-consistent charge Slater-Koster tables for density-functional based tight-binding (DFTB) for materials science simulations, TU-Dresden 2004-2009.

[183] Johannes Frenzel, Augusto F. Oliveira, Helio A. Duarte, Thomas Heine, and Gotthard Seifert. Structural and electronic properties of bulk gibbsite and gibbsite surfaces. *Zeitschrift fur Anorg. und Allg. Chemie*, 631(6-7):1267–1271, 2005.

[184] Luciana Guimarães, Andrey N Enyashin, Johannes Frenzel, Thomas Heine, Hélio A Duarte, and Gotthard Seifert. Imogolite Nanotubes: Stability, Electronic, and Mechanical Properties. *ACS Nano*, 1(4), 2007.

[185] Gonzalo Gutiérrez and Börje Johansson. Molecular dynamics study of structural properties of amorphous (formula presented). *Phys. Rev. B - Condens. Matter Mater. Phys.*, 65(10):1–9, 2002.

[186] Chang Eun Kim, Keith G. Ray, and Vincenzo Lordi. A density-functional theory study of the Al/AlOx/Al tunnel junction. *J. Appl. Phys.*, 128(15), 2020.

[187] M. Weides, R. C. Bialczak, M. Lenander, E. Lucero, Matteo Mariantoni, M. Neeley, A. D. O'Connell, D. Sank, H. Wang, J. Wenner, T. Yamamoto, Y. Yin, A. N. Cleland, and J. Martinis. Phase qubits fabricated with trilayer junctions. *Supercond. Sci. Technol.*, 24(5), 2011.

[188] N. Ishizawa, T. Miyata, I. Minato, F. Marumo, and S. Iwai. A structural investigation of α-Al 2 O 3 at 2170 K . *Acta Crystallogr. Sect. B Struct. Crystallogr. Cryst. Chem.*, 36(2):228–230, 1980.

[189] Sung Keun Lee, Sung Bo Lee, Sun Young Park, Yoo Soo Yi, and Chi Won Ahn. Structure of amorphous aluminum oxide. *Phys. Rev. Lett.*, 103(9):4–7, 2009.

[190] Elena O. Filatova and Aleksei S. Konashuk. Interpretation of the Changing the Band Gap of Al2O3 Depending on Its Crystalline Form: Connection with Different Local Symmetries. *J. Phys. Chem. C*, 119(35):20755–20761, 2015.

[191] I. Costina and R. Franchy. Band gap of amorphous and well-ordered Al2O3 on Ni3Al(100). *Appl. Phys. Lett.*, 78(26):4139–4141, 2001.

[192] Shuzheng Shi, Shuo Qian, Xiaojuan Hou, Jiliang Mu, Jian He, and Xiujian Chou. Structural and optical properties of amorphous Al2O3 thin film deposited by atomic layer deposition. *Adv. Condens. Matter Phys.*, 2018, 2018.

[193] C. Århammar, Annette Pietzsch, Nicolas Bock, Erik Holmström, C. Moyses Araujo, Johan Gråsjö, Shuxi Zhao, Sara Green, T. Peery, Franz Hennies, Shahrad Amerioun, Alexander Föhlisch, Justine Schlappa, Thorsten Schmitt, Vladimir N. Strocov, Gunnar A. Niklasson, Duane C. Wallace, Jan Erik Rubensson, Börje Johansson, and Rajeev Ahuja. Unveiling the complex electronic structure of amorphous metal oxides. *Proc. Natl. Acad. Sci. U. S. A.*, 108(16):6355–6360, 2011.

[194] Sushant Kumar Behera, Mayuri Bora, Sapta Sindhu Paul Chowdhury, and Pritam Deb. Proximity effects in graphene and ferromagnetic CrBr3 van der Waals heterostructures. *Phys. Chem. Chem. Phys.*, 21(46):25788–25796, 2019.

[195] Yipeng An, Jutao Jiao, Yusheng Hou, Hui Wang, Ruqian Wu, Chengyan Liu, Xuenian Chen, Tianxing Wang, and Kun Wang. Negative differential conductance effect and electrical anisotropy of 2D ZrB 2 monolayers. *J. Phys. Condens. Matter*, 31(6), 2019.

[196] W. F. Brinkman, R. C. Dynes, and J. M. Rowell. Tunneling conductance of asymmetrical barriers. *Journal of Applied Physics*, 41(5):1915–1921, 1970.

[197] L. S. Dorneles, D. M. Schaefer, M. Carara, and L. F. Schelp. The use of Simmons' equation to quantify the insulating barrier parameters in Al/AlOx/Al tunnel junctions. *Appl. Phys. Lett.*, 82(17):2832–2834, 2003.

[198] S. Bechstein, B. Beckhoff, R. Fliegauf, J. Weser, and G. Ulm. Characterization of an nb/al/alox/al/nb superconducting tunnel junction detector with a very high spatial resolution in the soft x-ray range. *Spectrochimica Acta Part B: Atomic Spectroscopy*, 59(2):215–221, 2004.

[199] John G. Simmons. Generalized Formula for the Electric Tunnel Effect between Similar Electrodes Separated by a Thin Insulating Film. *J. Appl. Phys.*, 34(6):1793–1803, 1963.

[200] John G. Simmons. Electric Tunnel Effect between Dissimilar Electrodes Separated by a Thin Insulating Film. *J. Appl. Phys.*, 34(9):2581–2590, 1963.

[201] K. Dalla Francesca, S. Lenfant, M. Laurans, F. Volatron, G. Izzet, V. Humblot, C. Methivier, D. Guerin, A. Proust, and D. Vuillaume. Charge transport through redox active [H 7 P 8 W 48 O 184] 33- polyoxometalates self-assembled onto gold surfaces and gold nanodots. *Nanoscale*, 11(4):1863–1878, 2019.

[202] Geng Min Lin, Chih Hsun Lin, Hao Howard Peng, Han Hsiao, Tsai Hui Wang, Ching Hwa Ho, Hsiu Fu Hsu, and Chun Hsien Chen. Effect of the Chemical Potentials of Electrodes on Charge Transport across Molecular Junctions. *J. Phys. Chem. C*, 123(36):22009–22017, 2019.

[203] Ayelet Vilan. Analyzing molecular current-voltage characteristics with the Simmons tunneling model: Scaling and linearization. *J. Phys. Chem. C*, 111(11):4431–4444, 2007.

[204] W. H. Rippard, A. C. Perrella, F. J. Albert, and R. A. Buhrman. Ultrathin aluminum oxide tunnel barriers. *Phys. Rev. Lett.*, 88:046805, Jan 2002.

[205] N. V. Nguyen, Oleg A. Kirillov, W. Jiang, Wenyong Wang, John S. Suehle, P. D. Ye, Y. Xuan, N. Goel, K.-W. Choi, Wilman Tsai, and S. Sayan. Band offsets of atomic-layer-deposited al2o3 on gaas and the effects of surface treatment. *Applied Physics Letters*, 93(8):082105, 2008.

[206] L.P.H Jeurgens, W.G Sloof, F.D Tichelaar, and E.J Mittemeijer. Structure and morphology of aluminium-oxide films formed by thermal oxidation of aluminium. *Thin Solid Films*, 418(2):89–101, 2002.

[207] A. Hasnaoui, O. Politano, J.M. Salazar, G. Aral, R.K. Kalia, A. Nakano, and P. Vashishta. Molecular dynamics simulations of the nano-scale room-temperature oxidation of aluminum single crystals. *Surface Science*, 579(1):47–57, 2005.

[208] T. Aref, A. Averin, S. van Dijken, A. Ferring, M. Koberidze, V. F. Maisi, H. Q. Nguyend, R. M. Nieminen, J. P. Pekola, and L. D. Yao. Characterization of aluminum oxide tunnel barriers by combining transport measurements and transmission electron microscopy imaging. *Journal of Applied Physics*, 116(7):073702, 2014.

[209] T. Holmqvist, M. Meschke, and J. P. Pekola. Double oxidation scheme for tunnel junction fabrication. *Journal of Vacuum Science & Technology B: Microelectronics and Nanometer Structures Processing, Measurement, and Phenomena*, 26(1):28–31, 2008.

[210] Ji Yeon Jung, Jae Hong Park, Yeon Jin Jeong, Kyu Ho Yang, Nam Ki Choi, Sun Hun Kim, and Won Jae Kim. Involvement of Bcl-2 family and caspases cascade in sodium fluoride-induced apoptosis of human gingival fibroblasts. *Korean J. Physiol. Pharmacol.*, 10(5):289–295, 2006.

[211] K Gloos, P J Koppinen, and J P Pekola. Properties of native ultrathin aluminium oxide tunnel barriers. *Journal of Physics: Condensed Matter*, 15(10):1733, mar 2003.

[212] Shin'ichi Morohashi and Shinya Hasuo. Experimental investigations and analysis for high-quality nb/al-alox/ nb josephson junctions. *Journal of Applied Physics*, 61(10):4835–4849, 1987.

[213] J. B. Barner and S. T. Ruggiero. Tunneling in artificial al_2o_3 tunnel barriers and al_2o_3-metal multilayers. *Phys. Rev. B*, 39:2060–2071, Feb 1989.